Metallophthalocyanine-based electrochemical sensors for accurate qualitative and quantitative analysis of emerging pollutants in water resources

by

Siyabonga Shoba

Submitted in the fulfilment of the requirements for the degree of

Doctor of Philosophy

in the School of Chemistry and Physics at the

University of KwaZulu-Natal

UNIVERSITY OF ™
KWAZULU-NATAL
INYUVESI
YAKWAZULU-NATALI

Supervisors: Prof. Irvin Booysen and Dr. Allen Mambanda

Declaration I - plagiarism

I, **Siyabonga Shoba**, declare that:

1. The research reported in this thesis, except where otherwise indicated, is my original research.
2. This thesis has not been submitted for any degree or examination at any other university.
3. This thesis does not contain other persons' data, pictures, graphs or other information, unless specifically acknowledged as being sourced from other persons.
4. This thesis does not contain other persons' writing unless specifically acknowledged as being sourced from other researchers. Where other written sources have been quoted, then:
    a. Their words have been re-written, but the general information attributed to them has been referenced
    b. Where their exact words have been used, then their writing has been placed in italics and inside quotation marks and referenced.
5. This thesis does not contain text, graphics or tables copied and pasted from the internet, unless specifically acknowledged, and the source is detailed in the thesis and the References sections.

[redacted] 28/03/2024

……… ……… ………………………………………

Signed Date

Declaration II - publications

Publications:

1. Shoba, S., Mambanda, A. and Booysen, I.N., 2024. *Electrospun Nanofiber Composite Utilized as an Electrocatalyst for the Detection of Acetaminophen in Multifarious Water Samples.* ***ACS Omega.***

2. Shoba, S., Mambanda, A. and Booysen, I.N., 2024. *Electrocatalytic effects of a clicked film of an asymmetric A3B (A= 3-oxyflavone, B= a-(ethynyl) benzyl alcohol) CoPc complex on a glassy carbon electrode for the detection of dopamine.* ***Journal of Electroanalytical Chemistry*, p.118086.**

3. **Shoba, S.,** Mambanda, A. and Booysen, I.N., 2024. *Electrocatalytic detection of Hg(II) using a platinum electrode modified with composite film of cobalt(II) phthalocyanine tetra-substituted with 1-(methoxymethyl)-benzotriazole groups and co-electropolymerized polypyrrole*. ***International Journal of Electrochemical Science.***

Manuscripts in preparation:

1. **Shoba, S.,** Mambanda, A. and Booysen, I.N., *Synergism in the electrocatalytic properties of cobalt phthalocyanine-carbon nanotube-polymeric electrospun nanofibers immobilized on a gold electrode for the detection of lead(II) ions*

[redacted] 19/11/2023

……… … ………………………………………

Signed (student) Date

[redacted]

28/03/2024

……………………………………… ………………………………………

Signed (supervisor) Date

[redacted]

… …………….. ………..28/03/2024……………………………

Signed (Co-supervisor) Date

Dedication in the isiZulu language

Kulomsebenzi ngiphakamisa umundeni wami wakwa Shoba ngokungeseka kanye nokungigqugquzela lapho sengifikelwa ukudikibala Phakathi nendlela ngiphelelwa Amandla okuphothula lomusebenzi.

Shoba

Mwelase

Ongaweli ngazibuko

Owela ngembambo zomfulo

Mathumba

Nduna ka Ndaba, emaphiseni

umagadla eguqile njengethole

Izandla zedlula ikhanda ngenikwenze kimi, niqhubeke nikwenze nakwabanye. Masiqhubeke njalo ngokubambisana nokuhloniphana.

Acknowledgments

First and foremost, I would like to thank God Almighty for giving me the strength and resilience to complete this work.

I would like to thank my supervisor, **Prof. I.N Booysen**, first for welcoming me to your research group and allowing me to conduct research with you on this project. I greatly appreciate your patience, guidance, assistance and encouragement during the study and writing of this work. Thank you.

I would like to give great thanks to my co-Supervisor Dr. A. Mambanda for his guidance, understanding and invaluable support that made this project a success. Thank you.

I am grateful to the **University of KwaZulu-Natal** for allowing me to make use of their laboratories, LAN and library to be able to conduct my research.

I gratefully acknowledge my colleagues: **Danica Moodley, Daniel Makanyane, Tariro Mapapiro, Kevin Kantize, Patrick Mangundu and Phakamani Dlamini** for willingly assisting, motivating and encouraging me, your support I highly appreciate.

I cannot close this chapter without referring to my friend; **Dr. Mthokozisi Mngun**i for his support and encouragement. My cousin, **Nhlakanipho B. Ngcobo** for love, support and his famous quote "**Ukubekezela kuzala impumelelo**".

Siphosethe Maqinana for your love and support, I appreciate you.

I would like to thank **uMam'Ntombi** for her encouragement and words of wisdom "**Awukho umshikashika ongenanzuzo Shoba, bekezela uzophumelela**". Mam'Ntombi, I truly appreciate the role you played in my life, continue to play that role of being a mom to us in that building, we love you.

Last, but not least, I gratefully acknowledge **CSIR, NRF** and the **University of KwaZulu-Natal**, I appreciate the financial support for my studies.

Abstract

Water is a precious resource and safeguarding it from pollution is paramount to ensure the well-being of both the environment and human health. Emerging contaminants such as pharmaceuticals and heavy metals pose significant threats, necessitating vigilant monitoring and appropriate action. Traditional laboratory-based analytical techniques like Gas Chromatography, ICP-OES and HPLC have been instrumental in quantifying pollutants. However, their high operational costs, maintenance requirements and the need for specialized personnel limit their widespread use, especially in resource-constrained countries. Electrochemical sensors have emerged as a promising solution. They provide real-time, portable and cost-effective options for on-site detection of pollutants in water. Current advancements in electrochemical sensors are centred around achieving selective detection using chemical modifiers, all while maintaining electrocatalytic sensitivity and reproducibility. These sensors can be tailored to target specific contaminants, making them highly efficient tools for monitoring water quality and ensuring the sustainability of this invaluable resource.

In the first experimental chapter, a glassy carbon electrode (GCE) was modified by an asymmetric metallophthalocyanine (MPc) complex, A_3B-CoPc-flav (where A = flavonyloxy substituent and B = an alkynyloxy substituent/molecular mast). The modification of an electrode was achieved *via* electrochemical grafting followed by clicked chemistry between the diazonium-functionalized GCE and the *a*-CoPc-flav3 to afford the GCE|clicked-*a*-CoPc-flav3. The chemically modified electrodes (CME) were utilized as electrocatalytic detectors for dopamine (DA) under optimized conditions. The response of the GCE|clicked-*a*-CoPc-flav3 was linear in the concentration range of 2 μM to 14 μM, attaining limits of detection and quantification of 0.311 and 0.942 μM, respectively, and high reproducibility (%RSD of 2.25%, N = 3). Interference studies were conducted, revealing a marginal shift in the DA peak potential in the presence of interfering substances. Despite this shift, the peak current intensity of DA remained largely unaffected, affirming the selectivity and accuracy of the CME. The analytical capabilities of the CME were further assessed using real water samples. The obtained percentage recoveries of (97.1%) of DA by the GCE|clicked-*a*-CoPc-flav3 and the well-established HPLC-MS method (113%) are both within the acceptable range of 80-120%.

In the second experimental chapter, a platinum electrode (Pt) was modified *via* the electropolymerization of polypyrrole (PPy) after its co-electrodeposition of *tetra*-[4-((1*H*-benzotriazole)methoxy)phthalocyaninato]cobalt(II) (CoPc-Bzt). The electrodeposition of CoPc-Bzt was performed in 1:1 DMF/acetonitrile containing 1 M tetrabutylammonium hexafluorophosphate (NBu_4PF_6) electrolyte over 20 cycles using cyclic voltammetry to afford a Pt|PPy/CoPc-Bzt (Bzt = benzotriazole). The resultant CME was prone to fouling by the analyte of interest, mercury(II). Due to fouling the differential pulse anodic stripping voltammetry (DPASV) was used to detect Hg(II) using the Pt|PPy/CoPc-Bzt within 10 µM to 100 µM linear range. The LOD and LOQ were found to be 3.11 and 10.00 µM, respectively. Interference studies illustrated that the detection capabilities of the CME were not affected by the presence of other heavy metal cations. The analytical performances of Pt|PPy/CoPc-Bzt (97.4%) and Inductively coupled plasma – optical emission spectroscopy (ICP-OES) (112.3%) are both within the acceptable range of 80-120%.

In the third experimental chapter, the Pb electrocatalytic sensing capability of a gold electrode modified *via* the adsorption of electrospun nanofibers (ENFs) and Nafion (Nf) as an annealed conductive top-layer was evaluated. The fabricated ENFs comprised of a core polymeric nanocomposite of *tetra*-4-(3-oxyflavonephthalocyaninato)cobalt(II) (CoPc-flav), the carboxylic acid functionalized multiwalled carbon nanotubes (*f*-MWCNTs) and polyaniline (PANI) encapsulated in a polyvinyl acetate (PVA) ENFs. The resultant CME, Au|ENFs-**1**-Nf was not prone to fouling as was found when using the bare and the other constructed CMEs whose signal stabilities were compromised by background electrolyte currents. The Au|ENFs-**1**-Nf electrode could detect the Pb(II) cations in a reproducible manner

(%RSD of 3.92%, N = 3) ranging from 8 to 125 µM, and limits of detection and quantification of 0.51 and 1.55 µM were obtained, respectively. However, the interference studies illustrated that the detection capabilities of the CME are severely compromised by the presence of other heavy metal cations. The analytical performance of the CME rendered a comparable percentage recovery (103%) with that of the ICP-OES (115%).

In the fourth experimental chapter, the nanofabrication and characterization of new conductive materials, PANI-CoPc-fur (**1**) ((PANI = polyaniline and CoPc-fur = *tetra*-4-(2-furanmethylthiophthalocyaninato)Co(II)) and PANI-CoPc-fur-*f*-MWCNTs (**2**) are reported. Subsequently, an electrospun nanofiber (ENF) composite was fabricated where the core comprised of **2** that was encapsulated with a PVA shell. The resultant nanoconjugate, ENFs-**2** was adsorbed on a glassy carbon electrode (GCE) followed by the immobilization of a permeable adhesion top layer of Nafion (Nf) to render the chemically modified electrode, GCE|ENFs-**2**-Nf. The classical physical properties of the electron-mediating layer for the CME synergistically aided in promoting its electrocatalytic activities. Consequently, the CME showed greater anodic and cathodic cyclic voltammetry (CV) peak currents compared to the bare GCE and other modified electrodes, indicating its higher sensitivity to acetaminophen (APAP), an emerging water pollutant of concern. Limits of detection and quantification (LOD and LOQ) values for APAP attained by squarewave voltammetry (SWV) were lower compared to those acquired using other electrochemical techniques. The detection of APAP at the GCE|ENFs-**2**-Nf attained by squarewave voltammetry (SWV) was linear from 10 to 200 µM of APAP and was reproducible (%RSD of 3.2%, *N* = 3). The respective calculated LOD and LOQ values of 0.094 and 0.28 µM were lower compared to those acquired using other electrochemical techniques. Analysis of APAP in the presence of commonly associated interferences metronidazole (MTZ) and dopamine (DA) illustrated a significant separation between the SWV peak potentials of APAP and MTZ, whereas there was some degree of overlap between the SWV current responses of APAP and DA. The analytical performance of the GCE|ENFs-**2**-Nf rendered a comparable percentage recovery (103.8%) with that of liquid chromatography–mass spectrometry (LC–MS) (106%).

Keywords: Emerging water pollutants, dopamine, mercury, lead, acetaminophen, electrocatalysis, chemically modified electrodes, metallophthalocyanines, electrospun nanofibers, electropolymerization, electrodeposition, selectivity, reproducibility, real sample analysis.

Table of contents

Declaration I - plagiarism i

Declaration II - publications ii

Acknowledgments..................... iv

Abstract..................... v

List of figures..................... xiii

List of tables..................... xx

List of schemes..................... xxii

Chapter 1..................... 1

Introduction..................... 1

1.1. General background:..................... 1

  1.1.1. Water pollution:..................... 1

  1.1.2. Pharmaceuticals as water pollutants:..................... 2

  1.1.3. Toxic heavy metals as water pollutants:..................... 4

  1.1.4. Conventional analytical methods for quantification of emerging pollutants:..................... 6

1.2. Rationale and motivation of the research study: 8

1.3. CoPcs as electrocatalysts: 15

1.4. Significance of conductive polymers and carbon-based nanomaterials: 17

1.5. Carbon nanotubes (CNTs): 20

1.6. CMEs with ENFs:..................... 22

References:..................... 25

Chapter 2..................... 34

Material and Instruments 34

2.1. Materials: 34

2.2. Instrumentation: 36

2.3. Fabrication of PVA-based ENFs using an Inveso nano spinner 24 multi-nozzle electrospinning/spraying machine: 37

2.4. Electrochemical studies were conducted using an Autolab Potentiostat equipped with:..... 38

Chapter 3..................... 40

The electrocatalytic effects of a clicked film of an asymmetric A_3B (A = 3-oxyflavone, B = α-(ethynyl)benzyl alcohol) CoPc complex on the detection of dopamine at a glassy carbon electrode..................... 40

3.1. Introduction: 40

3.2. Experimental: 43

3.2.1. Synthesis of tris-[4(3-oxyflavone)-4(1-phenyprop-2-yn-1-oxy)phthalocyaniato]cobalt(II) (α-CoPc-flav3) (1): 43

3.3. Results and discussion: 43

3.3.1. Synthesis and characterization: 43

3.4. Electrochemical studies: 51

3.4.1. Cyclic- and square-wave voltammetry: 51

3.5. Electrochemical modification and characterization: 55

3.6. Dopamine electrocatalysis: 63

3.6.1. Cyclic voltammetry: 63

3.7. Optimization of the electrocatalytic parameters of GCE|clicked-α-CoPc-flav3: 65

3.8. Conclusions 82

References: 83

Chapter 4 87

Exploring the Hg(II) electrocatalytic detection capabilities of a Pt electrode modified with an electron-mediating composite film of cobalt(II) phthalocyanine *tetra*-substituted with 1-(methoxymethyl)-benzotriazole groups and co-electropolymerized polypyrrole 87

4.1. Introduction: 87

4.2. Experimental: 90

4.2.1. Synthesis of 4-((1H-benzotriazole)methoxy)phthalonitrile (1) 90

4.2.2. Synthesis of tetra-[4-((1H-benzo[d][1,2,3]triazol-1-yl)methoxy)phthalocyaninato]cobalt(II) (CoPc-Bzt, 2): 91

4.3. Results and discussion: 91

4.3.1. Synthesis and spectral characterization: 91

4.3.2. Investigating the redox properties of 2: 96

4.3.3. Spectroelectrochemical experiments of CoPc-Bzt (2): 99

4.3.4. Modification of the bare platinum (Pt) electrode with a composite film of pyrrole(PPy) and CoPc-Bzt via electropolymerisation and electrodeposition: 101

4.3.5. Electrochemical impedance spectroscopy (EIS): 103

4.4. Optimization of the CME: 106

4.5. Conclusion: 125

References: 126

Chapter 5 130

Synergism in the electrocatalytic properties of electrospun cobalt phthalocyanine-carbon nanotube-polyaniline nanofibers immobilized on a gold electrode for the detection of lead(II) ions 130

5.1. Introduction: 130

5.2. Experimental: 133

5.2.1. Formation of the PANI-CoPc-flav composite and the PANI-CoPc-flav-f-MWCNTs (1) nanoconjugate: 133

5.2.2. Fabrication of PVA-based ENFs: 133

5.2.3. Fabrication of the Au|ENFs-1-Nf CME: 133

5.3. Results and discussion: 136

5.3.1. Synthesis, nanofabrication and characterization: 136

5.3.2. Comparative electron-transfer rates between the bare and respective CMEs: 148

5.4. Electrocatalytic detection of Pb(II) ions by the Au|ENFs-1-Nf: 151

5.4.1. Differential pulse anodic stripping voltammetry (DPV): 151

5.4.2. Signal stability of the modified electrodes: 154

5.4.3. Effective surface area and surface coverage: 157

5.4.4. Electrochemical impedance spectroscopy studies: 159

5.5. Optimization of parameters for DPASV analysis of Pb(II) using the Au|ENFs-1-Nf: 162

5.5.1. The effect of accumulation potential: 162

5.5.2. Accumulation time: 164

5.5.3. The effect of pH 166

5.5.4. Detection of Pb(II) ions using the Au|ENFs-1-Nf electrode: 168

5.5.5. Interference/Selectivity studies: 171

5.5.6. Standard additionanalysis of Pb(II) to the real water sample: 173

5.6. Conclusions: 177

References: 178

Chapter 6 182

An electrospun nanofiber composite utilized as an electrocatalyst for the detection of acetaminophen in multifarious water samples 182

6.1. Introduction: 182

6.2. Experimental: 185

6.2.1. Synthesis of the PANI-CoPc-fur (1) composite and the PANI-CoPc-fur-f-MWCNTs (2) nanoconjugate: 185

6.2.2. Fabrication of PVA-based ENFs: 185

6.2.3. Fabrication of the GCE|ENFs-2-Nf CME: 186

6.3. Results and discussion: 188

6.3.1. Synthesis, nanofabrication and characterization: 188

6.3.2. Electrocatalytic responses of the CMEs: 200

6.3.3. The effect of pH: 202

6.3.4. Effective surface area and surface coverage: 205

6.3.5. Electrochemical impedance spectroscopy studies: 207

6.3.6. Mechanism of electrocatalysis: 210

6.3.7. Hydrodynamic kinetic studies: 212

6.3.8. Diffusion-controlled kinetics: 214

6.3.9. Determination of analytical parameters: 215

6.3.10. Interference/Selectivity studies: 221

6.3.11. Real water sample analysis: 223

6.4. Conclusions: 226

References: 227

Chapter 7 232

Conclusions and future work 232

7.1. Conclusions: 232

7.2. Future work: 234

References: 236

List of figures

Figure 1.1: Sources of emerging water pollutants 2

Figure 1.2: Metallophthalocyanine structure showing non-peripheral (α-position 1-8) and peripheral (β-positions 9-16) sites of substitution. The purple center represents the metal in the center of the macrocycle. 16

Figure 1.3: A perspective of the polypyrrole (PPy) chain. 18

Figure 1.4: Structures of polyaniline (PANI) in its emeraldine base and salt form. 20

Figure 1.5: The structure of multi-wall carbon nanotubes (MWCNTs). 21

Figure 1.6: A pictorial representation of the core-shell ENFs. 23

Figure 2.1: A three-electrode system with a sample holder. 38

Figure 2.2: Electrochemical instrumentation set-up used during the research project 39

Figure 2.3: Interfacing of the Lambda 45 Perkin Elmer UV-Vis spectrophotometer with the Autolab potentiostat—galvanostat via an OTTLE cell for electronic spectroelectrochemical experiments. 39

Figure 3.1: Overlay solid-state FT-IR spectra comparison of the benzodinitriles (L1 and L2) as well as their corresponding asymmetric α-CoPc-flav3. 45

Figure 3.2: (**A**) Overlaid UV–Visible absorption spectra of α-CoPc-flav3 in DMF and DCM (**B**) Concentration effect on the absorbance of α-CoPc-flav3 in DMF. 46

Figure 3.3: Chemical structures of the radical fragment ions that were formed randomly due to the thermally-induced dissociations of α-CoPc-flav3 (**1**) in the presence of TFA. 49

Figure 3.4: (**A**) ESI-(+)-MS spectra of α-CoPc-flav3 without TFA and (**B**) with TFA added to promote ionization. (**C**) Theoretical pattern calculated via the isotopic mass calculator. 50

Figure 3.5: (**A**) Cyclic and (**B**) square-wave voltammograms of **α-CoPc-flav3** (**1**) at 100 mV/s. 53

Figure 3.6: CVs of 1 mM $K_3Fe(CN)_6$ solution containing 0.1 M KCl using the bare, azido-grafted and the GCE|clicked-α-CoPc-flav3. 57

Figure 3.7: Nyquist plots attained in a 5 mM $K_3[Fe(CN)_6]$ solution containing 0.1 M KCl using (A) bare GCE, (B) GCE|clicked-α-CoPc-flav3 while (c) shows the equivalent circuit used to fit the EIS data........ 60

Figure 3.8: Bode plots for 5 mM $[Fe(CN)_6]^{4-}/[Fe(CN)_6]^{3-}$ redox interconversion generated with the bare GCE and GCE|clicked-α-CoPc-flav3........ 61

Figure 3.9: (**A**) CVs of the GCE|clicked-α-CoPc-flav3 in pH 7.4 buffer solution at increasing scan rates (100 mV/s to 250 mV/s). (**B**) A plot of I_{pc} vs. scan rate measured at the redox couple **II**. 62

Figure 3.10: Stacked CVs attained using the bare GCE| and GCE|clicked-α-CoPc-flav3 in the electrolyte solution and 1.0 mM dopamine in PBS. 64

Figure 3.11: (A) Effect of pH on the SWV current responses of the GCE|clicked-α-CoPc-flav3 towards 1 mM DA in PBS; **(B)** a bar chart of the DA oxidation current responses at different pHs and **(C)** the correlation of pH and oxidation peak potential of DA pH. 66

Figure 3.12: (**A**) CVs of DA recorded at increasing scan rates (100 - 250 mV/s) using the GCE|clicked-α-CoPc-flav3, (**B**) the plot of peak current against the square root of scan rate and (**C**) a plot of potential against the log of scan rate........ 68

Figure 3.13: (**A**) Chronoamperograms of 0.8 mM DA in PBS (pH 6.2) at the GCE|clicked-α-CoPc-flav3 and (**B**) plot of I_c/I_b against $t^{1/2}$........ 70

Figure 3.14: (**A**) RDE-LSVs of the rotating GCE|clicked-α-CoPc-flav3 in PBS (pH 6.2) in the presence of 1 mM DA and at a scan rate of 0.015 V/s, (**B**) the Levich, (**C**) and the Koutecky-Levich plots........ 73

Figure 3.15: (**A**) SWVs recorded in varying concentrations of DA prepared in PBS (pH 6.30) using the GCE|clicked-α-CoPc-flav3. (**B**) Calibration curve of the current response of the GCE|clicked-α-CoPc-flav3 against DA concentration [DA]. 75

Figure 3.16: SWV responses of 1 mM DA in PBS in the presence and absence of 1 mM AA and NVP at the GCE|clicked-α-CoPc-flav3 m, pH = 6.3. 78

Figure 3. 17: (**A**) SWV responses at the GCE|clicked-α-CoPc-flav3 electrode after the standard addition of incremental volumes (2 mL) of 1.0 mM DA to 20 mL of real water sample. (**B**) Linear calibration plot. 80

Figure 3. 18: The real water sample (20.00 mL) spiked with incremental volumes (2.00 mL) of the 14.0 µM standard of DA detected using LC-MS (collected from the Amanzimtoti wastewater treatment plant). 81

Figure 4.1: Overlay solid-state FT-IR spectra of 4-((1H-benzo[d][1,2,3]triazol-1-yl)methoxy)phthalonitrile ligand **(1)** and CoPc-Bzt **(2)** complex................................92

Figure 4.2: UV–Visible spectrum of CoPc-Bzt (**2**) complex..93

Figure 4.3: ESI-(+)-MS spectra of **2** with TFA added to promote ionization. (**B**) Theoretical pattern calculated via the isotopic mass calculator. 94

Figure 4.4: Chemical structures of the radical fragment ions that are formed randomly due to the thermally-induced dissociations of CoPc-Bzt (**2**) in the presence of TFA...........95

Figure 4.5: (**A**) CV and (**B**) SWV of CoPc-Bzt at 100 mV/s. 97

Figure 4.6: UV–Vis spectral changes of CoPc-Btz at overpotentials applied at (**A**) –0.498 V, (**B**) −1.248 V, (**C**) 0.408 V (repeated at 0.650 V (dotted red line) and (**D**) 0.801 V. The initial spectrum is shown as a dashed line...100

Figure 4.7: CVs for the simultaneous electro-polymerization of 0.1 M pyrrole and co-electrodeposition of CoPc-Bzt on a Pt electrode at a scan rate of 0.1 V/s between the potential -1.5 to 1.5 V in an acetonitrile: DMF (1:1) blend using a 1 M NBu_4PF_6 as a supporting electrolyte: (**A**) 20 cycles and (**B**) 2 cycles. 102

Figure 4.8: Nyquist plots of the (**A**) bare Pt electrode and (**B**) Pt|PPy/CoPc-Bzt attained in a solution of 5 mM $[Fe(CN)_6]^{3/4-}$ prepared in PBS. (**C**) The equivalent circuit used to fit the EIS data...105

Figure 4.9: *Bode plots for the bare Pt and Pt|PPy/CoPc-Bzt electrodes.* 106

Figure 4.10: *DPASV responses of the bare Pt, Pt|PPy, Pt|CoPc-Bzt and Pt|PPy/CoPc-Bzt electrodes in 1 mM Hg^{2+} dissolved in 0.1 M HCl containing 0.4 M NaCl.*.......................................108

Figure 4.11: *(**A**) The CVs responses towards 5.0 mM $K_3[Fe(CN)_6]$ (prepared in 0.1 M KCl(aq)) using the Pt|PPy/CoPc-Bzt electrode for increasing scan rates. (**B**) A plot of I_{pa} vs square root of scan rate.*...110

Figure 4.12: *DPASV responses using the Pt|PPy/CoPc-Bzt electrode towards 1 mM Hg(II) electrocatalysis in 0.1 M HCl and 0.4 M NaCl at different accumulation potentials.* 112

Figure 4.13: *Optimization of experimental parameters at Pt|PPy/CoPc-Bzt on the DPASV peak currents of 1 mM Hg(II) in 0.1 M HCl and 0.4 M NaCl: Accumulation potential= -0.6* .114

Figure 4.14. *DPASV peak currents of 1 mM Hg (II) in 0.1 M HCl and 0.4 M NaCl (adjusted to target pH (1-9) using 1.M NaOH at Pt|PPy/CoPc-Bzt.* 116

Figure 4.15: *(**A**) DPASV responses of increasing concentrations of Hg(II) prepared in 0.1 M HCl and 0.4 M NaCl (pH = 8.28) using the Pt|PPy/CoPc-Bzt. (**B**): Calibration curve of the current*

response against Hg(II) concentration. Deposition conditions: accumulation time: 125 s and accumulation potential: -0.6 V. 119

Figure 4.16. (***A***) *DPASV responses of 1 g L^{-1} Hg^{2+} in 0.1 M HCl and 0.4 M NaCl (pH= 8.28) in the presence of 1 g L^{-1} Cd^{2+} and Pb^{2+} ions using Pt|PPy/CoPc-Bzt.* (***B***) *DPASV responses of 1 g L^{-1} Hg^{2+} only in 0.1 M HCl and 0.4 M NaCl (pH= 8.28).* ***Deposition conditions****: accumulation time 125 s and an accumulation potential -0.6 V.* 121

Figure 4.17: (**A**) DPASV responses at the Pt|PPy/CoPc-Bzt electrode after the standard addition of incremental volumes (mL) of 20 µM Hg(II) to 30 mL of real water sample. (**B**) Linear calibration plot. 123

Figure 4.18: A plot of emission intensity with increasing concentration of Hg(II) for the linear calibration of the ICP-OES........ 124

Figure 5.1: The structure of the CoPc-flav. 137

Figure 5.2: Overlayed UV-Visible absorption spectra of PANI, CoPc-flav and PANI-CoPc-flav nanocomposite........ 138

Figure 5.3: Stacked FTIR spectra of CoPc-flav, 4-(flavone-3-oxy)phthalonitrile, PANI, PANI-CoPc-flav (Q = quinoid, B = benzenoid), PANI-CoPc-flav-f-MWCNTs (**1**) and ENFs-**1**. 140

Figure 5.4: Stacked Raman spectra of CoPc-flav, PANI, PANI-CoPc-flav, f-MWCNTs and PANI-CoPc-flav-f-MWCNTs (**1**) nanocomposite. 142

Figure 5.5: Stacked X-ray diffractograms of CoPc-flav, PANI, PANI-CoPc-flav, f-MWCNTs, PANI-CoPc-flav-f-MWCNTs nanocomposite and ENFs-**1**. 144

Figure 5.6: SEM micrographs of (**A**) CoPc-flav, (**B**) PANI, (**C**) PANI-CoPc-flav, (**D**) PANI-CoPc-flav-f-MWCNTs (**1**), (**E**) ENFs-CoPc-PANI excluding f-MWCNTs and (**F**) ENFs-**1** (i.e. ENFs with embedded f-MWCNTs showing beaded woven-mats ENFs-**1**). 146

Figure 5.7: EDX micrographs of (A) ENFs and (B) ENFs-**1**. 147

Figure 5.8: (**A**) Cyclic voltammograms of 5 mM $K_3[Fe(CN)_6]$ in 0.1 M KCl. (**B**) Zoomed-in plot of all electrodes except Au|-PANI. 150

Figure 5.9: **(A)** DPASVs responses of 3 mM Pb(II) in 0.1 M sodium-acetate buffer (pH 5.0) obtained using the |Au, |Au-Nf,|Au-CoPc-flav, |Au-PANI, |Au-f-MWCNTs) and |Au-ENFs-**1**-Nf electrodes. **(B)** responses of each electrode in the electrolyte/buffer solution (no analyte). 153

Figure 5.10: Triplicated DPV scans of modified gold electrodes: (**A**) Au|-CoPc-flav, (**B**) Au|-f-MWCNTs, (**C**) Au|-PANI and Replicated DPASVs of (**D**) Au |ENFs-**1**-Nf in 1 mM Pb(II) ions dissolved in 0.1 M acetate buffer at pH 5.0. 156

Figure 5.11: (**A**) CVs of 5 mM $K_3Fe(CN_6)$ containing 0.1 M KCl (aq) at increasing scan rates as measured using the Au|ENFs-1-Nf electrode. (**B**) Plot of I_{pa} vs square root of scan rate. 158

Figure 5.12: Nyquist plots of 5 mM $K_3Fe_3(CN)_6$ dissolved in 0.1 M KCl at (**A**) |Au and electrode and (**B**) Au|ENFs-**1**-Nf electrodes. (**C**) The equivalent circuit is used to fit the EIS data. 161

Figure 5.13: Bode plots generated at 5 mM $K_3Fe(CN)_6$ dissolved in 0.1 M KCl with bare |Au and Au|ENFs-**1**-Nf electrodes. 161

Figure 5.14: DPASV responses of 1 mM Pb(II) at different accumulation potentials at the Au|ENFs-**1**-Nf electrode (at a deposition pH 1.15 and deposition time of 250 s). 163

Figure 5.15: DPASV responses of 1 mM Pb(II) at different accumulation times measured using theAu|ENFs-1-Nf electrode (at a deposition pH 1.15 and deposition of -0.8 V) . 165

Figure 5.16: DPASV responses of 3 mM Pb(II) at different pHs in acetate buffer at the Au|ENFs-**1**-Nf (at a deposition potential -0.8 V and deposition time of 250 s).... 167

Figure 5.17: (**A**) DPASV responses to different concentrations of Pb(II) at the Au|ENFs-**1**-Nf electrode. (**B**) Linear calibration plot. With a %RSD ≤ 5%, N = 3........................... 170

Figure 5.18: **(A)** DPASV analysis of a mixture of 1.0 g L^{-1} of Hg(II), Cd(II) and Pb(II) prepared in 0.1 M sodium acetate buffer solution using Au|ENFs-**1**-Nf, deposition conditions: pH = 1,15, accumulation time 250 s and accumulation potential -0.8 V. **(B)** Overlayed voltammograms of Pb(II) alone and Pb(II) in the presence of Cd(II) and Hg(II). 172

Figure 5.19: (**A**) DPASV responses at the Au|ENFs-1-Nf electrode after the standard addition of incremental volumes (μL) of 3.0 mM Pb(II) to 20 mL of real water sample. (**B**) Linear calibration plot. 175

Figure 5.20. A plot of emission intensity with increasing concentration of Pb(II) for the linear calibration of the ICP-OES. 176

Figure 6.1: The structure of CoPc-fur. 188

Figure 6.2: Overlay UV-Vis spectra of PANI, CoPc-fur and the PANI-CoPc-fur nanocomposite. 190

Figure 6.3: Stacked FT-IR spectra of PANI, CoPc-fur, PANI-CoPc-fur, PANI-CoPc-fur-f-MWCNTs and ENfs-**2**........192

Figure 6.4: Stacked Raman spectra of CoPc-fur, PANI, PANI-CoPc-fur, f-MWCNTs and PANI-CoPc-fur-f-MWCNTs........194

Figure 6.5: Stacked X-ray diffractograms (XRDs) of CoPc-fur, PANI, PANI-CoPc-fur, f-MWCNTs, PANI-CoPc-fur-f-MWCNTs and ENFs-**2** composites........196

Figure 6.6: SEM images of (**A**) CoPc-fur, (**B**) PANI, (**C**) PANI-CoPc-fur, (**D**) PANI-CoPc-fur-f-MWCNTs, (**E**) (PANI-CoPc-fur)PVA ENFs and (F) ENFs-2........198

Figure 6.7: EDX spectra of (A) ENFs and (B) ENFs-**2**........199

Figure 6.8: APAPs two electron quasi-reversible redox process on CME........201

Figure 6.9: CVs of 0.2 mM acetaminophen (APAP) in PBS using the bare GCE, GCE|Nf, GCE|CoPc-fur, GCE|PANI, GCE|f-MWCNTs and GCE|ENFs-**2**-Nf........202

Figure 6.10: DPV responses of APAP for the optimization of pH effects in PBS using the GCE|ENFs-**2**-NF........204

Figure 6.11: (A) CVs at increasing scan rates of 5 mM $K_3[Fe(CN_6)]$ prepared in an aqueous solution containing 0.1 M KCl at GCE|ENFs-**2**-Nf. (**B**) Plot of I_{pa} vs square root of scan rate........206

Figure 6.12: Nyquist plots of 5 mM $[Fe(CN)_6]$ prepared in 0.1 M KCl using the (**A**) bare GCE and (**B**) GCE|ENFs-**2**-NF. (**C**) The equivalent circuit is used to fit the EIS data........208

Figure 6.13: Bode plots generated at 5 mM $[Fe(CN)_6]$ prepared in 0.1 M KCl with bare GCE and GCE|ENFs-2-Nf........209

Figure 6.14: (A) Electrocatalytic CVs of APAP recorded at increasing scan rates (50-200 mV/s) using the GCE|ENFs-2-Nf. **(B)** The plot of peak current against the square root of scan rate and (**C)** plot of oxidation peak potential (E_{pa}) against the Log of scan rate........211

Figure 6.15: (**A**) RDE-LSVs of GCE|ENFs-**2**-Nf (1) in PBS (pH 3.09) in the presence of 1 mM APAP and a scan rate of 0.010 V/s, (**B**) the Levich, (**C**) and the Koutecky-Levich plots........213

Figure 6.16: (**A**) Chronoamperograms for GCE|ENFs-**2**-Nf in varying concentrations of mM APAP in pH 3.09 PBS buffer. A Potential of 0.508 V was applied (insert calibration graph at t = 5 s), (**B**) plot of $t^{1/2}$ Vs (I_{cat}/I_{buf}) and (**C**) plot of concentration vs slope........216

Figure 6.17: **(A)** Linear sweep voltammograms at GCE|ENFs-**2**-Nf in different concentrations of APAP, PBS buffer (pH = 3.09). **(B)** Calibration curve of current response vs concentration. 218

Figure 6. 18: **(A)** SWVs were recorded at different concentrations of APAP prepared in 0.1 M PBS (pH 3.11) using the |GCE-ENF-2-NF. **(B)** Calibration curve of the current response against APAP concentration (10 to 200 µM). 219

Figure 6.19: SWV responses of **(A)** 1 mM APAP in 0.1 M PBS in the presence of 1 mM of MTZ and DA, using the GCE|ENFs-**2**-Nf and **(B)** a comparison of the current responses of 1 mM APAP alone and in the presence of potential interferences (1 mM each of MTZ and DA). 222

Figure 6.20: **(A)** Overlay DPVs of the real water sample spiked with incremental volumes (0.5 mL) of the 3mM standard of APAP at the GCE|ENFs-2-Nf collected from the UMsunduzi river**,** **(B)** The standard addition calibration plot. 224

Figure 6.21: The real water sample spiked with incremental volumes (2 mL) of the 10 µM standard of APAP detected using LC-MS (collected from the UMsunduzi River). 225

List of tables

Table 1.1: Substituents and phthalocyanine used in this work...12

Table 2.1: List of commercially attained chemicals and their corresponding percentage purities...35

Table 3.1: Comparison of the voltammetric data (in V) between the novel **α-CoPc-flav3** as well as other tetra-substituted CoPc-flav and asymmetric CoPcs retrieved from literature. 54

Table 3.2: Redox potentials of the redox couples of **1** obtained via cyclic voltammetry.........54

Table 3.3: EIS data for a 5 mM $[Fe(CN)_6]^{3-/4}$ solution, collected using the bare GCE| and GCE|clicked-α-CoPc-flav3 electrodes. Error values are shown in brackets...........59

Table 3.4: Redox potential data for dopamine (DA) measured via CV using bare GCE and GCE|clicked-α-CoPc-flav3..64

Table 3.5: Comparison of catalytic rate constants for the detection of dopamine using CME. 71

Table 3.6: Comparison of LOD and LOQ values of the GCE|clicked-α-CoPc-flav3 other reported values in the literature for dopamine (DA)...76

Table 3.7: Measured peak area of DA of spiked (incremental addition of 2 mL of 1.0 mM DA to 20 mLAmanzimtoti water sample) by LC-MS...81

Table 4.1: Redox potentials of the redox couples attained via CV and SWV............................98

Table 4.2: Comparison of the voltammetric data (in V) between the novel **CoPc-Bzt** as well as other tetra-substituted CoPcs containing 1,2,4-triazol and imidazole retrieved from literature. 98

Table 4.3: EIS data collected in a 5 mM $[Fe(CN)_6]^{3-/4-}$ using bare Pt and modified (Pt|PPy/CoPc-Bzt electrodes.. 104

Table 4.4: Comparative analysis of LOD and LOQ values for the Pt|PPy/CoPc-Bzt electrode for the detection of Hg^{2+} against other CMEs reported in the literature................118

Table 4.5: Measured concentration of Hg(II) ions for the unspiked and spiked water sample collected along the Umngcwini stream, which joins the Umgeni river, water samples by ICP-OES. 124

Table 5.1: EIS data collected in a 5 mM $K_3Fe(CN)_6$ using bare|Au and Au|ENFs-**1**-Nf electrodes....160

Table 5.2: Comparison of LOD and LOQ values of the CMEs reported Pb(II) values in literature. 169

Table 5.3: Measured concentration of Pb(II) ions for the unspiked and spiked Amanzimtoti water samples by ICP-OES. 176

Table 6.1: EIS data collected in a 5 mM [$K_3Fe(CN)_6$] using bare and modified (|GCE-ENFs-**2**-Nf) electrodes....207

Table 6.2: Comparison of catalytic rate constants for the detection of APAP using CME....215

Table 6.3: Comparison of LOD values for GCE|ENFs-**2**-Nf towards the detection of APAP values reported in the literature. 221

Table 6.4: The measured LC-MS peak areas of APAP spiked in 20 mL of the Umsunduzi River water sample after the incremental addition of 2 mL of 10 µM APAP. 225

List of schemes

Scheme 3.1: Synthesis of the A_3B (A = 4-(3-oxyflavone), B = α-(ethynyl)benzyl alcohol) asymmetric α-CoPc-flav3 (**1**). 44

Scheme 3.2: Electrochemical grafting of the 4-azido benzodiazonium to the GCE interface and the Cu(I)-catalysed clicking of a-CoPc-flav3 to the grafted azido groups to produce the GCE|clicked-α-CoPc-flav3. 56

Scheme 4.1: Synthetic scheme for CoPc-Bzt. 90

Scheme 4.2: Schematic representation of the electro-polymerization of 0.1 M pyrrole and co-deposition of CoPc-Bzt films at the Pt. 103

Scheme 5.1: Sequential fabrication method of the Au|ENFs-**1**-Nf CME including the current responses for the differential pulse anodic stripping voltammetric (DPASV) analysis of a series of dilute Pb(II) ions standards. 135

Scheme 6.1: The sequential nanofabrication methods of the ENFs and electrode modification techniques employed to afford the CME. 187

Chapter 1

Introduction

1.1. General background

1.1.1. Water pollution

Water is a precious and limited resource that needs to be protected from pollution that emanates from improper waste disposal practices.[1] Various complex and interconnected human activities contribute to the generation of significant amounts of pollutants such as emerging contaminants (*e.g.* pharmaceuticals) and heavy metal pollutants. Key drivers of waste generation include industrial production, transportation, agriculture, and waste disposal practices, especially for urban municipalities, refer to **Figure 1.1.**[2,3,4]

Globally, the reuse or recycling of water, along with the safe discharge of treated water into downstream water resources, necessitates regular laboratory monitoring of water quality if such practices are to be sustained.[5,6] This monitoring ensures that the water intended for reuse meets appropriate standards and does not negatively impact the bulk water quality in reservoirs. Addressing this challenge requires the development and implementation of effective strategies and plans to mitigate water pollution, with a focus on monitoring and maintaining water quality.[7]

Given the scarcity of water in semi-arid regions, it is imperative to adopt measures that promote sustainable water management practices, including the prevention and reduction of pollution. By implementing robust monitoring systems and employing appropriate technologies, it becomes possible to identify and address potential sources of contamination, ensuring the safe and responsible use of water resources. Such actions are vital for safeguarding water quality, protecting ecosystems and supporting the well-being of communities in water-stressed areas.

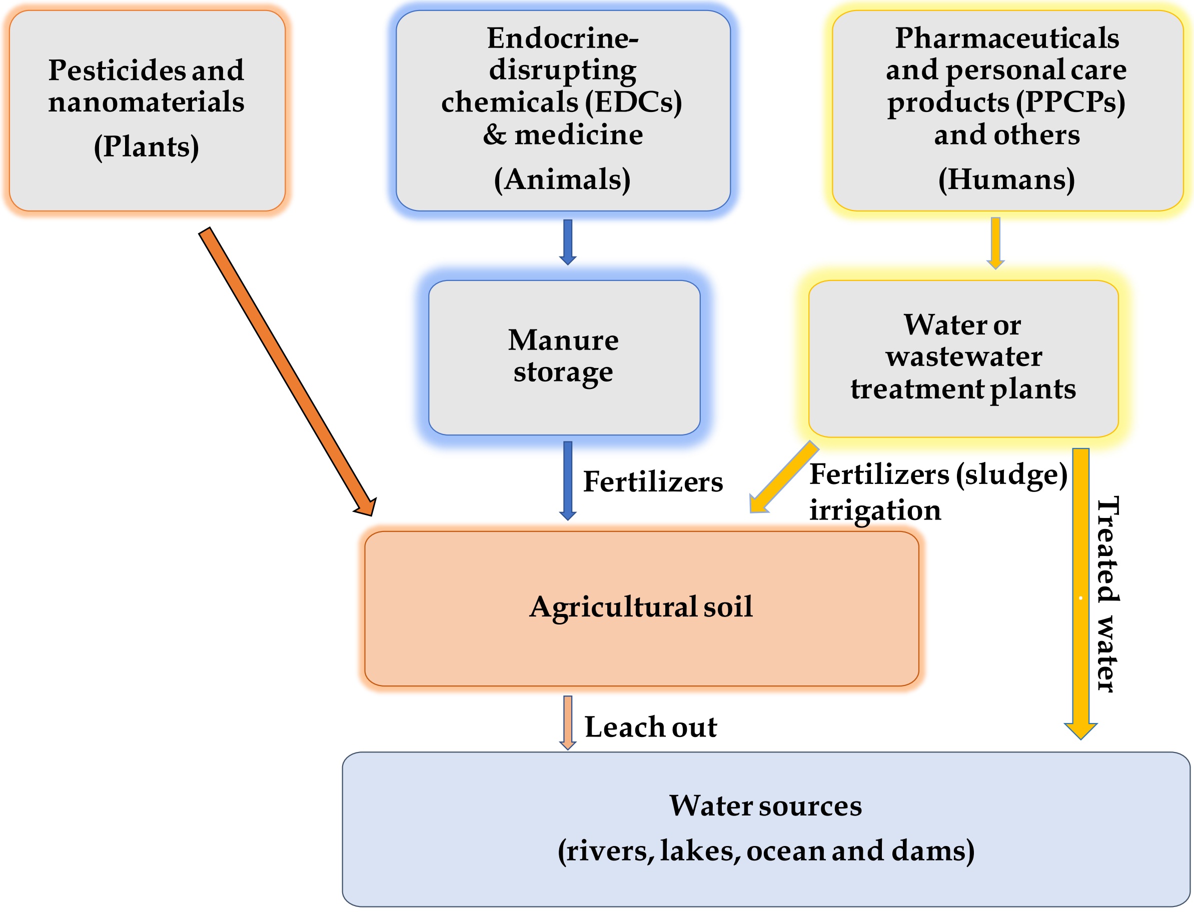

Figure 1.1: *Sources of emerging water pollutants.*

1.1.2. *Pharmaceuticals as water pollutants*

Despite the global use of pharmaceuticals for disease treatment and prevention in humans and animals, they are considered part of the group of so-called 'emerging pollutants' (which are synthetic or naturally occurring compounds or microbes that are generally not monitored). These pollutants occur as ultra-low concentration residues in partially-treated effluent water due to their incomplete removal by conventional chemical-co-biochemical treatment of domestic liquid waste in most wastewater treatment plants.[8,9] The widespread reliance on pharmaceutical drugs which are often used for symptom control rather than curing ailments, contributes to their higher concentrations in water.[10,11] Disposal of pharmaceutical wastes and unintended leakages form the salient pollution pathways and this pose a great ecological risk and threat to the eco-balancing of aquatic ecosystems as well as the reuse of water for human and animal consumption.[9,11]

Wastewater is a major source of emerging pollutants and related pollutants in natural water resources. Despite the integrated (chemical) treatment of waste influents, effluents from conventional wastewater treatment plants still contain trace levels of toxic pollutants, including pharmaceutical residues due to the complexity of the matrices of the water and also the low concentration levels of these contaminants.[10,12] Water treatment plants in European countries such as Spain were reported to have overall removal efficiencies as low as 6% (for carbamazepine) [13] to 12.5%.[14] Additionally, the leakage and planned disposal of waste from pharmaceutical companies and hospitals contribute to the contamination of water resources, although to a lesser extent.[14]

The treatment of influent sewer water has not reached a quality level that guarantees the complete removal of pollutants, thereby posing a risk of carrying contaminants in wastewater directly to surface water and causing high pollution levels in local rivers.[15] In South Africa there are laws and regulations for the safe disposal and reuse of treated water, though they are not strictly enforced. This leaves floodgates for rampant pollution of the national hydrological basins and wetlands.[16] This requires analytical monitoring of the pollutants in these aquatic ecosystems as an avenue to enforce good water quality and compliance with waste disposal standards and guidelines.[16]

The presence of pharmaceuticals in water bodies has adverse effects on the biological functions and ecological roles of aquatic organisms. In mammals and humans, the ill-health effects include the development of antibacterial resistance, disruption in physiological processes, increased cancer cases, and reproductive dysfunction.[16-18] In South Africa, the pollution of water supplies by emerging pollutants, including pharmaceuticals, has been on the rise.[19,20] Pollution monitoring of over-the-counter non-steroidal anti-inflammatory drugs (NSAIDs), commonly used drugs and selected antibiotic residues in the water and sediments of the Msunduzi, Springfield, Mbokodweni and Umngeni rivers in the KwaZulu-Natal (KZN) province have been conducted. Residues of these compounds were detected at trace levels of variable ranges.[21-26]

However, data on the occurrence of the broad spectrum of pharmaceuticals and heavy metals along the Msunduzi and Umgeni rivers as well as other major rivers in South Africa are still limited. These findings highlight the urgent need for comprehensive monitoring and mitigation strategies to identify and quantify the presence of pharmaceutical residues in water. Such strategies are also useful in assessing the removal efficiency of the pollutants in water treatment processes to prevent the discharge of partially treated effluent from recycling processes. Such pollution would otherwise cause adverse effects on the aquatic ecosystems, with the potential to disturb biodiversity. These water quality monitoring strategies ensure the provision of safe water resources for human and animal use.

1.1.3. Toxic heavy metals as water pollutants

Certain metal elements (*e.g.* Fe, Co, Mn, Zn, Cu, Co, Cr, Se, Ca and Mg) or their stipulated ions are essential for vital biological processes at lower (microgram range) concentrations. However, they can be highly toxic at concentrations higher than that required by the body.[27,28] The majority of metal elements (*p*-block elements e.g. As and Pb) and lighter *d*-block elements (e.g. Cd, Hg and Cr) are highly toxic to both animals and humans, even at low concentrations.[28,29] These metals are naturally occurring constituents of the earth's crust, cannot be destroyed and are highly soluble in aqueous medium.[30,31]

Due to population growth, industrialization, and urbanization, water bodies have become contaminated with heavy metals at concentrations that are higher than the geological background.[32,33] Furthermore, the heavy metal pollution of soil and water is contributed mainly by human activities in the agricultural and mining industries.[34,35] Some metals are acute toxins and poisonous. In addition, heavy metal cations in soils can be absorbed by the roots of plants and accumulate in the tissues of plants thereby contaminating the food products and ultimately animals at the top of the food chain.[28,36] Higher concentrations of toxic heavy metals, particularly mercury and lead have been discovered in the river and beach sediments of KZN at low concentration levels.[37-40]

Drinking of contaminated water, inhalation of contaminated air particulates and consumption of contaminated sea foods (fish, lobsters, crabs, shrimps, prawns, and crayfish clams, mussels and snails) or bottom-sediment feeders (mussels crabs) can expose animals/birds-of-prey as well as humans to trace levels of Hg. Chronic exposure leads to the bioaccumulation of the element to levels that can be lethal to the top-level animal in the pyramidal food chain. Mercury is well known acute toxin in mammals; in humans it irreversibly binds to thio-amino acids in cells of vital organs such as kidneys and liver, causing permanent damage. It also impairs the central nervous and reproduction systems and angiogenesis of cells leading to cancers. Chronic exposure to this element can lead to mental retardation and cerebral palsy in children.[41]

Lead (Pb) is widely used as an anti-knocking additive in the smooth combustion of petrol in automobile engines, as components of Pb/PbO batteries, metallic coating and water-soluble paints as well as in smelting and refining processes.[42-44] Human exposure to lead contamination can occur through drinking water, direct contact, consumption of food exposed to lead and inhalation of air polluted by car emissions.[42] Lead poisoning affects the normal functions of the liver, lungs, kidneys, bone marrow cells and the nervous system. It affects the normal functions of sex hormones and impairs the reproductive system.[44-46]

Considering the widespread prevalence of pharmaceutically-derived and metal-based pollutants in our environment and the detrimental effects these toxins have on health, there is a need for the development of simple, cost-effective and reproducible technologies for mobile as well as rapid water quality monitoring of heavy metals.

1.1.4. Conventional analytical methods for quantification of emerging pollutants

Quantification of pharmaceutical residues and heavy metals at ultralow levels in natural and wastewater samples is commonly achieved using laboratory-based analytical techniques. Pharmaceutical residues are quantified reliably by high-performance liquid chromatography-mass spectrometry (HPLC-MS) or HPLC with a photodiode array/fluorescence detector (HPLC-PDA/FLOUR). Those that are volatile can analyzed routinely by gas chromatography with mass spectrometry (GC-MS).

Heavy metal elements are simultaneously quantified by sensitive atomic spectroscopic techniques such as inductively coupled plasma optical emission spectroscopy (ICP OES) and ICP coupled to a mass spectrometer (ICP-MS). These techniques have reliable precision and sensitivity for most of the toxic metal elements and have limits of detection (LODs) in the parts per billion (ppb) and sub-parts per billion to femto levels, respectively.[47,48] Although these techniques provide highly accurate analytical data, they can only be executed in an analytical laboratory. Training of scientific staff is mandatory for the meticulous operation of the traditional instruments the majority of which are expensive. The analytical methods should be adopted for rigorous development and validation studies. Consequently, these factors limit the applications of the afore mentioned techniques in the qualitative and quantitative analysis of polluted water bodies for onsite and real-time analysis.

To address the need for real-time and portable analyzers for on-site detection of emerging pollutants in water, the development of electrochemical sensors has gained attention. Electrochemical sensors offer several advantages, including rapid response times, high sensitivity, cost-effectiveness, simplicity, and the potential for miniaturization.[48,49] Current trends are based on enhancing preferential detection capabilities by using chemical modifiers that promote selective interaction with the target analyte as opposed to interferents. The mechanism of selectivity should not compromise the electrocatalytic sensitivity and reproducibility of chemically modified electrodes (CMEs).

Fundamentally, CMEs render enhanced electrochemical signals towards a target analyte if the film can mediate the electron transfer between the analyte and electrode surface.[50] It implies that the redox reaction of the target analyte should occur within the same narrow potential window as for the coupled redox reaction of the modifier (the mediator) and the bare, thereby indirectly enhancing the rate of electron transfer between the analyte and bare conductive substrates. This rudimentary definition of electrocatalytic sensors can be expanded to include the design of CMEs containing components bearing suitable recognition elements with an electrocatalytic effect on the analyte redox reaction.[51,52] These elements within the modifier film promote coupled charge transfer interactions between the latter analyte and the surface of the bare electrode.

An interesting dimension is to electrospun these electron-mediating nanomaterials (electrocatalysts) as nanofibers (NFs) when they are embedded together with high-conductivity nanomaterials. Electrospun nanofiber (ENF)-based electrode films are chemically more durable and have larger effective surface areas and active catalytic site loadings.[53,54] Their filter-fill and capability allow analytes to potentially sorb and permeate within their films, and thus potentially concentrate them close to the embedded electrocatalysts and other electron-mediating nanomaterials. Consequently, enhanced electron-transfer kinetics at the ENFs-modified electrode surface. Predominately, chemically modified electrodes have been used as voltammetric, amperometric and impedimetric sensors of various analytes in environmental samples including residues of pollutants of concern and priority for monitoring.[55,56] They have also been used as sensitive spectroelectrochemical sensors by monitoring the spectral changes that accompany an electroactive analyte when it undergoes a redox transformation at a set potential. Such data is useful in the equivocal assignment of peaks independently observed in the cyclic voltammograms of the respective analyte as well as the delineation of the possible products of the redox reaction.[57,58]

1.2. Rationale and motivation of the research study

In South Africa, water pollution is a scourge of national proportions and thus, innovative strategies and technologies to prevent and protect water sources have to be developed. These range from continuously monitoring the quality of water used for consumption, agricultural and industrial purposes to the deployment of cleaner treatment technologies that minimize the rampant discharge of residues of environmental contaminants of concern. From the pollution monitoring front, the use of environmentally friendly, cheaper and sensitive analytical methods such as electrochemical sensors can allow real-time detection of all forms of pollutants be it in a water treatment, industrial waste-discharge canal or in water-source resources (national water rivers and dams that supply fresh and potable water). The main objective of this research work was to design and fabricate new cobalt(II) phthalocyanine (CoPc)-derived CMEs) and explore their electrocatalytic sensing capabilities towards pharmaceutical residues (dopamine, acetaminophen) and toxic metal elements (Hg, Pb) in real samples. For metal pollutants, the performance of the CMEs was assessed by a comparative analysis with the inductively coupled plasma-optical emission spectrometric technique.

As bare electrodes are prone to surface passivation and through poor sensitivities, electron-mediating films comprised of peripherally *tetra*-substituted cobalt phthalocyanines (CoPcs) and their composites were used to modify bare electrode surfaces. The motivation behind the use of the CoPc composite modifiers stems largely from promoting electrocatalytic sensitivity and selectivity. In this work, electron-mediating capabilities of CoPcs with different peripheral substituents at the surface of various bare electrodes were explored. These N_4-metallocyclic complexes have been reported to display optimal redox properties under applied potential which is facilitated by the delocalized 18 *pi*-electrons and the redox active central metal.[59-63] Positioning substituents with varying stereo-electronic properties in the peripheral (β) or non-peripheral (α) positions on the Pc of the metal complex does not only alter their redox properties but can mechanistically induce selective detection of target analytes.[64-66]

Moreover, the planar surface due to the extended *π*-surfaces enables their immobilization to form robust electrode surfaces as well as the compositing with other complementary conductive materials.[67] Fabrication methods range from simple adsorption "drop-dry", to electrodeposition and electropolymerization, followed by self-assembled monolayer formation on specifically Au electrodes and electrochemical grafting of GCE and then clicking of CoPc monomers on the latter.[67-69] CoPcs have also been incorporated in various bulk composite or nanoarchitecture thin films which serve as intermediating surfaces that increase electron transfer kinetics between the analyte solution and the bare electrode surfaces. Thus, the above-mentioned favorable features of CoPcs make them well-suited for fabricating selective, sensitive and reproducible electrochemical sensors for pollutant screening in real water samples.

In this research work, several CoPc substituents were utilized as components that can induce a specific recognition towards analytes through complementary intermolecular interactions, *see* **Table 1.1**. For example, in one of the studies, a low symmetry A_3B CoPc-flav complex with an asymmetric (A_3B) quartet substituents, (*tris*-[4(3-oxyflavone)-4(1-phenyprop-2-yn-1-oxy)phthalocyaniato]cobalt(II)) was synthesized. The complex has the 'antenna' moieties (the three peripheral 'A' substituents) on the CoPc, anchored to the electrode surface *via* a triazolyl-linked 'ground tackle' (B) formed from the click reaction between the pre-grafted azides (masts) and the alkynyl linker (B) of the A_3B CoPc-flav.[70] Specifically, the A groups were all hydroxyflavonyl groups while the B anchoring group was an ethynylbenzyl unit. By combining these components, a novel substituted CoPc structure was formed.

Flavonoids are natural bioactive compounds that serve crucial electrobiochemical roles in plants.[71,72] Their incorporation as substituents is thought to improve the selectivity and sensitivity of biosensors when targeting specific biological analytes.[73] To further explore this aspect, a low symmetry A_3B CoPc-flav complex were synthesized (*vide supra*) where the sensor containing the clicked A_3B CoPc-flav complex makes use of its flavonyl antenna groups to enhance the selective detection of dopamine while assuring CME robustness with the aid of its clicked functionality.

In this research study, benzotriazole-methoxy groups were incorporated into a CoPc complex as peripheral substituents to impart selectivity on the CME-containing electron-mediating films incorporating this metal complex. The primary mode of interaction between the analyte of concern, mercury(II) and the modifying thin film occurred through the nitrogen atoms of the benzotriazoles. Moreover, the capability of the CME to differentiate between the analyte of concern and other heavy metal interferents is fundamentally based on their strength of interactions with the benzotriazole active sites.[74] Another beneficial trait of benzotriazole is its characteristic passivation of the redox-active metal substrates for corrosion protection and we foresaw imparting of this trait onto the redox behaviour of the CoPc-Bzt modified electrodes to render stability and in turn reproducible electrocatalytic performances.[75-77]

Indicative of flavone as a plant-based secondary metabolite, the furan is an *O*-heterocyclic moiety that is common to various natural products found within the bran of most small seed grains.[78,79] Chohan *et al*., have already shown that a furan *tetra*-substituted CoPc (CoPc-fur) film immobilized on a GCE portrayed electrocatalytic activities towards bio-analyte, *L*-cysteine oxidation.[78] In this research study, the hypothesis that the repurposing of CoPc-fur as a component within a polymeric nanocomposite electrode modifier may facilitate the binding affinity through diverse non-covalent interactions such as π-π stacking and hydrogen bonding was tested.

Table 1.1: *Substituents and phthalocyanine used in this work: tris-[4(3-oxyflavone)-4(1-phenyprop-2-yn-1-oxy)phthalocyaninato]cobalt(II) (a-CoPc-flav3), tetra-[4-((1H-benzotriazole)methoxy)phthalocyaninato]cobalt(II), (CoPc-Btz), tetra-4-(3-oxyflavonephthalocyaninato)cobalt(II), (CoPc-flav) and tetra-4-(2-furanmethylthiophthalocyaninato)cobalt(II), (CoPc-fur).*

Substituent	**CoPc-X (X= substituent)**
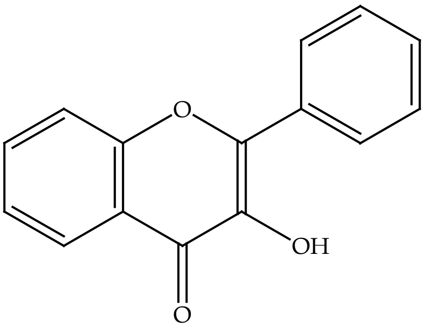 3-Hydroxyflavone and 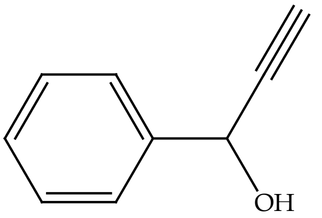 Ethynylbenzyl alcohol	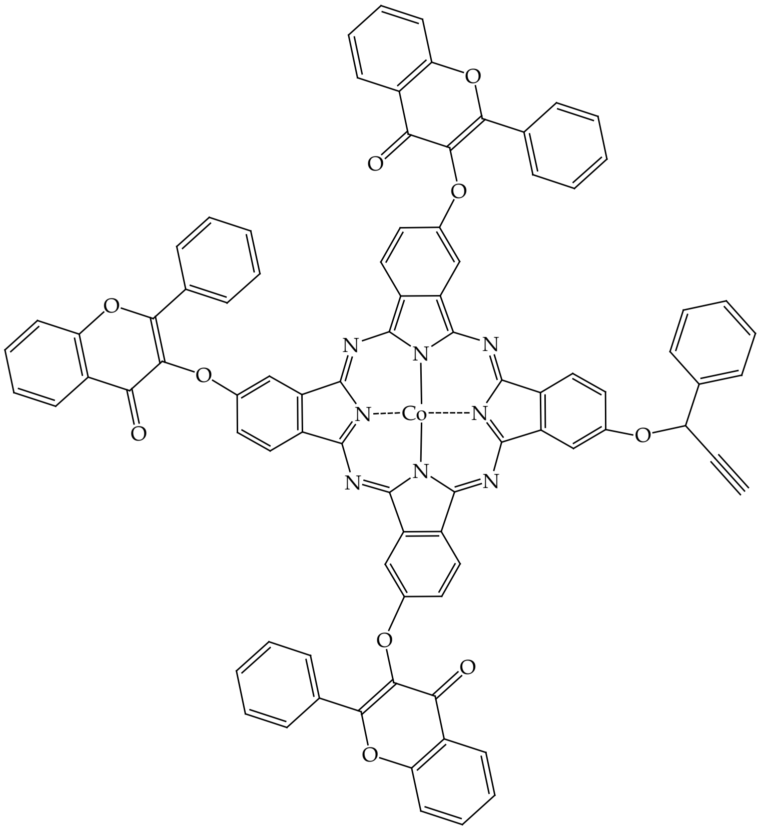 α-CoPc-flav3

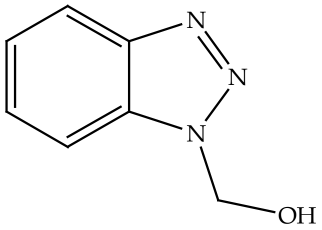 1*H*-benzotriozole-1-methanol	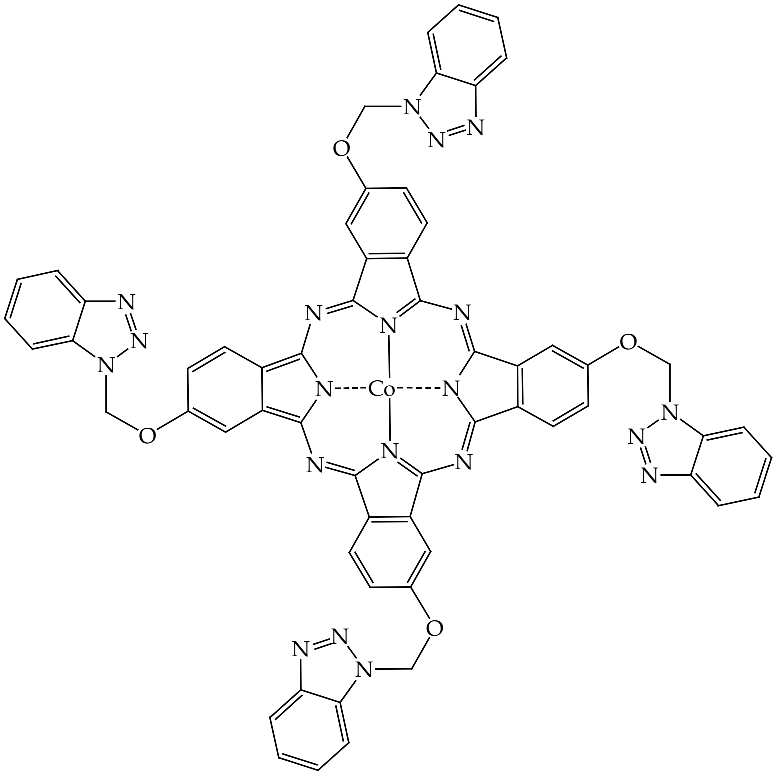 CoPc-Btz
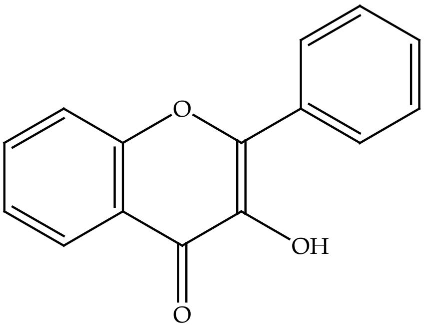 3-Hydroxyflavone	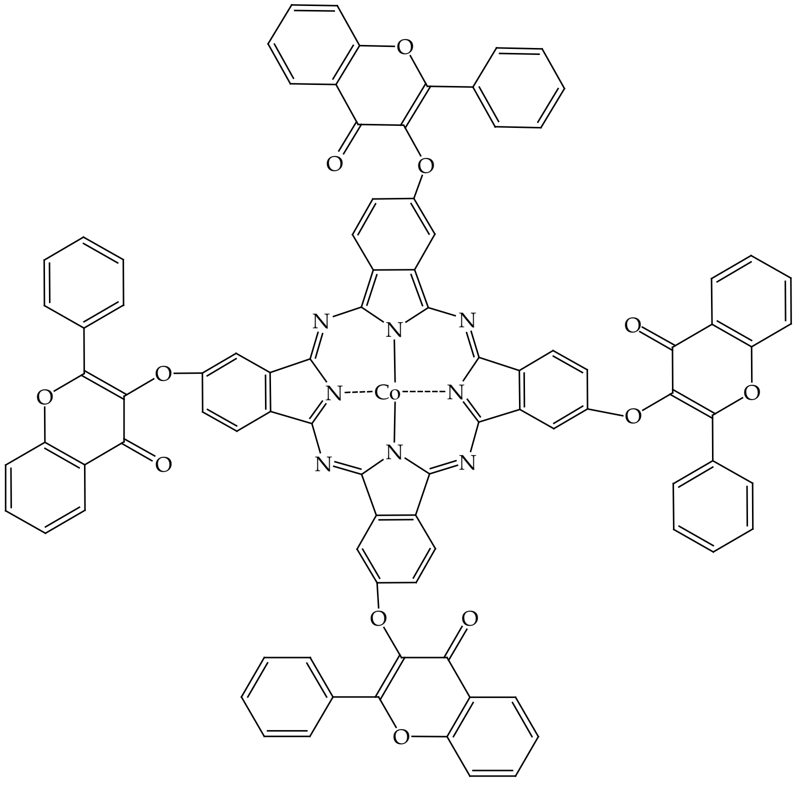 CoPc-flav

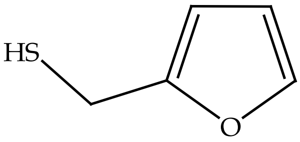 2-furan methanethiol	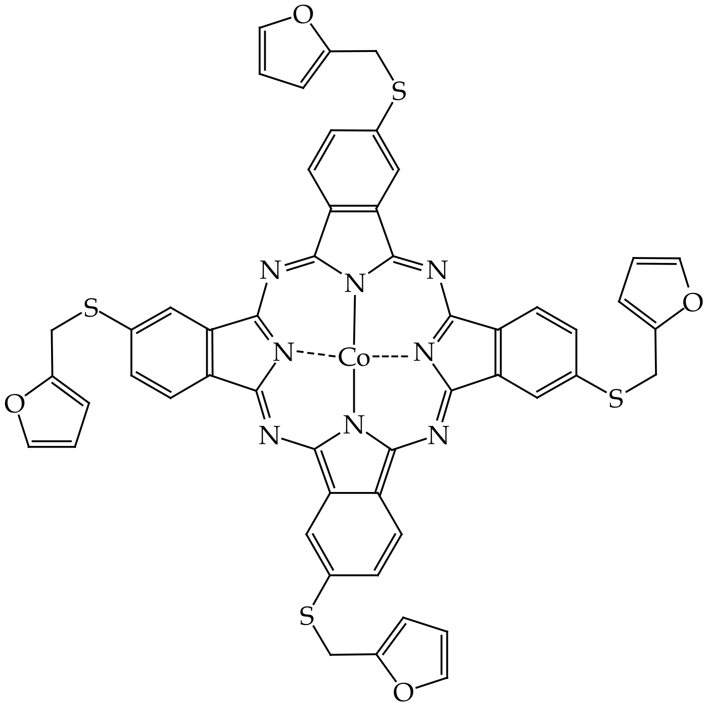 CoPc-fur

Various electron mediators such as polypyrrole (PPy), polyaniline (PANI) and carboxylic acid functionalized multiwalled carbon nanotubes (*f*-MWCNTs) as well as their combinations were assessed to enhance the electrochemical conductivity of their CMEs. This innovative CME design approach aimed to leverage the conductivity-enhancing properties of these mediators, while simultaneously harnessing the selective recognition capability inherent in the CoPc substituents. The resulting chemically modified electrode (CME) thin films were designed to synergistically discern the target analyte, capitalizing on the combined attributes of CoPc substituents and electron mediators. Furthermore, their CoPc conjugates were embedded into cores of electrospun nanofibers (ENFs) with polyvinyl acetate (PVA) shells and nanofabrication of these ENFs avoids the leaching of CMEs which is a wide-spread technical challenge with CMEs prepared via adsorption “drop-dry method”.

1.3. CoPcs as electrocatalysts

As reiterated, the electrocatalytic capabilities of CoPcs are largely attributed to the metal- and Pc-based redox properties which manifest in the form of the Co(I)|Co(II) and Co(II)|Co(III) redox couples while the Pc(-2) ligand can sequentially undergo redox transformations. More specifically, the respective oxidations of the Pc ring occur through the loss of one or two electrons, resulting in Pc(-1) and Pc(0) while reduction involves the successive additions of one to four electrons, yielding Pc(-3), Pc(-4), Pc(-5), and Pc(-6).[81-83] In conjunction with their redox properties, the planar structure of CoPcs allows them to be immobilized flat on bare electrode surfaces rendering stable mono- or multilayers stabilized by *pi*-conjugation on the GCEs or by direct covalent bonding with metallic substrates, *see* **Figure 1.2**. High-resolution transmission electron microscopy has revealed that the positions of sulphur-containing substituents can render CoPcs with varying orientations ranging from umbrella, octopus, and vertical.[84,85] Another core benefit to the use of CoPcs as thin conductive films is the fine-tuning of their redox potentials by varying the steric and electronic factors of substituents. Ultimately, the latter renders metal and Pc-centred redox properties within the potential windows of different analyte types.

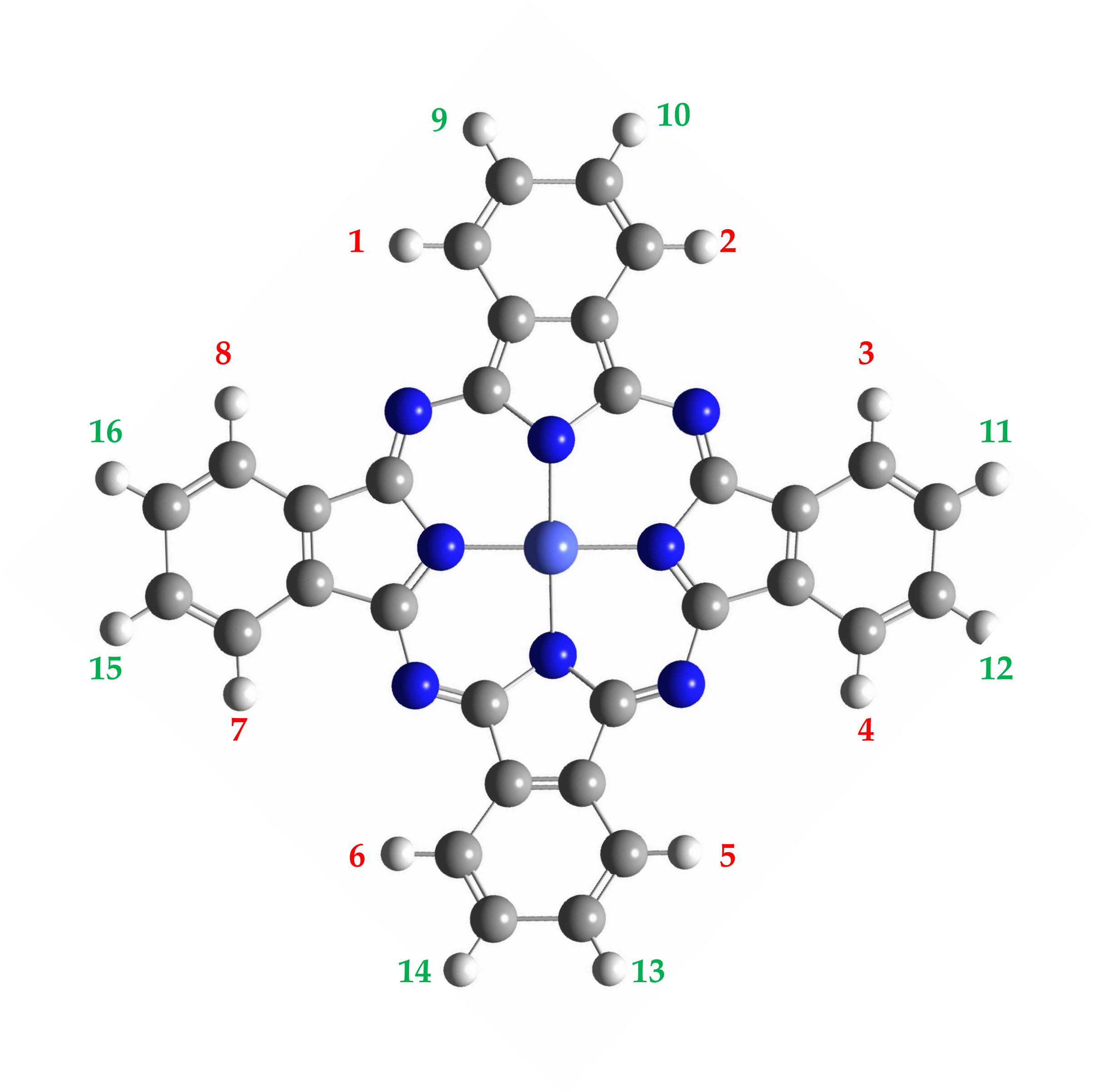

Figure 1.2: *Metallophthalocyanine structure showing non-peripheral (a-position 1-8) and peripheral (β-positions 9-16) sites of substitution. The purple center represents the metal in the center of the macrocycle.*

These conducive attributes have made monomeric CoPcs good electrocatalysts on different electrode substrates for the detection of water pollutants. For example, Moraes *et al.* developed an electrochemical sensor for the direct determination of Carbaryl in water.[86] They utilized a glassy carbon electrode modified with cobalt phthalocyanines and multi-walled carbon nanotubes where the sensor exhibited an ultrahigh sensitivity of 5.46 ± 0.02 nmol L^{-1} (equivalent to 1.09 ± 0.02 μg L^{-1}) for carbaryl in water.[86] These heterogenous catalysts have been also conjugated with biomass-derived supports as shown in the example of a CME created from the dropping and drying of a CoPc-chitosan composite which was afterwards applied in the voltammetric determination of sulphanilamide.[87] This CME could even detect the water pollutants at lower limit of 0.27 μmol dm^{-3} than the former CoPc-MWCNT modified electrode.

Currents trends entails the employment of low-symmetry cobalt phthalocyanines to modified GCEs by stepwise electrochemical-grafting of the substrate followed by click chemistry catalyzed by an appropriate Cu(I) salt.[88] Nyokong and co-workers has showed that an asymmetrical CoPc clicked to a GCE afforded statistically accepted percentage recovery of mercury(II) in a laboratory tap water. Interestingly, this CoPc contains three benzothiazole antenna groups (per CoPc molecule) which are conveniently exposed to the bulk sample solutions for distinguishing between the heavy metal cations of Hg(II), Cu(II), Pb(II) and Cd(II). The basis of selective electrocatalytic sensing capabilities of this CME were ascribed on the varying coordination affinities of the respective cations towards the hard nitrogen and soft sulphur donor atoms. This mechanism of electrocatalytic activity rendered nanomolar level detection limits of 81.94 nM for Hg(II), 327.71 nM for Pb(II), 55.87 nM for Cu(II), and 347.06 nM for Cd(II).[88]

1.4. Significance of conductive polymers and carbon-based nanomaterials

Combined physical properties of monomers that can be covalently linked in a linear arrangement resulting in long chain polymers and these effects can be further enhance through interlocking polymer chains which render advanced three-dimensional bulk polymeric structures.[89] For instance, with respect to electronic effects, these polymers are conductive where they generally display enhanced monomer-derived electronic properties as well as polymer-chain length-dependent properties.[90] It is well document that the high tensile strength of conductive polymers can render mechanical strength to CMEs modified with polymeric composites.

In electrochemical sensor development, working electrodes have been modified either by *in situ* electropolymerization of monomers on the latter or *via* the drop-dry method of bulk polymers.[91-94] As expected, *in situ* electropolymerization is a more reproducible electrode modification method that renders electrocatalytic signals with high precision. Apart from the good mechanical strength, conductivity and induced charge-conduction, these polymers can facilitate selective detection through auxiliary interactions with the analyte of concern thereby enhancing its selectivity as well as the electrode current response. For this research study, the following conductive polymers were considered: polypyrrole (PPY) and polyaniline (PANI).

Polypyrrole (PPy) stands out as a widely utilized conducting polymer in commercialized applications due to its superior conductivity, excellent solution stability and facile fabrication methods.[95] In electrode modification, a PPy electrode film prevents fouling associated with most bare conductive substrates.[96,97] PPy is biocompatible with the working environment, thus making it an attractive choice for various electrochemical applications.[98] The molecular structure of PPy comprises a conjugated backbone of anti-configured pyrrole monomers, linked linearly by C-C bonds. The linear polymer chains of PPy typically adopt a planar conformation within the film, with a parallel orientation to one another.[99] This arrangement facilitates efficient longitudinal charge transfer and enhances the overall conductivity of the modified electrode. **Figure 1.3** depicts the polymeric structure of PPy, highlighting the repeating pyrrole units and the extended conjugated system that contributes to its unique electronic properties.

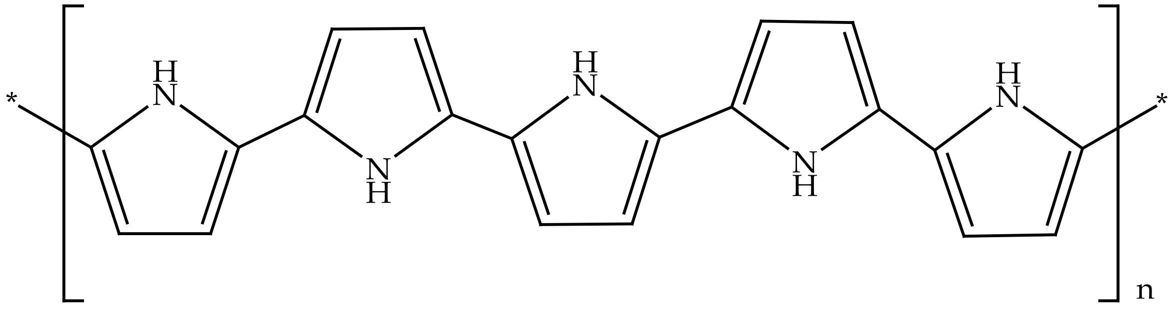

Figure 1.3*: A perspective of the polypyrrole (PPy) chain.*

Furthermore, conductive polymers have been utilized in a complementary manner to synergistically improve the sensitivity and stability of CMEs. Like the contrasting effects of a CME with an adsorbed film of phytic acid (PA) functionalized polypyrrole (PPy)/graphene oxide (GOx) nanocomposite against a CME containing the latter with a top permeable polymeric Nafion (Nf) layer where the latter rendered higher electrocatalytic currents and structural integrity than the former. The aforementioned favourable features of the CME rendered low limits of detection and selectivity towards targeted metals.[100]

Recently, polyaniline (PANI) has found diversified applications across various scientific disciplines as a conducting organo-polymer, owing to its chargeable acidic form, affordability, ease of synthesis, and remarkable stability.[101,102] In the solid state, PANI exhibits three distinct polyforms, namely, emeraldine (base and salt), leucoemeraldine, and pernigraniline.[103,104] Each form exhibits unique characteristics in terms of colour, conductivity and stability

Among the different forms of PANI, the emeraldine is the most common and versatile. It is synthesized mainly *via* the oxidative polymerization of aniline under acidic conditions, using persulphate as an oxidant and hydrochloric acid as the acidic dopant, resulting in the formation of the crystalline salt. The solution of emeraldine salt is highly conductive and exhibits a vibrant green color.[103,104] Neutralization of the emeraldine hydrochloride salt with an alkali converts it into the blue-coloured emeraldine conjugate base, which is non-conductive. This reversible protonation (doping) and deprotonation (de-doping) of the N atoms of PANI modulate the electrical and optical properties of PANI.[103,105]

Figure 1.4 illustrates the structural representation of the emeraldine form of PANI, highlighting its repeating unit and the extended conjugated backbone responsible for its unique conductivity and other properties. The ability to switch between conductive and non-conductive states makes emeraldine PANI a promising material for various applications, including sensors, actuators, energy storage devices and electronic devices.

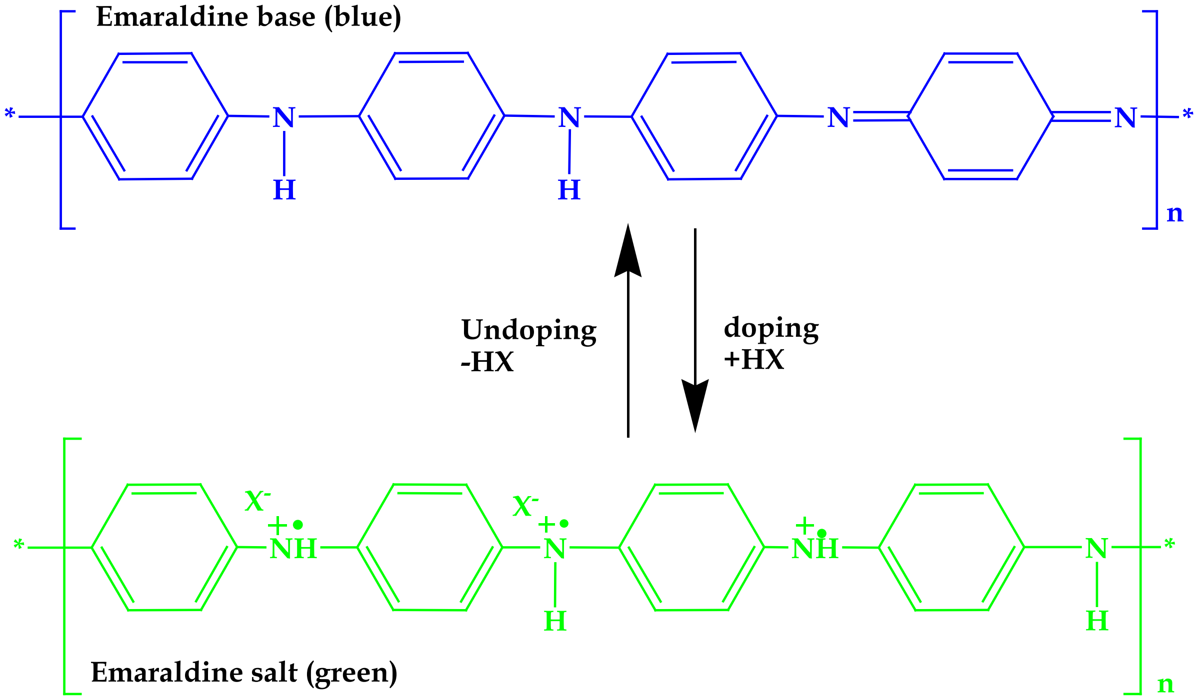

Figure 1.4: *Structures of polyaniline (PANI) in its emeraldine base and salt form.*

1.5. Carbon nanotubes (CNTs)

Carbon nanotubes (CNTs) are tubular graphene structures composed of concentric sheets of *sp*^{2}-hybridized carbon atoms. CNTs can be classified into two types: single-walled carbon nanotubes (SWCNTs) and multi-walled carbon nanotubes (MWCNTs).[106] Fabrication of single-walled (SW) or multi-walled (MW) CNTs and their boron or nitrogen-doped analogues are dependent on the nanofabrication methods used.[106-108] Predominately, arc discharge and laser ablation generally produced high-purity SWCNTs with either open or close-ended tubes, respectively.[109,110] By far the most versatile nanofabrication technique is Chemical Vapour Deposition (CVD) which generates a mixture of SWCNTs and MWCNTs in higher quantities, see **Figure 1.5**.[110-112] The semi-conducting or metallic electronic properties of CNTs can closely related with their network structures.[113,114]

The conducive electronic properties coupled with their high mechanical and chemical stability make them ideal heterogenous supports for MPcs.[64,115] MPcs with various substituents have been adsorbed on the surfaces and cavities of these CNTs but due to the inherent nature of *pi-pi* stacking interactions, leaching of MPcs is prone to occur. Chemical modification of CNTs has allowed improved processability due to lower aggregation and hence better dispersion in solution. Carboxylic acid or ethylenediamine functionalized CNTs have been covalently linked to CoPcs and the modification of working electrodes using these CoPc carbon nanotube conjugates has allowed more swifter electron transfer than using only CoPc-modified electrodes.[116-118]

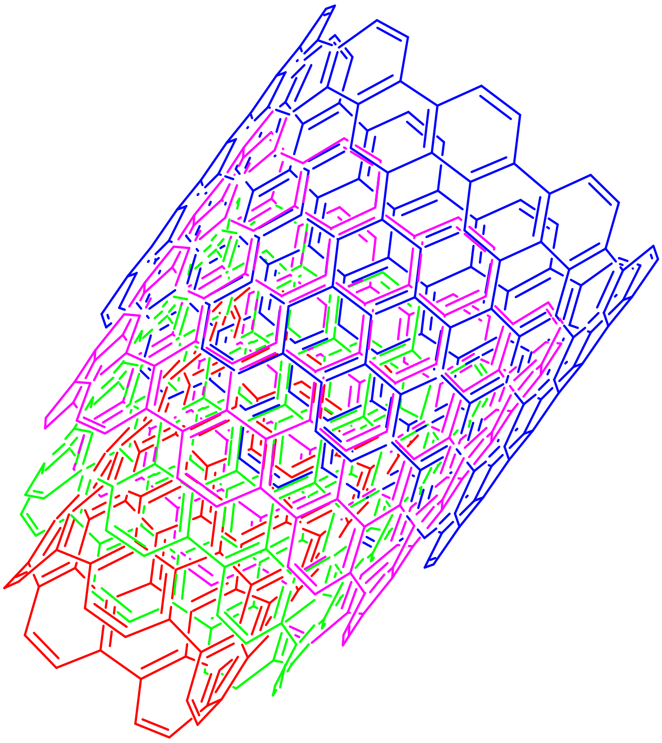

Figure 1.5: *The structure of multi-wall carbon nanotubes (MWCNTs).*

1.6. CMEs with ENFs

Electrospun nanofibers can be fundamentally defined as polymers with diameters at nanoscale and this polymeric nanomaterial is fabricated by electrospinning. The set-up of the electrospinning process is well-documented as well as the influences of its solution, instrumental and ambient parameters are widely described.[119-121] Composites of ENFs with inorganic, organic or other nanomaterials have been achieved through in-situ electrospinning or post-modification by simple adsorption of the solutes into ENFs pore.[122-124] Alternatively, ENFs can be functionalized and can be covalently bound with molecules containing appropriate functional groups.[125-127] Recent advances in ENFs include the nanofabrication of core-shell ENFs where the core and shell are different polymers and the loading of molecular solutes occupies the inner core. In comparison to bulk dispersed polymeric electron mediator films, ENFs offer a large volume-to-surface area ratio which enables higher loading of nanomaterials, the latter of which can serve as electrocatalytic sites. Thus, the high catalytic loading results in enhanced interactions with target analytes. In addition, ENFs possess adjustable 3D structures that depend on various aspect ratios such as fibre diameter, thickness, length and pore size.

Among the few examples of an ENFs-based electrochemical biosensor is the ENFs sensor platform which was a composite nanomaterial comprised of graphene oxide (GO), gold nanoparticles (AuNPs) and Cu nanoflower-glucose oxidase (Cu NFlG) embedded in poly(vinyl alcohol) (PVA), see **Figure 1.6** These GO NFs composite was immobilized onto a gold chip. The Cu NFlG @AuNPs-GO modified Au chip detected glucose down to a limit of 0.018 μM.[128]

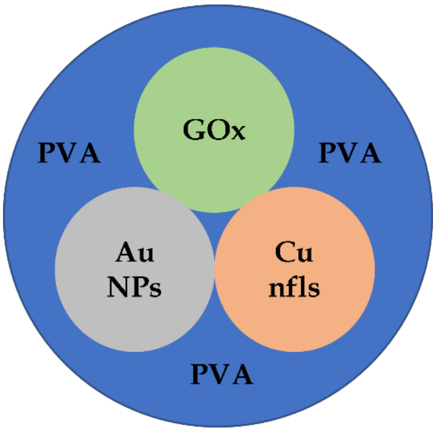

Figure 1.6: *A pictorial representation of the core-shell ENFs.*

In a similar approach, a biosensor based on ELP-OPH/BSA/TiO_2 nanofibers and *f*-MWCNTs (where ELP-OPH = lastin-like polypeptide-organophosphate hydrolase and BSA = bovine serum albumin) was designed for the sensitive and selective determination of *p*-nitrophenyl-substituted organophosphate pesticides in aqueous systems. The modification of the glassy carbon electrode (GCE) involved the preparation of a mixture comprising TiO_2 nanofibers (TiO_2-ENFs) and carboxylated multi-walled carbon nanotubes (*f*-MWCNTs) with an appropriate volume ratio of TiO_2-ENFs suspension and *f*-MWCNTs suspension. This mixture was then directly drop-cast onto the surface of the GCE followed by the immobilization of a 0.05 wt% Nafion (NF) top layer. The porous Nafion membrane acted as a binder of the TiO_2-NFs/c-MWCNTs on the GCE. The biosensor detected methyl parathion and parathion down to limits of 12 nM and 10 nM, respectively.[129]

In summary, the aims and objectives are as follows: The aim of this research project is to develop and characterize the redox behaviour of MPc chemically modified gold (Au), Platinum (Pt) or glass carbon electrodes (GCE) that can be applied for accurate qualitative and quantitative analysis of selected pharmaceuticals and heavy metals in natural water resources. This can be achieved through the following objectives:

1. To synthesize and characterise tetra-substituted MPc (M = Co(II)) i.e. asymmetric and symtrical substituted MPcs, substituents =3-Hydroxyflavone, ethynylbenzyl alcohol, 1-(methoxymethyl)-benzotriazole, and 2-furanmethanethiol). The redox character of these MPc will be investigated using various voltammetric techniques.
2. To fabricate glassy carbon and Pt modified electrodes utilizing the MPcs listed in (i) their CNTs composites and compare (against bare electrode) their redox characters as well as their electrocatalytic detection of selected pharmaceuticals and heavy metals (Dopamine, mercury, lead and acetaminophen) in water.
3. Embedding of synthesized nanoconjugates (CoPc-flav-PANI-f-MWCNTs) into PVA nanofibers using electrospinning. Characterisation of electrospun nanofibers via spectroscopic and microscopic techniques.
4. To investigate the general mechanism of electrocatalytic effect of the MPcs and nanofibers.
5. Adjust as advised to formation and use of asymmetric,(Click chemistry?) as advised To evaluate the performance of the chemically modified electrodes in the presence of interferences *i.e.*compounds with similar structures to the emerging pollutants in water.
6. To investigate the convection- and diffusion-controlled electron transfer kinetics.
7. To identify the mechanism of electrocatalytic activity of the MPcs and PVA nanofibers.
8. To conduct analysis on real samples attained from river and local municipalities in KwaZulu-Natal.

1.7. References

(1) Brack, W.; Altenburger, R.; Schüürmann, G.; Krauss, M.; Herráez, D. L.; van Gils, J.; Slobodnik, J.; Munthe, J.; Gawlik, B. M.; van Wezel, A. *Science of the total environment* **2015**, *503*, 22.

(2) Aryampa, S.; Maheshwari, B.; Sabiiti, E.; Bateganya, N. L.; Bukenya, B. *Sustainability* **2019**, *11*, 5523

(3) Abdel-Shafy, H. I.; Mansour, M. S. M. *Egyptian Journal of Petroleum* **2018**, *27*, 1275.

(4) Gavrilescu, M.; Demnerová, K.; Aamand, J.; Agathos, S.; Fava, F. *New biotechnology* **2015**, *32*, 147.

(5) Bekele, E.; Page, D.; Vanderzalm, J.; Kaksonen, A.; Gonzalez, D. *Water* **2018**, *10,* 457

(6) Paranychianakis, N. V.; Salgot, M.; Snyder, S. A.; Angelakis, A. N. *Critical Reviews in Environmental Science and Technology* **2015**, *45*, 1409.

(7) Geissen, V.; Mol, H.; Klumpp, E.; Umlauf, G.; Nadal, M.; van der Ploeg, M.; van de Zee, S. E.; Ritsema, C. J. *International soil and water conservation research* **2015**, *3*, 57.

(8) K'oreje, K.; Vergeynst, L.; Ombaka, D.; De Wispelaere, P.; Okoth, M.; Van Langenhove, H.; Demeestere, K. *Chemosphere* **2016**, *149*, 238.

(9) Zenker, A.; Cicero, M. R.; Prestinaci, F.; Bottoni, P.; Carere, M. *Journal of environmental management* **2014**, *133*, 378.

(10) Khan, N. A.; Ahmed, S.; Farooqi, I. H.; Ali, I.; Vambol, V.; Changani, F.; Yousefi, M.; Vambol, S.; Khan, S. U.; Khan, A. H. *TrAC Trends in Analytical Chemistry* **2020**, *129*, 115921.

(11) Gumbi, B. P.; Moodley, B.; Birungi, G.; Ndungu, P. G. *Environmental Science and Pollution Research* **2017**, *24*, 20015.

(12) Sui, Q.; Cao, X.; Lu, S.; Zhao, W.; Qiu, Z.; Yu, G. *Emerging Contaminants* **2015**, *1*, 14.

(13) Santos, J.; Aparicio, I.; Alonso, E. *Environment International* **2007**, *33*, 596.

(14) Balakrishna, K.; Rath, A.; Praveenkumarreddy, Y.; Guruge, K. S.; Subedi, B. *Ecotoxicology and environmental safety* **2017**, *137*, 113.

(15) Ngumba, E.; Gachanja, A.; Tuhkanen, T. *Science of the Total Environment* **2016**, *539*, 206.

(16) Rimayi, C.; Odusanya, D.; Weiss, J. M.; de Boer, J.; Chimuka, L. *Science of the Total Environment* **2018**, *627*, 1008.

(17) Kolpin, D. W.; Furlong, E. T.; Meyer, M. T.; Thurman, E. M.; Zaugg, S. D.; Barber, L. B.; Buxton, H. T. *Environmental science & technology* **2002**, *36*, 1202.

(18) Odendaal, C.; Seaman, M. T.; Kemp, G.; Patterton, H. E.; Patterton, H.-G. *South African Journal of Science* **2015**, *111*, 01.

(19) Agunbiade, F. O.; Moodley, B. *Environmental Monitoring and Assessment* **2014**, *186*, 7273.

(20) Shehu, Z.; Nyakairu, G. W. A.; Tebandeke, E.; Odume, O. N. *Science of The Total Environment* **2022**, *852*, 158303.

(21) Matongo, S.; Birungi, G.; Moodley, B.; Ndungu, P. *Chemosphere* **2015**, *134*, 133.

(22) Matongo, S., Birungi, G., Moodley, B. and Ndungu, P. *Environmental Science and Pollution Research* **2015**, *22*, 10298.

(23) Akpotu, S. O.; Moodley, B. *Journal of Environmental Management* **2018**, *209*, 205.

(24) Archer, E.; Wolfaardt, G. M.; Van Wyk, J. H. *Water Sa* **2017**, *43*, 684.

(25) Hlengwa, N.B.; Mahlambi, P.N. *Bulletin of Environmental Contamination and Toxicology* **2020,** *104*, 464.

(26) Mlunguza, N.Y., Ncube, S., Mahlambi, P.N., Chimuka, L. and Madikizela, L.M., *Environmental Monitoring and Assessment* **2020**, *192*, pp.1-14.

(27) Zoroddu, M.A., Aaseth, J., Crisponi, G., Medici, S., Peana, M. and Nurchi, V.M. *Journal of Inorganic Biochemistry* **2019**, *195*,120.

(28) Shilpi, G.; Shilpi, S.; Sunita, S. *International Journal of Pharmacy and Pharmaceutical Sciences* **2015**, *7*, 0975.

(29) Zamora-Ledezma, C.; Negrete-Bolagay, D.; Figueroa, F.; Zamora-Ledezma, E.; Ni, M.; Alexis, F.; Guerrero, V. H. *Environmental Technology & Innovation* **2021**, *22*, 101504.

(30) Duruibe; Ogwuegbu; Egwurugwu *International Journal of Physical Sciences* **2007**, *2*, 112.

(31) Rajkumar, M.; Ae, N.; Prasad, M. N. V.; Freitas, H. *Trends in Biotechnology* **2010**, *28*, 142.

(32) Raikwar, M. K.; Kumar, P.; Singh, M.; Singh, A. *Veterinary World* **2008**, *1*, 28.

(33) Hu, Y.; Liu, X.; Bai, J.; Shih, K.; Zeng, E. Y.; Cheng, H. *Environmental Science and Pollution Research* **2013**, *20*, 6150.

(34) Xu, X.; Zhao, Y.; Zhao, X.; Wang, Y.; Deng, W. *Ecotoxicology and Environmental Safety* **2014**, *108*, 161.

(35) Li, F.-j.; Yang, H.-w.; Ayyamperumal, R.; Liu, Y. *Chemosphere* **2022**, *308*, 136396.

(36) Singh, J.; Kalamdhad, A. S. *International Journal of Research in Chemistry and Environment* **2011**, *1*, 15.

(37) Elumalai, V.; Sujitha, S.B; Jonathan, M.P. *Marine Pollution Bulletin* **2022**, *180*, 113742.

(38) Naidoo, S.; Pillay, S.; Bissessur, A.; Ballabh, H.; Naicker, D. *Journal of Earth System Science* **2018**, *127*, 1.

(39) Pillay, S., Naidoo, K., Bissessur, A., Agjee, N., Pillay, K., Purves, B., Pillay, R. and Ballabh, H. *Journal of Human Ecology* **2014,** *47*, 155.

(40) Vetrimurugan, E., Shruti, V.C., Jonathan, M.P., Roy, P.D., Sarkar, S.K., Rawlins, B.K. and Villegas, L.E.C. *Marine Pollution Bulletin* **2019**, *149*, 110555.

(41) Shokr, L. A.; Hassan, M. A.; Elbahy, E. F. *Benha Veterinary Medical Journal* **2019**, *36*, 40.

(42) Renu, K.; Chakraborty, R.; Myakala, H.; Koti, R.; Famurewa, A. C.; Madhyastha, H.; Vellingiri, B.; George, A.; Gopalakrishnan, A. V. *Chemosphere* **2021**, *271*, 129735.

(43) Mousavi, S. M.; Brodie, G.; Payghamzadeh, K.; Raiesi, T.; Strivastava, A. *Journal of Advances in Environmental Health Research* **2022**, *10*, 1.

(44) Li, Y.; Ortiz, G. G. R.; Uyen, P. T. M.; Cong, P. T.; Othman, S. I.; Allam, A. A.; Unar, A.; Afridi, H. I. *Environmental Research* **2023**, *231*, 115913.

(45) González Rendón, E. S.; Cano, G. G.; Alcaraz-Zubeldia, M.; Garibay-Huarte, T.; Fortoul, T. I. *Toxicology and Industrial Health* **2018**, *34*, 128.

(46) Massányi, P.; Massányi, M.; Madeddu, R.; Stawarz, R.; Lukáč, N. *Toxics* **2020**, *8*, 94.

(47) Ismail, W. N. W.; Mokhtar, S. U. *Emerging Contaminants* **2020**.

(48) Pardeshi, S.; Dhodapkar, R. *Environmental Research* **2022**, *212*, 113359.

(49) Kaur, H.; Kumari, N.; Sharma, A.; Sachdeva, M.; Mutreja, V. *Materials Today: Proceedings* **2022**, *48*, 1673.

(50) Lakshmi, D.; Whitcombe, M. J.; Davis, F.; Sharma, P. S.; Prasad, B. B. *Electroanalysis* **2011**, *23*, 305.

(51) Prakash, S.; Chakrabarty, T.; Singh, A. K.; Shahi, V. K. *Biosensors and Bioelectronics* **2013**, *41*, 43.

(52) Harper, A.; Anderson, M. R. *Sensors* **2010**, *10*, 8248

(53) Zhang, B.; Kang, F.; Tarascon, J.-M.; Kim, J.-K. *Progress in Materials Science* **2016**, *76*, 319.

(54) Ji, D.; Fan, L.; Li, L.; Mao, N.; Qin, X.; Peng, S.; Ramakrishna, S. *Carbon* **2019**, *142*, 379.

(55) Adeniji, T. M.; Stine, K. J. *Coatings* **2023**, *13*, 381.

(56) Magro, C.; Mateus, E. P.; Raposo, M.; Ribeiro, A. B. *Environmental Reviews* **2018**, *27*, 202.

(57) Garoz-Ruiz, J.; Perales-Rondon, J. V.; Heras, A.; Colina, A. *Electroanalysis* **2019**, *31*, 1254.

(58) Demir, F.; Yenilmez, H. Y.; Koca, A.; Bayır, Z. A. *Journal of Electroanalytical Chemistry* **2019**, *832*, 254.

(59) Zagal, J. H.; Griveau, S.; Silva, J. F.; Nyokong, T.; Bedioui, F. *Coordination Chemistry Reviews* **2010**, *254*, 2755.

(60) Kurt, Ö.; Koca, A.; Gül, A.; Burkut Koçak, M. *Synthetic Metals* **2015**, *206*, 72.

(61) Kantize, K.; Ngwenya, V.; Booysen, I. N.; Mambanda, A. *Polyhedron* **2021**, *203*, 115235.

(62) Ndebele, N.; Nyokong, T. *Diamond and Related Materials* **2023**, *132*, 109672.

(63) Wang, H.; Bu, Y.; Dai, W.; Li, K.; Wang, H.; Zuo, X. *Sensors and Actuators B: Chemical* **2015**, *216*, 298.

(64) Yang, S.; Yu, Y.; Gao, X.; Zhang, Z.; Wang, F. *Chemical Society Reviews* **2021**, *50*, 12985.

(65) Kumar, A.; Vashistha, V. K.; Sharma, V. *Inorganic Chemistry Communications* **2021**, *127*, 108518.

(66) Arıcan, D.; Arıcı, M.; Uğur, A. L.; Erdoğmuş, A.; Koca, A. *Electrochimica Acta* **2013**, *106*, 541.

(67) Demir, E.; Silah, H.; Uslu, B. *Critical Reviews in Analytical Chemistry* **2022**, *52*, 425.

(68) Ozoemena, K. I.; Nyokong, T. *Talanta* **2005**, *67*, 162.

(69) Mashazi, P.; Nyokong, T. *Microchimica Acta* **2010**, *171*, 321.

(70) Mpeta, L.S.; Sen, P.; Nyokong, T. *Journal of Electroanalytical Chemistry* **2020**, *860*, 113896.

(71) Panche, A. N.; Diwan, A. D.; Chandra, S. R. *Journal of Nutritional Science* **2016**, *5*, e47.

(72) Dias, M. C.; Pinto, D. C. G. A.; Silva, A. M. S. *Molecules* **2021**, *26*, 5377.

(73) Chohan, S.; Booysen, I. N.; Mambanda, A. *Polyhedron* **2015**, *102*, 284.

(74) Koçyiğit, Ü. M.; Taslimi, P.; Tüzün, B.; Yakan, H.; Muğlu, H.; Güzel, E. *Journal of Biomolecular Structure and Dynamics* **2022**, *40*, 4429.

(75) Recloux, I.; Andreatta, F.; Druart, M.-E.; Coelho, L. B.; Cepek, C.; Cossement, D.; Fedrizzi, L.; Olivier, M.-G. *Journal of Alloys and Compounds* **2018**, *735*, 2512.

(76) Hrimla, M.; Bahsis, L.; Laamari, M. R.; Julve, M.; Stiriba, S.-E. *International Journal of Molecular Sciences* **2021**, *23*, 16.

(77) Sharifiyan, M. S.; Shanaghi, A.; Moradi, H.; Chu, P. K. *Surface and Coatings Technology* **2017**, *321*, 36.

(78) Seok, Y.-J.; Her, J.-Y.; Kim, Y.-G.; Kim, M. Y.; Jeong, S. Y.; Kim, M. K.; Lee, J.-y.; Kim, C.-i.; Yoon, H.-J.; Lee, K.-G. *Toxicological Research* **2015**, *31*, 241.

(79) Gao, C.; Li, Y.; Pan, Q.; Fan, M.; Wang, L.; Qian, H. *Journal of Cereal Science* **2021**, *99*, 103178.

(80) Chohan, S.; Booysen, I. N.; Mambanda, A.; Akerman, M. P. *Inorganica Chimica Acta* **2016**, *447*, 183.

(81) Liao, M.S.; Scheiner, S. *Journal of Computational Chemistry* **2002**, *23*,1391.

(82) Ough, E.; Gasyna, Z.; Stillman, M.J. *Inorganic Chemistry* **1991**, *30*, 2301.

(83) Felton, R. H.; Linschitz, H. *Journal of the American Chemical Society* **1966**, *88*, 1113.

(84) Li, Z.; Lieberman, M.; Hill, W. *Langmuir* **2001**, *17*, 4887.

(85) Nyokong, T.; Bedioui, F. *Journal of Porphyrins and Phthalocyanines* **2006**, *10*, 1101.

(86) Moraes, F. C.; Mascaro, L. H.; Machado, S. A.; Brett, C. M. *Talanta* **2009**, *79*, 1406.

(87) de Moura Junior, F. G.; Veloso, W. B.; de Oliveira Junior, J. A.; Kraatz, H.-B.; da Silva, I. S.; Dantas, L. M. F. *Monatshefte für Chemie-Chemical Monthly* **2021**, *152*, 895.

(88) Fomo, G.; Nwaji, N.; Nyokong, T. *Journal of Electroanalytical Chemistry* **2018**, *813*, 58.

(89) Kulkarni Vishakha, S.; Butte Kishor, D.; Rathod Sudha, S. *International Journal of Research in Pharmaceutical and Biomedical Science* **2012**, *3*, 1597.

(90) Katz, H. E.; Searson, P. C.; Poehler, T. O. *Journal of Materials Research* **2010**, *25*, 1561.

(91) Jafari, S.; Dehghani, M.; Nasirizadeh, N.; Azimzadeh, M. *Journal of Electroanalytical Chemistry* **2018**, *829*, 27.

(92) Zhang, M.; Nautiyal, A.; Du, H.; Wei, Z.; Zhang, X.; Wang, R. *Electrochimica Acta* **2021**, *376*, 138037.

(93) Fayemi, O. E.; Adekunle, A. S.; Kumara Swamy, B. E.; Ebenso, E. E. *Journal of Electroanalytical Chemistry* **2018**, *818*, 236.

(94) Rashed, M. A.; Faisal, M.; Alsaiari, M.; Alsareii, S. A.; Harraz, F. A. *Electrocatalysis* **2021**, *12*, 650.

(95) Chougale, U.; Thombare, J.; Fulari, V.; Kadam, A. *International conference on energy-efficient technologies for sustainability* **2013**, 18, 1078.

(96) Jia, M.-y.; Zhang, Z.-m.; Yu, L.-m.; Wang, J.; Zheng, T.-t. *Colloids and Surfaces B: Biointerfaces* **2018**, *164*, 247.

(97) Desroches, P. E.; Silva, S. M.; Gietman, S. W.; Quigley, A. F.; Kapsa, R. M. I.; Moulton, S. E.; Greene, G. W. *ACS Applied Bio Materials* **2020**, *3*, 8032.

(98) Ramanaviciene, A.; Ramanavicius, A. *Critical Reviews in Analytical Chemistry* **2002**, *32*, 245.

(99) Street, G.; Lindsey, S.; Nazzal, A.; Wynne, K. *Molecular Crystals and Liquid Crystals* **1985**, *118*, 137.

(100) Dai, H.; Wang, N.; Wang, D.; Ma, H.; Lin, M. *Chemical Engineering Journal* **2016**, *299*, 150.

(101) Genies, E.; Boyle, A.; Lapkowski, M.; Tsintavis, C. *Synthetic Metals* **1990**, *36*, 139.

(102) Bhadra, S.; Khastgir, D.; Singha, N. K.; Lee, J. H. *Progress in Polymer Science* **2009**, *34*, 783.

(103) Boeva, Z. A.; Sergeyev, V. G. *Polymer Science Series C* **2014**, *56*, 144.

(104) Stejskal, J.; Kratochvíl, P.; Jenkins, A. D. *Polymer* **1996**, *37*, 367.

(105) Le, T.-H.; Kim, Y.; Yoon, H. Electrical and Electrochemical Properties of Conducting Polymers. *Polymers* [Online Early Access]. DOI: 10.3390/polym9040150. Published Online: 2017.

(106) Jana, D.; Sun, C.-L.; Chen, L.-C.; Chen, K.-H. *Progress in Materials Science* **2013**, *58*, 565.

(107) Su, D. S.; Perathoner, S.; Centi, G. *Chemical Reviews* **2013**, *113*, 5782.

(108) Chadha, U.; Sinha, S.; Jonna, J.; Goswami, M.; Ghani, H.; Nair, K.; Pandey, N.; Kataray, T.; Selvaraj, S. K.; Bhardwaj, P.; Banavoth, M.; Sonar, P. *ECS Journal of Solid State Science and Technology* **2022**, *11*, 041003.

(109) Soni, S. K.; Thomas, B.; Kar, V. R. *Materials Today Communications* **2020**, *25*, 101546.

(110) Alayan, H. M.; Aljumaily, M. M.; Alsaadi, M. A.; Mjalli, F. S.; Hashim, M. A. *Toxicological & Environmental Chemistry* **2021**, *103*, 282.

(111) Shah, K. A.; Tali, B. A. *Materials Science in Semiconductor Processing* **2016**, *41*, 67.

(112) Pant, M.; Singh, R.; Negi, P.; Tiwari, K.; Singh, Y. *Materials Today: Proceedings* **2021**, *46*, 11250.

(113) Charlier, J.-C.; Blase, X.; Roche, S. *Reviews of Modern Physics* **2007**, *79*, 677.

(114) Huang, Y. Y.; Terentjev, E. M. *Advanced Functional Materials* **2010**, *20*, 4062.

(115) Zagal, J. H.; Griveau, S.; Ozoemena, K. I.; Nyokong, T.; Bedioui, F. *Journal of Nanoscience and Nanotechnology* **2009**, *9*, 2201.

(116) Mugadza, T.; Nyokong, T. *Synthetic Metals* **2010**, *160*, 2089.

(117) He, D.; Peng, Y.; Yang, H.; Ma, D.; Wang, Y.; Chen, K.; Chen, P.; Shi, J. *Dyes and Pigments* **2013**, *99*, 395.

(118) Chidawanyika, W.; Nyokong, T. *Carbon* **2010**, *48*, 2831.

(119) Patel, P. R.; Gundloori, R. V. N. *Polymers for Advanced Technologies* **2023**, *34*, 44.

(120) Islam, M. S.; Ang, B. C.; Andriyana, A.; Afifi, A. M. *SN Applied Sciences* **2019**, *1*, 1248.

(121) Ahmed, J. *Medical Devices and Sensors* **2021**, *4*, e10136.

(122) Obaid, M.; Abdelkareem, M. A.; Kook, S.; Kim, H.-Y.; Hilal, N.; Ghaffour, N.; Kim, I. S. *Critical Reviews in Environmental Science and Technology* **2020**, *50*, 1727.

(123) Huang, W.; Xiao, Y.; Shi, X. *Advanced Fiber Materials* **2019**, *1*, 32.

(124) Toriello, M.; Afsari, M.; Shon, H. K.; Tijing, L. D. *Membranes* **2020**, *10*, 204.

(125) El-Aswar, E. I.; Ramadan, H.; Elkik, H.; Taha, A. G. *Journal of Environmental Management* **2022**, *301*, 113908.

(126) Niemczyk-Soczynska, B.; Gradys, A.; Sajkiewicz, P. *Polymers* **2020**, *12*, 2636.

(127) Chen, H.; Huang, M.; Liu, Y.; Meng, L.; Ma, M. *Science of The Total Environment* **2020**, *739*, 139944.

(128) Baek, S. H.; Roh, J.; Park, C. Y.; Kim, M. W.; Shi, R.; Kailasa, S. K.; Park, T. J. *Materials Science and Engineering: C* **2020**, *107*, 110273.

(129) Bao, J.; Hou, C.; Dong, Q.; Ma, X.; Chen, J.; Huo, D.; Yang, M.; Abd El Galil, K. H.; Chen, W.; Lei, Y. *Biosensors and Bioelectronics* **2016**, *85*, 935.

Chapter 2

Material and Instruments

2.1. Materials:

The inorganic and organic precursors were procured from Sigma-Aldrich and used without any further purification, see **Table 2.1**. A basic catalyst, 1,8-diazabicyclo[5.4.0]undec-7-ene (DBU), an acidic catalyst, trifluoroacetic acid (TFA), chloroform and an electrochemical analysis grade supporting electrolyte were purchased from the same supplier. Reagent grade organic solvents, phosphorus pentoxide (P_2O_5), molecular sieves (4 Å), silicon dioxide (silica) for column chromatography and silica plates for thin layer chromatography were procured from Merck SA.

Dimethylformamide (DMF) was freshly distilled and stored over molecular sieves before use to ensure its purity. Aluminium oxide (alumina) for polishing the working electrodes was supplied by Metrohm. Carboxylic acid functionalized multi-walled carbon nanotubes (*f*-MWCNTs) were acquired from Sigma-Aldrich. The analytical grade analytes were obtained from Sigma-Aldrich and capital research distributors (CRD) are also listed in **Table 2.1**. References to the sources and catalogues of these chemicals can be found on the websites of Sigma-Aldrich (www.sigmaaldrich.com) and Merck SA (www.merckmillipore.com).

Table 2.1: *List of commercially used chemicals and their percentage purities.*

Chemicals	Purity
4-Nitrophthalonitrile	99%
Potassium carbonate	99.5%
3-Hydroxyflavone	≥ 98%
Ethynylbenzyl alcohol	97%
Cobalt(II) chloride	97%
1,8-diazabicyclo[5.4.0]undec-7-ene (DBU)	98%
Aniline	≥ 99.0%
Ammonium persulfate	≥ 98%
Methyl-2-pyrrolidinone	≥ 99.7%
Polyvinyl alcohol	98-99%
Dimethylformamide (DMF)	≥ 99.9%
Dimethyl sulfoxide *(DMSO)–d_6*	99.9%
1*H*-benzotriazole-1-methanol (HBzt)	98%
Pyrrole	≥ 97%
2-Furanmethanethiol	98%
Tetrabutylammonium tetrafluoroborate ($TBABF_4$)	99%
Mercury(II) sulphate	≥ 99%
Dopamine hydrochloride (DA.HCl)	98%
Paracetamol (Acetaminophen, APAP)	≥ 99%
Lead(II) nitrate ($PbNO_3$)	≥ 99%

2.2. *Instrumentation:*

Various instruments were used for material characterization and the experimental measurements:

- FTIR spectra of synthesized complexes, polymers and conjugates were recorded using a Bruker Alpha FTIR spectrometer with an ATR platinum Diamond 1 reflectance accessory.
- NMR experiments were performed on a 400 MHz Bruker NMR spectrometer using d^6-DMSO as the solvent.
- UV-Vis spectroscopy was carried out using an Agilent Cary 60 UV-Vis spectrophotometer.
- Melting points were determined using a Stuart SMP3 melting point apparatus.
- Mass spectrometry (MS) analysis was conducted using a Waters Micromass LCT Premier MS instrument with an electrospray ionization (ESI) source and a time-of-flight (TOF) mass analyzer.
- Elemental analysis was performed using a CHNS-O Flash 2000 organic Elemental analyzer.
- Raman spectra were recorded using a Renishaw in Via Raman microscope.
- Powder XRD diffractograms were obtained using a Miniflex600-PXRD instrument.
- Scanning electron microscope (SEM) images were acquired using a Zeiss EVO LS15 microscope operating under high vacuum conditions.
- The real water samples for dopamine and acetaminophen were analyzed using a Shimadzu LC-MS-2020 with a Shim-pack GIST-HP 3 µm C18 column (4.6 x 150 mm), equipped with a Shim-pack guard column was used to conduct comparative real sample studies.
- Analytical Pb(II) and Hg(II) standards and the real water samples were prepared in 2% nitric acid (Pb) and 2%HCl (Hg) before being analysed using a Shimadzu ICPE-9800 Inductively coupled plasma optical emission spectroscopy (ICP-OES) spectrometer set at wavelength of 220.35 nm. The argon gas was set at pressure of 460.02 kPa, the radiofrequency was 0.50 kW while the auxiliary and plasma

gas flows were 0.60 and 5.00, respectively. Temperatures of 37.99°C and -14.87°C were maintained for the spectrometer and the charge coupled device, respectively.

2.3. *Fabrication of PVA-based ENFs using an Inveso nano spinner 24 multi-nozzle electrospinning/spraying machine:*

The electrospinning technique was used to create spider-web textured nanofibers. The step-by-step description of the process is as follows:

I. Preparation of the PVA solution:

- 0.10 g of polyvinyl alcohol (PVA) was dissolved in 10 mL of ultrapure water. The mixture was heated at 80 °C with constant stirring until a viscous emulsion was formed.

II. Dispersion of PANI-CoPc-flav or -fur-*f*-MWCNTs nanocomposite:

- 0.05 g of PANI-CoPc-*f*-MWCNTs nanocomposite was dispersed in 5 mL of 1-methyl-2-pyrrolidinone (NMP). The NMP solution containing the nanocomposite was heated and stirred at 50 °C for 1 hour to ensure proper dispersion.

III. Mixing the solutions:

- The NMP solution containing the nanocomposite was added to the PVA emulsion. The resulting mixture was stirred overnight at 40 °C to ensure thorough dispersion of the nanocomposite within the PVA matrix. This step allowed for the integration of the PANI-CoPc-*f*-MWCNTs nanocomposite into the PVA solution.

IV. Electrospinning process:

- The viscous solution obtained from the previous step was transferred to a syringe. The syringe was connected to the head of an Inveso nanospinner 24 multinozzle electrospinning/spraying machine. The solution was then extruded from the spinneret at a voltage of 16 kV. The flow rate of the solution was set to 0.5 mL/hr to control the rate of electrospinning. The distance between the capillary tube and the collector (aluminium foil) was maintained at 80 mm. Under these conditions, the solution was electrospun to form spider-web textured electrospun nanofibers (ENFs).

2.4. Electrochemical studies were conducted using an Autolab Potentiostat equipped with:

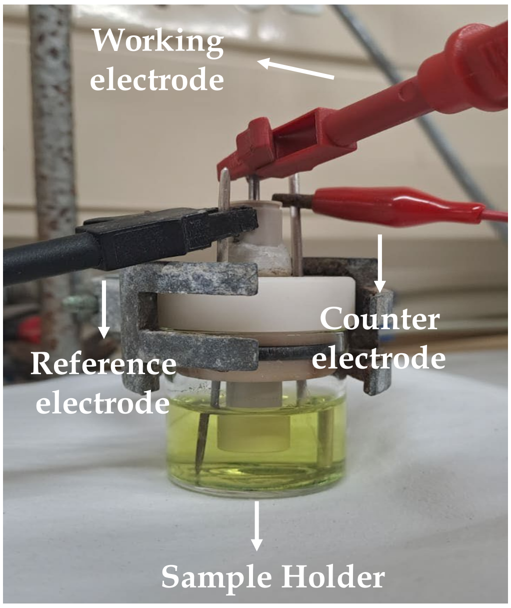

Figure 2.1: *A three-electrode system with a sample holder.*

- A three-electrode system comprising Pt/Au or glassy carbon working electrodes. A pseudo Ag|AgCl reference electrode and a Pt wire counter electrode, *see* **Figure 2.1**.
- The Autolab Nova 1.7 software was used for instrumentation operation and data analysis, see the picture of the dual Autolab potentiostat-galvanostat in **Figure 2.2**.
- Spectroelectrochemical experiments were performed in a UV-Vis spectrophotometer connected to the dual Autolab potentiostat-galvanostat using a Specac optically transparent thin-layer electrochemical (OTTLE) cell, *see* **Figure 2.3**.

- The Autolab potentiostat-galvanostat is equipped with an FRA32M module for electrochemical impedance spectroscopy and the experiments were conducted at 1.2 V.
- The Autolab potentiostat-galvanostat could be linked to the Autolab rotating disk electrode motor for hydrodynamic experiments.

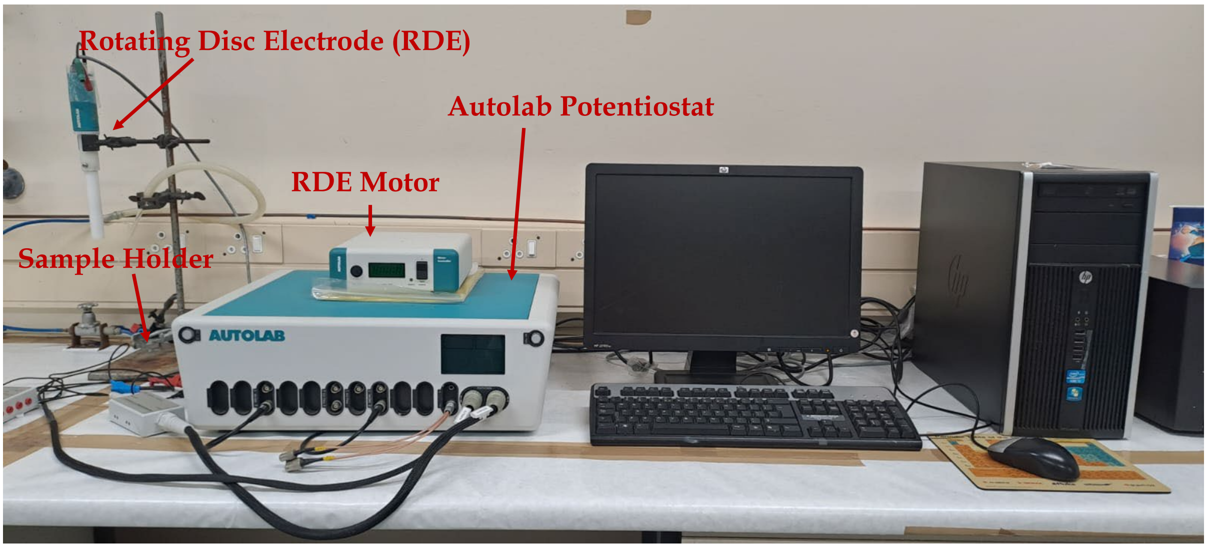

Figure 2.2: *Electrochemical instrumentation set-up using during this research project.*

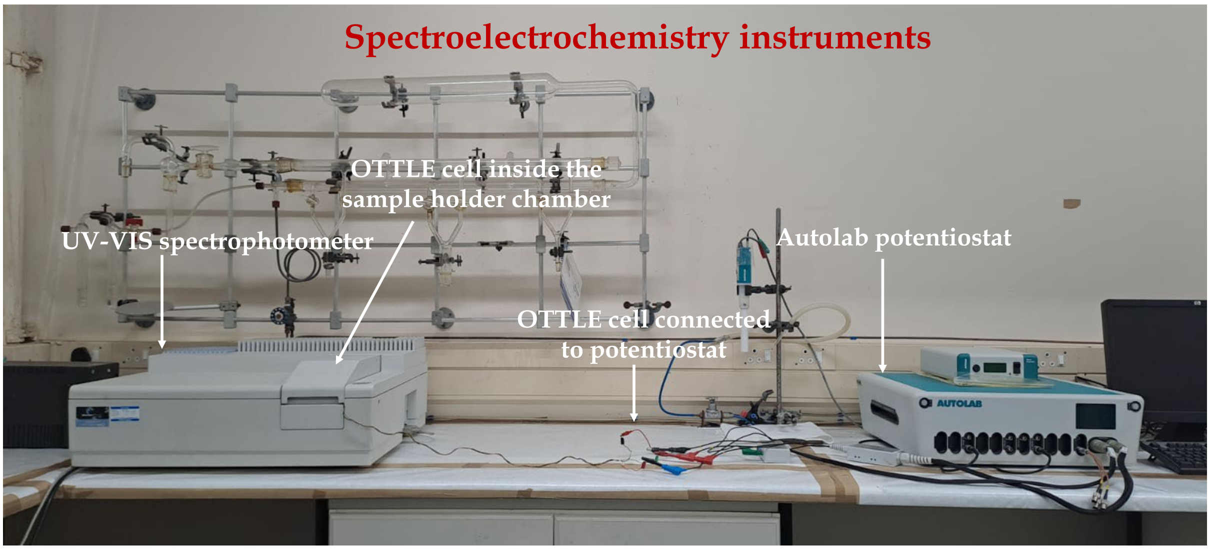

Figure 2.3: *Interfacing of the Lambda 45 Perkin Elmer UV-Vis spectrophotometer with the Autolab potentiostat – galvanostat via an OTTLE cell for electronic spectroelectrochemical experiments.*

Chapter 3

Electrocatalytic effects of a clicked film of an asymmetric A_3B (A = 3-oxyflavone, B = α-(ethynyl)benzyl alcohol) CoPc complex on a glassy carbon electrode for the detection of dopamine

3.1. Introduction

Cobalt phthalocyanines (CoPcs) are dyes with a redox-active metal at the centre of a two-dimensional tetrapyrrolic macrocyclic structure, forming a delocalized 18 π-electron system.[1] This conjugated π-electron system enables CoPcs to undergo metal- and Pc-based redox processes, facilitating swift electron transfer between the electrode interface and the CoPc itself.[2,3] By altering the stereo-electronic properties of CoPc substituents, their redox potentials and electrochemical sensitivities can be modified. Additionally, CoPcs have been used as electron-mediating films on various substrates, resulting in chemically modified electrodes (CMEs) that have been applied in electrocatalytic sensing for water pollutant detection and as biosensors.[4]

The use of symmetrically substituted CoPcs as electrocatalysts is more commonly reported due to their higher conversion yields and easier purification compared to their asymmetrical counterparts.[5,6] These CoPcs, along with their nanoconjugates, have been immobilized on electrode surfaces using the drop-dry method. Asymmetrical CoPcs of the type, A_3B, form more robust chemically modified glassy carbon electrodes (GCEs) when diazonium groups are electrochemically pre-grafted for the subsequent reaction with the alkynyloxy functionality of the 'B' peripheral substituents of the A_3B CoPc complex. Thus, the reaction, also known as the Click chemistry reaction is catalyzed by a Cu(I)-catalyst.[7-9] In this design strategy, the 'B' moiety reacts with the grafted azido moiety to form a triazolyl linker that anchors the Co(II)Pc-flav3 containing the coordinated three 'A' groups. This indirectly co-join their functional groups to the electrode surface, thereby enhancing the electrochemical sensing and specificity of the CMEs *via* analyte recognition interactions.

In a previous study, it was demonstrated that GCEs modified with a peripherally tetra-substituted flavone CoPc (CoPc-flav) and its composite with multiwalled carbon nanotubes (CoPc-flav-MWCNTs) exhibited higher electrocatalytic activity for dopamine than bare GCEs.[10] Building on this knowledge, an asymmetrical CoPc (A_3B) bearing three 3-hydroxyflavonyloxy (A) and α-(ethynyl)benzyl alcohol (B) groups have been developed. The B group serves as an anchor of the entire CoPc molecule to the surface of the GCE to form a modified electrode referred to hereafter as GCE|clicked-α-CoPc-flav3). The 3'A' groups promote the selective sensing of analytes such as dopamine through direct complementary interactions (e.g. hydrogen bonding) that constitute the recognition capability of the modifier. We anticipate that the metal-based oxidation and reduction couple of α-CoPc-flav3 will primarily catalyze the redox transformation of dopamine, based on the previous work showing that the Co(II/III) redox couple of the symmetrical 'A'$_4$-CoPc-flav was within the potential window of the target analyte.[10]

Dopamine (DA) is a neurotransmitter found in the synaptic gaps of the central nervous system and this has influenced the development of electrochemical biosensors for its selective detection and quantitative analysis in biological samples. However, from an environmental point of view, its bioactivity coupled with unsafe disposal practices qualifies it into the group of classified water pollutants of concern.[11] Dopamine is marketed under the brand name Intropin and is commonly used to treat symptoms associated with low blood pressure, a sluggish heartbeat, and cardiac arrest in the absence of epinephrine.[12,13] It is prescribed for newborns with very low blood pressure, while its functional analogues, norepinephrine are preferred for raising low blood pressure in adults.[14] Dopamine can enter wastewater directly through negligent disposal of Intropin-contaminated waste or as a microbial metabolite of levodopa and indirectly through the entrainment of contaminated urine and faeces.

In this study, we will optimize the electrochemical parameters of the fabricated GCE|Clicked-α-CoPc-flav3 towards DA. Furthermore, the analytical performance towards DA is compared to the results with liquid chromatography-mass spectrometry (LC-MS) analysis to validate the performance of the CME.

3.2. Experimental

3.2.1. *Synthesis of tris-[4(3-oxyflavone)-4(1-phenyprop-2-yn-1-oxy)phthalocyaniato]cobalt(II) (a-CoPc-flav3) (1)*

tris-[4(3-oxyflavone)-4(1-phenyprop-2-yn-1-oxy)phthalocyaniato]cobalt(II) (**1**) was synthesized from the 3:1 cyclotetramerization reaction between 4-(flavone-3-oxyl)phthalonitrile (0.6035 g, 1.6530 mmol) and 4-(1-phenylprop-2-yn-1-oxyl)phthalonitrile (0.1420 g, 0.5502 mmol) with anhydrous cobalt(II) chloride (0.0722 g, 0.5561 mmol) and drops of DBU mixed in *n*-pentanol (20 cm^3). The reaction mixture was stirred at 140 °C for 6 h under a nitrogen atmosphere. After 6 h, the mixture was cooled to room temperature, and the crude compound was precipitated out by the addition of cold methanol. Thereafter, it was washed with cold hexane and dried under vacuum. Yield: 28%; m.p. > 310 ^oC; IR (ν_{max}/cm^{-1}): v(C≡C-H) 3253, br; ν(C=O) 1650, s; ν(C-O-C) 1244, 1080, s. UV–*Vis* [DMF, λ_{max} (ε, M^{-1} cm^{-1})]: 674 nm (34770), 610 nm (12590), 294 nm (56500). Molecular mass (*m/z*): Calcd: 1409.35. Found: 1410.74 $[M+H]^+$, 1411.30 $[M+2H]^+$, 1413.27 $[M+4H]^+$.

3.3. Results and discussion

3.3.1. *Synthesis and characterization of (1)*

The derivatized phthalonitriles 4-(flavone-3-oxyl)phthalonitrile L-1 and 4-(1-phenylprop-2-yn-1-oxyl)phthalonitrile L-2 were synthesized in the same manner as reported by Chohan *et al.*[10] and Mpeta *et al.*[8], respectively. In particular, the individual base-catalyzed nucleophilic substitution reactions of 4-nitrophthalonitrile with 3-hydroxyflavone and α-(ethynyl)benzyl alcohol were conducted in the presence of a base, potassium carbonate. The formation of the respective free ligands was confirmed spectroscopically and their purities were confirmed using mass spectrometry and elemental analysis. The characterization data were aligned with those reported by the aforementioned previous studies.[8,10] Subsequently, the statistical cyclotetramerization reaction was done using cobalt(II) chloride, one-fold of L-2 and three-fold of L-1 with 6 drops of DBU resulting in a crude green product that was rigorously purified *via* preparative column chromatography to afford α-CoPc-flav3 (**1**) in a moderate yield of 42%, *see* **Scheme 3.1**.

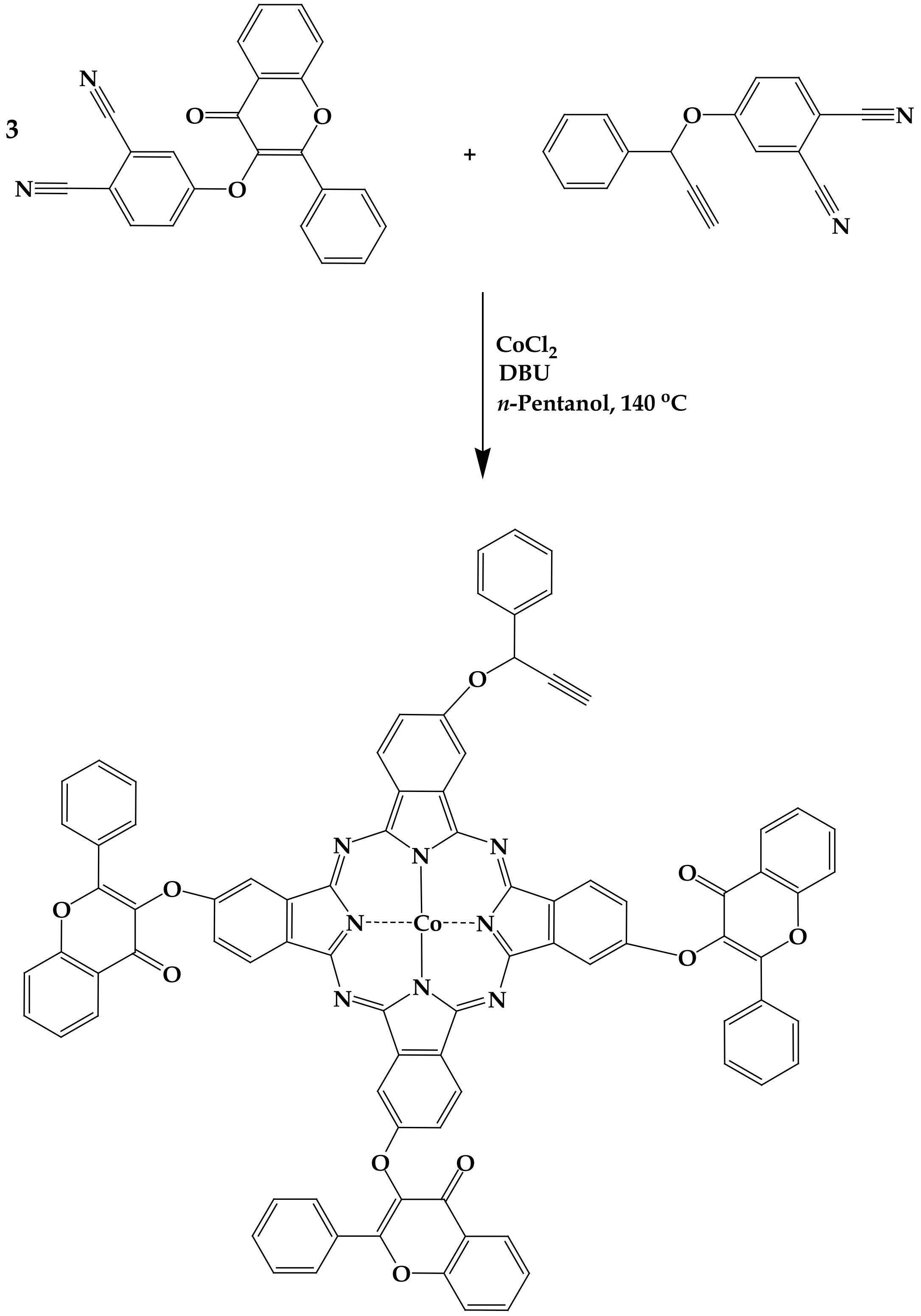

Scheme 3.1: *Synthesis of the A$_3$B (A = 4-(3-oxyflavone), B = a-(ethynyl)benzyl alcohol) asymmetric a-CoPc-flav3 (***1***).*

The solid-state FT-IR spectrum of the asymmetric α-CoPc-flav3 did not feature the peak associated with nitrile (CN) vibrations of neither of the starting benzonitriles, see **Figure 3.1**. This was the first indicator that cyclotetramerization did occur. Moreover, additional evidence that the asymmetric α-CoPc-flav3 had been successfully separated from the symmetrical CoPc-flav is that the $v(C{=}O)_{flavone}$ and the $v(\equiv C\text{-}H)$ signals are common features in both the metal complex (at 1650 cm^{-1} for $v(C{=}O)_{flavone}$ and 3253 cm^{-1} for $v(\equiv C\text{-}H)$) and its free-ligands (L1: at 1640 cm^{-1} for $v(C{=}O)_{flavone}$ and L2: at 3250 cm^{-1} for $v(\equiv C\text{-}H)$). The L2 and the asymmetric α-CoPc-flav3 also shows a $v(C{\equiv}C)$ band at 2200 cm^{-1}.

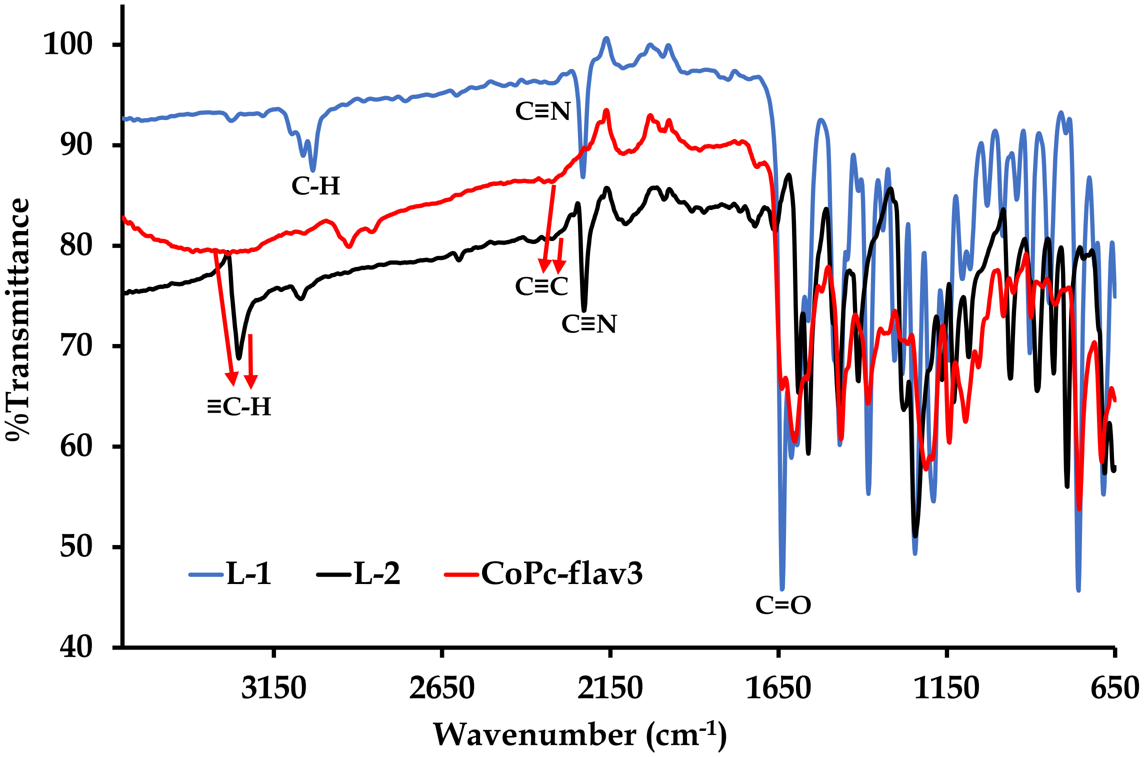

Figure 3.1: *Overlaid solid-state FT-IR spectra comparison of the benzodinitriles (L1 and L2) as well as their corresponding asymmetric a-CoPc-flav3.*

UV-Visible absorption spectra of α-CoPc-flav3 were recorded in both coordinative and non-coordinative solvents, *see* **Figure 3.2**. The spectrum collected in deaerated DMF displayed an intense *Q*-absorption band at 669 nm, associated with the π-π* electronic transition originating from the highest occupied frontier orbitals of the Pc ligand. Additionally, a more intense B band was observed at 320 nm. Typically, this band is attributed to the π-π* electronic transition originating from the lower molecular orbitals of the Pc ligand.[15-17]

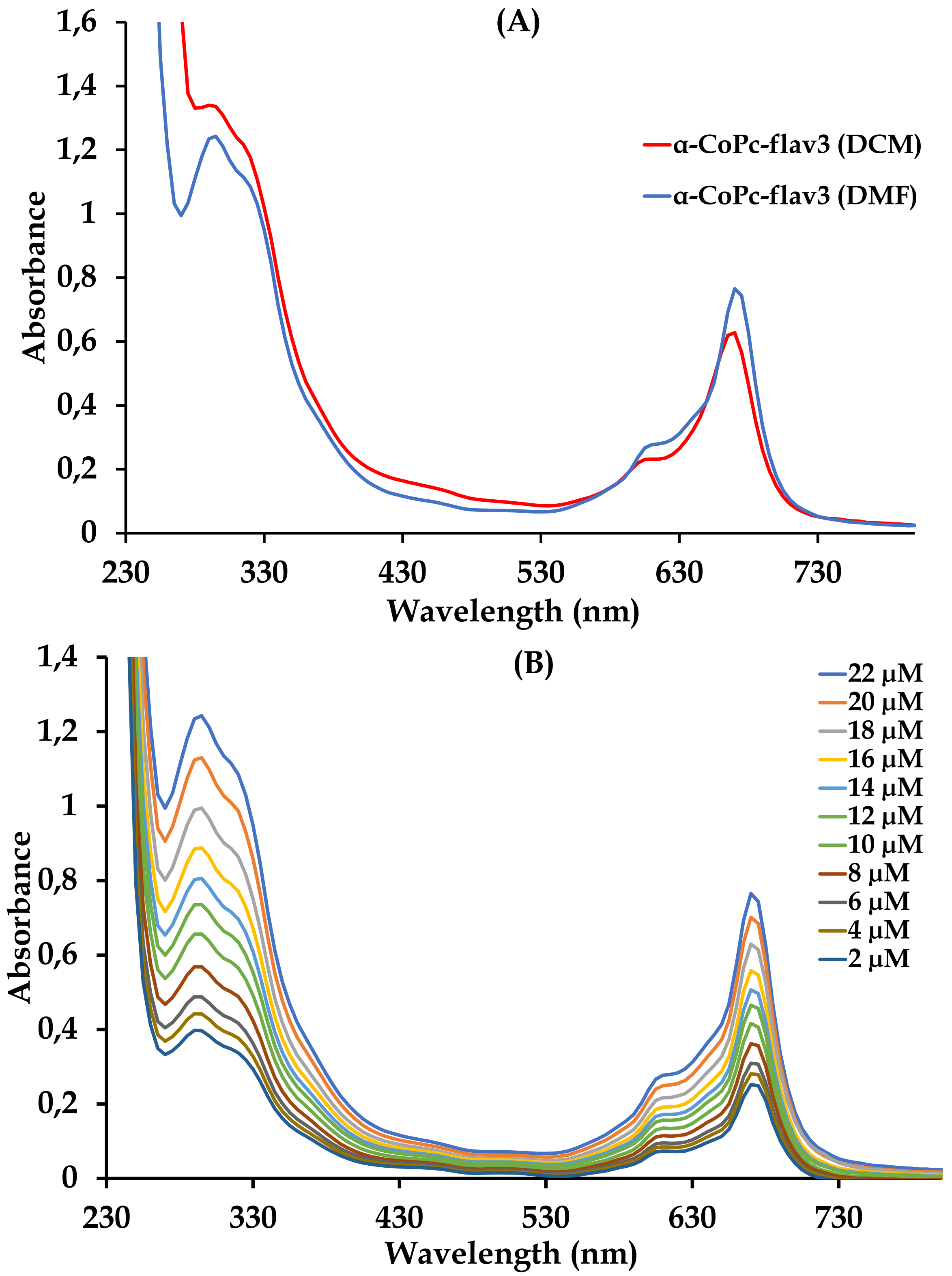

Figure 3.2: *(A) Overlaid UV–Visible absorption spectra of α-CoPc-flav3 in DMF and DCM (B) Concentration effect on the absorbance of α-CoPc-flav3 in DMF.*

Comparative analyses were conducted between the electronic spectra of α-CoPc-flav3 in DCM and DMF, refer to **Figure 3.2A**. A change in solvent polarity from DCM (less polar) to DMF (more polar and aprotic) causes a slightly red shift in the peak absorption ($\lambda_{max:}$) from 660 nm to 674 nm, with no visible colour differences between the two solutions.[18] The absorbance of α-CoPc-flav3 at different concentrations in DMF was recorded. As shown in **Figure 3.2B**, increasing the concentration (in the range from 10^{-6} to 10^{-5} M) of the α-CoPc-flav3 resulted in a progressing increase in the intensity of the Q band. Furthermore, there were no notable shifts in the electronic transitions nor was the formation of new bands associated with aggregation observed. However, there was a substantial broadening of the *Q*-band with increasing concentrations. Indicatively, the vibronic band also exhibits hypochromism while a shoulder at 610 nm progressively becomes more pronounced and this can be associated with aggregated CoPc species. These electronic spectral observations are synonymous with other CoPcs which have shown aggregation in coordinative solvents such as DMF.[19-21]

The mass spectrum of the α-CoPc-flav3 (**1**) was recorded using a Waters Micromass LCT Premier ESI-(+)-TOF mass spectrometer. As depicted in **Figure 3.4A**, the mass spectrum recorded without adding trifluoroacetic acid (TFA) as a protonation agent shows a base peak at *m/z* value of 1397.2438 amu and other discernible peaks within the *m/z* range of 1410.7472 to 1414.3146 amu. However, the peaks are superimposed on a high baseline background, suggesting poor ionization of the α-CoPc-flav3 in the absence of the protonation agent. To improve the ionization efficiency of the α-CoPc-flav3 (**1**), TFA was introduced to the solution of α-CoPc-flav3, to improve its ionization and the mass spectrum was re-recorded, see **Figure 3.4B**. The characteristic isotopic peaks (for comparison to the theoretical pattern, see **Figure 3.4C**). However, several additional peaks at lower *m/z* values also appeared in the spectrum. These peaks at the lower *m/z* range are tentatively assigned to radical ions of TFA, or due to its induced thermal reactions with the solvent and the metal complex. These peaks could not be readily assigned.

As illustrated in **Figure 3.3,** the peak observed at 1397.2438 amu can be attributed to the [M - (CH)]$^{\bullet+}$ fragment ion, formed by the thermal ionization of the terminal CH group of the ethynyl moiety. Other prominent peaks were observed in the experimental spectrum at *m/z* values of 1295.11 ([M - (*benzyl*)*ethyne*]$^{+\bullet}$) and 1190.81 ([M - (*flavone*)]$^{+\bullet}$. Meanwhile, the isotopic peaks which appeared at 1410.7472, 1411.302 and 1413.2773 amu values are all associated with the isotopic distributions of elements in the molecular ion and match those in the theoretical pattern calculated using the isotopic mass calculator as shown in **Figure 3.4C**. The matching of these isotopic molecular ion peaks (which are all due to ions related to the α-CoPc-flav3) confirms its successful synthesis.

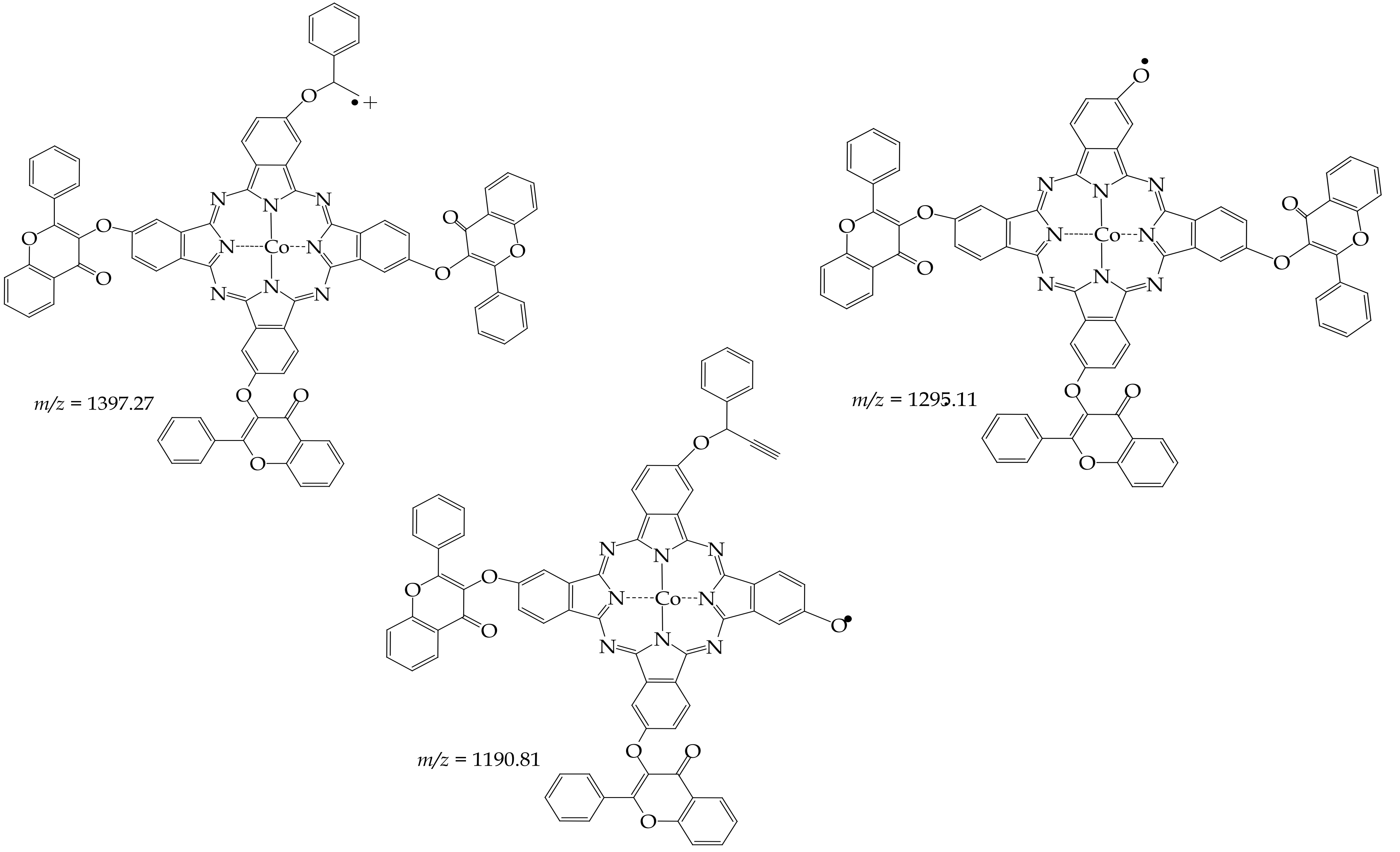

Figure 3.3: *Chemical structures of the* radical *fragment ions that are formed randomly due to the thermally-induced dissociations of* α-CoPc-flav3 ***(1)*** *in the presence of TFA.*

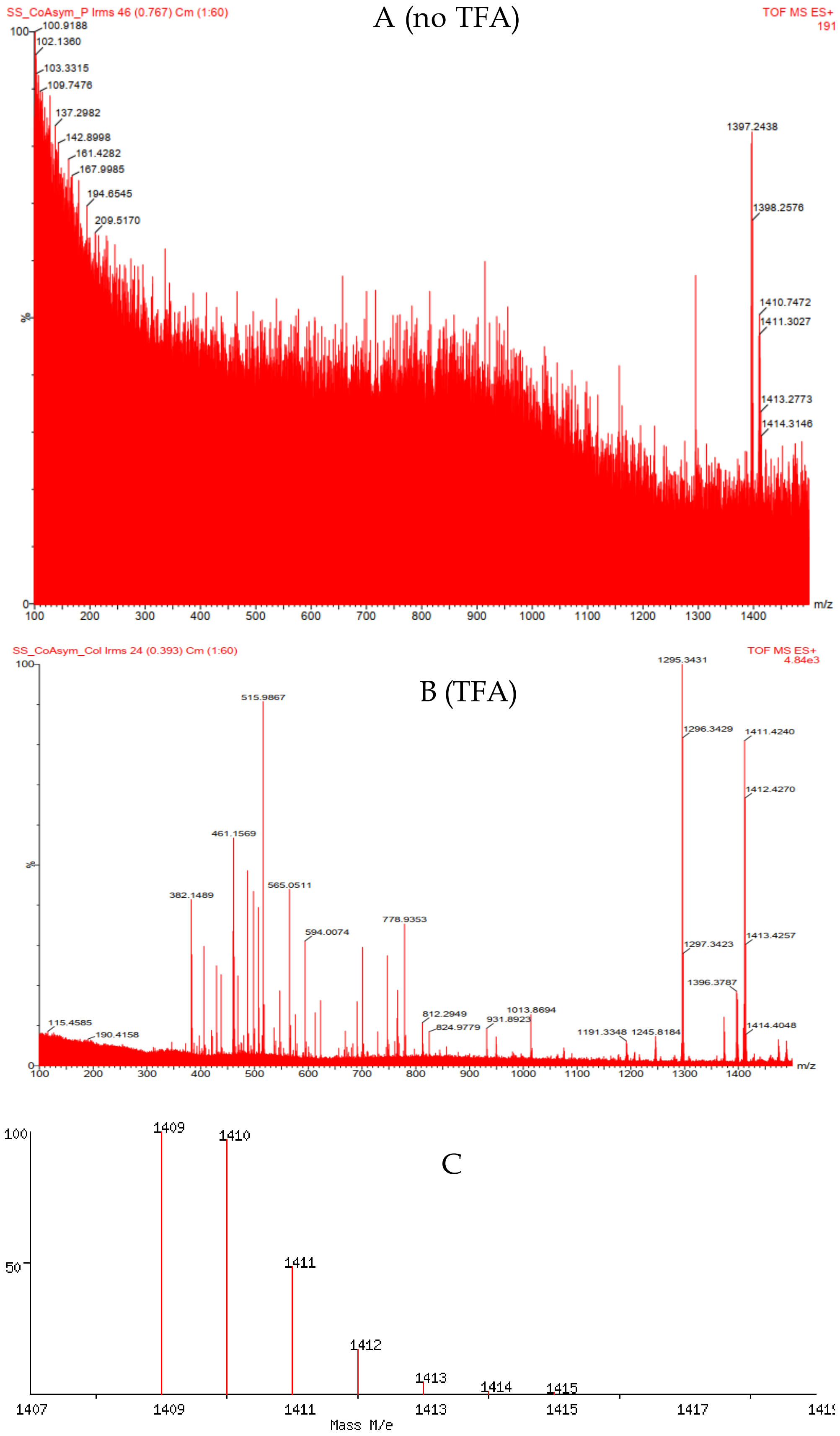

Figure 3.4: *(**A**) TOF-MS spectra of a-CoPc-flav3 without TFA and (**B**) with TFA added to promote ionization. (**C**) Theoretical pattern calculated via the isotopic mass calculator.*

3.4. Electrochemical studies

3.4.1. Cyclic- and square-wave voltammetry

The redox properties of α-CoPc-flav3 were investigated using both cyclic and square-wave voltammetry in DMF containing 0.1 M $TBABF_4$, as illustrated in **Figure 3.5**. The redox couples **I** to **IV** are assigned according to literature trends, refer to **Table 3.1**.[10,22-24] Both CV and SWV revealed four distinct redox processes (**I** - **IV**). Redox processes **II** and **III** are readily assigned to the metal-based Co(II)/Co(I) and Co(II)/Co(III) redox couples, respectively while redox process **IV** corresponds to the Pc-based $Pc^{(-2)}/Pc^{(-1)}$ redox process as detailed in **Table 3.1**. All these mentioned redox processes are quasi-reversible. The remaining peaks are Pc ring-based, and peak **I** corresponds to the $Pc^{(-2)}/Pc^{(-3)}$. It is worth noting that Chohan *et al.,*[10] synthesized a tetra-substituted 'A'$_4$-CoPc-flav, as shown in **Table 3.1**.

The comparison CV data of the synthesized α-CoPc-flav3, which is an asymmetrically substituted A_3B structure, and that reported for the tetra-substituted CoPc-flav (a symmetrical A_4) reported by Chohan *et al.*,[10] provides valuable insights into the differences in their redox behaviour. In the case of α-CoPc-flav3, the Pc (phthalocyanine) reduction and oxidation processes occur at slightly lower potentials compared to the symmetric CoPc-flav. This suggests that the A_3B asymmetric substituents of α-CoPc-flav3 exert a push (by the 3'A' moieties) and pull (by the alkyne moiety of B) effect on the Pc pi-ring electron system which modulates and facilitates the swift electron transfer within the Pc moiety and towards the electrode surface, making these redox processes more accessible at lower potentials.[25]

Conversely, the oxidation and reduction peaks of the cobalt(II) ion in the α-CoPc-flav3 occur at more negative and positive potentials, respectively, compared to the A_4 tetra-substituted CoPc-flav. This could be attributed to the specific electronic effects induced by the asymmetric substituents of the former. The nature and position of substituents can significantly influence the electronic properties and redox behaviour of the metal centre, leading to shifts in the oxidation and reduction potentials.[26] The quasi-reversibility of redox processes **III** and **IV** are emphasized by the separation in their peak potential (ΔE_p) values which are both greater than 58 mV (compared to ferrocene's at a bare GCE).[23] The ΔE_p value of redox couple **II** is equal to 105 mV and is thus classified as reversible while redox process **I** is irreversible, *see* **Table 3.2**.[27]

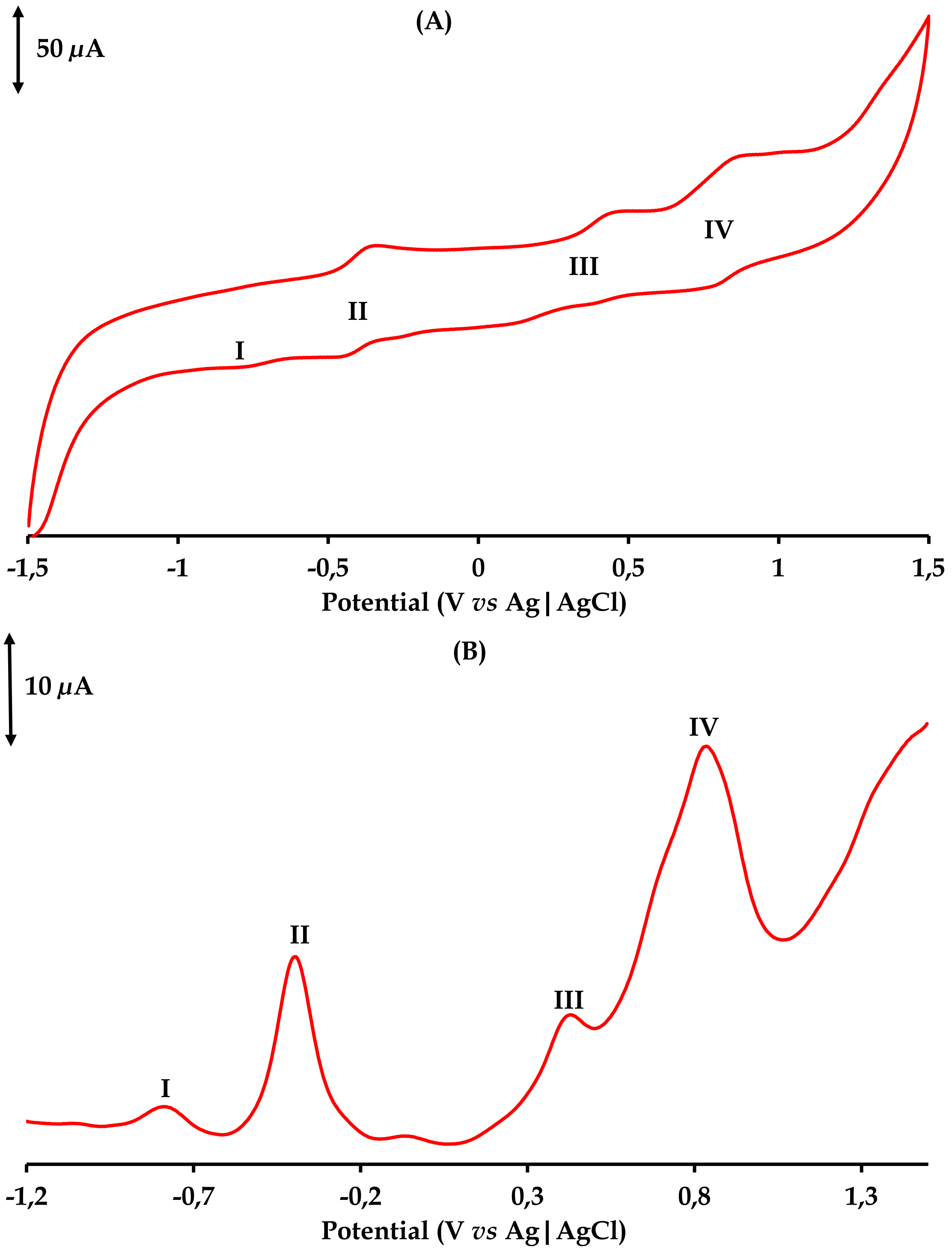

Figure 3.5: *(A) Cyclic and (B) square-wave voltammograms of* **a-CoPc-flav3** *(***1***) at 100 mV/s.*

Table 3.1: *Comparison of the voltammetric data (in V) between the novel* ***a-CoPc-flav3*** *as well as other tetra-substituted CoPc-flav and asymmetric CoPcs retrieved from literature.*

	$M^{I}Pc^{2-}/M^{I}Pc^{3-}$ (I)	$M^{II}Pc^{2-}/M^{I}Pc^{2-}$ (II)	$M^{II}Pc^{2-}/M^{III}Pc^{2-}$ (III)	$M^{III}Pc^{2-}/M^{III}Pc^{1-}$ (IV)	**Reference**
α-CoPc-flav3	-0.785	-0.397	0.434	0.842	This work
CoPc-flav	-0.845	-0.366	0.405	1.058	[10]
CoPc-5 (A_3B)	-0.78	-0.12	0.70	1.13	[22]
PC1 (A_3B)	-1.45	-0.38	0.77	1.07	[23]
CoPc-court	-1.24	-0.31	0.35	1.00	[24]

Abbreviations: **Flav:** *flavone;* **CoPc-5:** *[2,9,16-tri-(2,4-di-tert-buthylphenoxy)-23-(4-[6-carboxy-2-naphtoxy])-phthalocyaninato cobalt(II);* **PC1:** *Mono (pyridine-4-oxy)-tris(tert-butyl)phthalocyaninato Co(II) (Pc1) and* **CoPc-Cour:** *1(4),8(11),15(18),22(25)-tetra[4-(4-methoxyphenyl)-8-methylcoumarin-7 oxy]phthalocyaninatocobalt(II).*

Table 3.2: *Redox potentials of the redox couples of* **1** *obtained via cyclic voltammetry*

Redox couple	E_{pa} (V)	E_{pc} (V)	ΔE_p (V)
I	-0.785	-	-
II	-0.350	-0.455	0.105
III	0.451	0.381	0.07
IV	0.856	0.783	0.073

3.5. Electrochemical modification and characterization

3.5.1. Electrode modification

The modification of the glassy carbon electrode (GCE) was achieved *via* electrochemical grafting of neutral diazonium radicals formed from the reduction of the azido benzodiazonium ions. The radicals rapidly grafted to form strong C-C bonds with carbon components of the GCE. Thus, the successful grafting of the radicals is marked by a reduction in the peak current at -0.6 V for subsequent CVs as reported in the literature.[28-31] As per literature trends, a substantial decrease in current was observed during the second CV cycle which is ascribed to the surface passivation of the azido benzodiazonium groups that form an electrochemically less conductive film.[29,31,32] Thereafter, the low symmetry α-CoPc-flav3 was covalently clicked *via* its α-(ethynyl)benzyl alcohol group and the pre-grafted benzo-azido groups on the electrode surface in the presence of a Cu(I) catalyst to form a triazolyl linking anchor which confines the α-CoPc-flav3 on the surface to form the GCE|clicked-α-CoPc-flav3, see **Scheme 3.2**.

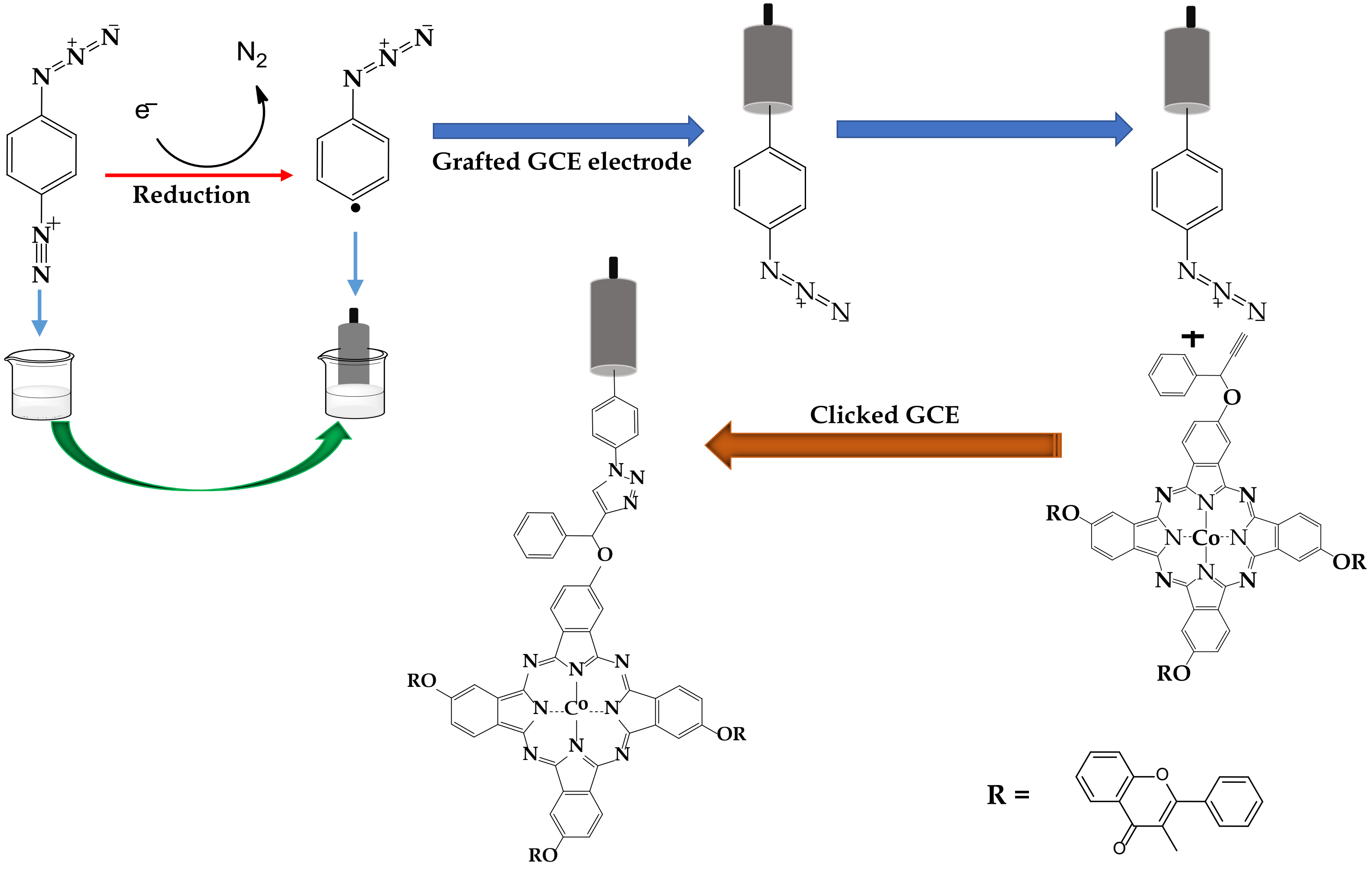

Scheme 3.2: *Electrochemical grafting of the 4-azido benzodiazonium to the GCE interface and the Cu(I)-catalysed clicking of a-CoPc-flav3 to the grafted azido groups to produce the GCE|clicked-a-CoPc-flav3.*

3.5.2. Characterization of the GCE|grafted/-clicked-a-CoPc-flav3

The electrochemical behaviours of the GCE|grafted /-clicked-α-CoPc-flav3 were contrasted relative to the bare GCE in a standard aqueous redox probe, potassium ferricyanide in KCl as a supporting electrolyte, see **Figure 3.6.** Lower redox peak currents were observed for the GCE|-grafted which illustrates the characteristic blocking effect of the grafted benzo-azido layer which limits the redox interconversion of the Fe(III)/Fe(II) ion system at the surface of the modified GCE|.[33,34] In addition, the wider ΔE_p value for the grafted GCE is typical of the retardation of the redox processes occurring at the electrode surface.[33] Upon further modification by clicking, no Fe(III)/Fe(II) redox interconversion peaks are observed because the modifier film of the GCE|clicked-α-CoPc-flav3 is virtually non-ion-permeable. These trends are similar to what has been reported in other studies for clicked GCEs modified by low-symmetry MPcs.[7,34]

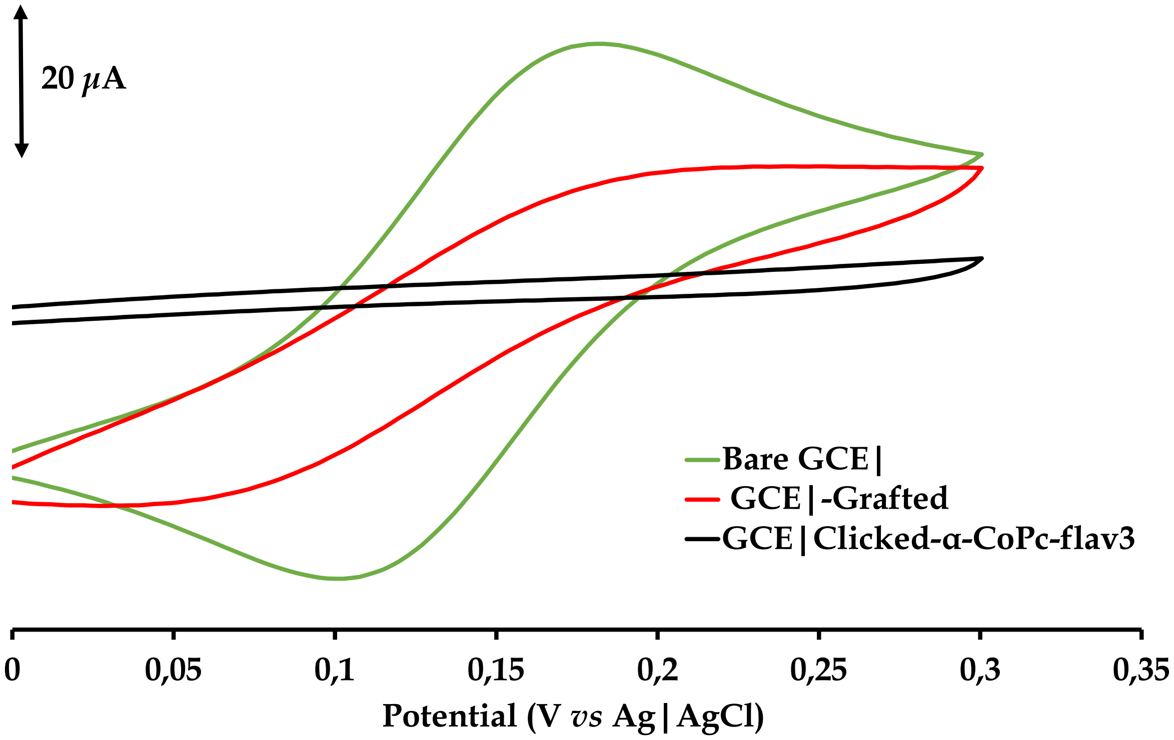

Figure 3.6: *CVs of 1 mM $K_3Fe(CN)_6$ solution containing 0.1 M KCl using the bare, azido-grafted and the GCE|clicked-a-CoPc-flav3.*

3.5.3. Electrochemical impedance spectroscopy

The study of charge transfer kinetics at the bare or GCE|clicked-α-CoPc-flav3/electrolyte interface for the $[Fe(CN)_6]^{4-}/[Fe(CN)_6]^{3-}$ redox interconversion was conducted by employing electrochemical impedance spectroscopy (EIS). EIS is an informative and non-destructive technique for probing the nature of the electron-mediating film and elucidating its electron transfer rates. Nyquist and Bode plots are graphical representations that are frequently employed to probe the electrical impedance behaviours of electrocatalytic films thereby giving valuable insights into the rate of charge transfer, especially across electrode interfaces.[35]

Within the low-frequency region, specifically in the diffusion-controlled range of the Nyquist plots, a semi-circle is observed. This semi-circle's diameter signifies the resistance to charge transfer within the interfacial film of the GCE|clicked-α-CoPc-flav3, as illustrated in **Figure 3.7**. At higher frequencies, the plot assumes a linear character known as the Warburg line, indicating diffusion-kinetic control. Semi-circular /arch lines are discernible on the low-frequency regions of the Nyquist plots for both the unmodified GCE and the CME, representing the diffusion-controlled charge transfer within the thin clicked-α-CoPc-flav3 film and bare while the linear correlations in the high-frequency regions represent the respective infinite Warburg impedance.

By fitting the data to the standard equivalent resistance circuit, several key parameters are derived: the charge transfer resistance (R_{CT}), the Warburg impedance (Z_W), the capacitance (C_{dl}), and the electrolyte resistance (R_S), as outlined in **Table 3.3**. Notably, the bare GCE exhibits a significantly lower R_{CT} (1318 Ω) in comparison to CME (18600 Ω). A higher R_{CT} value implies lower ionic conductivity of the electrode surface. Therefore, it can be asserted that the modified electrodes are less conductive than their bare counterparts, thereby corroborating the blocking effect of the grafted-modifier film also observed in the comparative CV voltammograms.

The Bode graphs show that the phase angle for the bare GCE (~71°) is greater than that of GCE|clicked-α-CoPc-flav3, which is ~ 61°, see **Figure 3.8**. It may be concluded that both electrodes exhibit leaky capacitor behaviour since their phase angles are less than the desired 90° for a genuine capacitor.[36] The frequency shift observed in the cyclic CME compared to the bare electrode, along with the calculated n value of less than 1 (n = 0.783), strongly indicates the microstructural differences between the two. The shift to a more negative frequency is an indication the surface of the GCE|clicked-α-CoPc-flav3 is less conductive. The value of n = 0.783 is indicative of a more rough surface. This provides additional evidence supporting the altered microstructure of GCE|clicked-α-CoPc-flav3.[4] The rougher surface can impact various electrochemical behaviours and can be a crucial factor in enhancing the electrocatalytic activity and sensitivity of the electrode.[37]

Table 3.3: *EIS data for a 5 mM $[Fe(CN)_6]^{3-/4}$ solution, collected using the bare GCE| and GCE|clicked-a-CoPc-flav3 electrodes. Error values are shown in brackets.*

GCE	**R_S (Ω)**	**R_{CT} (Ω)**	**Z_w (μMho)**	**C_{dl} (μMho)**	***n***
Bare	100 (1.8)	1318.7 (0.3)	1.6 (5.3)	1.14 (6.4)	0.90
clicked-α-CoPc-flav3	87.0 (1.2)	18600 (2.3)	69.5 (4.2)	4.08 (7.1)	0.78

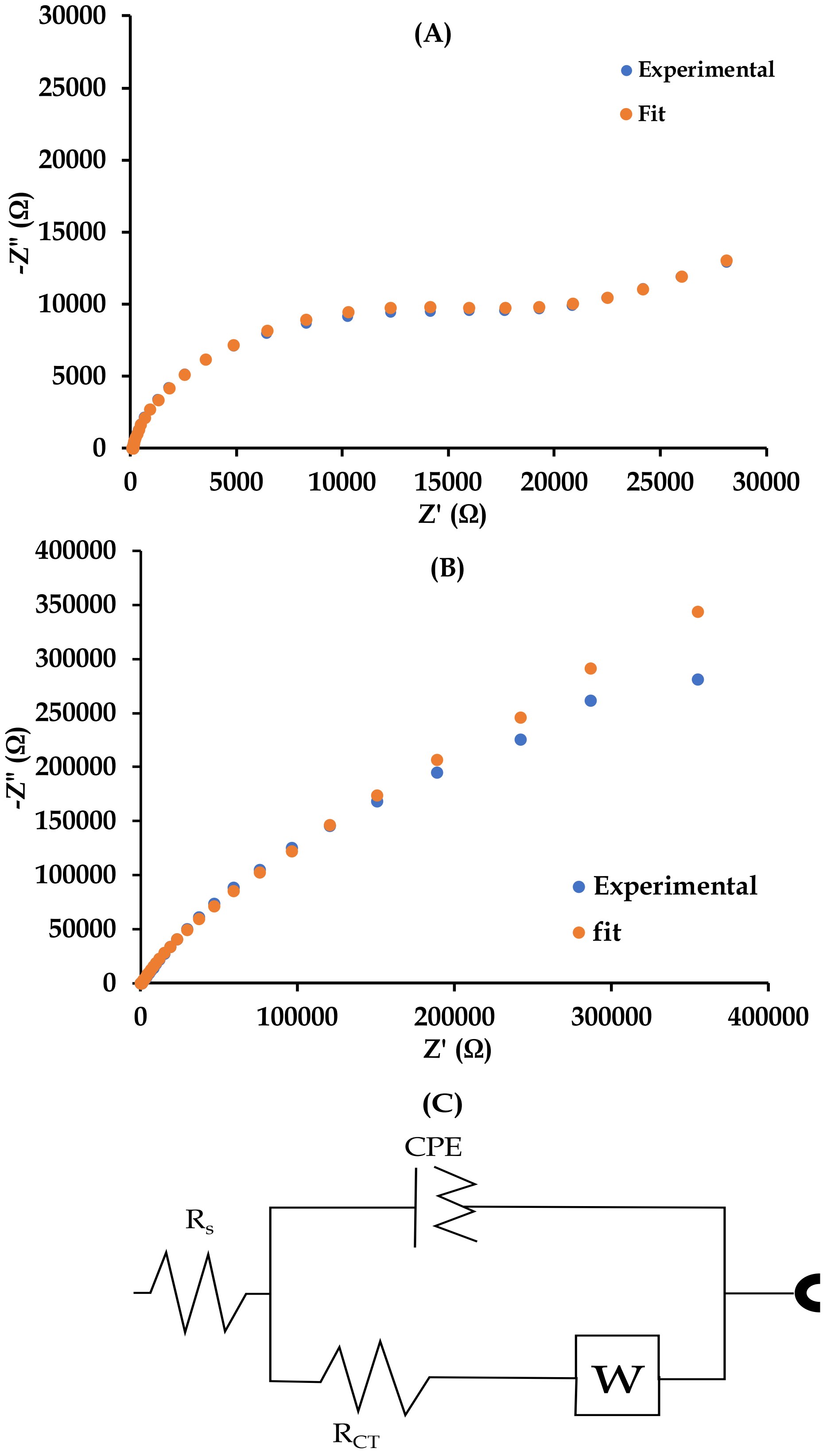

Figure 3.7: *Nyquist plots attained in a 5 mM $K_3[Fe(CN)_6]$ solution containing 0.1 M KCl using (A) bare GCE, (B) GCE|clicked-a-CoPc-flav3 while (C) shows the equivalent circuit used to fit the EIS data.*

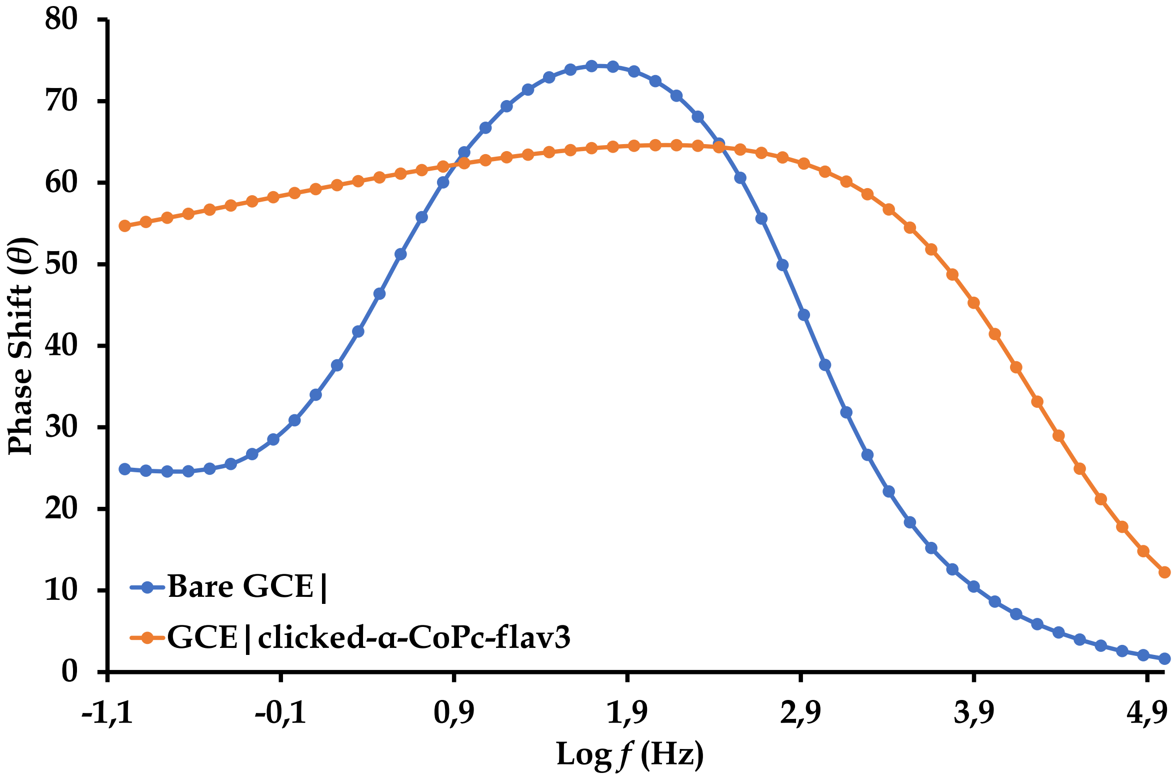

Figure 3.8: *Bode plots for 5 mM [Fe(CN)$_6$]$^{4-}$/[Fe(CN)$_6$]$^{3-}$ redox interconversion generated with the bare GCE and GCE|clicked-a-CoPc-flav3.*

3.5.4. *Surface coverage of the GCE|clicked-a-CoPc-flav3*

To further confirm the modification of the glassy carbon electrode, the surface coverage (Γ) of the GCE|clicked-α-CoPc-flav3 was investigated by cyclic voltammetry (CV). The number of moles of the clicked-α-CoPc-flav3 embedded in the modifier film per unit area was calculated using **equation 3.1** to obtain the surface coverage (Γ), as reported by Kantize *et al.*[4]

$$I_{pc} = \frac{n^2 F^2 A \Gamma (v)}{4RT} \quad \textbf{(3.1)}$$

In **Equation 3.1**, I_{pc} represents the peak current of the cobalt redox (*viz.* Co(III)/Co(II)) process, n is the number of transferred electrons, F is the Faraday constant, A is the surface area (0.071 cm^2) of the bare GCE, v is the scan rate, R is the gas constant, and T is the temperature. The calculated surface coverage value for the GCE|clicked-α-CoPc-flav3 was determined to be 1.50 x 10^{-10} mol/cm^2. This value is consistent with those previously reported for monolayer electrodeposited films on electrode surfaces, such as 1 x 10^{-10} mol/cm^2.[38] The widened redox couples observed in CVs of the GCE|clicked-α-CoPc-flav3 (**Figure 3.9A**), especially for redox process **II** (Co(III)/Co(II)), suggest that the bare GCEs had indeed been successfully modified by a passivating film of molecules of the clicked-α-CoPc-flav3.

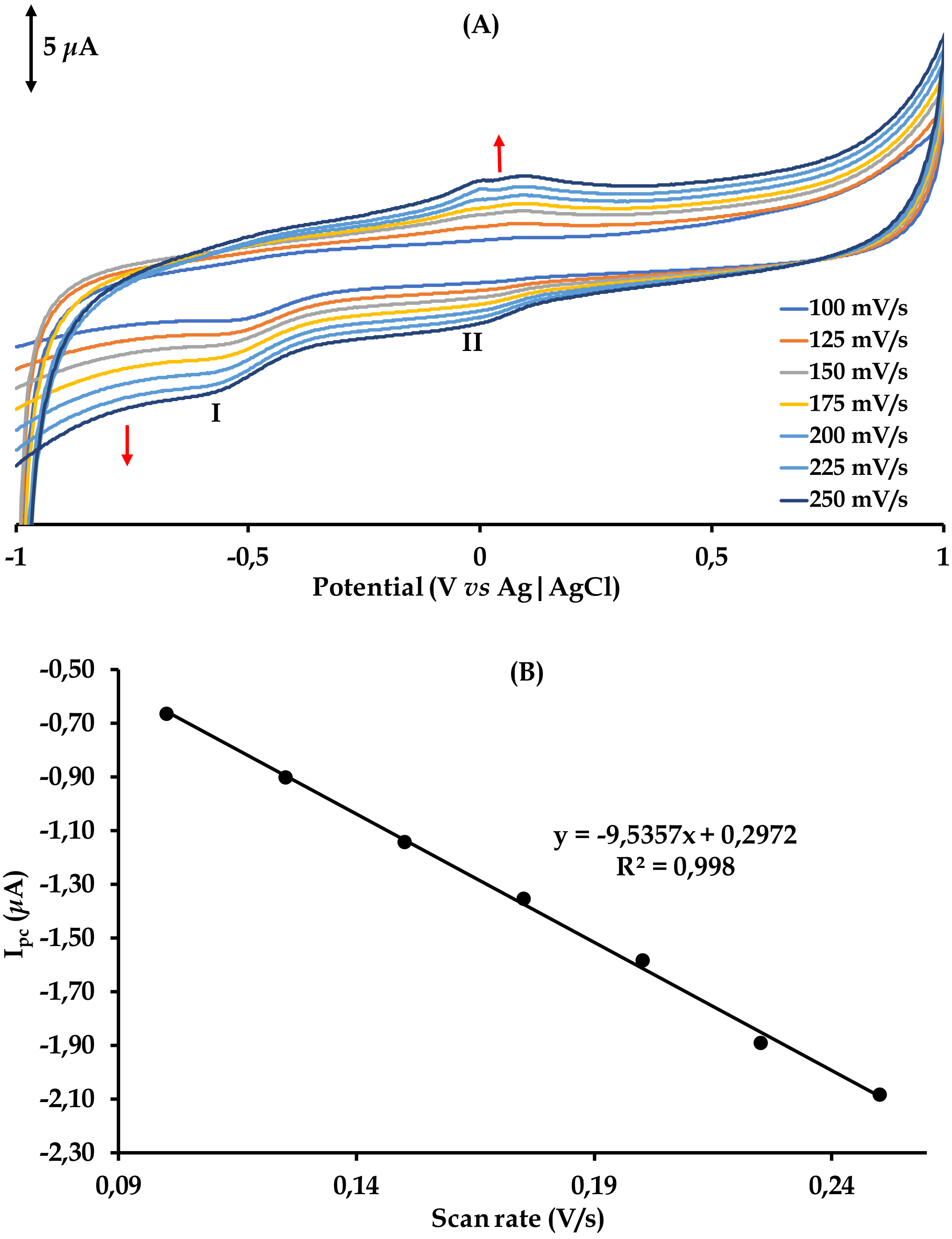

Figure 3.9: *(A) CVs of the GCE|clicked-a-CoPc-flav3 in pH 7.4 buffer solution at increasing scan rates (100 mV/s to 250 mV/s). (**B**) A plot of I_{pc} vs. scan rate measured at the redox couple **II**.*

3.6. Dopamine electrocatalysis

3.6.1. Cyclic voltammetry

Comparing the stacked cyclic voltammograms (CVs) of 1 mM dopamine (DA) in PBS and the buffer alone using both the bare GCE|and the respective GCE|clicked-α-CoPc-flav3 reveals distinct electrochemical sensitivities of the electrodes towards the analyte. For the unmodified GCE, a current response for the oxidation of dopamine (DA) occurs at 0.21 V and is significantly higher than the background current exhibited in the buffer solution as depicted in **Figure 3.10**.

The cathodic return peak appears at 0.044 V. As expected, the current responses of the GCE|clicked-α-CoPc-flav3 were significantly higher than that of the bare, showing the enhanced rate of electron transfer facilitated by the monolayer of the clicked film of **1**, evident from the lower ΔE_p value of 61 mV compared to the bare GCE's 156 mV, refer to **Table 3.4**. These observations underscore the electrocatalytic and mediating roles of the clicked α-CoPc-flav3 film. Notably, DA's redox potentials measured by the CME fall within the same potential window [0 V to 0.8 V] as the Co(II)/Co(III) redox process in PBS using the GCE|clicked-α-CoPc-flav3. This proximity in potential ranges suggests that the metal-based Co(II)/Co(III) redox process facilitates the electrocatalysis of the analyte, as previously described.[27] Characteristically, dopamine in PBS at pH 7.4 is oxidized in a multistep redox pathway at the GCE|clicked-α-CoPc-flav3 interface, see **Scheme A1**.[39] The two oxidative single-electron transfers are accompanied with intramolecular proton transfers which can either occur tandemly or in a stepwise manner after each oxidative electrochemical process.[40] During the electrocatalysis of DA (A), the semi-quinone (B) intermediate formed after the first oxidation followed by the oxidative formation of the quinone (C) analog.

Table 3.4: *Redox potential data for dopamine (DA) measured via CV using bare GCE and GCE|clicked-a-CoPc-flav3*

	E_{pa} *(V)*	E_{pc} *(V)*	ΔE_p *(V)*
Bare GCE|	0.205	0.049	0.156
GCE|clicked-α-CoPc-flav3	0.142	0.081	0.061

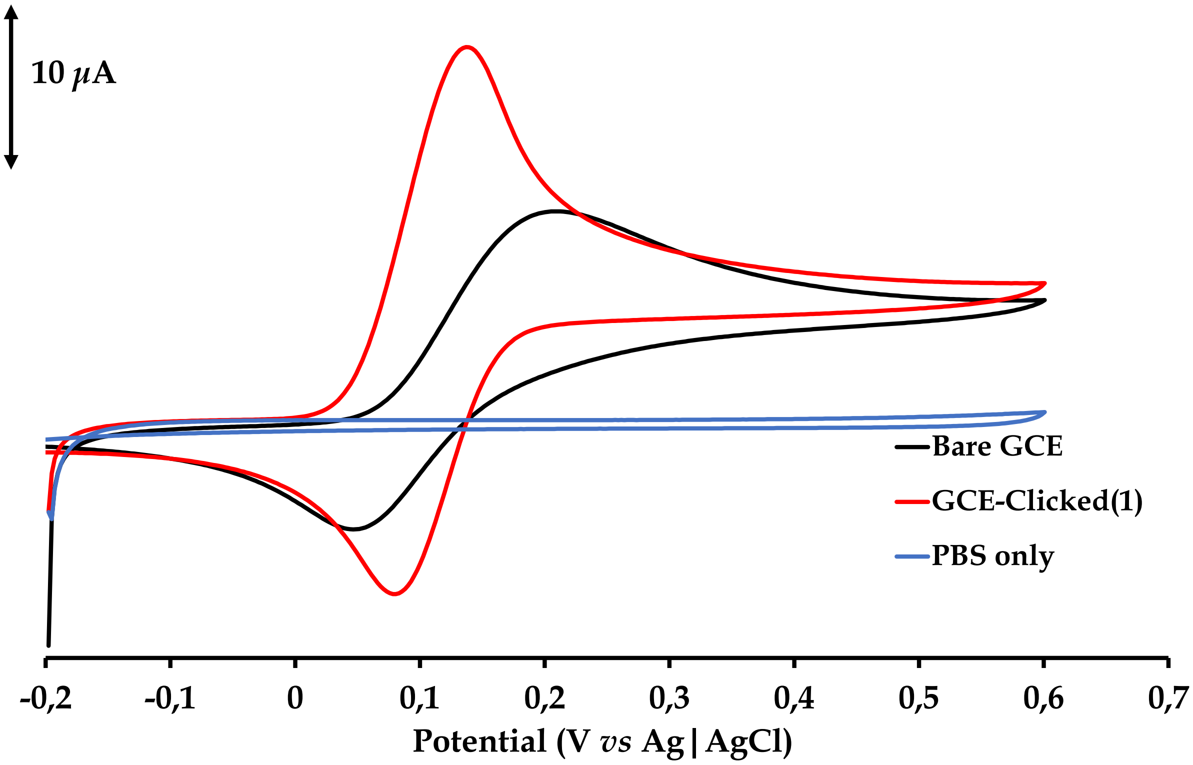

Figure 3.10: *Stacked CVs attained using the bare GCE| and GCE|clicked-a-CoPc-flav3 in the electrolyte solution and 1.0 mM dopamine in PBS.*

3.7. Optimization of the electrocatalytic parameters of GCE|clicked-α-CoPc-flav3

3.7.1. pH studies, stability and reproducibility

The optimal pH (PBS buffer) for the electrocatalytic detection of dopamine (DA) at the GCE|clicked-α-CoPc-flav3 was investigated using square-wave voltammetry within the pH values ranging from 3.0 to 7.3 as shown in **Figure 3.11**. Gradual shifts towards higher SWV peak potentials were observed as the pH decreased. Alongside these shifts, there were gradual decreases in SWV peak currents, except for the SWV data collected at pH 6. Consequently, a pH of 6.3 provided the optimal electrochemical activity for the CME in detecting DA. The preference for pH 6.3 over pH 7.3 is attributed to the former producing a sharper and more sensitive signal.

Similar trends have been reported previously, where a good linear relationship between pH values and peak potentials was observed.[41] However, it is noteworthy that the calculated slope of -99.2 mV/pH is significantly different from the expected correlation slope for the ion exchange activity for protons, which is -59.2 mV/pH at 25 °C. Thus, the magnitude of the calculated slope suggests a coupled two-electron, concerted two-proton oxidation process occurring at the GCE|clicked-α-CoPc-flav3 interface.[42,43]

Replicated CVs (N = 8) of 1 mM of DA in a PBS solution (pH 6.20) were recorded at the GCE|clicked-α-CoPc-flav3 surface to test its stability, see **Figure A1**. The current responses decreased for the first two scans (**Figure A1B**), while the peak potentials shifted higher and from the 3rd scan, both the peak currents and potentials became stable.[40] The %RSD was found to be 0.295% (N = 8) showing good reproducibility and stability of the GCE|clicked-α-CoPc-flav3 during the detection of DA. In fact, the electrocatalytic performances of the GCE|clicked-α-CoPc-flav3 can be correlated with other reported CMEs displaying good structural integrity of their respective electron-mediating layers.[40,44-46]

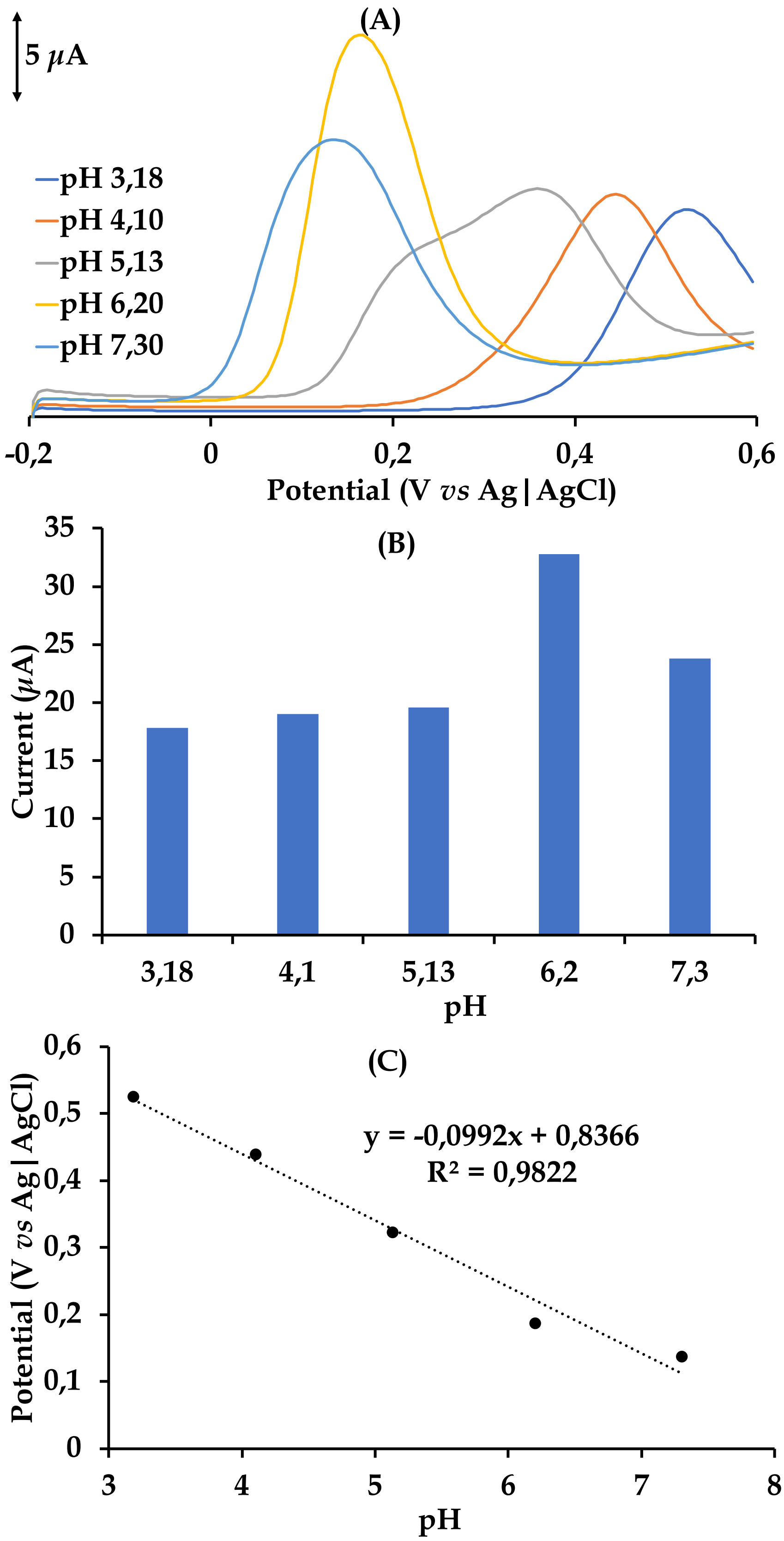

Figure 3.11: ***(A)*** *Effect of pH on the SWV current responses of the GCE|clicked-a-CoPc-flav3 towards 1 mM DA in PBS;* ***(B)*** *a bar chart of the DA oxidation current responses at different pHs and* ***(C)*** *the correlation of pH and oxidation peak potential of DA pH.*

3.7.2. Electrochemical kinetics of the GCE|clicked-a-CoPc-flav3

The CVs for DA recorded utilizing the GCE|clicked-α-CoPc-flav3 at various scan rates are shown in **Figure 3.12A**. The electrocatalytic responses of the GCE|clicked-α-CoPc-flav3 towards the oxidation of DA are shown by the correlated rise in currents with an increase in the scan rate which is also accompanied by gradual shifts in the oxidation potentials. **Figure 3.12B** illustrates that the current signal increases linearly with the square root of the scan rates, implying that the electro-oxidation of DA at the GCE|clicked-α-CoPc-flav3 is diffusion-controlled.

A plot of E_{pa} against log v was used to calculate the Tafel slope according to **equation 3.2**,

$$E_{pa} = \frac{2.3RT}{2(1-\alpha)Fn_{\propto}} log\, v + K \tag{3.2}$$

where the number of electrons involved in the rate-determining step is $n_{\propto}$, the scan rate is v, and K is the intercept from the linear equation and the transfer coefficient α. The calculated Tafel slope for the GCE|clicked-α-CoPc-flav3 was found to be 196 mV/decade. The Tafel slope falls outside the range of 30 - 120 mV/decade for typical reversible redox couples and is associated with quasi-reversible redox couples for which there is a slower rate of electron transfer at the electrode interface. It may also be an indication of significant interactions between the substrate and the electron-mediating thin layer.[47] In fact, the latter is supported by progressive shifts in oxidation redox potentials with increasing scan rates observed as observed in **Figure 3.11**.[48]

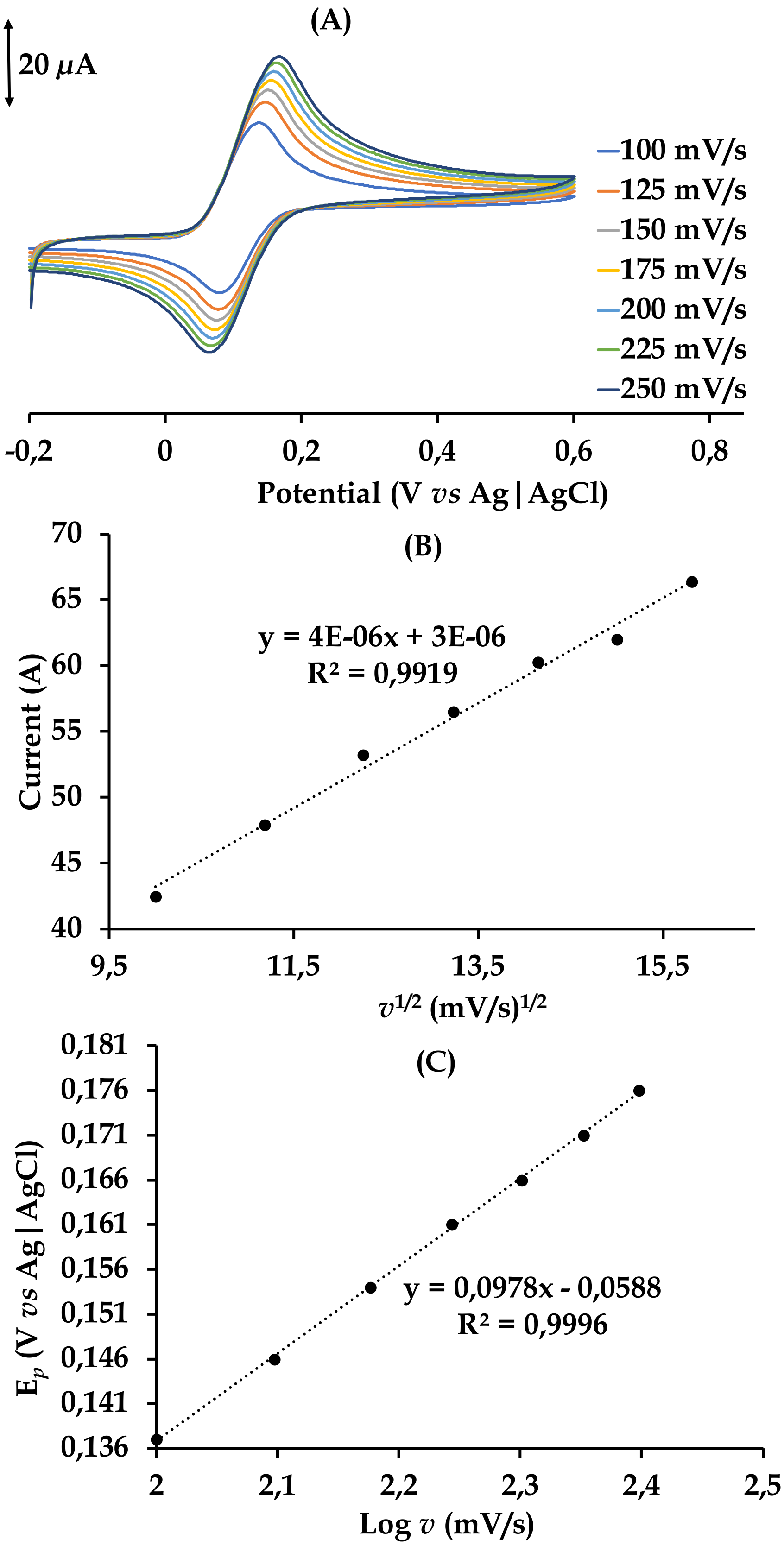

Figure 3.12: *(A) CVs of DA recorded at increasing scan rates (100 - 250 mV/s) using the GCE|clicked-a-CoPc-flav3, (**B**) the plot of peak current against the square root of scan rate and (**C**) a plot of potential against the log of scan rate.*

3.7.3. *Convection- and diffusion-controlled rate constants*

The single-step chronoamperometric data for the oxidation of 0.8 mM DA and species found in the PBS as a background electrolyte were recorded to obtain the diffusion-controlled rate constant for the oxidation of the former at the GCE|clicked-α-CoPc-flav3, see **Figure 3.13**. To record the chronoamperograms of DA or species in the background electrolyte, an overpotential of 0.14 V (for the E_{pa} of DA, see the CVs at the CME in **Figure 3.11)** was applied to the GCE|clicked-α-CoPc-flav3. The evolution of the current was monitored within a time interval of 5 – 20 s from the onset. The electrocatalytic rate constant was calculated from the slope of a plot of the normalized currents for the oxidations of DA against $\boldsymbol{t^{1/2}}$, according to the simplified equation **3.3**,

$$\frac{I_c}{I_b} = \pi^{1/2}(kC_o t)^{1/2} \qquad (\mathbf{3.3})$$

In **equation 3.3,** I_c and I_b are the different catalytic limiting currents obtained using the GCE|clicked-α-CoPc-flav3 and the bare GCE, C_0 is the molar concentration of DA (1 mM), *k* is the electrocatalytic rate constant, and *t* is the time elapsed in seconds. The diffusion-controlled rate constant for the GCE|clicked-α-CoPc-flav3 was found to be 8.47 x10^4 M^{-1} s^{-1}. As shown in **Table 3.5**, the order of magnitude (10^4 M^{-1} s^{-1}) is comparable to the previously reported data.[10,49-51]

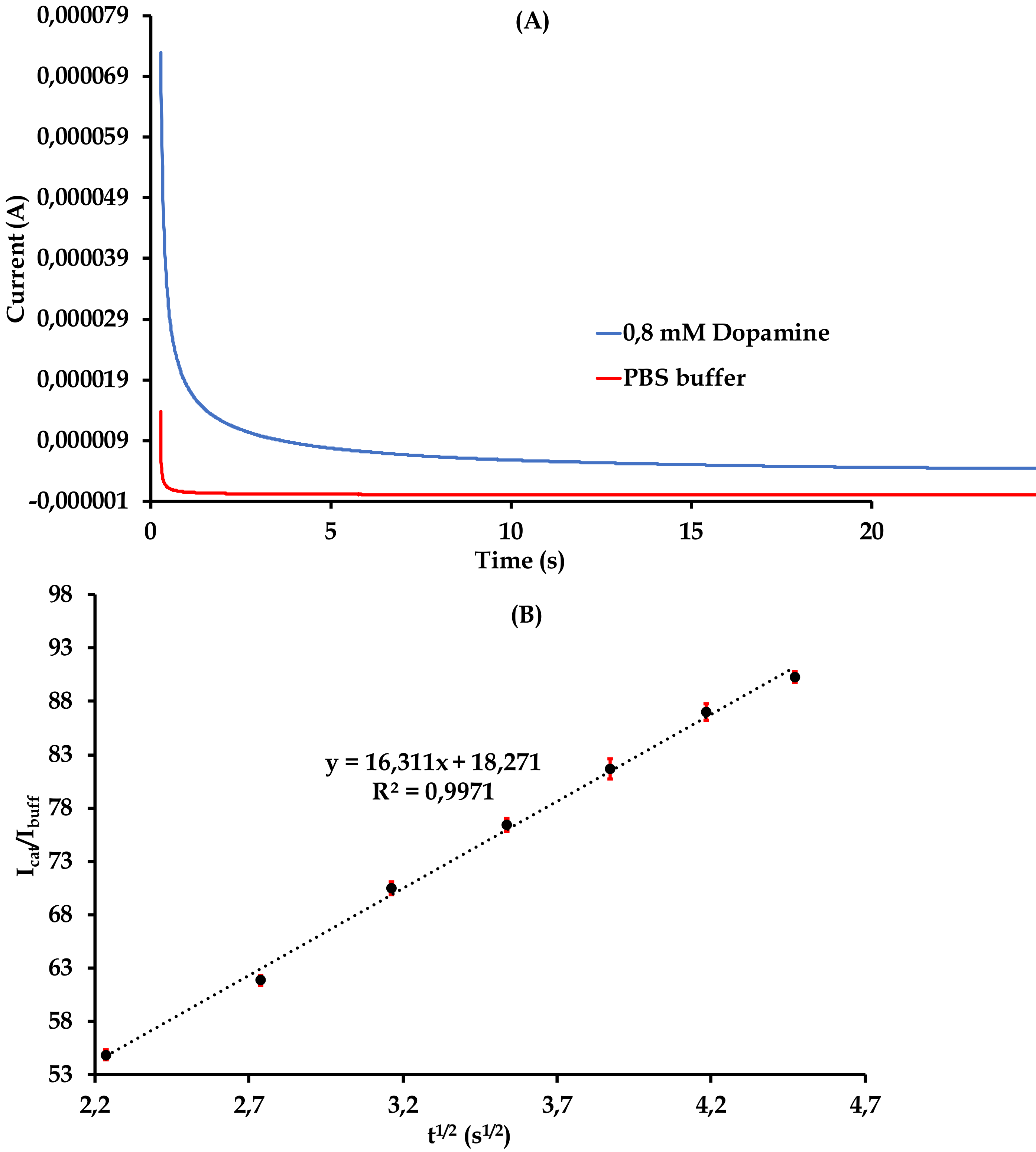

Figure 3.13: *(A) Chronoamperograms of 0.8 mM DA in PBS (pH 6.2) at the GCE | clicked-a-CoPc-flav3 and (**B**) plot of* I_c/I_b *against* $t^{1/2}$.

Table 3.5: *Comparison of catalytic rate constants for the detection of dopamine using CME.*

Modifying Layer	**analyte**	***k*, (M^{-1} s^{-1})**	**Reference**
GCE | clicked-a-CoPc-flav3	Dopamine	8.47×10^4	This work
CoPc-flav-GCE	Dopamine	7.83×10^5	[10]
BNDCNPE	Dopamine	18.22×10^3	[49]
AC–CPE	Dopamine	40.90×10^4	[50]
GCE/1@NGQDs	Dopamine	3.84×10^2	[51]

Abbreviations: ***CoPc-flav***: *tetra-4-(3-oxyflavonephthalocyaninato)Co(II);* ***BNDCNPE:*** *[1,1'-binaphthalene]-4,4'-diol-modified carbon nanotube paste electrode;* ***AC–CPE***: *Activated carbon - carbon paste electrode and* **GCE/1@NGQDs:** *Tetra-4-((-1,3-bis(dimethylamino)propan-2-yl)oxy)phthalocyaninatocobalt(II)-nitrogen-doped graphene quantum dot conjugate.*

Hydrodynamic convection-dominating kinetics was investigated using a rotating disk electrode (RDE) at various rotation rates while simultaneously collecting the linear sweep voltammograms (LSVs) at a low scan rate to minimize the diffusion of the analyte, see **Figure 3.14(A)**.[52,53] At higher rotation rates, the rough surface of the RDE together with its rotatory motion induces an eddy swirl of the solution, and hence eddy currents flow through the CME as can be seen by the wavy LSVs recorded at higher rotation rates. These trends in the eddy currents between the CME and the bare GCE contrast the lower phase angle and lower n (0.783) values that were observed in the electrochemical impedance spectroscopy (EIS) data which implied the clicked-α-CoPc-flav3 modifier film had less charge capacitance. Convection-controlled mass transport was substantiated by applying the Levich equation (**Eq. 3.4**) where a linear relationship was attained between the limiting current (I_L) and the square root of the rotational speeds ($w^{1/2}$) of the rotating disk electrode (RDE).

$$I_L = 0.62nFAD^{2/3}v^{-1/6}\omega^{1/2}C_0 \tag{3.4}$$

where D is the substrate's diffusion coefficient, A is the electrode area, v is the kinematic viscosity, ω is the rotation rate and C_0 is the bulk concentration of the analyte. In general, the kinetic and mass transport parameters may be separated using the Koutecky-Levich equation (**Equation 3.5**), and the convection-controlled rate constant was calculated using this equation.[52,54]

$$\frac{1}{I_L} = \frac{1}{nFC_0k\Gamma} + \frac{1}{0{,}62nFAD^{\frac{2}{3}}v^{-\frac{1}{6}}C_0\omega^{\frac{1}{2}}} \tag{3.5}$$

The Koutecky-Levich plot of $1/I_L$ against $1/\omega^{1/2}$ rendered a linear relationship (**Figure 3.14**(**C**)) from which a rate constant of 1.38 x 10^4 M^{-1} s^{-1} for the oxidation of DA at the surface of the rotating GCE|clicked-α-CoPc-flav3 was calculated using the y-intercept. This rate constant is comparable to that for the diffusion-controlled process determined using GCE|clicked-α-CoPc-flav3.

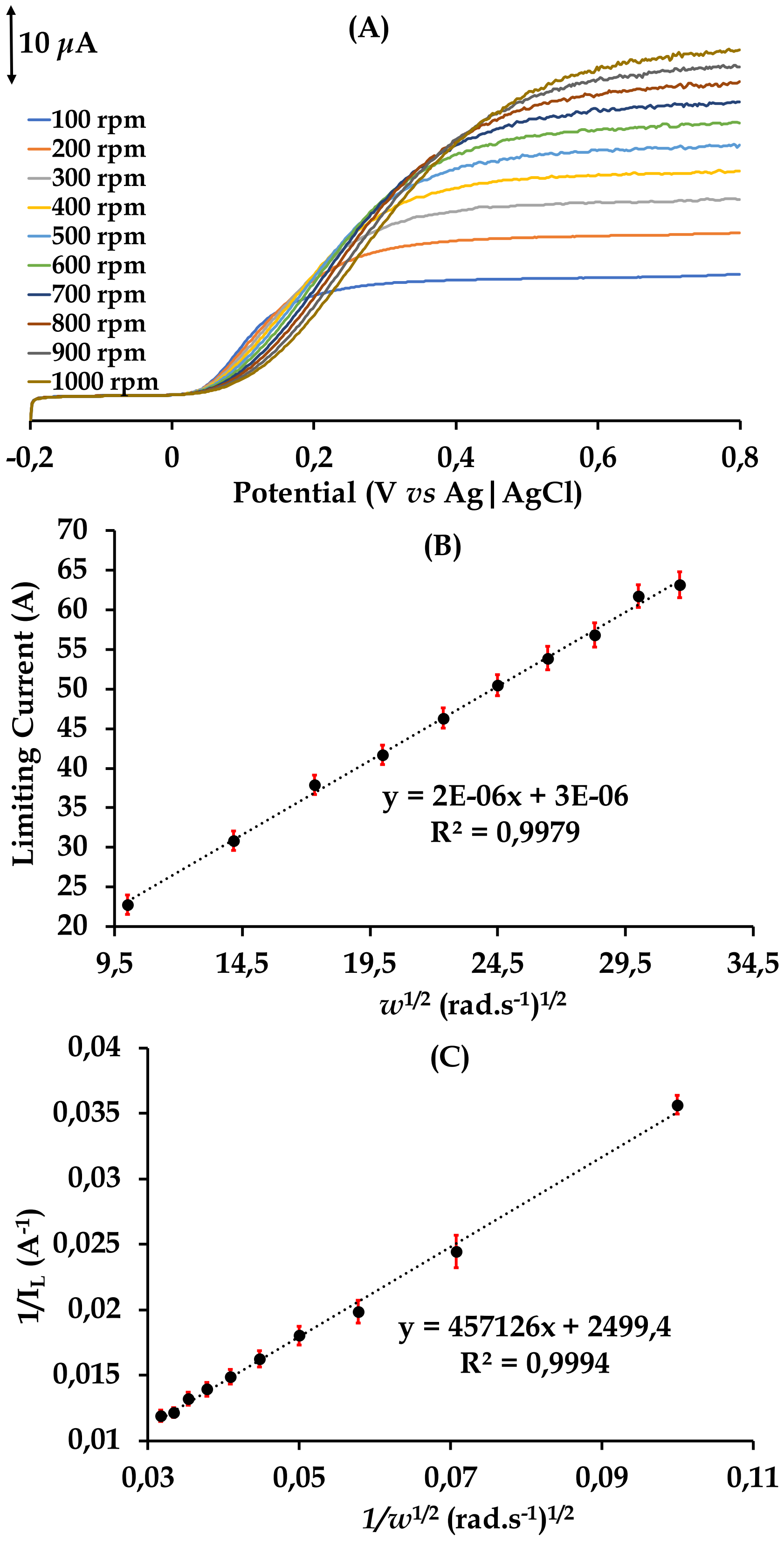

Figure 3.14*: (A) RDE-LSVs of the rotating GCE | clicked-a-CoPc-flav3 in PBS (pH 6.2) in the presence of 1 mM DA and at a scan rate of 0.015 V/s, (***B***) the Levich, (***C***) and the Koutecky-Levich plots.*

3.7.4. Square wave voltammetry studies

At the GCE|clicked-α-CoPc-flav3 interface, the oxidation currents of DA increased linearly with incrementing concentrations in the range from 2 μM to 14 μM with a high correlation coefficient ($R^2 = 0.9956$), *see* **Figure 3.15**. The calibration equation obtained from the linear regression was:

$$I = 3.0 \times 10^{-7}[DA] + 1.0 \times 10^{-6} \quad (\mathbf{3.6})$$

To determine the limit of detection (LOD) and limit of quantification (LOQ), the following equations were used: LOD = ($3*\text{std}_b/k$) and LOQ = ($10*\text{std}_b/k$), where std_b is the standard deviation of the blank and k is the slope of the linear calibration curve. As shown in **equation 3.6**, the GCE|clicked-α-CoPc-flav3 demonstrated a LOD of 0.311 μM and a LOQ of 0.942 μM for the detection of DA with a %RSD range of 0.21 to 5.11% in different concentrations, (N = 3), which is within the acceptable data confidence interval. These results indicate that the CME is capable of detecting DA at very low concentrations (sub-micromolar range) with high sensitivity and precision.

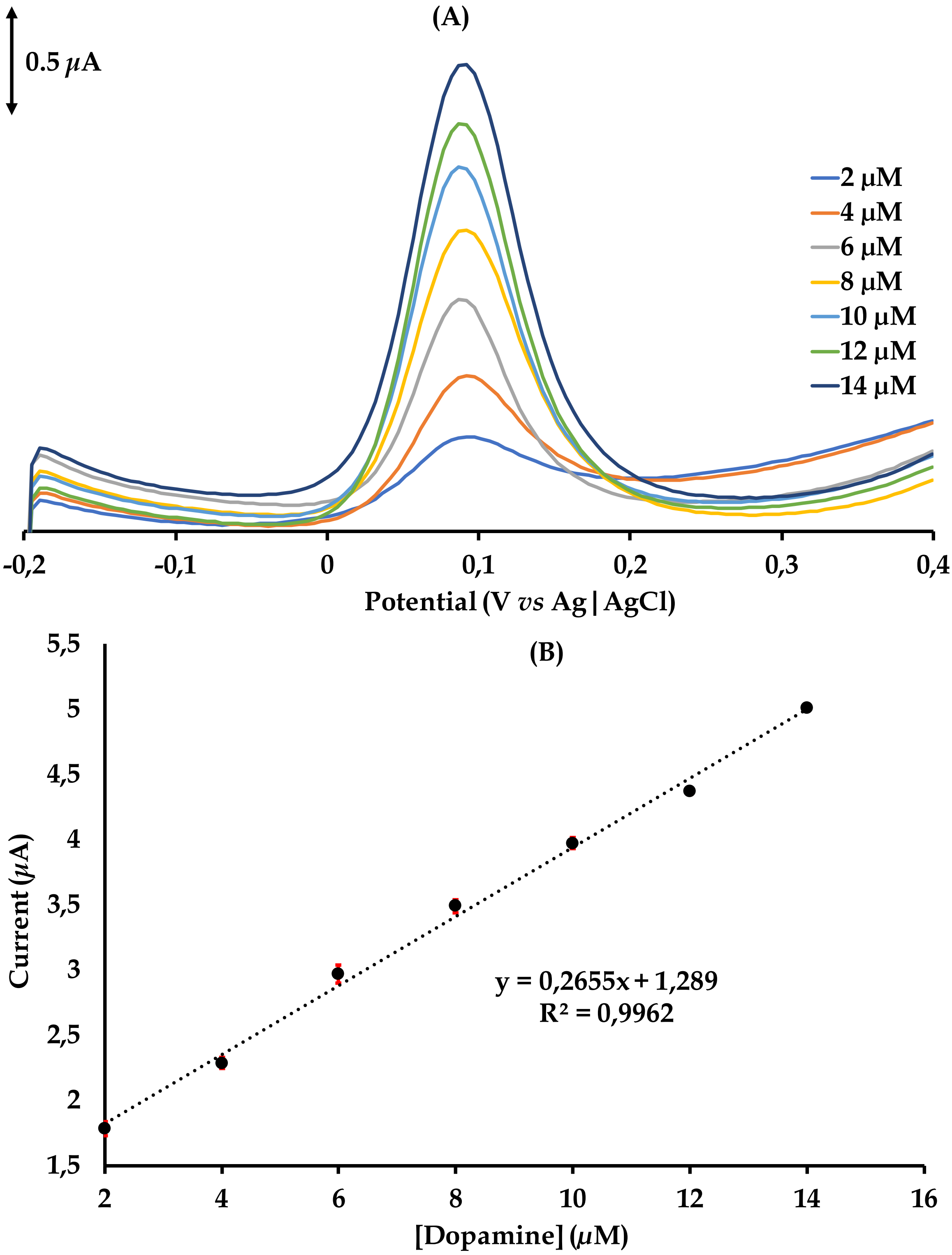

Figure 3.15: *(**A**) SWVs recorded in varying concentrations of DA prepared in PBS (pH 6.30) using the GCE|clicked-a-CoPc-flav3. (**B**) Calibration curve of the current response of the GCE|clicked-a-CoPc-flav3 against DA concentration [DA].*

Comparing the calibration parameter values for the detection of DA measured by the GCE|clicked-α-CoPc-flav3 with other glassy carbon-modified electrodes reported in the literature, it is observed that the former exhibits a narrower linear range (2 - 14 µM) but has a comparable LOD (0.31 µM) with most of the examples shown in **Table 3.6**. For instance, Nurzulaikha *et al.*[55] reported a GCE|G-SnO_2 for the detection of DA with a LOD of 1 µM and a linear range of 0-100 µM. While the linear range of the CME was wider than that of the GCE|clicked-α-CoPc-flav3, its LOD was higher than that of the latter electrode. The Mn(O)OH (manganese oxide hydroxide) modified electrode reported by Cao et al.[56] achieved a LOD of 0.1 µM and a linear range of 1.2-200 µM for DA detection, making it slightly more sensitive at low concentrations compared to the GCE|clicked-α-CoPc-flav3.

Table 3.6: *Comparison of LOD and LOQ values of the GCE|clicked-a-CoPc-flav3 other reported values in the literature for dopamine (DA).*

Type of electrode/ method	LOQ	LOD	Linear range	Reference
GCE|clicked-α-CoPc-flav3	0.94 µM	0.31 µM	2 - 14 µM	This work
GCE/Graphene	NR	2.64 µM	4 – 100 µM	[57]
GCE/G-SnO_2	NR	1 µM	0 – 100 µM	[55]
PPyNWs/PtNPs	NR	0.6 µM	1-77 µM	[58]
Nano-MnOOH	NR	0.1 µM	1.2 – 200 µM	[56]
Pd/PEDOT/rGO	NR	0.14 µM	1–200 µM	[59]

Abbreviations: ***G-SnO*$_2$** *(graphene-tin oxide);* ***PPyNWs/PtNPs*** *(platinum nanoparticles/polypyrrole nanowire);* ***Mn(O)OH*** *(manganese oxide hydroxide);* ***Pd/PEDOT/rGO*** *(poly(3,4-ethylenedioxythiophene) functionalized reduced graphene oxide with palladium nanoparticles);* ***NR*** *(not reported).*

3.7.5. *Interference studies*

The selectivity assessment of the GCE|clicked-α-CoPc-flav3 towards dopamine (DA) is a crucial step, especially in complex samples like wastewater where interferences can be abundant. In this case, two significant interferences were considered: ascorbic acid (AA) and nevirapine (NVP). AA, a common component in many biological samples, possesses oxidation potentials similar to DA, making their distinction challenging.[60] On the other hand, NVP, a prevalent ingredient of antiretroviral drugs is increasingly found in water bodies due to its widespread use. The electrochemical detection of NVP in water has been recently reported by Kantize *et al.*[61] Thus, the quantitative analysis of DA residues in surface water using highly specific CMEs is desired, given the rampant usage of antiretroviral drugs in South Africa, where the study was conducted.

The SWV responses of 1 mM DA in PBS in the presence and absence of 1 mM AA and NVP at the GCE|clicked-α-CoPc-flav3, pH = 6.3 are shown in **Figure 3.16**. The CME can detect DA in the presence of AA and NVP, with no discernible changes in the current intensity of DA coupled with distinctive peaks with good baseline resolution. However, a notable shift in the DA peak position towards higher potentials is observed (from 0.142 V to 0.375 V). This shift is attributed to the competitive adsorption of AA and NVP on the electrode surface, modifying the electrochemical behaviour.

The ability of the GCE|clicked-α-CoPc-flav3 to maintain the DA peak intensity and still resolve it from potential interferences (AA and NVP) is a positive indicator of its selectivity even if it were to be used in multifarious water samples. This implies that the electrode can accurately detect DA even in the presence of substances with similar oxidation potentials, a critical characteristic for reliable detection in samples with complex matrices.

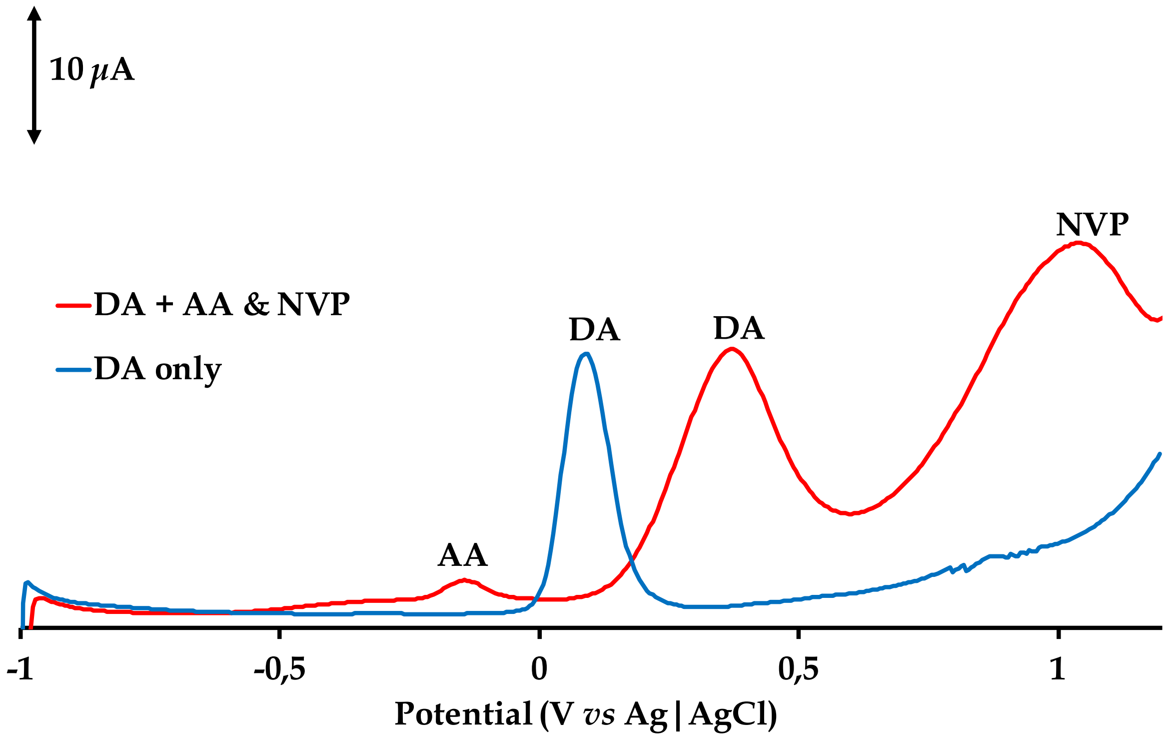

Figure 3.16: *SWV responses of 1 mM DA in PBS in the presence and absence of 1 mM AA and NVP at the GCE|clicked-a-CoPc-flav3 m, pH = 6.3.*

3.7.6. DA standard addition analysis in the wastewater sample

The GCE|clicked-α-CoPc-flav3 was employed to measure the concentration of dopamine (DA) in a wastewater sample collected from the Amanzimtoti wastewater treatment (WWT) plant. Previous reports have highlighted that this WWT does not completely remove pharmaceutically-derived water pollutants.[62] The SWV current responses of both the wastewater sample and the added calibration standards are illustrated in **Figure 3.17**. There was no discernable signal for the unspiked water sample, implying that the concentration of DA in the Amanzimtoti wastewater was lower than the limit of detection (LOD = 0.31 μM *vide supra*) of the GCE|clicked-α-CoPc-flav3.

Consequently, the sample (20.00 mL) was subsequently spiked with 2.00 mL volumes of a 1.00 mM DA standard obtaining a linear calibration plot from which a DA recovery of 97.1% and an %RSD range of 2.1 to 3.5% in different concentrations (N = 3, and is less than ≤ 5%, the acceptable precision limit) were deduced. These results suggest that the GCE|clicked-α-CoPc-flav3 can accurately detect and quantify DA in real water samples with good precision. This makes it a dependable sensor for environmental monitoring applications, as evidenced by the recovery rate which falls within the acceptable accuracy range of 80-120%, and the unrecovered DA is likely to be due to electrode fouling by other contaminants present in the water sample.

Furthermore, to gauge the accuracy of the GCE|clicked-α-CoPc-flav3 for detecting DA in real samples, it was spiked with incremental volumes of 14.0 µM dopamine (DA) and analyzed by the fabricated GCE|clicked-α-CoPc-flav3 and the results are presented in **Figure 3.17.** Using the standard addition data, the DA recovery of the GCE|clicked-α-CoPc-flav3 was calculated to be 97.1%

The calibration of DA in unspiked and spiked water samples was performed using the HPLC-MS to validate the performance of the new electrode towards HPLC-MS and the results are presented in **Table 3.7** and **Figure 3.18.** A 113% recovery of DA was calculated. The remarkable agreement between the recoveries of DA by the HPLC-MS reference method and the fabricated GCE|clicked-α-CoPc-flav3 validates the accuracy and the high accuracy and reliability of the latter towards sensing DA in real water samples. This reinforces its credibility as a sensor for monitoring DA in the environment.

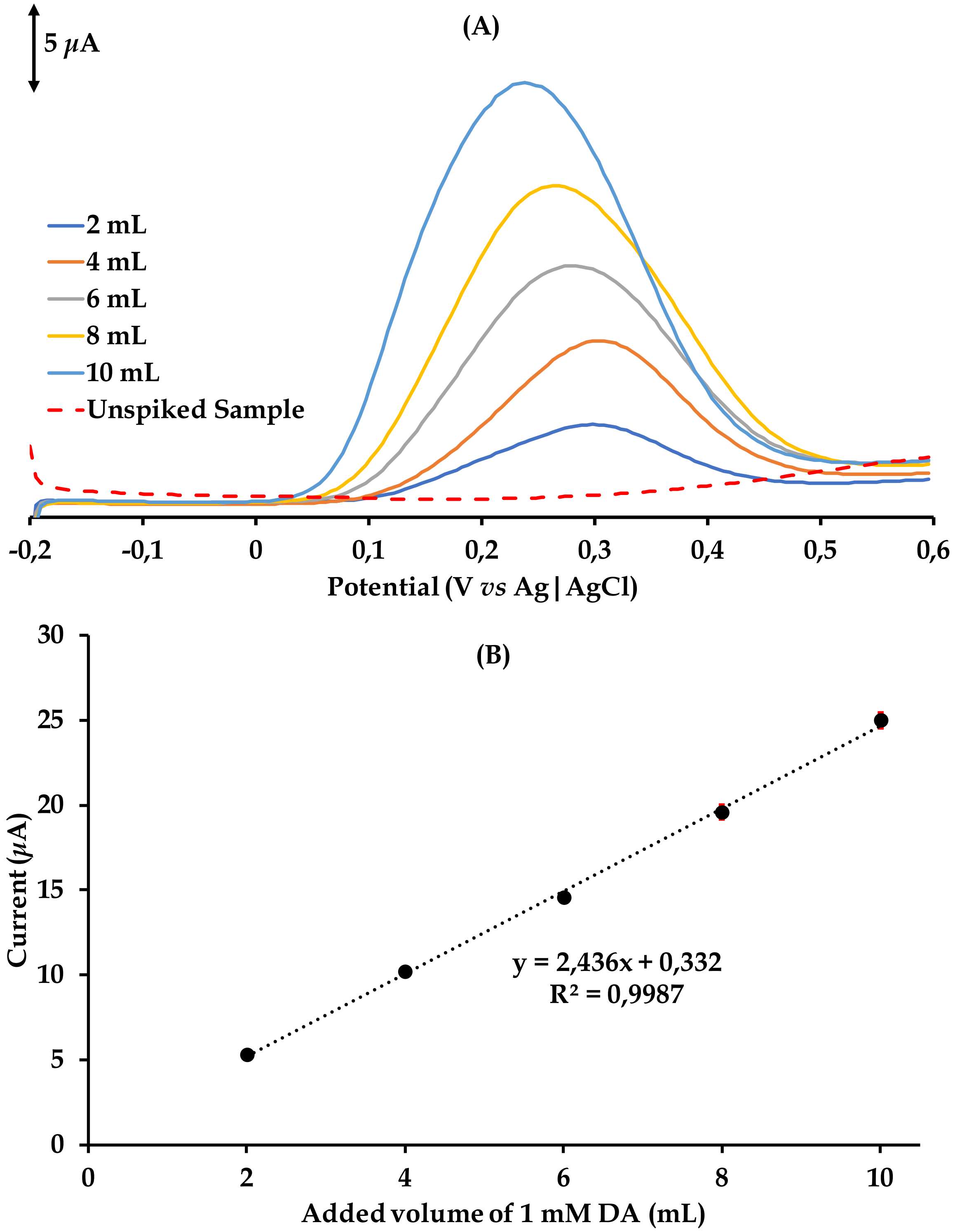

Figure 3.17: *(A) SWV responses at the GCE | clicked-a-CoPc-flav3 electrode after the standard addition of incremental volumes (2 mL) of 1.0 mM DA to 20 mL of real water sample. (**B**) Linear calibration plot.*

Table 3.7: *Measured peak area of DA of spiked (incremental addition of 2 mL of 1.0 mM DA to 20 mL Amanzimtoti water sample) by LC-MS.*

Added Volume (mL)	Retention time (min)	Peak area
2.00	4.010	2103899
4.00	4.010	2259575
6.00	4.012	2481018
8.00	4.015	2600569
10.00	4.015	2805902

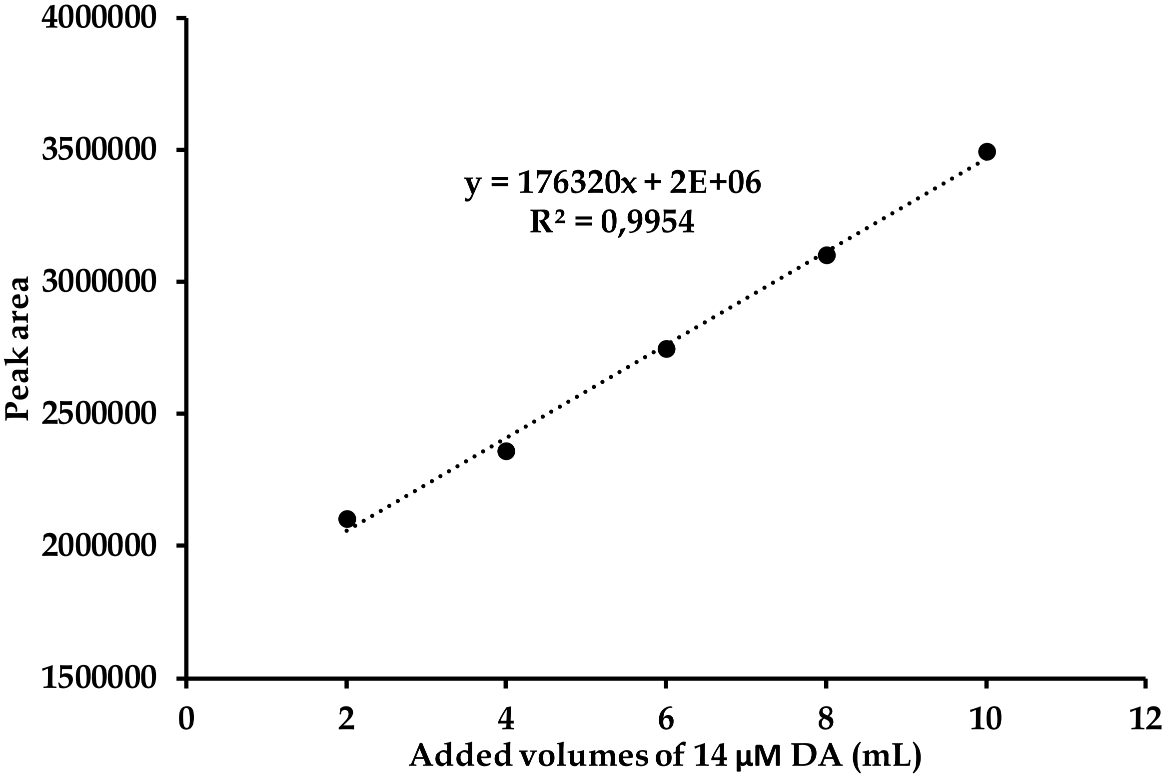

Figure 3.18: *The real water sample (20.00 mL) spiked with incremental volumes (2.00 mL) of the 14.0 µM standard of DA detected using LC-MS (collected from the Amanzimtoti wastewater treatment plant).*

3.8. Conclusions

The metal complex, α-CoPc-flav3 was confirmed using various spectroscopic techniques including FTIR spectroscopy, UV-Visible absorption spectrophotometry and high-resolution mass spectrometry. The complex was used to modify the GCE (GCE|clicked-α-CoPc-flav3) and this electrode showed a a higher response current compared to the bare GCE electrode in the detection of dopamine (DA). Additionally, the GCE|clicked-α-CoPc-flav3 exhibited excellent reproducibility and precision in detecting dopamine standards, with calibration RSD values below 5%. It also demonstrated selectivity for dopamine even in the presence of interfering pharmaceutical medications such as ascorbic acid (AA) and nevirapine (NVP).

Analysis of spiked real water samples by the GCE|clicked-α-CoPc-flav3 yielded consistent results, with a recovery of 97% and %RSD values within the acceptable range of ±20%. The accuracy and precision of this electrode in detecting DA in Amanzimtoti wastewater without the need for prior sample clean-up were further demonstrated. Moreover, the close agreement between the performance of the GCE|clicked-α-CoPc-flav3 and the more definitive HPLC-MS (113% percentage recovery) method underscores its accuracy and reliability in detecting DA in real water samples. This highlights its potential as a valuable tool for environmental monitoring applications.

3.9. References

(1) Ji, W.; Wang, T.-X.; Ding, X.; Lei, S.; Han, B.-H. *Coordination Chemistry Reviews* **2021**, *439*, 213875.

(2) Brown, M. D.; Schoenfisch, M. H. *Electrochimica Acta* **2018**, *273*, 98.

(3) Gounden, D.; Nombona, N.; van Zyl, W. E. *Coordination Chemistry Reviews* **2020**, *420*, 213359.

(4) Kantize, K.; Booysen, I. N.; Mambanda, A. *Journal of Electroanalytical Chemistry* **2019**, *850*, 113391.

(5) Yuan, R.; Wei, Y.; Musikavanhu, B.; Tang, M.; Xue, Z.; Wang, A.; Zhang, J.; Qiu, X.; Zhao, L. *Molecular Catalysis* **2023**, *534*, 112805.

(6) Breloy, L.; Yavuz, O.; Yilmaz, I.; Yagci, Y.; Versace, D.-L. *Polymer Chemistry* **2021**, *12*, 4291.

(7) O'Donoghue, C. S. J. N.; Shumba, M.; Nyokong, T. *Electroanalysis* **2017**, *29*, 1731.

(8) Mpeta, L. S.; Fomo, G.; Nyokong, T. *Journal of Coordination Chemistry* **2018**, *71*, 1623.

(9) Mayukh, M.; Lu, C.-W.; Hernandez, E.; McGrath, D. V. *Chemistry – A European Journal* **2011**, *17*, 8472.

(10) Chohan, S.; Booysen, I. N.; Mambanda, A. *Polyhedron* **2015**, *102*, 284.

(11) Sivaranjanee, R.; Senthil Kumar, P.; Saravanan, R.; Govarthanan, M. *Chemosphere* **2022**, *294*, 133779.

(12) Gardella, L. A.; Zaroslinski, J. F.; Possley, L. H. *American Journal of Hospital Pharmacy* **1975**, *32*, 575.

(13) Wright, J. S.; Newman, D. C.; Torda, T. A. *Medical Journal of Australia* **1977**, *1*, 651.

(14) Becker, D. E. *Anesthesia Progress* **2012**, *59*, 159.

(15) Sindelo, A.; Mafukidze, D. M.; Nyokong, T. *Photodiagnosis and Photodynamic Therapy* **2022**, *38*, 102760.

(16) Harmandar, K.; Granados-Tavera, K.; Gezgin, M.; Nebioğlu, M.; Şişman, İ.; Cárdenas-Jirón, G.; Atilla, D.; Gürek, A. G. *New Journal of Chemistry* **2022**, *46*, 714.

(17) Li, Q.; Sun, Z.; Zhou, M.; Liang, Q.; Li, Z.; Xu, S. *Journal of Materials Science* **2019**, *30*, 6277.

(18) Anandhan, K.; Cerón, M.; Perumal, V.; Ceballos, P.; Gordillo-Guerra, P.; Pérez-Gutiérrez, E.; Castillo, A. E.; Thamotharan, S.; Percino, M. J. *RSC Advances* **2019**, *9*, 12085.

(19) Burat, A. K.; Koca, A.; Lewtak, J. P.; Gryko, D. T. *Synthetic Metals* **2011**, *161*, 1537.

(20) Bilgiçli, A. T.; Yaraşır, M. N.; Kandaz, M.; İlik, C.; Demir, A.; Bağcı, S. *Synthetic Metals* **2015**, *206*, 33.

(21) Karakılıç, E.; Alım, Z.; Günel, A.; Baran, A. *Journal of Molecular Structure* **2022**, *1257*, 132630.

(22) Gümrükçü Köse, G.; Keser Karaoğlan, G.; Neccaroğlu Işık, S.; Akyüz, D.; Koca, A. *Synthetic Metals* **2020**, *264*, 116386.

(23) Acar, E. T.; Tabakoglu, T. A.; Atilla, D.; Yuksel, F.; Atun, G. *Polyhedron* **2018**, *152*, 114.

(24) Odabaş, Z.; Orman, E. B.; Durmuş, M.; Dumludağ, F.; Özkaya, A. R.; Bulut, M. *Dyes and Pigments* **2012**, *95*, 540.

(25) Robin Nxele, S.; Nkhahle, R.; Nyokong, T. *Journal of Electroanalytical Chemistry* **2021**, *900*, 115730.

(26) de Saja, J. A.; Rodríguez-Méndez, M. L. *Advances in Colloid and Interface Science* **2005**, *116*, 1.

(27) Ngwenya, V.; Booysen, I. N.; Mambanda, A. *Journal of Coordination Chemistry* **2019**, *72*, 1131.

(28) Griveau, S.; Mercier, D.; Vautrin-Ul, C.; Chaussé, A. *Electrochemistry Communications* **2007**, *9*, 2768.

(29) Lacroix, J. C.; Trippe-Allard, G.; Ghilane, J.; Martin, P. *Advances in Natural Sciences: Nanoscience and Nanotechnology* **2014**, *5*, 015001.

(30) Nxele, S. R.; Mashazi, P.; Nyokong, T. *Electroanalysis* **2015**, *27*, 2468.

(31) Mpeta, L. S.; Sen, P.; Nyokong, T. *Journal of Electroanalytical Chemistry* **2020**, *860*, 113896.

(32) Pally, D.; Bertagna, V.; Cagnon, B.; Alaaeddine, M.; Benoit, R.; Podvorica, F. I.; Vautrin-Ul, C. *Journal of Electroanalytical Chemistry* **2018**, *817*, 101.

(33) Coates, M.; Nyokong, T. *Electrochimica Acta* **2013**, *91*, 158.

(34) Coates, M.; Nyokong, T. *Journal of Electroanalytical Chemistry* **2012**, *687*, 111.

(35) Orazem, M. E.; Tribollet, B. *Electrochimica Acta* **2008**, *53*, 7360.

(36) Lakshminarayanan, V.; Sur, U. K. *Pramana* **2003**, *61*, 361.

(37) Lee, Y.-J.; Park, J.-Y. *Biosensors and Bioelectronics* **2010**, *26*, 1353.

(38) Matemadombo, F.; Nyokong, T. *Electrochimica Acta* **2007**, *52*, 6856.

(39) Bacil, R.P.; Chen, L.; Serrano, S.H.; Compton, R.G. *Physical Chemistry Chemical Physics* **2020**, *22*, 607.

(40) Ndebele, N.; Sen, P.; Nyokong, T. *Journal of Electroanalytical Chemistry* **2021**, *886*, 115111.

(41) Liu, J.; Sun, L.; Li, G.; Hu, J.; He, Q. *Materials Research Bulletin* **2021**, *133*, 111050.

(42) Zare, H. R.; Rajabzadeh, N.; Nasirizadeh, N.; Mazloum Ardakani, M. *Journal of Electroanalytical Chemistry* **2006**, *589*, 60.

(43) Kamyabi, M. A.; Narimani, O.; Monfared, H. H. *Journal of the Brazilian Chemical Society* **2011**, *22*.

(44) Gumilar, G.; Kaneti, Y.V.; Henzie, J.; Chatterjee, S.; Na, J.; Yuliarto, B.; Nugraha, N.; Patah, A.; Bhaumik, A.; Yamauchi, Y. *Chemical science* **2020**, *11*, 3644.

(45) Sun, Z.; Sun, S.; Jiang, X.; Ai, Y.; Xu, W.; Xie, L.; Sun, H.B.; Liang, Q. *Biosensors and Bioelectronics* **2022**, *211*, 114367.

(46) Wahab, M.A.; Hossain, S.A.; Masud, M.K.; Park, H.; Ashok, A.; Mustapić, M.; Kim, M.; Patel, D.; Shahbazi, M.; Hossain, M.S.A.; Yamauchi, Y. *Sensors and Actuators B: Chemical* **2022**, *366*, 131980.

(47) Zen, J. M.; Senthil Kumar, A.; Chang, M. R. *Electrochimica Acta* **2000**, *45*, 1691.

(48) Sunil Kumar Naik, T. S.; Mwaurah, M. M.; Kumara Swamy, B. E. *Journal of Electroanalytical Chemistry* **2019**, *834*, 71.

(49) Mazloum-Ardakani, M.; Ahmadi, S. H.; Mahmoudabadi, Z. S.; Heydar, K. T.; Mirjalili, B. F. *Analytical Methods* **2013**, *5*, 6982.

(50) Farahi, A.; Hammani, H.; Kajai, A.; Lahrich, S.; Bakasse, M.; El Mhammedi, M. A. *International Journal of Environmental Analytical Chemistry* **2020**, *100*, 295.

(51) Ndebele, N.; Sen, P.; Nyokong, T. *Journal of Electroanalytical Chemistry* **2021**, *886*, 115111.

(52) Sayadi, A.; Pickup, P. G. *Electrochimica Acta* **2016**, *215*, 84.

(53) Chen, W.; Xu, M.-L.; Li, M.-F.; Wei, Z.; Cai, J.; Chen, Y.-X. *Journal of Electroanalytical Chemistry* **2020**, *872*, 114042.

(54) Treimer, S.; Tang, A.; Johnson, D. C. *Electroanalysis* **2002**, *14*, 165.

(55) Nurzulaikha, R.; Lim, H. N.; Harrison, I.; Lim, S. S.; Pandikumar, A.; Huang, N. M.; Lim, S. P.; Thien, G. S. H.; Yusoff, N.; Ibrahim, I. *Sensing and Bio-Sensing Research* **2015**, *5*, 42.

(56) Cao, X.; Cai, X.; Wang, N. *Sensors and Actuators B: Chemical* **2011**, *160*, 771.

(57) Kim, Y.-R.; Bong, S.; Kang, Y.-J.; Yang, Y.; Mahajan, R. K.; Kim, J. S.; Kim, H. *Biosensors and Bioelectronics* **2010**, *25*, 2366.

(58) Mazzotta, E.; Caroli, A.; Primiceri, E.; Monteduro, A. G.; Maruccio, G.; Malitesta, C. *Journal of Solid State Electrochemistry* **2017**, *21*, 3495.

(59) Choe, J. E.; Ahmed, M. S.; Jeon, S. *Journal of The Electrochemical Society* **2016**, *163*, B113.

(60) Sajid, M.; Nazal, M. K.; Mansha, M.; Alsharaa, A.; Jillani, S. M. S.; Basheer, C. *TrAC Trends in Analytical Chemistry* **2016**, *76*, 15.

(61) Kantize, K.; Booysen, I. N.; Mambanda, A. *International Journal of Electrochemical Science* **2022**, *17*, 22067.

(62) Matongo, S.; Birungi, G.; Moodley, B.; Ndungu, P. *Chemosphere* **2015**, *134*, 133.

Chapter 4

Exploring Hg(II) electrocatalytic detection capabilities of a Pt electrode modified with an electron-mediating composite film of cobalt(II) phthalocyanine *tetra*-substituted with 1-(methoxymethyl)-benzotriazole groups and co-electropolymerized polypyrrole

4.1. Introduction

Industrial effluents emanating from direct metal production industries such as mining and metal refining have led to large-scale pollution of governmental reservoirs and natural water resources.[1,2] Indicatively, downstream metal-based beneficiation companies such as metal re-recycling industries, battery production plants, thermal power stations, cement manufacturing and agricultural commodities have also been culprits of heavy cation pollution.[3] The presence of these heavy metal cations like mercury in the aquatic environment does not only harms the bio-aquatic ecosystem but also the food chain with respect to fish and animal life through to humans.[4,5]

The use of cobalt phthalocyanines (CoPcs) to modify electrodes for the electrochemical detection of mercury ions in water sources is an imperative as mercury is an environmental persistent pollutant and annual water quality surveys have recorded escalating concentrations.[6,7] CoPcs are cyclo-planar metal complexes with a central cobalt ion surrounded by a planar macrocyclic structure which has delocalized π-electron system. This allows them to undergo metal-based and ligand-based redox processes, which enables efficient electron transfer between the electrode interface and the CoPc molecules.[8,9] The current general consensus for CoPc-modified electrodes that have shown selective and sensitive electrocatalytic sensing is that their substituents have played a vital role in the mechanism of analyte interaction.[10,11]

Consequently, a Pt electrode modified with an electron-mediating composite film comprising of an electrodeposited cobalt(II) phthalocyanine *tetra*-substituted with 1-(methoxymethyl)-benzotriazole groups (CoPc-Bzt) and a conductive polypyrrole (PPy), was utilized for the electrocatalytic sensing of mercury in stimulated or real samples. The electron-donating capability of the appended benzotriazole moieties does not only increase the electron density of the CoPc core but they also act as *N*-heterocyclic ligands for elemental mercury that has been adsorbed on the CME surface. Indicatively, the nitrogen donor atoms of the stabilizing polypyrrole can coordinate to reduced mercuric ions at the CME interface while its inherent conductive nature encourages faster electron transfer kinetics.[12]

Benzotriazole has been widely used as a corrosion inhibitor due to its ability to form stable and protective thin films on metal surfaces.[13,14] Adsorption of benzotriazole derivatives on metallic surfaces is based on coordination bonding where a protective layer that inhibits further corrosion reactions.[14,15] Hence, it is perceived that the electrodeposition of CoPc-Bzt on a Pt electrode will lead to physical coordinative bonding between the nitrogen donor atoms of the substituents and the Pt substrate; contributing to robustness of our chemically-modified electrode. In fact, the benzotriazole moiety contains three nitrogen atoms, which provide multiple coordination sites for metal cations, leading to strong metal-complex interactions but not all nitrogen donors are accessible to the planar substrate in tandem.[16,17]

Furthermore, the development of this Pt chemically modified electrode (CME) using a composite coating of *tetra*-[4-(1-(methoxymethyl)-benzotriazole)phthalocyaniato]cobalt(II) (CoPc-Bzt) and co-polymerized polypyrrole (PPy) offers a promising platform for sensitive and selective detection of trace levels of metal elements, particularly Hg^{2+} ions in aqueous media. Polypyrrole (PPy) films are well-known for their high conductivity, chemical stability and mechanical strength which make them excellent materials for binding and coating electrocatalysts to create ultrathin films on electrode surfaces.[18,19] When combined with CoPc-Bzt, which contains benzotriazole substituents, the composite coating is expected to exhibit synergistic effects at the electrode interface, leading to enhanced electrocatalytic properties and improved sensing performance.

The literature reports on the sensitive and selective detection of Hg(II) ions using composites of carbon nanomaterials and PPy provides valuable insights into the potential mechanisms of the CoPc-Bzt and PPy composite. It has been hypothesized that Hg(II) ions adsorb electrostatically to the surface groups on carbon nanomaterials and selectively coordinate to PPy *via* its nitrogen atoms.[20,21] This dual binding mechanism enables the composite to have a high adsorption capacity for Hg(II) ions and a strong coordinating affinity, allowing for selective detection of micromolar levels of Hg(II) in sample solutions.[20,21] The incorporation of CoPc-Bzt into the composite further enhances its electrochemical properties, potentially leading to improved sensitivity and selectivity for Hg(II) detection. The coordination properties of the benzotriazole substituents in CoPc-Bzt may facilitate the specific binding and electrocatalytic behaviour towards Hg(II) ions, contributing to the overall performance of the modified electrode.

4.2. Experimental

4.2.1. *Synthesis of 4-((1H-benzotriazole)methoxy)phthalonitrile (1)*

This ligand presented in **Scheme 4.1** was successful synthesized as per the method reported by Dilber *et al.*[22]

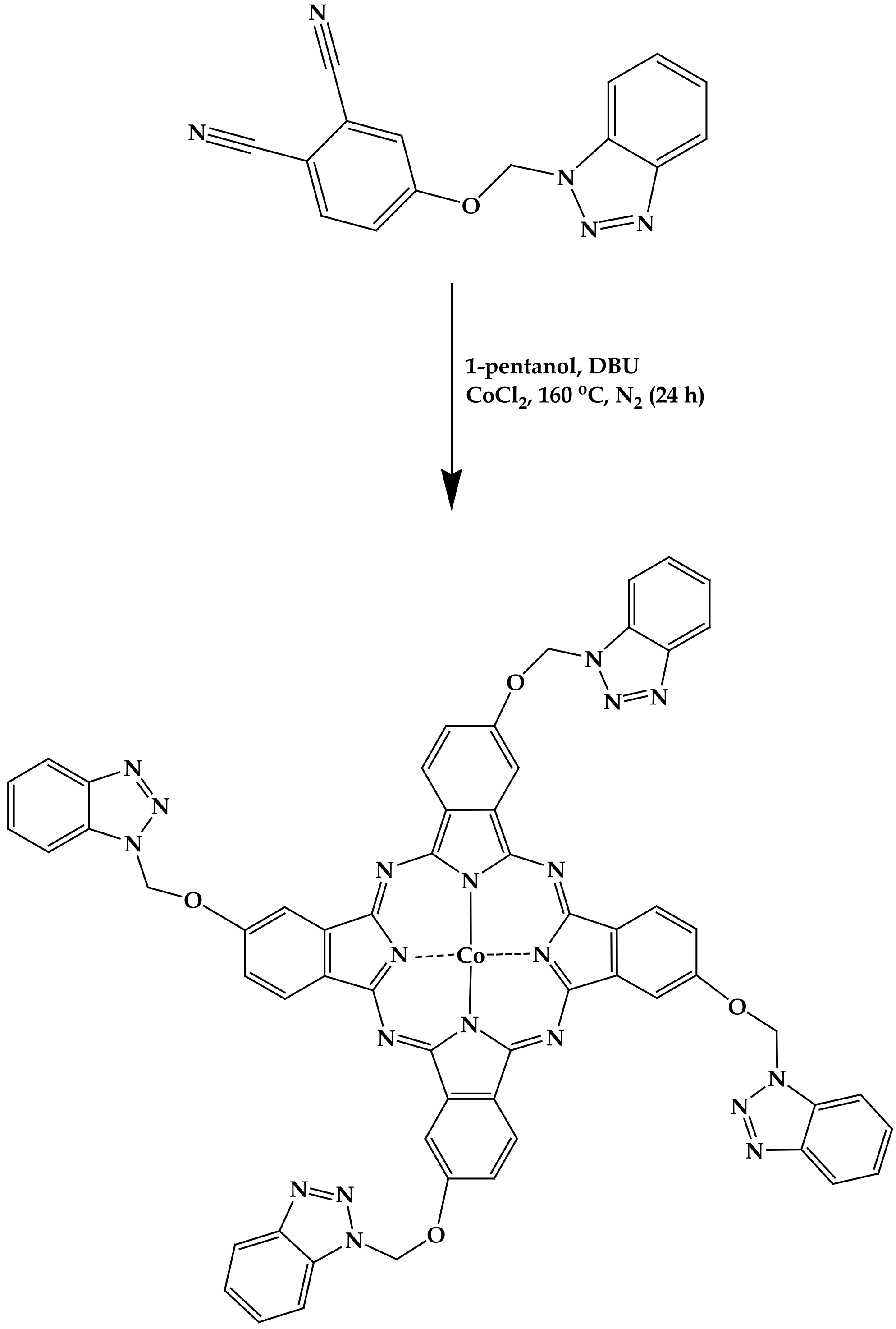

Scheme 4.1: *Synthetic scheme for CoPc-Bzt.*

4.2.2. Synthesis of tetra-[4-((1H-benzo[d][1,2,3]triazol-1-yl)methoxy)phthalocyaninato]cobalt(II) (CoPc-Bzt, 2)

A novel metallocyclic complex, CoPc-Bzt was synthesized *via* a 4:1 molar cyclotetramerization reaction between 4-((1*H*-benzotriazole)methoxy)phthalonitrile (1.0004 g, 3.6 mmol) and anhydrous cobalt chloride (0.1169 g, 0.9mmol) with few drops of catalytic 1,8-Diazabicyclo[5.4.0]undec-7-ene (DBU) were mixed in 1-pentanol (30 mL). Subsequently, the reaction mixture was stirred while heating at 160 °C for 24 h under a nitrogen atmosphere. Thereafter, it was cooled down to room temperature, then precipitated out by the dropwise addition of *n*-hexane. A dark green precipitate was filtered, washed with cold hexane, methanol and ethanol and then dried under vacuum. The crude product was purified by silica gel column chromatography eluting it with $CHCl_3$: MeOH (9:1) to give the pure dark green CoPc-Bzt, *see* **Scheme 4.1**. Yield: 31%. M.P. (^oC):>280. FT-IR (ν_{max}/cm^{-1}): v(-C-H) 2908-2836, w; ν(C=N) 1615, m; ν(C=C, aromatic) 1595-1601, m; ν(C–O–C) 1089, 1168, m. [DMF, λ_{max} (ε, M^{-1} cm^{-1})]: 749 nm (65800), 640 nm(23700), 329 nm (85300). Molecular mass (*m/z*): Calcd: 1159.26. Found: 1156.38 $[M-3H]^+$.

4.3. Results and discussion

4.3.1. Spectral characterization of CoPc-Bzt

Firstly, *tetra*-substituted analogues of CoPc-Bzt where the cavities are occupied by Zn, Cu or MnCl have been reported.[22] The overlay FTIR spectra of the derivatized phthalonitrile **1** and its CoPc **2** illustrated a sharp nitrile (C≡N) vibration at 2200 cm^{-1} for the former while this analogous IR stretch is absent for **2** indicating the cyclotetramerization reaction was successful, see **Figure 4.1**. In addition, the typical aliphatic and aromatic -C-H vibrational peaks of **2**'s Bzt groups (appearing in the range 2908-2836 cm^{-1}) also appear in the spectrum of CoPc-Bzt complex (between 2956 and 2876 cm^{-1}) reaffirming the presence of the Bzt moieties within **2**. The aforementioned spectral changes also hint at the fact that the electronic properties of the Bzt substituents in **2** differ from that of the Bzt group in **1** since those of **2** vibrates at lower energies. Additionally, characteristic vibrations at 1250-1050 cm^{-1}

corresponded to ether groups (C-O-C), while the vibration at 1606-1595 cm^{-1} corresponded to the C=C bond alkene of the aromatic ring within the benzotriazole ligand (**1**). Interestingly, this peak appeared sharp in benzotriazole (**1**) but was broadened in CoPc (**2**), indicating variations in the orientation of these benzotriazole groups about their individual aliphatic linkers.

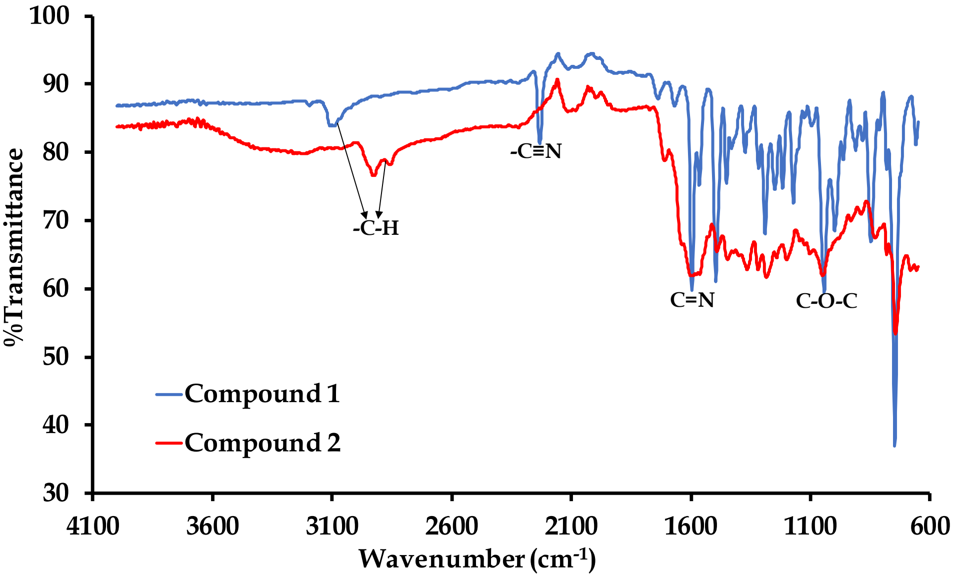

Figure 4.1: *Overlay solid-state FT-IR spectra of 4-((1H-benzo[d][1,2,3]triazol-1-yl)methoxy)phthalonitrile ligand* **(1)** *and CoPc-Bzt* **(2)** *complex.*

The absorption spectrum of compound **2** in deaerated DMF exhibits a pronounced peak in the visible range, with a maximum absorption wavelength of 749 nm (*Q*-band), a higher energy shoulder at 669 nm and *B*-band at 329 nm, as shown in **Figure 4.2.** These *Q*- and *B*-bands fall well within the typical ranges for CoPcs peripherally substituted with *N*-heterocyclic electron-donating groups, specifically 600–750 nm for the *Q*-band and 250–300 nm for the *B*-band.[23-25] Both unmetallated and metalated Pcs produces the *Q*- and *B*-bands which arises from π-π^* electronic transitions between the highest π-molecular orbitals (HOMO) and the lowest energy antibonding π^* orbitals (LUMOs). However, the position of the *Q*-bands can be altered by metalation and the nature of the substituents in the peripheral or non-peripheral positions.[25,26]

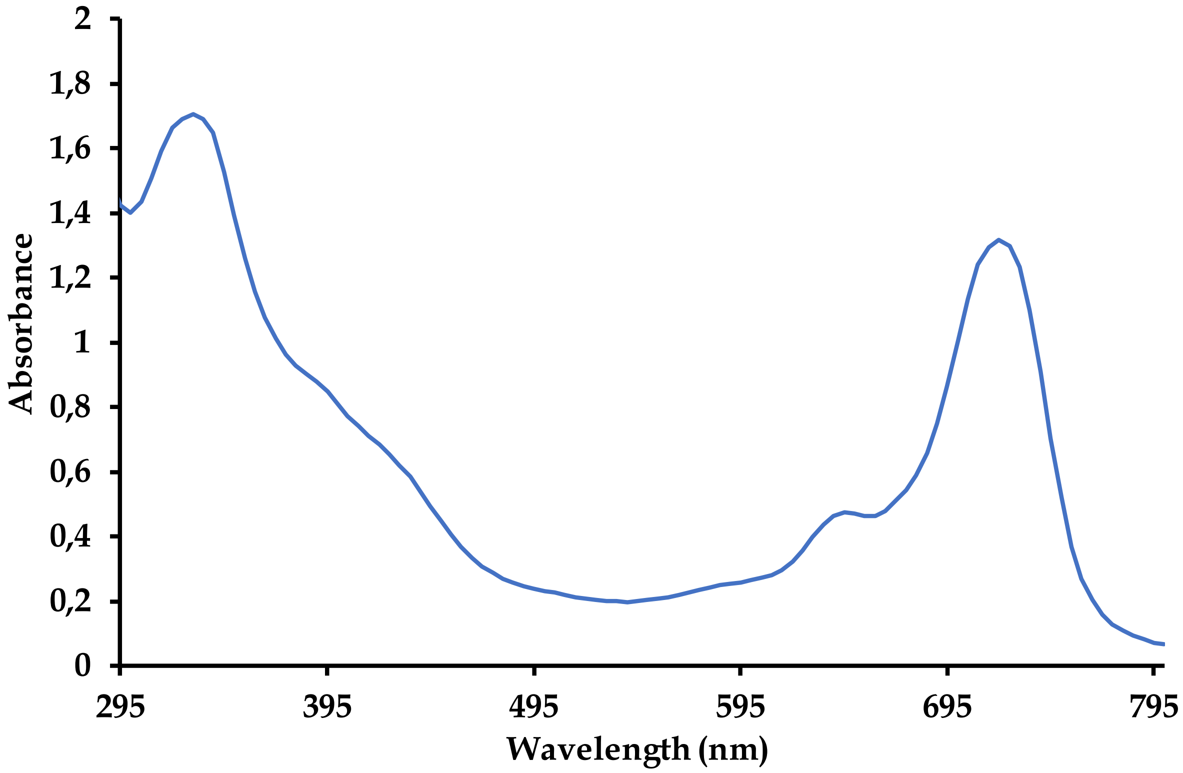

Figure 4.2: *UV–Visible spectrum of CoPc-Bzt (**2**) complex.*

The mass spectrum of CoPc-Bzt reveals a base peak at an *m/z* value of 1156.38 amu, corresponding to its deprotonated pseudo-molecular ion, $[M\text{-}3H]^+$. The exact nominal mass of the parent mono-cation of CoPc-Bzt (M) is calculated to be 1159.26 amu using the isotopic mass calculator available at sisweb.com, as shown in **Figures 4.3** and **4.4**. To enhance the ionization of CoPc-Bzt, trifluoroacetic acid (TFA) was introduced to the CoPc solution, and the mass spectrum was re-recorded. However, in addition to the characteristic isotopic peaks (as compared to the theoretical pattern in **Figure 4.3B**), several additional peaks at lower *m/z* values were observed, tentatively assigned to either radical ions of TFA or ions resulting from the fragmentation of the complex and its substituents.[27]

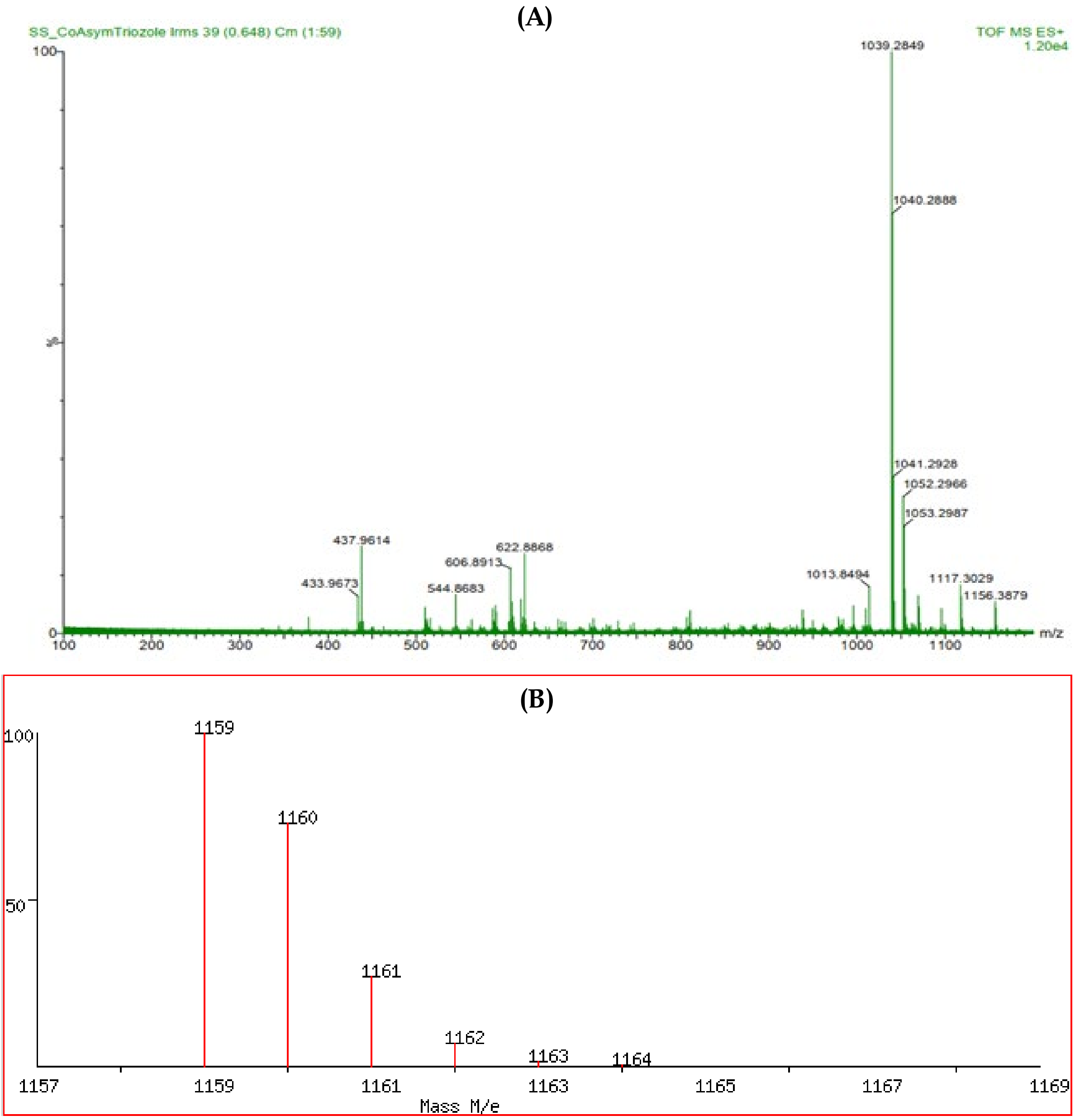

Figure 4.3: *TOF-MS spectra of* **2** *with TFA added to promote ionization. (***B***) Theoretical pattern calculated via the isotopic mass calculator.*

As depicted in **Figure 4.4**, the peak observed at 1053.2966 amu can be attributed to the [M - (phenyldiazene)]••, where 2-phenyldiazene has been lost (*i.e.* –(phenyldiene)). Other prominent peaks observed in the experimental spectrum appears at *m/z* values of 1039.2649, 1040.2666, and 1041.2926 which are associated with the isotopic distribution of ([M - 1*H*-benzotriazole]•) and 1013.8494 amu ([M - (1-(methoxymethyl)-1*H*-benzotriazole]•).

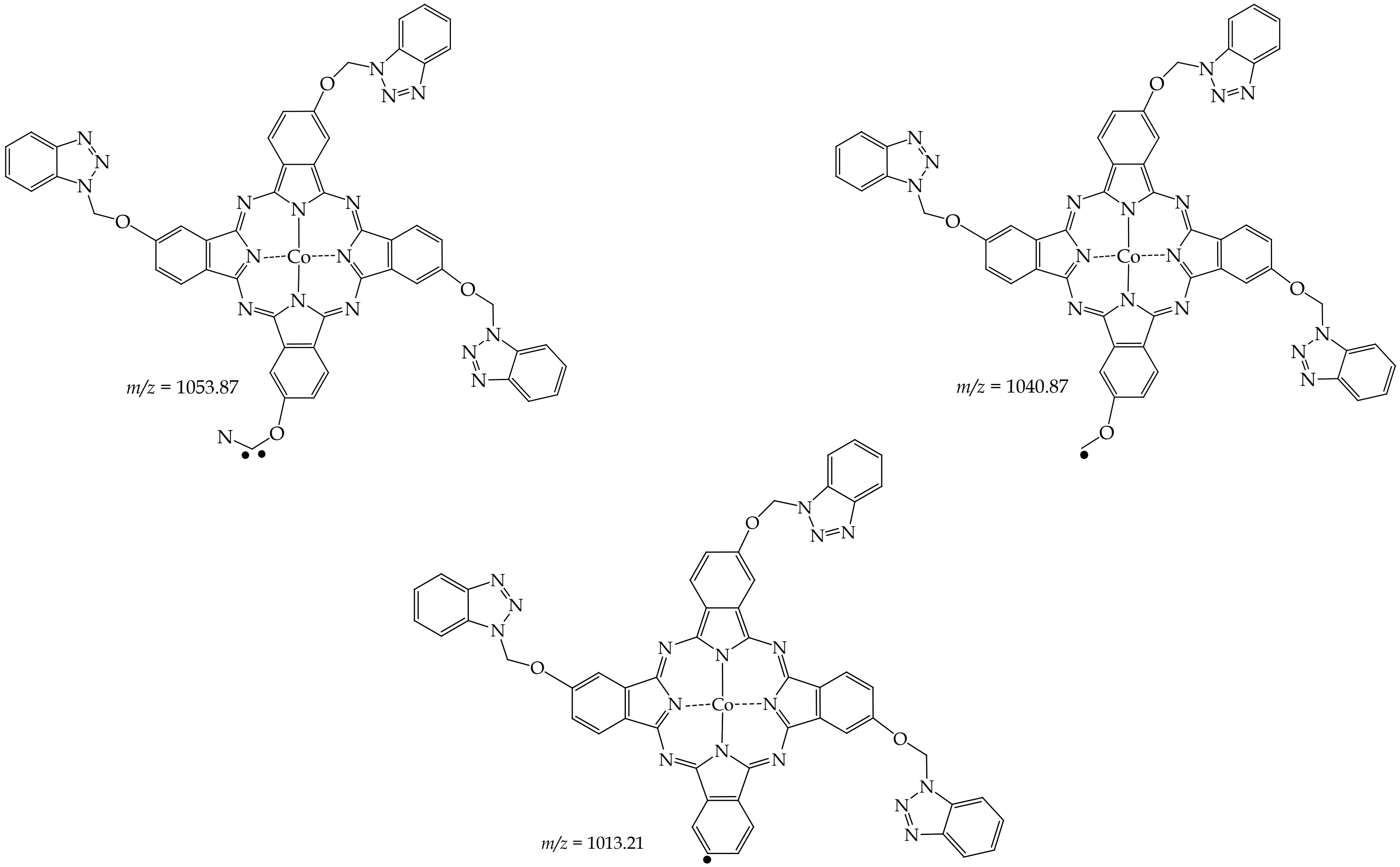

Figure 4.4: *Chemical structures of the radical fragment ions that are formed randomly due to the thermally-induced dissociations of CoPc-Bzt* (**2**) *in the presence of TFA.*

4.3.2. *Investigating the redox properties of 2*

The voltammetric analysis of compound **2** revealed the presence of four distinct redox processes, as shown in **Figure 4.5**. Redox couples **I** and **II** are considered quasi-reversible because the peak separation potential (ΔE) is greater than the standard reference ferrocene (106 mV) obtained using the bare platinum electrode.[28] In contrast, redox processes **III** and **IV** are deemed irreversible, as indicated in **Table 4.1**. Employing the more sensitive SWV technique, it became apparent that CoPc-Bzt monomers undergo aggregation during redox processes **I** and **II**, resulting in three additional peaks within its SWV. This aggregation is primarily driven by π-π^* intermolecular interactions, predominantly occurring between the coplanar and π-conjugated Pc macrocyclic faces.[29,30]

Assignments of the specific redox processes were initially made by comparing their corresponding redox potentials with those of structurally-related CoPcs containing similar *N*-heterocyclic substituents, as detailed in **Table 4.2**.[31-34] According to this comparative analysis, redox process **III** is attributed to the irreversible oxidation of $Co^{II}Pc^{-2}$ to $Co^{III}Pc^{-2}$, while the quasi-reversible redox couple **II** is assigned to $Co^{II}Pc^{-2}/Co^{I}Pc^{-2}$. Thus, within the positive potential window, the electron-donating capability of the 1-(methoxymethyl)-benzotriazole substituents renders the Pc-core more electron-rich, promoting the oxidation of Co(II) over the reduction of the resultant Co(III) species. Conversely, within the negative potential window, both the reduction and oxidative waves of redox process **II** are indicative of monomeric CoPcs. These trends are in line with CoPcs containing similar *N*-heterocyclic substituents reported in the literature.[31-34] In fact, this trend also extends to the redox properties of the Pc^{2}-ring, where redox couple **I**, assigned to $Co^{I}Pc^{-2}/Co^{I}Pc^{-3}$, and redox process **IV**, which represents the ring oxidation of $Co^{I}Pc^{2-}$ to $Co^{I}Pc^{1-}$, are quasi-reversible and irreversible, respectively, as indicated in **Table 4.1**

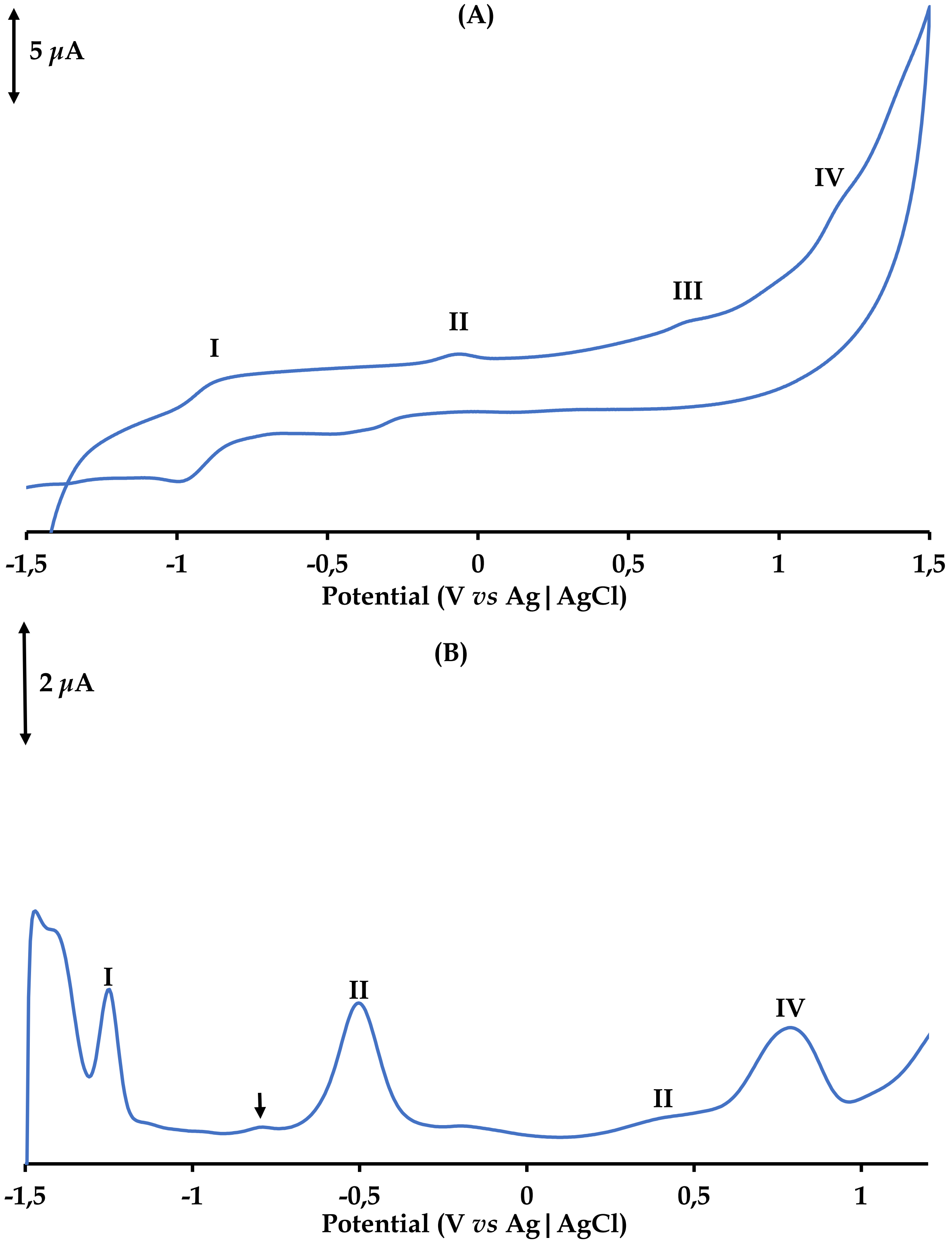

Figure 4.5: *(**A**) CV and (**B**) SWV of CoPc-Bzt at 100 mV/s. The arrows represent peaks associated with aggregation.*

Table 4.1: *Redox potentials of the redox couples attained via CV and SWV.*

Redox couple	**E_{pa} (V)**	**E_{pc} (V)**	**ΔE (V)**
I	-0.8652	-0.9775	0.1123
II	-0.06683	-0.3525	0.2857
III	0.7493	-	-
IV	1.2027	-	-

Table 4.2: *Comparison of the voltammetric data (in V) between the novel* ***CoPc-Bzt*** *as well as other tetra-substituted CoPcs containing 1,2,4-triazol and imidazole retrieved from literature.*

	$M^{I}Pc^{2-}/M^{I}Pc^{3-}$ (I)	**$M^{II}Pc^{2-}/M^{I}Pc^{2-}$ (II)**	**$M^{II}Pc^{2-}/M^{III}Pc^{2-}$ (III)**	**$M^{III}Pc^{2-}/M^{III}Pc^{1-}$ (IV)**	**Reference**
CoPc-Bzt	-1.248	-0.498	0.408	0.801	This work
CoPc-DIT	-1.09	-0.75	0.10	0.51	[31]
CoPc-MPT	-1.40	-0.38	0.40	0.91	[32]
CoPc-FMTE	-1.45	-0.40	NR	0.92	[33]
CoPc-MET	-1.27	-0.44	0.52	0.85	[34]

Abbreviation: CoPc-DIT: [2,9,16,23-tetraphthalocyaninato-cobalt(II)], **CoPc-MPT:** *tetra*-(4-(2-(4-methyl-5-phenyl-4H-1,2,4-triazol-3-ylthio)ethoxy)phthalocyaninato)cobalt(II), **NR:** Not reported, **CoPc-FMTE:** *tetra*-(4-(2-ethoxy)phthalocyaninato)cobalt(II), **CoPc-MET:** 2(3),9(10),16(17),23(24)-*Tetrakis*-4-(3,4-dimethoxyphenethyl)-5-ethyl-2*H*-1,2,4-triazol-3(4*H*)-one phthalocyaninato cobalt (II)

4.3.3. Spectroelectrochemical experiments of CoPc-Bzt (2)

Spectroelectrochemistry was used to study the designated redox pairs in more detail. In particular, substantial disaggregation was found when the first reduction peak (redox couple **II**) was analyzed. This process resulted in the development of a distinct monomeric state, as shown in **Figure 4.6A**, accompanied with a red-shifted *Q*-band detected at 706 nm. A red-shifted *Q*-band rand the emergence of a new peak at about 480 nm are distinctive traits linked to Co^{I} specie formation.[35,36] Thus, the electronic spectral alterations of redox couple **II** confirms its assignment as $Co^{II}Pc^{-2}/Co^{I}Pc^{-2}$. Additionally, the presence of diffuse isosbestic points at 397, 563, and 688 nm is a fingerprint feature of mixed-valence species in solution.[35] Furthermore, the *Q*- and *B*-bands both decrease and the charge transfer band shifts to a longer wavelength (at 479 nm) when exposed to negative overpotentials relative to redox pair **I**, see **Figure 4.6B**. These characteristic electronic spectral alterations are associated with the $Co^{I}Pc^{-2}/Co^{I}Pc^{-3}$ redox pair.[28]

The voltammetry data, showed that the redox processes **III** and **IV** are essentially overlapping due to aggregation. Consequently, two subsequent overpotentials of 0.408 and 0.650 V were over applied relative to redox couple **III** for completion of the metal-based oxidation. Applying the first overpotential, the UV-Vis spectral changes associated with redox couple **III** revealed an increase in the intensity of the *Q*-band. After the second overpotential was induced, the formation of a low intensity CT band in the vicinity of 360 nm appears, indicative of metal oxidation within a $Co^{II}Pc$ core, as shown in **Figure 4.6C**.[35,37] Therefore, the voltammetric assignment of redox couple **III,** attributed to the $Co^{II}Pc^{-2}/Co^{III}Pc^{-2}$ redox process, is substantiated by the acquired spectroelectrochemical data. In addition, the characteristic *Q*-band increase is accompanied by the disappearance of the electronic transition associated with the aggregate and a reduction of the *B*-band.[38] When applying positive overpotentials relative to redox couple **IV**, both the *Q*- and *B*-bands experience a significant decrease, signalling Pc^{-2} oxidation and thereby confirming the assignment of redox couple **IV** as $Co^{III}Pc^{-2}/Co^{III}Pc^{-1}$, as illustrated in **Figure 4.6D**. [37]

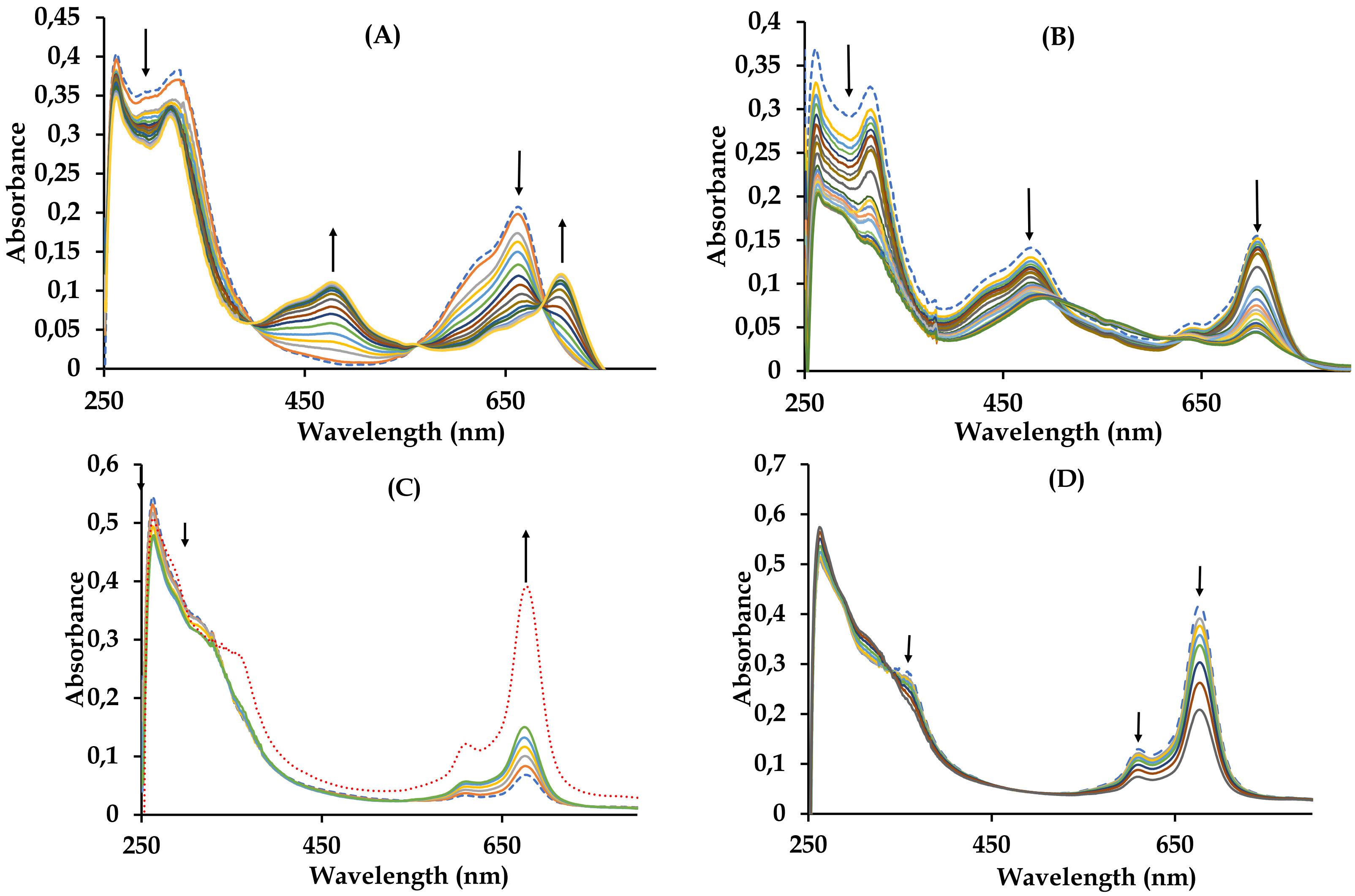

Figure 4.6: *UV–Vis spectral changes of CoPc-Btz at overpotentials applied at (**A**) –0.498 V, (**B**) −1.248 V, (**C**) 0.408 V (0.650 V for the dotted red line) and (**D**) 0.801 V. The initial spectrum is shown as a dashed line.*

4.3.4. Modification of the bare platinum (Pt) electrode with a composite film of pyrrole(PPy) and CoPc-Bzt via electropolymerisation and electrodeposition

The electropolymerization of PPy onto the bare Pt electrode was conducted using the method reported by Zhou and Heinze.[39] Electropolymerization of 0.1 M PPy and co-electrodeposition of CoPc-Bzt (0.1 M) in 1: 1 (v: v, DMF: acetonitrile) containing 1 M NBu_4PF_6 on a Pt electrode were tandemly conducted over 20 cycles *via* cyclic voltammetry, see **Figure 4.7.** As per literature, an increase in the current density for each subsequent cycle (shown as stacked voltammograms) indicates the co-electrocoating of the formed PPy/CoPc-Bzt composite films on the Pt electrode surface, refer to **Scheme 4.2.** The CV of the chemically modified electrode (CME), Pt|PPy/CoPc-Bzt exhibits three discernible peaks. Comparative analysis between the overlay CV profile generated using the CME and that produced from the electrodeposition of the CoPc-Bzt reveals significant shifts which can be attributed to variable sample matrixes being analysed.

The redox properties of pyrrole polymeric films on various substrates are well documented and hence, as per literature trends, the recorded reduction peak potential $E_{pc(\mathrm{PPy})}$, was recorded at 0.1 V shifted to 0.5 V when using the CME while the oxidation peak potential, $E_{pa(\mathrm{PPy})}$ which was recorded at -0.2 V whereas in **Figure 4.7**, it appears at 0.1 V in the CVs of the composite film of PPy/CoPc-Bzt.[39] Also, worth noting is that the irreversible Co(II) oxidative wave is observed at 1.2 V and the irreversible Pc ring oxidation peak observed at 1.4 V. Comparing the CV peaks of the CoPc-Bzt, it is evident that the Co and Pc ring oxidation peaks shifted to higher potentials in the presence of PPy. The redox peaks shifted to higher potentials in subsequent scan cycles, in line with the formation and growth of the PPy conducting film, hence the modification of the Pt surface as depicted in **Scheme 4.2**.

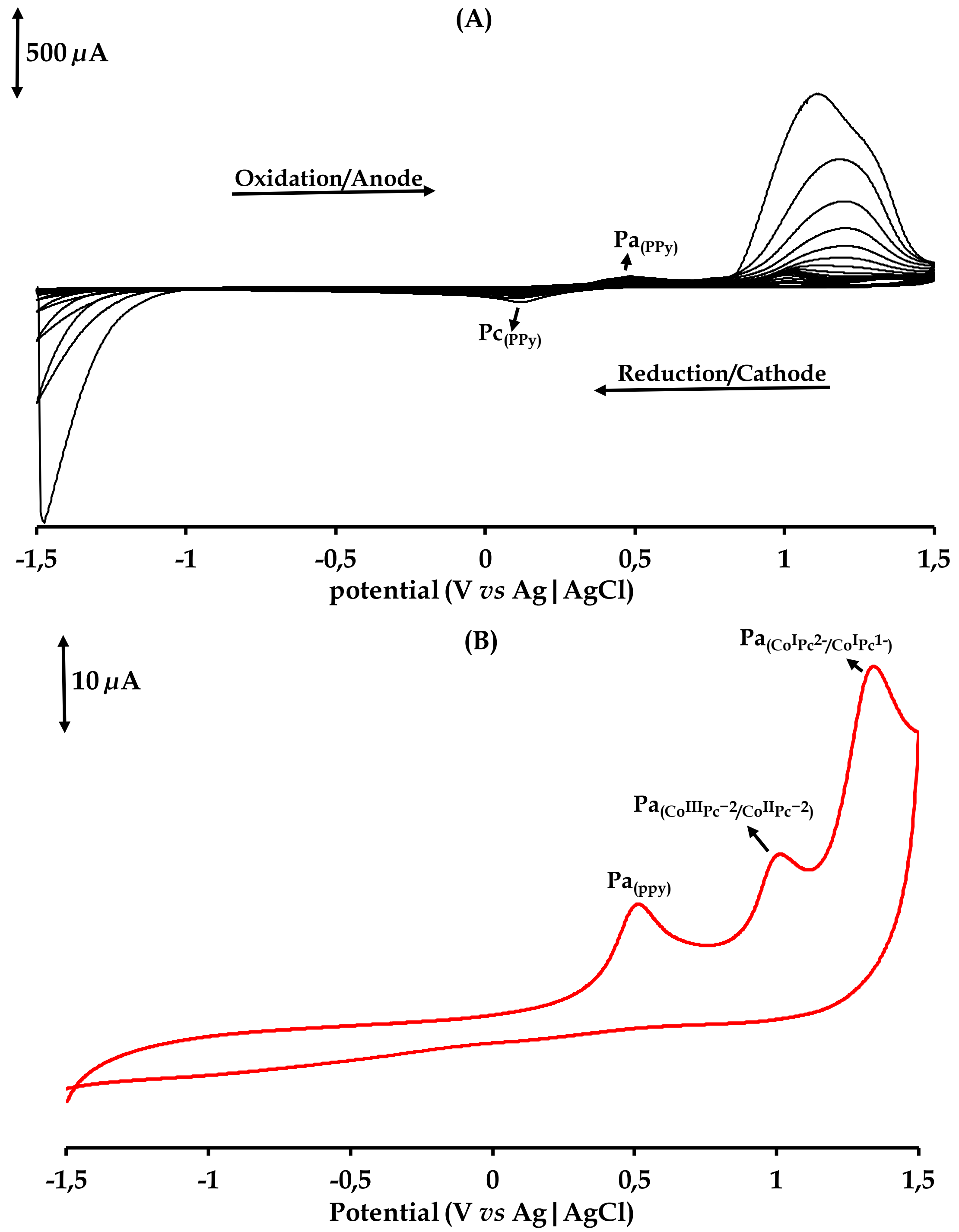

Figure 4.7: *CVs for the simultaneous electro-polymerization of 0.1 M pyrrole and co-electrodeposition of CoPc-Bzt on a Pt electrode at a scan rate of 0.1 V/s between the potential -1.5 to 1.5 V in an acetonitrile: DMF (1:1) blend using a 1 M NBu_4PF_6 as a supporting electrolyte: (**A**) 20 cycles and (**B**) 2 cycles.*

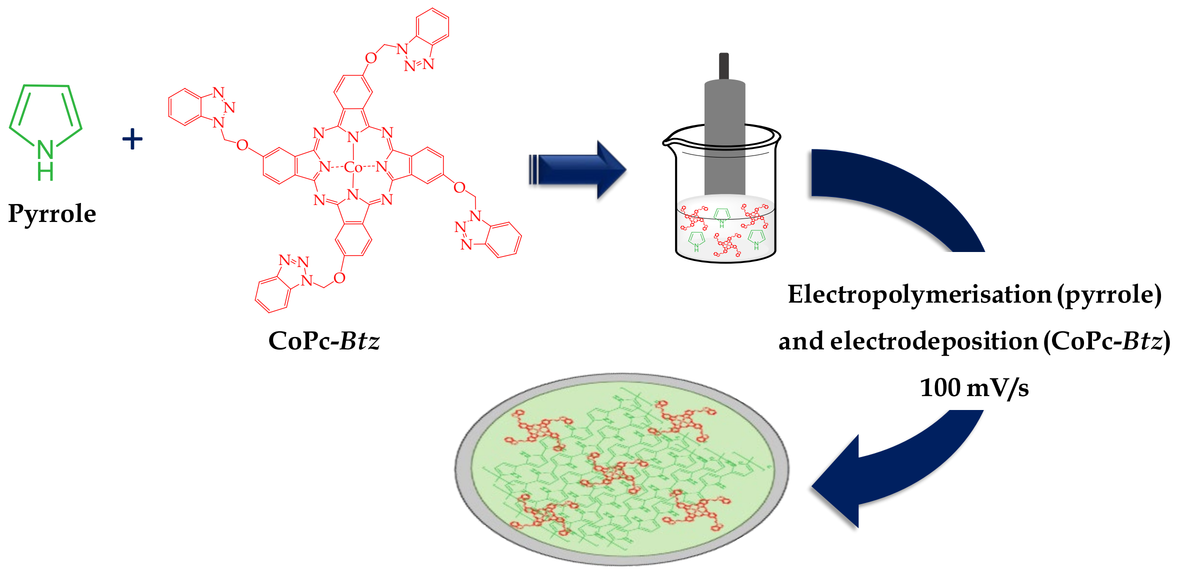

Scheme 4.2: *Schematic representation of the electro-polymerization of 0.1 M pyrrole and co-deposition of CoPc-Bzt films at the Pt.*

4.3.5. Electrochemical impedance spectroscopy (EIS)

Charge transfer characteristics of the PPy/CoPc-Bzt composite film on the Pt substrate were probed in a 5 mM potassium ferricyanide by EIS, see **Figure 4.8**. The charge transfer resistance (R_{CT}) and hence the conductance of the electrodes were deduced by fitting the EIS data, refer to **Table 4.3**.[40] Nyquist diagrams of the bare Pt and Pt|PPy/CoPc-Bzt electrodes show that impedance plots are marked by a depressed semi-circle for the Pt|PPy/CoPc-Bzt (compared to the bare Pt electrode) in the high-frequency domain, *see* **Figure 4.8**. The diameter of the semi-circular part of the plot represents the relative magnitude of the R_{CT} values of the interfacial films of the electrode and the lower this value, the more conductive the film. Since the Nyquist diameter for the Pt|PPy/CoPc-Bzt electrode is significantly smaller than that of the bare Pt, it can be concluded that the former electrode surface exhibits better ionic conductivity and a faster electrode charge transfer interface.[40,41]

The Bode plot of the Pt|PPy/CoPc-Bzt has a phase angle of ~10°, compared to ~58° for the bare Pt electrode, see **Figure 4.9**. The phase angles of the two electrodes were both less than 90°, (which is the optimal value for a capacitor), further confirmed the pseudo-capacitance behaviour that the electron-mediating film induces on the CME within the redox probe. Of particular interest, is that the latter confirms the uneven surface morphology of the Pt|PPy/CoPc-Bzt, which is the probable reason for the substantial deviation between the phase angles of the latter and the unmodified Pt electrode. The immobilized electron-mediating film's non-uniformity is supported by the fact that its *n*-value, a depression angle-related constant, is less than 1 (0.527), see **Table 4.3**.[42]

Table 4.3: *EIS data collected in a 5 mM $[Fe(CN)_6]^{3-/4-}$ using bare Pt and modified (Pt|PPy/CoPc-Bzt electrodes..*

Pt electrode	Rs (Ω)	Rct (Ω)	Zw (μMho)	CPE (μMho)	*n*
Bare	213 (1.2)	3.08 (0.6)	69.6 (1.8)	1.20 (3.3)	0.886
PPy/CoPc-Bzt	198 (0.8)	14.2 (6.8)	177 (5)	86.5 (8.2)	0.527

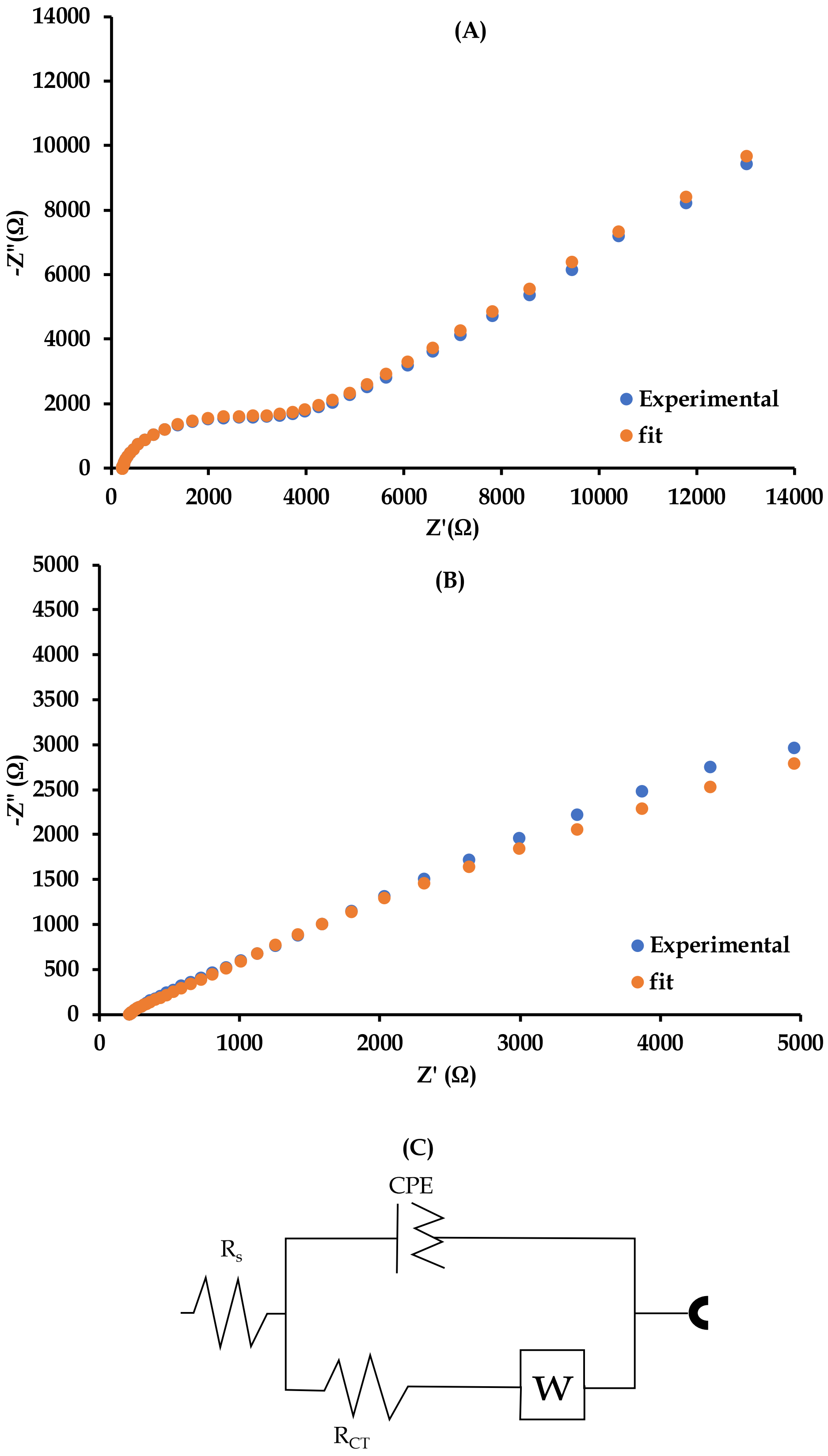

Figure 4.8: *Nyquist plots of the (**A**) bare Pt electrode and (**B**) Pt|PPy/CoPc-Bzt attained in a solution of 5 mM* $[Fe(CN)_6]^{3/4-}$ *prepared in PBS. (**C**) The equivalent circuit used to fit the EIS data.*

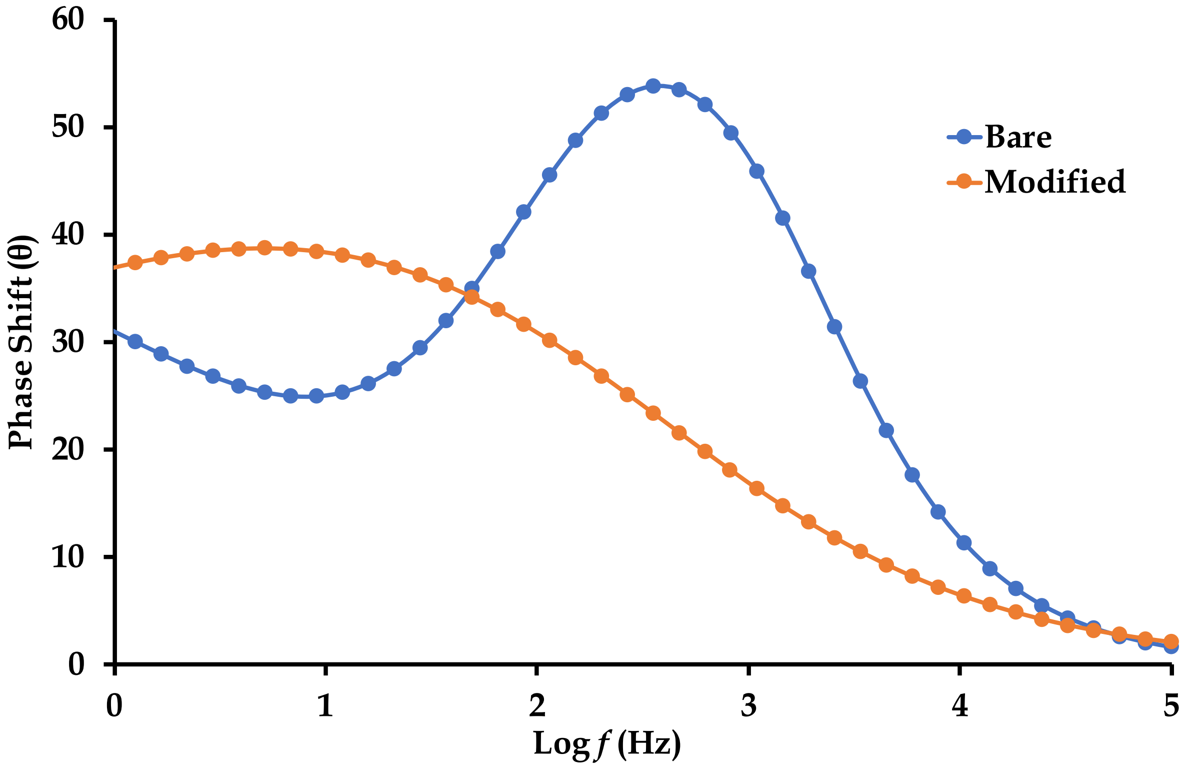

Figure 4.9: *Bode plots for the bare Pt and Pt|PPy/CoPc-Bzt electrodes.*

4.4. Optimization of the CME

4.4.1. *Differential pulse anodic stripping voltammetry (DPASV) of Hg^{2+} using the bare and the chemically modified electrodes (CMEs)*

The Hg^{2+} stripping currents at the bare (Pt) and the individual CMEs (*viz.* the PPy electropolymerized (Pt|PPy), CoPc-electrodeposited (Pt|CoPc-Bzt) and co-electropolymerized PPy and CoPc-electrodeposited (Pt|PPy/CoPc-Bzt) were investigated by differential pulse anodic stripping voltammetry (DPASV) in an electrolyte comprising 0.1 M HCl and 0.4 M NaCl. The Hg^{2+} ions were reduced to Hg(0) which accumulated at the electrode surfaces under optimal experimental conditions at an accumulation potential of -0.6 V. This was followed by the anodic stripping of the Hg(0) by scanning the potential of the electrodes between -1.0 V and +1.0 V, see **Figure 4.10**. Oxidative stripping of Hg(0) at the Pt occurred at a potential of 0 V but this peak was broad and poorly resolved. Although the bare Pt afforded a less positive potential than that of the Pt|PPy, Pt|CoPc-Bzt and Pt|PPy/CoPc-Bzt which generated I_{pa} values from 16 mV to 35 mV, respectively. These CMEs afforded stripping currents of Hg(0) which were three to eight folds higher than that of the Pt bare electrode.

Structurally, the coating film of PPy, CoPc-Bzt or their composite (PPy/CoPc-Bzt) increased the electrode surface areas relative to the bare thereby providing more binding sites of the nanocomposite for electrochemical deposition of Hg^{2+} on the different electrode surfaces. Moreover, the higher electrical conductivity of PPy boosted the rate of charge transfer of the combined films resulting in faster electrode kinetics.[43] As depicted in **Figure 4.10**, the composite film for the Pt|PPy/CoPc-Bzt gave the highest stripping current density than that of other individual electron-mediating components. This also implied it had the largest effective surface area compared to the electrodes. The incremental enhancement in the sensitivity of the modified electrodes towards Hg signifies the individual mediation/catalytic roles as well as synergism between the components of the modifiers.

Additionally, the surface chemistry of the modifiers contributed synergistically to the enhanced detection of Hg^{2+} by the modified electrodes. Stripping of Hg(0) was mediated by favourable interactions between Hg^{2+} and the nitrogen atoms of the CoPc-Bzt as well as those of the PPy film.[12] Resultantly, the Pt|PPy/CoPc-Bzt which combined the mediating chemistries of the highly conductive PPy and the electrocatalytic CoPc-Bzt turned out to be the best of the modified electrodes for the electrochemical detection of Hg^{2+} ions.

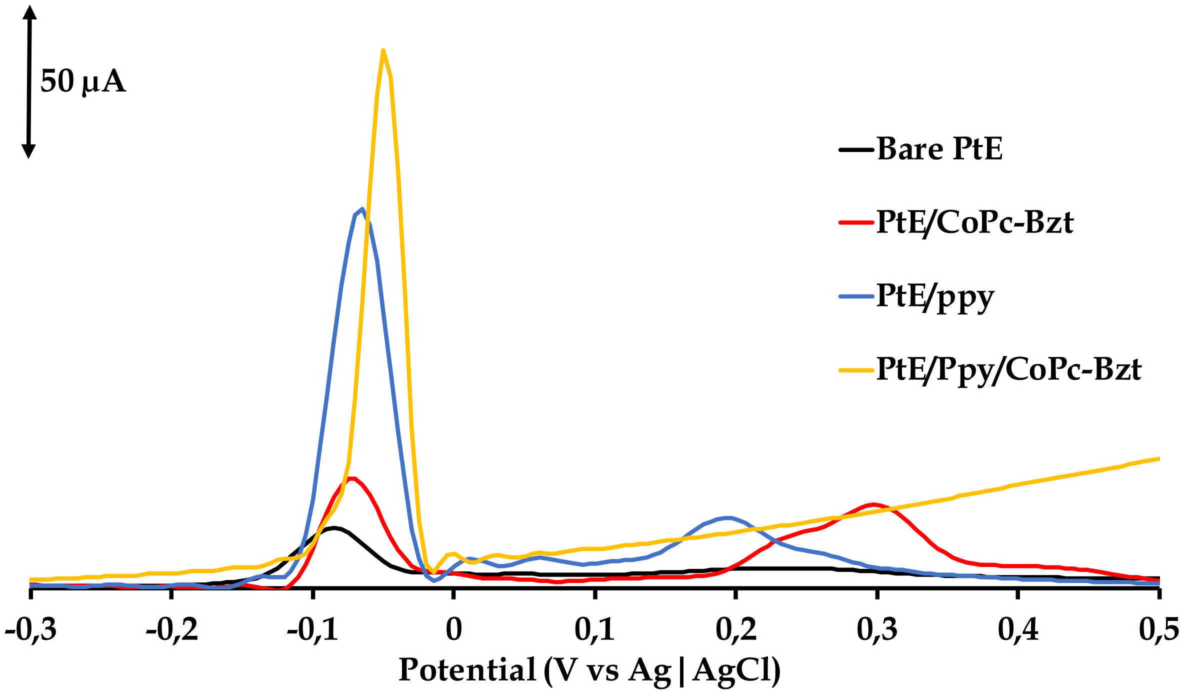

Figure 4.10: *DPASV responses of the bare Pt, Pt|PPy, Pt|CoPc-Bzt and Pt|PPy/CoPc-Bzt electrodes in 1 mM Hg^{2+} dissolved in 0.1 M HCl containing 0.4 M NaCl.*

4.4.2. *Effective surface area and surface coverage*

The investigation on the microstructure surfaces of the CMEs were advanced to the determination of the effective surface area of Pt|PPy/CoPc-Bzt electrode, (the most sensitive CME) was calculated using its responses towards 5 mM $K_3[Fe(CN)_6]$ in 0.1 M KCl at various scan rates, see **Figure 4.11A**. The Randles-Sevcik equation (Eq. 4.1) was used to calculate the effective surface area of the modified electrode.[44]

$$I_{pa} = 2.69\ x10^5 n^{3/2} AC\sqrt{Dv} \qquad (4.1)$$

where n is the number (n = 1) of electrons transferred, A is the effective surface area, D is the diffusion coefficient of $K_3[Fe(CN)_6]$, v is the scan rate, C is the bulk molar concentration of $K_3[Fe\ (CN)_6$. The effective surface area was calculated using the slope of the plot of the oxidation peak currents against the square root of scan rates, as shown in **Figure 4.11B**. The CME's relative effective surface area was found to be 0.144 cm^2, which is approximately twice higher than the bare Pt electrode's (0.071 cm^2). This confirmed the successful surface modification of the latter. The increase is due to the intricate surface crevices of the modifier films onto which the analyte (Hg^{2+}) adsorbed. This implies the film has more exposed active sites for interacting with Hg^{2+} ions than the electrode modified with individual conducting films.

The effective surface area of the modified electrodes determined using Eq. (4.1), and the total charge determined from the area under the peak in **Figure 4.11B**, were both used to determine the surface coverage using Eq. (4.2)

$$\Gamma = \frac{Q}{nFA} \tag{4.2}$$

where Γ is the surface coverage, n is the number of transferred electrons, F is the Faraday constant, and A is the effective area of the electrode. The calculated surface coverage value of PPy/CoPc-Bzt nanocomposite was $7.51\ x\ 10^{-08}$ mol cm^{-2} and it is higher than $1.0\ x\ 10^{-10}$ mol cm^{-2} reported for MPcs lying flat on the surface of the electrode.[44]

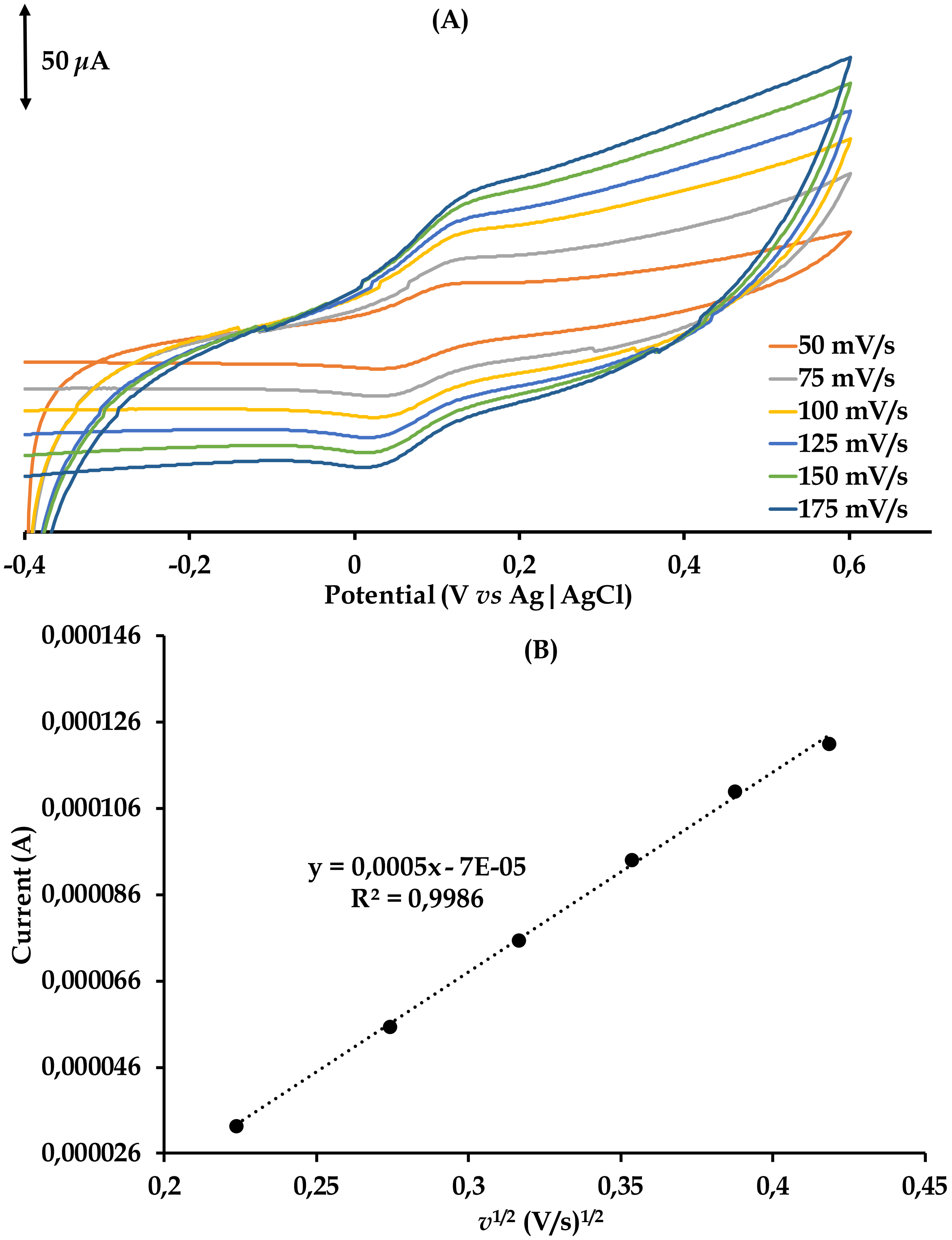

Figure 4.11: *(**A**) The CVs responses towards 5.0 mM $K_3[Fe(CN)_6]$ (prepared in 0.1 M KCl(aq)) using the Pt|PPy/CoPc-Bzt electrode for increasing scan rates. (**B**) A plot of I_{pa} vs square root of scan rate.*

4.4.3. Stability and reproducibility

The first three current responses (cycles) exhibited a significant decrease, indicating some instability or adjustment period of the electrode to the experimental conditions, *see* **Figure A2**. This could be attributed to factors such as electrode conditioning or stabilization of the electrochemical system. From the 4th to 6th cycle, there was a slight decrease in current response, suggesting some ongoing adjustment or stabilization process. However, from the 7th scan onwards, the peak currents became stable, indicating that the electrode had reached a steady-state condition for detecting Hg(II) ions. The %RSD (relative standard deviation) of 4.42% calculated from the 10 replicated measurements indicates good reproducibility of the Pt|PPy/2 electrode for detecting Hg(II). This suggests that the electrode's performance is consistent across multiple measurements, indicating its reliability for analytical applications.

4.4.4. Accumulation Potential

In 0.1 M HCl and 0.4 M NaCl solution, the effect of accumulation potential on the stripping current of Hg occurring at Pt|PPy/CoPc-Bzt electrode interface was investigated, and the results are shown in **Figure 4.12**. The investigation of accumulation potential was conducted in the potential range of -1.0 V to +0.2 V. The stripping current of the CME increased linearly when the accumulation potential was increased from -1.0 V to -0.6 V (optimal accumulation potential: -0.6 V). Upon increasing potential beyond -0.6 V, a progressive decrease in the stripping peak current was observed in a linear manner.

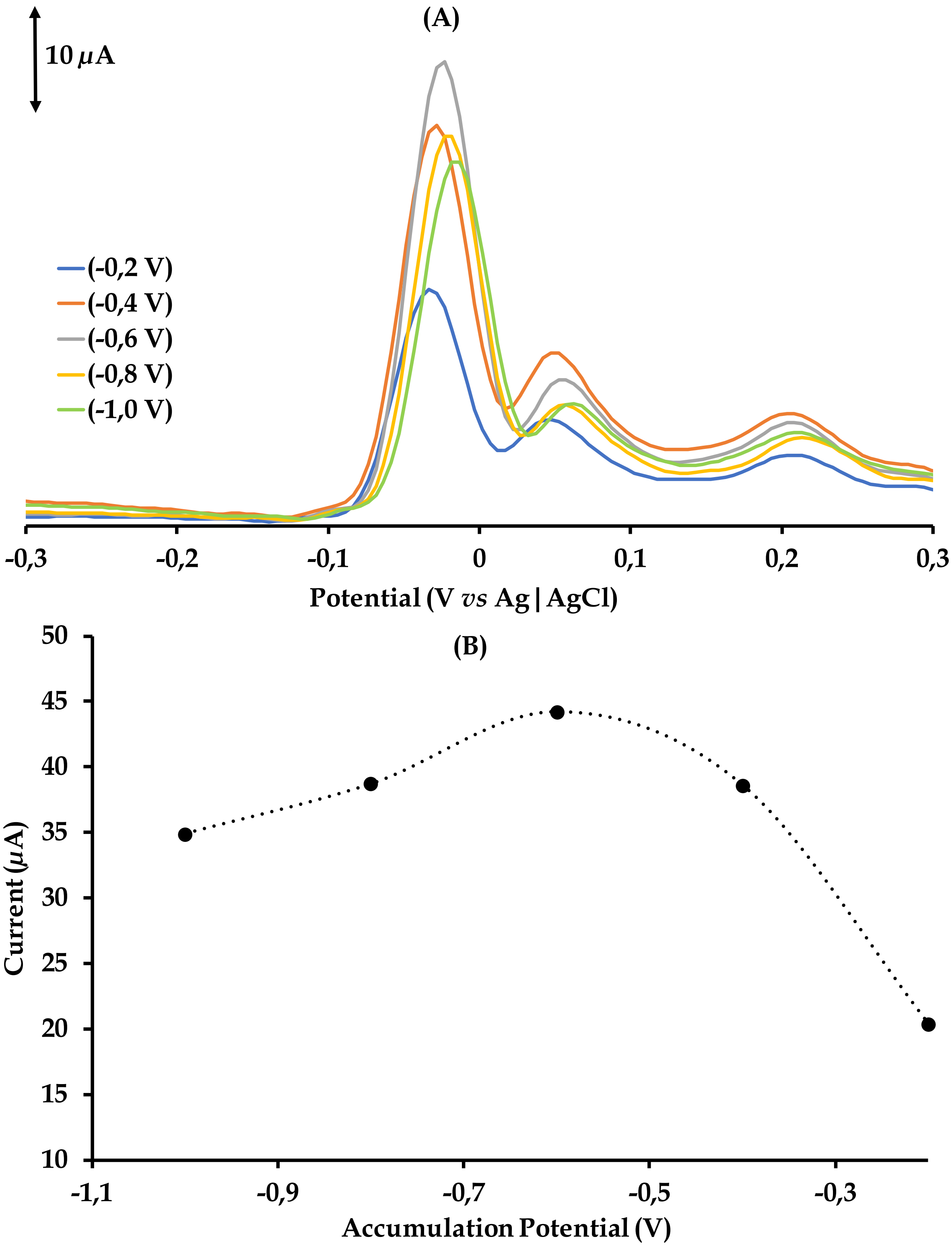

Figure 4.12: *DPASV responses using the Pt|PPy/CoPc-Bzt electrode towards 1 mM Hg(II) electrocatalysis in 0.1 M HCl and 0.4 M NaCl at different accumulation potentials.*

4.4.5. Accumulation Time

The effect of accumulation time on the CV response towards 1 mM Hg(II) was studied in the range of 0-175 s at a fixed potential of -0.6 V at the Pt/PPy/CoPc-Bzt and was conducted *via* DPASV, see **Figure 4.13**. Increasing the deposition time of Hg(0) up to 75 s, resulted in a steady increase of the stripping current. There was a slight decrease at 100 s while it increased at 125 s, giving a stripping current that is slightly higher to that obtained at 75 s. However, when the deposition time was set to values greater than 125 s, the stripping current decreased linearly. This suggests that deposition time greater than 125 s, saturated the accessible sites at the modified electrode for Hg(0) adsorption.[45] Thus, the deposition time of 125 s was chosen for the experiments that are presented ahead.

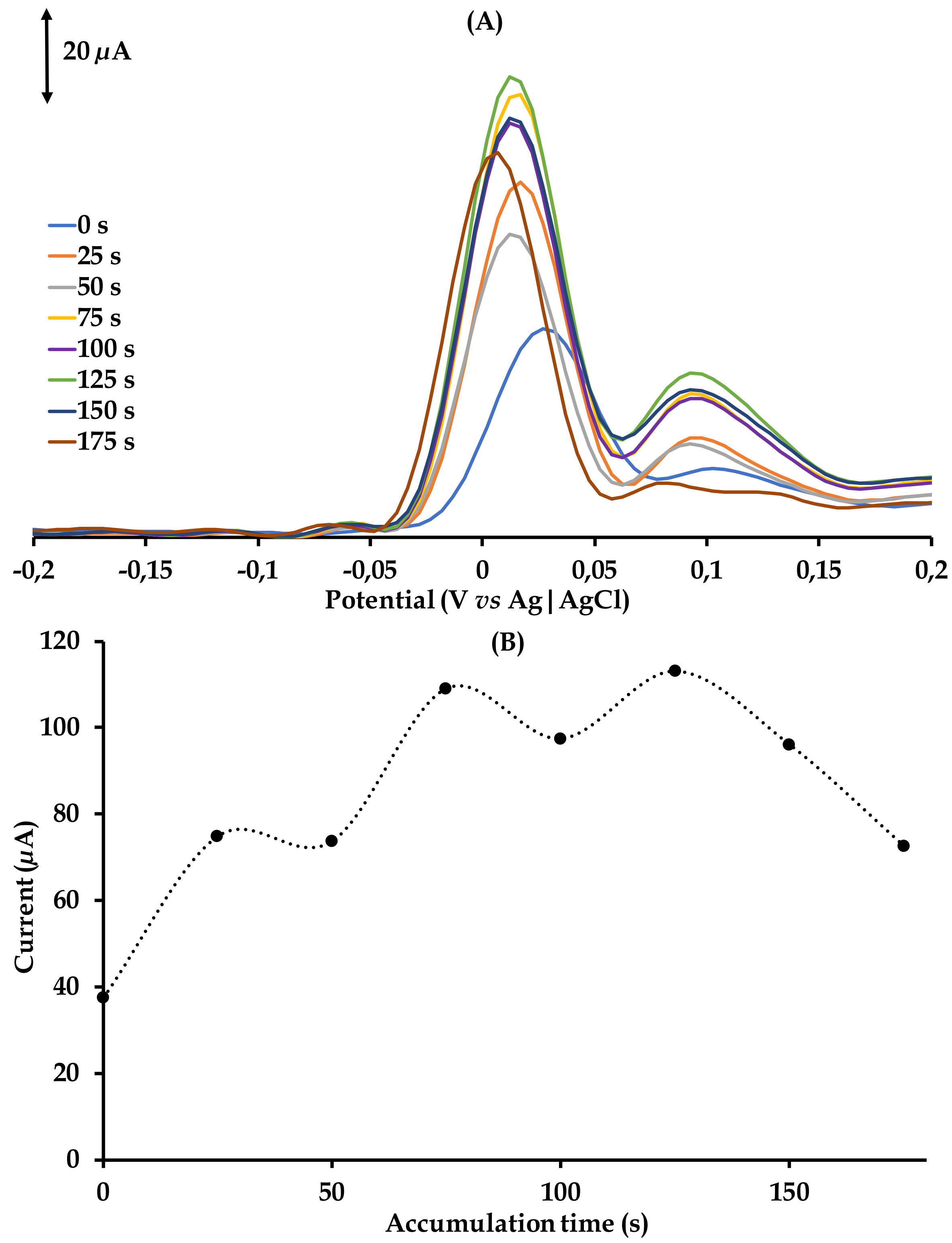

Figure 4.13: *Optimization of experimental parameters at Pt | PPy/CoPc-Bzt on the DPASV peak currents of 1 mM Hg(II) in 0.1 M HCl and 0.4 M NaCl: Accumulation potential= -0.6*

4.4.6. pH effect

The effect of pH on the stripping currents of Hg(0) was investigated within the pH range of 1 to 9 with the Pt|PPy/CoPc-Bzt set at optimum accumulation and stripping conditions. It is commonly known that the pH of the buffer solution has a considerable impact on the stripping current of the target metal ion.[46] The anodic stripping signals of the Hg increased with increasing pH (1 - 8) as shown in **Figure 4.14B**, and the highest stripping current was found at pH 8.28. Given that PPy exists in their reduced state and thus conductive form under basic media, the increase in currents was due to an increase in the formation of the conducting form as the pH was increased. Mercury ions are soft Lewis acids and coordinated to PPy more in the unprotonated form stable complexes in line with the hard-soft acids and bases (HSAB) theory. Beyond pH 8, the stripping current decreases. This is due to the hydrolysis of Hg^{2+}, precipitating the ions as $Hg(OH)_2$.[12,47]

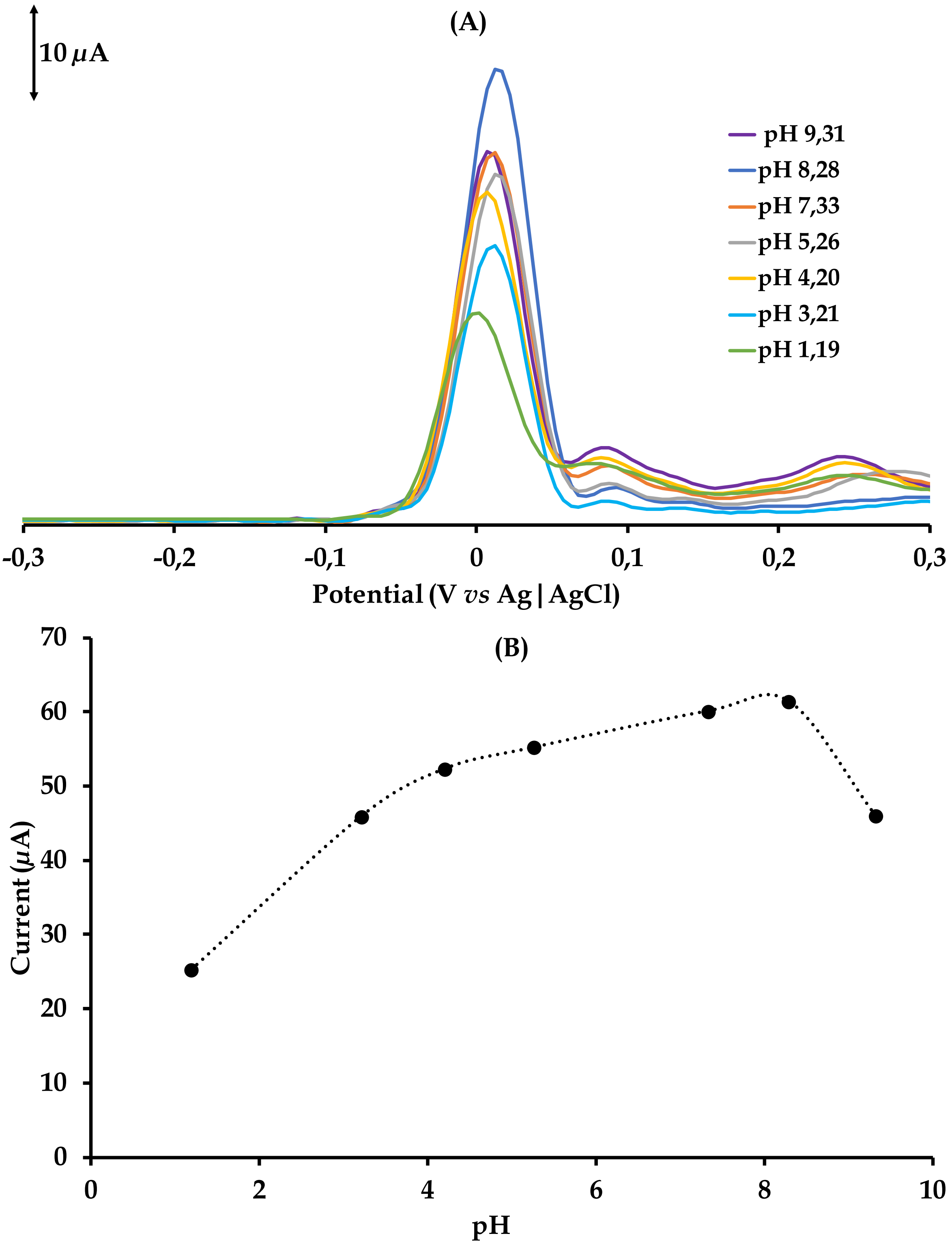

Figure 4.14. *DPASV peak currents of 1 mM Hg (II) in 0.1 M HCl and 0.4 M NaCl (adjusted to target pH (1-9) using 1.M NaOH at Pt|PPy/CoPc-Bzt.*

4.4.7. Determination of Hg^{2+} ions using Pt|PPy/CoPc-Bzt

The DPASV responses of Pt|PPy/CoPc-Bzt towards varying concentrations of Hg^{2+} are presented in **Figure 4.15**. The stripping current of Hg^{2+} exhibited a linear increase with rising concentrations of $Hg^{2+,}$ indicating a linear response within the range of 10 μM to 100 μM. To determine the limit of detection (LOD) and limit of quantification (LOQ), the following equations were employed: LOD = $(3*std_b/k)$ and LOQ = $(10*std_b/k)$, where std_b represents the standard deviation of the blank and k is the slope of the linear calibration curve, as depicted in **Figure 4.15B**. The obtained calibration curve is shown in equation 4.3:

$$I = 0.4805\ \mu M\ [Hg] + 6{,}1661,\ R^2 = 0.9921 \qquad (4.3)$$

The calculated limit of detection (LOD) for Hg^{2+} was found to be 1.11 μM, while the limit of quantitation (LOQ) was determined to be 3.72 μM. A calibration reproducibility ranging from 1.4 to 5.4% RSD (N = 3) was established at different concentrations of Hg^{2+}. For comparative purposes, **Table 4.4** presents an analysis of the analytical performance of Pt|PPy/CoPc-Bzt with other Pt electrodes modified with polypyrrole or metallophthalocyanine. Kantize *et al.*,[48] reported a SAMs-CoPc-Bzm|Poly(3-HT)-AuE electrode for Hg^{2+} detection with an LOD of 40.6 μM whereas the Pt|PPy/CoPc-Bzt exhibited a lower LOD compared to this electrode. Mahmoudian *et al.*[49] demonstrated a polypyrrole-coated platinum nanospherical composite/glassy carbon electrode with an impressive LOD of 0.277 nM with a wider linear range for Hg(II) detection, indicating higher sensitivity at low concentrations compared to the Pt|PPy/CoPc-Bzt.

Table 4.4: *Comparative analysis of LOD and LOQ values for the Pt|PPy/CoPc-Bzt electrode for the detection of* Hg^{2+} *against other CMEs reported in the literature.*

Type of electrode	**LOD**	**LOQ**	**Linear range**	**Reference**
Pt|PPy/CoPc-Bzt	1.11 µM	3.72 µM	10 – 100 µM	This work
SAMs-CoPc-Bzm|Poly(3-HT)-AuE	40.6 µM	NR	337 – 3370 µM	[49]
GCE/PPy/Pct/GR	4 fM	NR	4 - 20 fM	[12]
Pt/PPy NSs/GCE	0.277 nM	0.924 nM	5 - 500 nM	[50]
N,S-carbon/Sep	0.1 µg L^{-1}	NR	0.4 - 85.0 µg L^{-1}	[51]
Clicked-CoPc/GCE	81.94 nM	NR	0 - 0.1 mM	[52]

Abbreviations: NR: Not Reported, **SAMs-CoPc-Bzm|Poly(3-HT)-AuE:** Self assemble monolayer of *tetra*-4-(benzothiazole-2-methoxy) phthalocyaninato)cobalt| 3-hexylthiophene-gold electrode, **GCE/PPy/Pct/GR:** glassy carbon electrode/polypyrrole/pectin/graphene reduced oxidase, **Pt/PPy NSs/GCE:** polypyrrole-coated platinum nanospherical composite/glassy carbon electrode, **N,S-carbon/Sep:** N,S-dual-doped carbon/sepiolite.

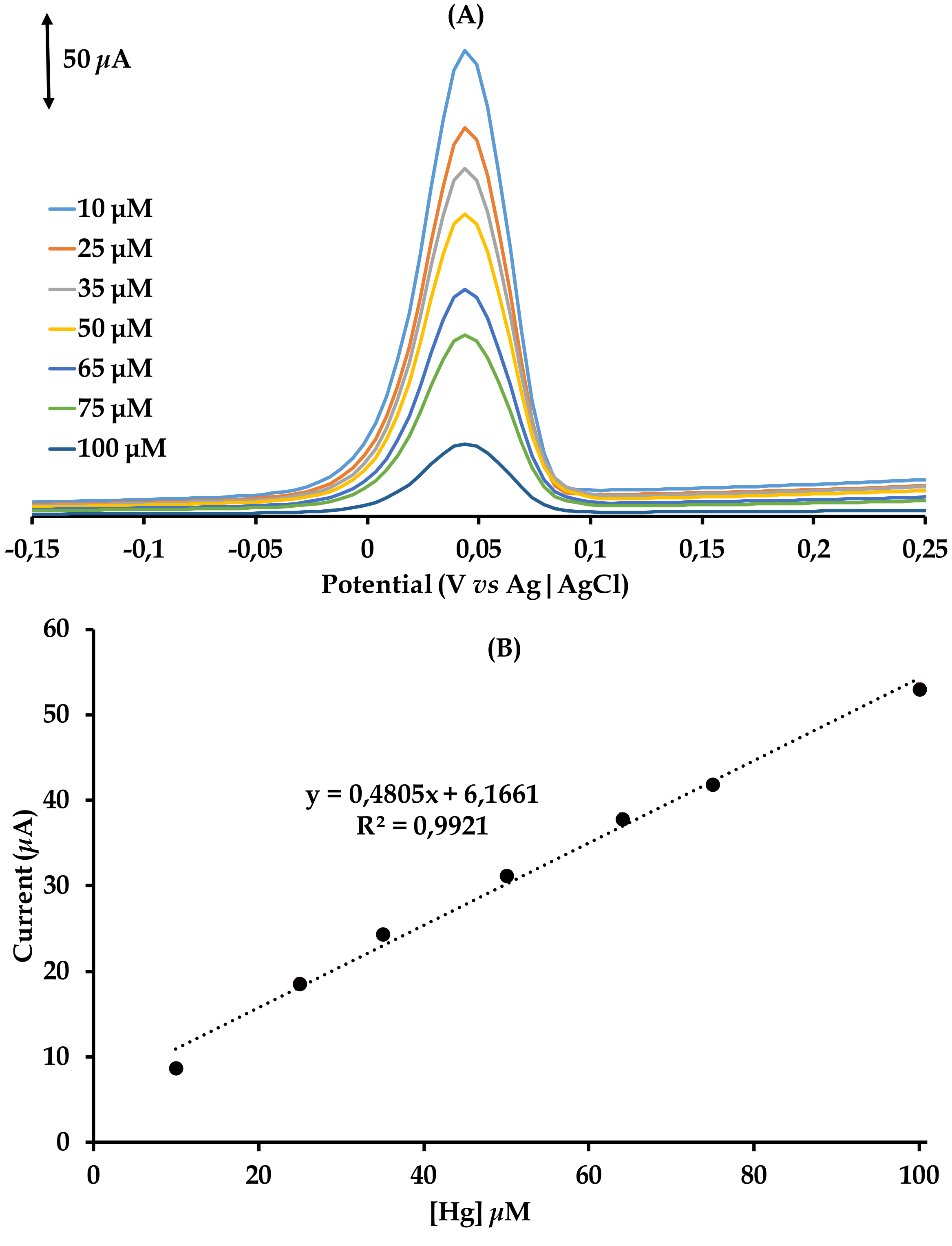

Figure 4.15: *(**A**) DPASV responses of increasing concentrations of Hg(II) prepared in 0.1 M HCl and 0.4 M NaCl (pH = 8.28) using the Pt|PPy/CoPc-Bzt. (**B**): Calibration curve of the current response against Hg(II) concentration. Deposition conditions: accumulation time: 125 s and accumulation potential: -0.6 V.*

4.4.8. Interference studies

The selectivity of the Pt|PPy/CoPc-Bzt towards Hg^{2+} was evaluated in the presence of Cd^{2+} and Pb^{2+} ions. The DPASV response for 1.0 g L^{-1} Hg^{2+} in 0.1 M HCl and 0.4 M NaCl at the Pt|PPy/CoPc-Bzt in the presence of 1.0 g L^{-1} of Cd^{2+} and Pb^{2+} ions was recorded and is presented in **Figure 4.16**. The peaks corresponding to each metal cation could be readily distinguished.

The presence of Cd^{2+} and Pb^{2+} ions affected the size of the Hg^{2+} peak, causing a decrease, but the stripping potential position of Hg^{2+} remained unaffected at the Pt|PPy/CoPc-Bzt. However, the stripping currents for both Cd^{2+} and Pb^{2+} ions were notably lower and broader compared to Hg^{2+}. This is attributed to formation of strong bonds between the soft Lewis acid (Hg^{2+}) and the soft bases of the film modifiers (soft N donor groups on the PPy and CoPc-Bzt) according to Pearson classification of acids and bases reactions. This resulted in higher stripping currents for Hg^{2+} compared to other metal ions. It is known that Cd^{2+} coordinates strongly with harder 'O' donors, which are absent on the modifier film of the electrode. Consequently, its stripping current is ill-defined, *i.e.*, low and broad.[52]

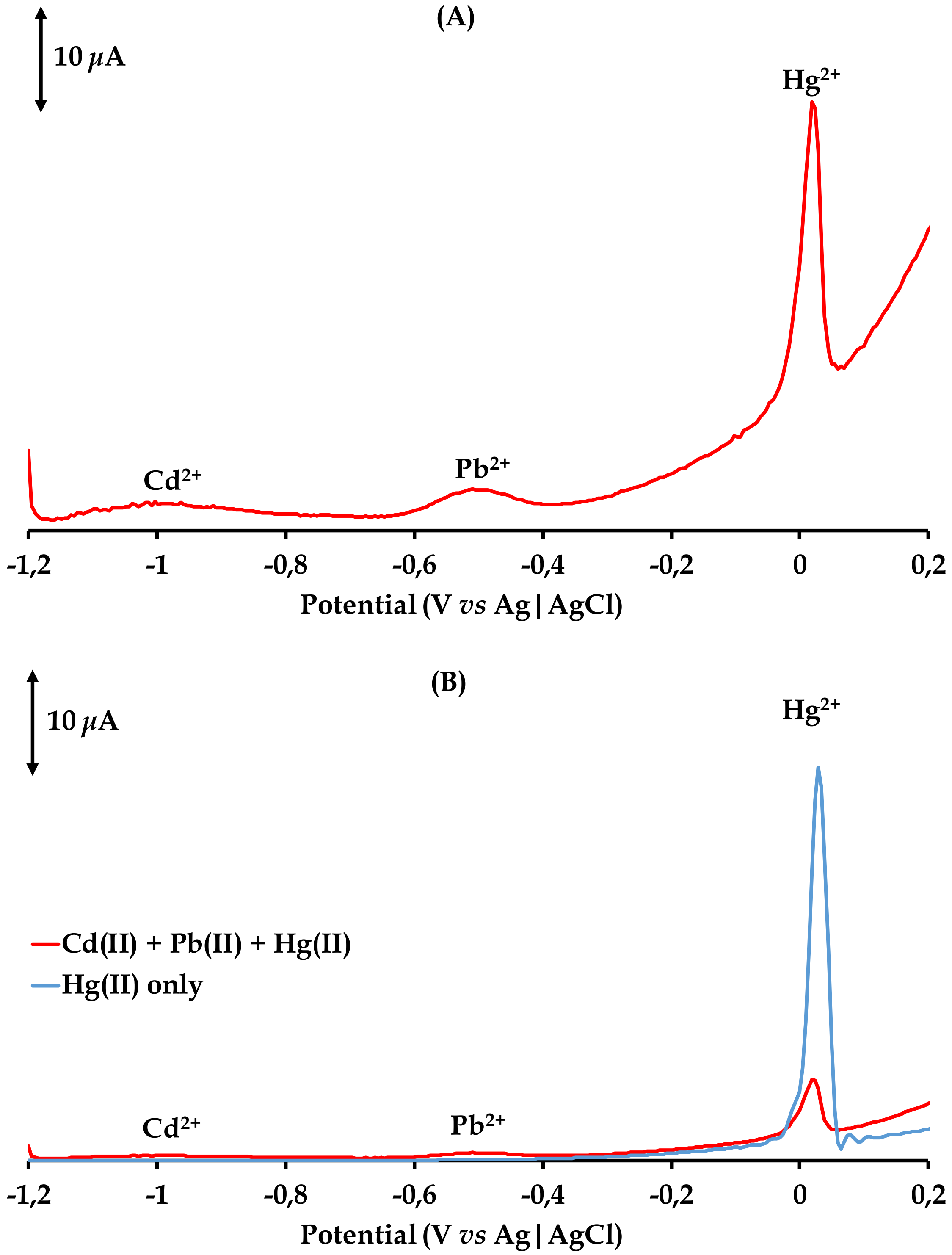

Figure 4.16. (***A***) *DPASV responses of 1 g L^{-1} Hg^{2+} in 0.1 M HCl and 0.4 M NaCl (pH= 8.28) in the presence of 1 g L^{-1} Cd^{2+} and Pb^{2+} ions using Pt|PPy/CoPc-Bzt.* (***B***) *DPASV responses of 1 g L^{-1} Hg^{2+} only in 0.1 M HCl and 0.4 M NaCl (pH= 8.28).* ***Deposition conditions****: accumulation time 125 s and accumulation potential -0.6 V.*

4.4.9. Real water sample analysis

The concentration of Hg^{2+} ions in a water sample collected from the Umngcwini stream, which flows into the Umgeni River, was determined using the Pt|PPy/CoPc-Bzt. The responses of the CME to the Hg^{2+} calibration standards and the real water sample are depicted in **Figures 4.17**. **Figure 4.17A** illustrates that there was no detectable signal for Hg^{2+} in the real water sample, indicating that the concentration of Hg^{2+} in the Umngcwini stream water was below the limit of detection (LOD) of the Pt|PPy/CoPc-Bzt, calculated to be 1.11 µM.

To validate this, the water sample was spiked with incremental volumes (2.00 mL) of a 20.0 µM Hg^{2+} standard. Analysis of the calibration data yielded a percentage recovery of Hg^{2+} of 97.4% with a calibration reproducibility ranging from 2.0 to 4.2% RSD (N = 3) established at different concentrations of Hg^{2+} falling within the acceptable accuracy range of 80-120%. This confirms the ability of the Pt|PPy/CoPc-Bzt to accurately detect and quantify Hg^{2+} ions in real water samples, establishing its reliability for environmental monitoring applications.

Furthermore, the concentration of Hg^{2+} in a real water sample was analyzed using ICP-OES before and after spiking with 12.0 ppm Hg^{2+}, and the results are presented in **Figure 4.18** and **Table 4.5** to determine the %recovery. This comparison was undertaken to validate the accuracy of the Pt|PPy/CoPc-Bzt for detecting Hg^{2+} in real samples against the more established ICP-OES method. The concentration of Hg^{2+} in the water sample before and after spiking was found to be 0.223 and 13.7 ppm, respectively, resulting in a Hg^{2+} recovery of 112.3%.

This recovery value is consistent with the 97.4% (2.92 µM) estimated from the standard method using the Pt|PPy/CoPc-Bzt. The values obtained by the Pt|PPy/CoPc-Bzt and the ICP-OES are both within the acceptable recovery range of 80-120%.[53,54]

Thereby validating the accuracy and reliability of the former in detecting Hg^{2+} in real water samples.

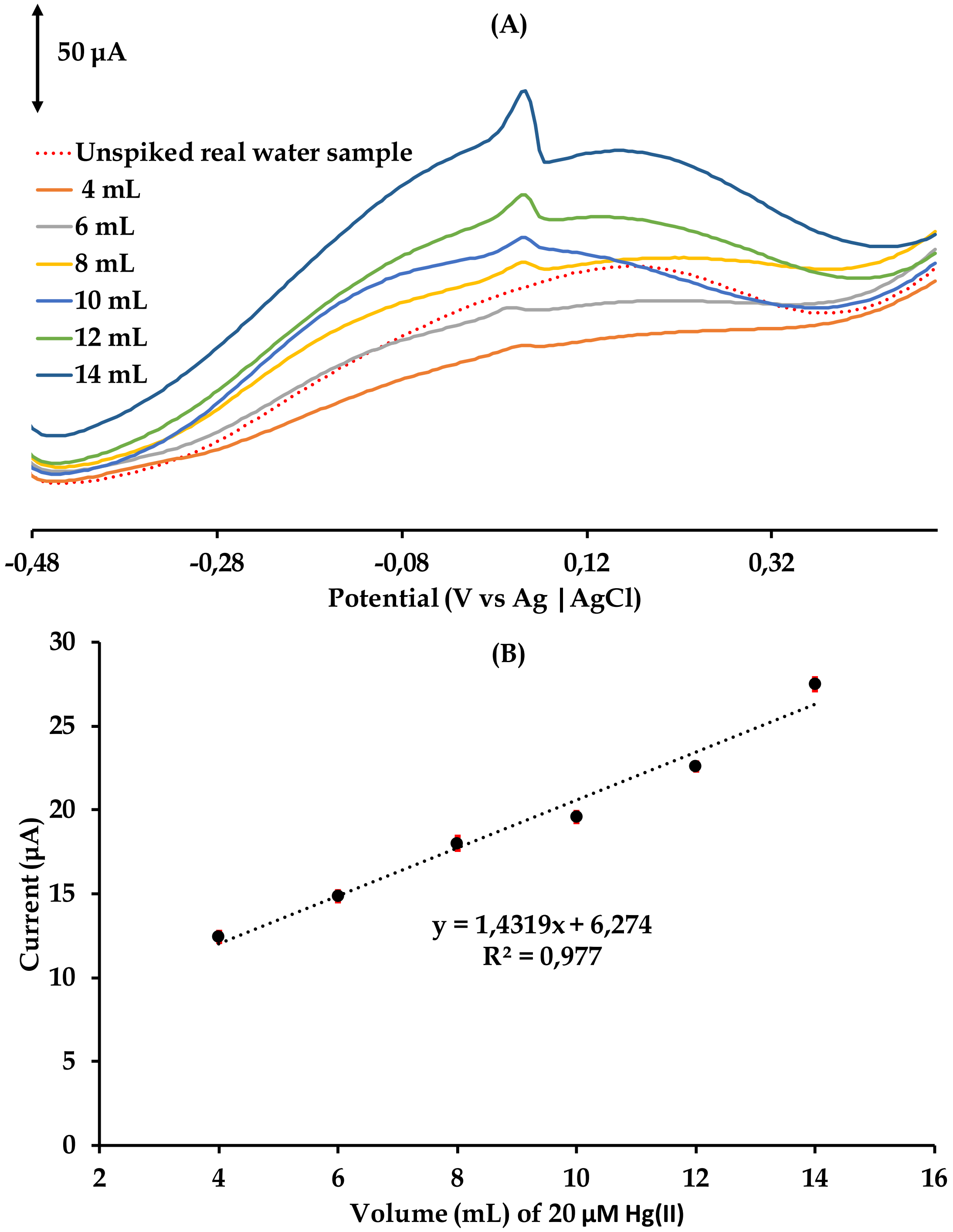

Figure 4.17: *(A) DPASV responses at the Pt|PPy/CoPc-Bzt electrode after the standard addition of incremental volumes (mL) of 20 µM Hg(II) to 30 mL of real water sample.* ***(B)*** *Linear calibration plot.*

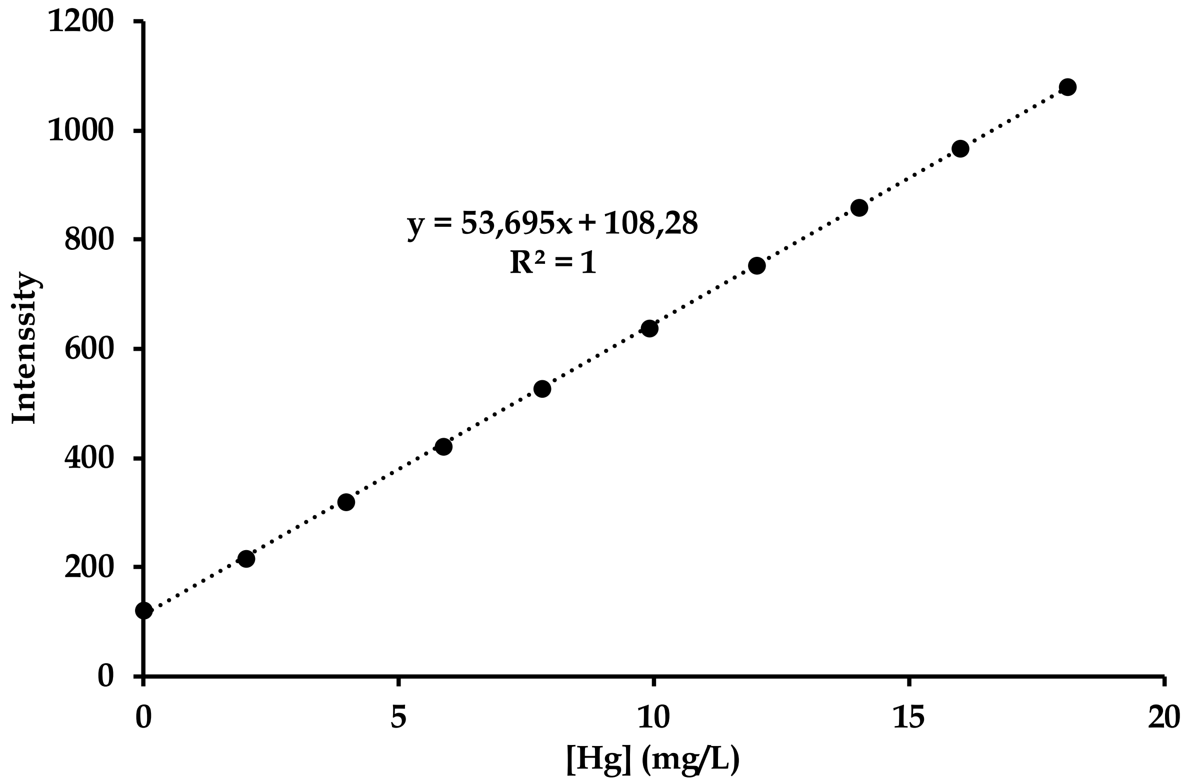

Figure 4.18: *A plot of emission intensity with increasing concentration of Hg(II) for the linear calibration of the ICP-OES.*

Table 4.5: *Measured concentration of Hg(II) ions for the unspiked and spiked water sample collected along the Umngcwini stream, which joins the Umgeni river, water samples by ICP-OES.*

Sample name	**[Hg], ppm**
Unspiked Umngcwini stream water (20.00 mL)	0,223
Umngcwini stream water spiked at 12 ppm Hg(II)	13.7

4.5. Conclusions

The morphological features of CoPc-Bzt were confirmed using various physicochemical techniques, including FTIR, UV-Vis, TOF-MS and elemental analysis. The successful electro-coating of the bare Pt electrode was confirmed *via* the cyclic voltammetry. The performance of the Pt|PPy/CoPc-Bzt was found to surpass that of the bare Pt electrode. The electrocatalytic activity of the Pt|PPy/CoPc-Bzt towards Hg^{2+} was significantly superior. Moreover, it demonstrated selectivity for Hg^{2+} ions in the presence of other interfering heavy metal ions like Pb^{2+} and Cd^{2+}. The percentage recovery of Hg^{2+} by our fabricated Pt|PPy/CoPc-Bzt and the ICP-OES were both within the acceptable recovery range of 80-120%. In particular, the percentage Hg^{2+} recoveries of 97% and 112% were attained when using CME and ICP-OES, respectively.

4.6. References

(1) Mohammed, A. S.; Kapri, A.; Goel, R. *Biomanagement of Metal-Contaminated Soils* **2011**, 1.

(2) Chowdhary, P.; Bharagava, R. N.; Mishra, S.; Khan, N. *Environmental Concerns and Sustainable Development: Air, Water and Energy Resources* **2020**, 1, 235.

(3) Collivignarelli, M. C.; Abbà, A.; Bestetti, M.; Crotti, B. M.; Carnevale Miino, M. *Water, Air, & Soil Pollution* **2019**, *230*, 101.

(4) Iloms, E.; Ololade, O. O.; Ogola, H. J. O.; Selvarajan, R. *International Journal of Environmental Research and Public Health* **2020**, 17, 1096

(5) Ali, S.; Mansha, M.; Baig, N.; Khan, S. A. *The Chemical Record* **2022**, *22*, e202100327.

(6) Braune, B. M.; Outridge, P. M.; Fisk, A. T.; Muir, D. C. G.; Helm, P. A.; Hobbs, K.; Hoekstra, P. F.; Kuzyk, Z. A.; Kwan, M.; Letcher, R. J.; Lockhart, W. L.; Norstrom, R. J.; Stern, G. A.; Stirling, I. *Science of The Total Environment* **2005**, *351-352*, 4.

(7) Wang, X.-p.; Yao, T.-d.; Wang, P.-l.; Wei, Y.; Tian, L.-d. *Science of The Total Environment* **2008**, *394*, 134.

(8) Zagal, J. H.; Griveau, S.; Silva, J. F.; Nyokong, T.; Bedioui, F. *Coordination Chemistry Reviews* **2010**, *254*, 2755.

(9) de la Torre, G.; Bottari, G.; Sekita, M.; Hausmann, A.; Guldi, D. M.; Torres, T. *Chemical Society Reviews* **2013**, *42*, 8049.

(10) Shahrokhian, S.; Kamalzadeh, Z.; Bezaatpour, A.; Boghaei, D. M. *Sensors and Actuators B: Chemical* **2008**, *133*, 599.

(11) Demir, E.; Silah, H.; Uslu, B. *Critical Reviews in Analytical Chemistry* **2022**, *52*, 425.

(12) Arulraj, A. D.; Devasenathipathy, R.; Chen, S.-M.; Vasantha, V. S.; Wang, S.-F. *Journal of Colloid and Interface Science* **2016**, *483*, 268.

(13) Petrunin, M.; Maksaeva, L.; Gladkikh, N.; Makarychev, Y.; Maleeva, M.; Yurasova, T.; Nazarov, A. *Coatings* ***2020***, *10*, p.362.

(14) Castaldo, R.; de Luna, M. S.; Siviello, C.; Gentile, G.; Lavorgna, M.; Amendola, E.; Cocca, M. *Journal of Cultural Heritage* **2020**, *44*, 317.

(15) Recloux, I.; Mouanga, M.; Druart, M.-E.; Paint, Y.; Olivier, M.-G. *Applied Surface Science* **2015**, *346*, 124.

(16) Mohammadpour, Z.; Zare, H. R. *Crystal Growth & Design* **2021**, *21*, 3954.

(17) Daviddi, E.; Shkirskiy, V.; Kirkman, P. M.; Robin, M. P.; Bentley, C. L.; Unwin, P. R. *The Journal of Physical Chemistry C* **2022**, *126*, 14897.

(18) Gribkova, O. L.; Kabanova, V. A.; Nekrasov, A. A. *Russian Journal of Electrochemistry* **2019**, *55*, 1110.

(19) Teles, F. R. R.; Fonseca, L. P. *Materials Science and Engineering: C* **2008**, *28*, 1530.

(20) Palanisamy, S.; Thangavelu, K.; Chen, S.-M.; Velusamy, V.; Chang, M.-H.; Chen, T.-W.; Al-Hemaid, F. M. A.; Ali, M. A.; Ramaraj, S. K. *Sensors and Actuators B: Chemical* **2017**, *243*, 888.

(21) Wang, M.; Yuan, W.; Yu, X.; Shi, G. *Analytical and Bioanalytical Chemistry* **2014**, *406*, 6953.

(22) Dilber, G.; Altunparmak, H.; Nas, A.; Kantekin, H.; Durmuş, M. *Spectrochimica Acta Part A: Molecular and Biomolecular Spectroscopy* **2019**, *217*, 128.

(23) Aktas Kamiloglu, A.; Karaca, H.; Çelik, G.; Acar, İ.; Kantekin, H. *Journal of Chemical Research* **2020**, *44*, 367.

(24) Özceşmeci, İ.; Gelir, A.; Gül, A. *Dyes and Pigments* **2012**, *92*, 954.

(25) Güzel, E.; Güney, S.; Kandaz, M. *Dyes and Pigments* **2015**, *113*, 416.

(26) Nyokong, T. In *Functional Phthalocyanine Molecular Materials* **2010**, 145, 45.

(27) Özer, M.; Altındal, A.; Özkaya, A. R.; Bekaroğlu, Ö. *Dalton Transactions* **2009**, 3175.

(28) Akinbulu, I. A.; Nyokong, T. *Polyhedron* **2010**, *29*, 1257.

(29) Breloy, L.; Yavuz, O.; Yilmaz, I.; Yagci, Y.; Versace, D.-L. *Polymer Chemistry* **2021**, *12*, 4291.

(30) Odabaş, Z.; Kara, H.; Özkaya, A. R.; Bulut, M. *Polyhedron* **2012**, *39*, 38.

(31) Yabaş, E.; Sülü, M.; Saydam, S.; Dumludağ, F.; Salih, B.; Bekaroğlu, Ö. *Inorganica Chimica Acta* **2011**, *365*, 340.

(32) Demirbaş, Ü.; Akyüz, D.; Akçay, H. T.; Koca, A.; Menteşe, E.; Kantekin, H. *Journal of Molecular Structure* **2018**, *1173*, 205.

(33) Çakır, D.; Bekircan, O.; Biyiklioglu, Z. *Synthetic Metals* **2015**, *201*, 18.

(34) Yalazan, H.; Akyüz, D.; Ünlüer, D.; Koca, A.; Kantekin, H.; Sancak, K. *Polyhedron* **2020**, *180*, 114419.

(35) Chohan, S.; Booysen, I. N.; Mambanda, A.; Akerman, M. P. *Journal of Coordination Chemistry* **2015**, *68*, 1829.

(36) Kılıçaslan, M. B.; kantekin, H.; Koca, A. *Dyes and Pigments* **2014**, *103*, 95.

(37) Chohan, S.; Booysen, I. N.; Mambanda, A.; Akerman, M. P. *Inorganica Chimica Acta* **2016**, *447*, 183.

(38) Özgül, G.; Taştemel, A.; Özkaya, A. R.; Bulut, M. *Polyhedron* **2015**, *85*, 181.

(39) Zhou, M.; Heinze, J. *Electrochimica Acta* **1999**, *44*, 1733.

(40) Ghanbari, K.; Bathaie, S. Z.; Mousavi, M. F. *Biosensors and Bioelectronics* **2008**, *23*, 1825.

(41) Kamil, A. M.; Hussein, F. H.; Halbus, A. F.; Bahnemann, D. W. *International Journal of Photoenergy* **2014**, *2014*.

(42) Kantize, K.; Booysen, I. N.; Mambanda, A. *International Journal of Electrochemical Science* **2022**, *17*, 22067.

(43) Parnell, C. M.; Chhetri, B. P.; Mitchell, T. B.; Watanabe, F.; Kannarpady, G.; RanguMagar, A. B.; Zhou, H.; Alghazali, K. M.; Biris, A. S.; Ghosh, A. *Scientific Reports* **2019**, *9*, 5650.

(44) Shumba, M.; Centane, S.; Chindeka, F.; Nyokong, T. *Journal of Electroanalytical Chemistry* **2017**, *791*, 36.

(45) Sultan, S.; Shah, A.; Khan, B.; Nisar, J.; Shah, M. R.; Ashiq, M. N.; Akhter, M. S.; Shah, A. H. *ACS Omega* **2019**, *4*, 16860.

(46) Fu, X.-C.; Wu, J.; Nie, L.; Xie, C.-G.; Liu, J.-H.; Huang, X.-J. *Analytica Chimica Acta* **2012**, *720*, 29.

(47) Zhao, Z.-Q.; Chen, X.; Yang, Q.; Liu, J.-H.; Huang, X.-J. *Chemical Communications* **2012**, *48*, 2180.

(48) Kantize, K.; Ngwenya, V.; Booysen, I. N.; Mambanda, A. *Polyhedron* **2021**, *203*, 115235.

(49) Mahmoudian, M. R.; Basirun, W. J.; Alias, Y. *RSC Advances* **2016**, *6*, 36459.

(50) Ghanei-Motlagh, M.; Baghayeri, M. *Materials Chemistry and Physics* **2022**, *285*, 126127.

(51) Fomo, G.; Nwaji, N.; Nyokong, T. *Journal of Electroanalytical Chemistry* **2018**, *813*, 58.

(52) Hatai, J.; Pal, S.; Bandyopadhyay, S. *RSC Advances* **2012**, *2*, 10941.

(53) Turner, K. A.; Frinack, J. L.; Ettore, M. W.; Tate, J. R.; Graziani, M. S.; Jacobs, J. F. M.; Booth, R. A.; McCudden, C. R.; Keren, D. F.; Delgado, J. C.; Zemtsovskaja, G. *Clinical Chemistry and Laboratory Medicine*. **2020**, *58*, 533.

(54) Mahan, C.; Bonchin, S.; Figg, D.; Gerth, D.; Collier, C. *Journal of Analytical Atomic Spectrometry* **2000**, *15*, 929.

Chapter 5

Synergism in the electrocatalytic properties of electrospun cobalt phthalocyanine-carbon nanotube-polyaniline nanofibers immobilized on a gold electrode for the detection of lead(II) ions

5.1. Introduction

Elemental lead (Pb) and its compounds find extensive applications in the automotive manufacturing, oil refinery, paint and ammunition industries.[1,2] In all these processes, regulatory protocols on the use and storage and disposal of Pb-containing products should be strictly adhered to due to the high toxicity of Pb and its compounds. However, in developing or third-world economies, these regulatory guidelines are either lacking or often not enforced, leading to widespread environmental pollution impacts. [3]

Consumption of Pb-contaminated water and food, inhalation of polluted air and dermal contact with Pb-containing products or wastes are some of the critical exposure routes through which animals and humans are poisoned by Pb(II) ions.[4] Lead poisoning can lead to neurological damage, fetal development inhibition, organ dysfunction and brain damage in mammals.[4,5] Therefore, it is crucial to develop electrochemical sensors for seamless detection of Pb species in real water samples. In fact, the potential of electrochemical sensors have been illustrated used in the routine monitoring of trace concentration levels of toxic metal ions such as Pb(II) in various environmental samples that includes water for domestic and industrial uses.[5,6]

Unmetallated phthalocyanines (H_2Pcs) and derivatives containing redox-active metal centres (MPcs) have been widely used as electrocatalysts on various working electrode substrates.[7] The planar structure of these macrocyclic compounds facilitates their adsorption onto bare electrodes, while their 18 π-electron system, coupled with the electroactive metal centre, provides optimal ligand and metal-based redox properties, respectively.[7,8] The redox properties of MPcs can be tailored through the introduction of electron-donating or -withdrawing substituents at their peripheral or non-peripheral positions. Furthermore, the role of MPc substituents has expanded to encompass selective analyte recognition, chemical modification of bare electrodes, and the fabrication of MPc nanocomposites.[7-10]

In this study, we describe the stepwise construction of a gold (Au) CME (*viz.* Au|ENFs-**1**-Nf) for the sensitive detection of Pb(II) ions. Firstly, we fabricated a nanocomposite PANI-CoPc-flav-*f*-MWCNTs (**1**) comprising of polyaniline (PANI), a β-tetrasubstituted flavone CoPc (CoPc-flav) and carboxylic acid-functionalized multiwalled carbon nanotubes (*f*-MWCNTs). The nanocomposite was then embedded into polyvinyl alcohol (PVA) through electrospinning, resulting in electrospun nanofibers (ENFs) denoted as (PANI-CoPc-flav-*f*-MWCNTs)PVA (ENFs-**1**). A sonicated suspension of ENFs-**1** was drop-casted onto the Au bare electrode and subsequently annealed by a layer of Nafion (Nf) to prevent the former from leaching. This formed a polymeric nanohybrid (*viz.* ENFs-**1**-Nf) film which was conductive and permeable to the metal-based pollutant, Pb(II). Therefore, the Nf component does not only enhances electron mediation but also acts as a connecting matrix for the chemical modifiers within the ENFs-**1** film.[11]

The incorporation of PANI and *f*-MWCNTs into the thin film of Au|ENFs-**1**-Nf CME is justified based on their complementary physical properties. In particular, PANI provides high conductivity, while *f*-MWCNTs contribute to mechanical stability, enhancing the inherent electron-mediating capabilities of CoPc-flav and ensuring the structural integrity of the nanocomposite film.[12-15] Similar to CMEs reported in other studies, the ternary components of the ENFs-**1** nanocomposite increase the effective electrocatalytic surface areas, resulting in higher current signals.[16-18] Constituents of the ENFs-**1** film are interconnected by the conductive Nafion (Nf) polymeric chains, forming a nanostructure that exhibits high ion permeability.[19,20]

Furthermore, the electrocatalytic selectivity of the Au|ENFs-**1**-Nf CME primarily arises from the diverse properties of the hard and soft donor atoms present in the respective components of the ENFs-**1**-Nf thin film. These donor atoms enable the selective detection of Pb(II) in the presence of other heavy and 3*d*-base metal cations. Recovery studies and a comparison with ICP-OES studies were conducted to evaluate the quantitative performance of the developed CME.

5.2. Experimental

5.2.1. Formation of the PANI-CoPc-flav composite and the PANI-CoPc-flav-f-MWCNTs (1) nanoconjugate

The formation of PANI was conducted following a previously reported method.[21] Subsequently, CoPc-flav (0.1103 g, 0.0728 mmol) was added to a 50 mL aqueous solution of 1.0 M HCl and PANI, and then the mixture was stirred for 1 h to ensure uniform dispersion of the CoPc-flav. The resulting solution was left standing overnight to allow the PANI-CoPc-flav to settle. The PANI-CoPc-flav was collected by filtration and afterwards dried in a vacuum oven at 80 °C to obtain a dark green composite.

To further enhance the electrochemical properties of the composite, functionalized multi-walled carbon nanotubes (*f*-MWCNTs) were incorporated. More specifically, a mass of 0.2103 g of *f*-MWCNTs was added to a mixture containing 0.5002 g of PANI-CoPc-flav in 3 mL of *N, N′*-dimethylformamide (DMF). The mixture was subjected to sonication for 3 h to form the PANI-CoPc-flav-*f*-MWCNTs composite with uniformly dispersed *f*-MWCNTs within the PANI-CoPc-flav matrice.

5.2.2. Fabrication of PVA-based ENFs

The fabrication of PVA-based ENFs was done following the method reported in **Chapter 2.**

5.2.3. Fabrication of the Au|ENFs-1-Nf CME

The bare gold electrode (Au|, 1.5 mm radial disk) was initially cleaned using a hot solution of hydrogen peroxide and sulfuric acid (Piranha solution) in a 1:3 volume to volume ratio at 120 ^{o}C to ensure firm adhesion of the modifier film onto the bare Au| electrode. It was also thoroughly polished with aqueous alumina slurries, followed by sonication in DMF and ethanol. The electrode was then rinsed with ultra-pure water to remove any alumina residue. Next, a 10 mg mass of ENFs-**1** was dispersed in 2 mL of DMF through sonication for 1 h to obtain a well-dispersed suspension. The suspension was thereafter drop-casted onto the surface of the polished Au| electrode and dried in the oven (40 °C) for 24 h. A 20 µL solution of 0.05 (*w/v*)% Nafion (Nf) was thereafter loaded onto the pre-dried Au|-ENFs-1 CME and dried under a stream of nitrogen at room temperature, to the fabricated CME (Au|-ENFs-**1**-Nf).

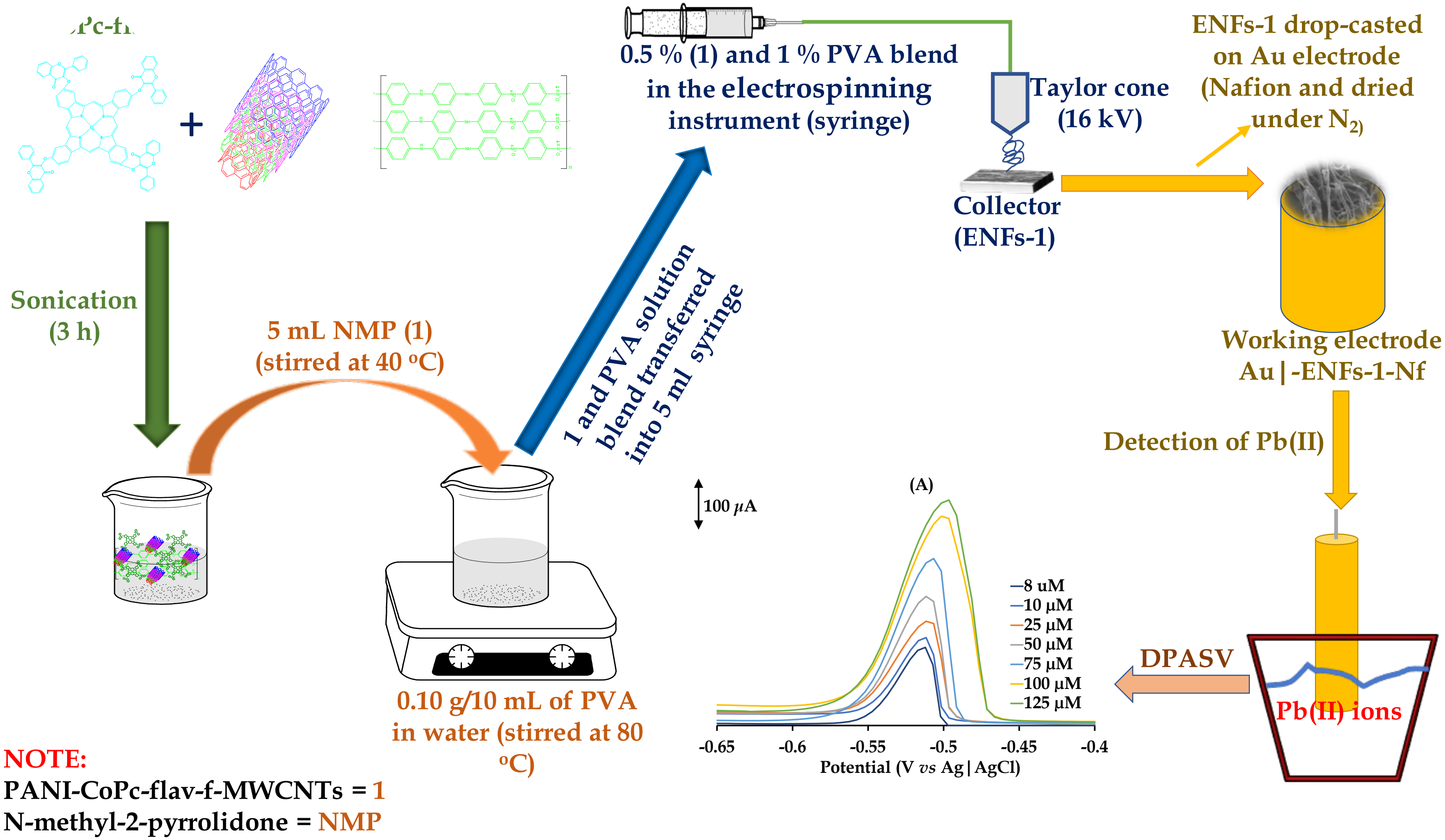

Scheme 5.1: *Sequential fabrication method of the Au|ENFs-**1**-Nf CME including the current responses for the differential pulse anodic stripping voltammetric (DPASV) analysis of a series of dilute Pb(II) ions standards.*

]]>

5.3. Results and discussion

5.3.1. *Synthesis, nanofabrication and characterization*

As per the experimental procedure reported by Chohan *et al.* (2015),[22] the cyclotetramerization of 4-(flavone-3-oxy)phthalonitrile onto the Co(II) ion was performed in the presence of a mild base, 1,8-diazabicyclo[5.4.0]undec-7-ene (DBU) at elevated temperature under a nitrogen atmosphere, see **Figure 5.1.** The structural elucidation of CoPc-flav was corroborated by mass spectrometry and the data agreed with that was previously published. To synthesize the emeraldine salt of PANI, aniline was oxidized using ammonium persulfate, followed by ionization of the aniline groups with hydrochloric acid (HCl).[23] The resulting PANI emeraldine salt was then combined with the CoPc-flav complex by overnight stirring.

To improve the dispersion and compatibility of the components, the resulting composite was sonicated in the presence of functionalized multi-walled carbon nanotubes (*f*-MWCNTs), leading to the formation of PANI-CoPc-flav-*f*-MWCNTs (**1**) nanoconjugate. Furthermore, to facilitate the dissolution and homogeneity of the molecular components, the nanoconjugate was dispersed in *N*-methyl-2-pyrrolidone (NMP). This homogeneous suspension was then added to a polyvinyl alcohol (PVA) emulsion, resulting in a viscous polymer blend. Afterwards, the bulk polymeric blend was subjected to electrospinning to render the electrospun nanofibers, ENFs-**1** of variable texture.

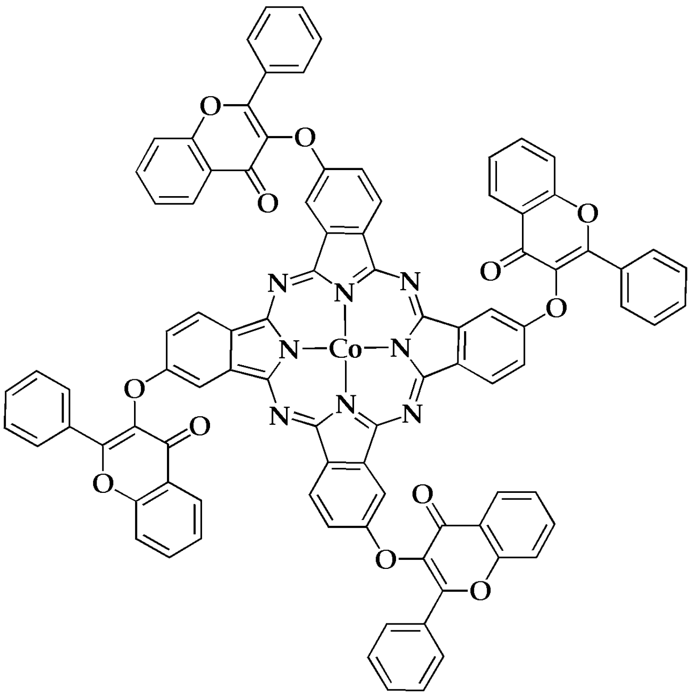

Figure 5.1: *The structure of the CoPc-flav.*

Overlapping absorbance bands observed in the electronic spectra of CoPc-flav and PANI observed (*see* **Figure 5.2**) within the range of 200-400 nm are associated with π-π* electronic transitions within the PANI backbone and the Soret (B)-band of the phthalocyanine (Pc) ring, respectively.[24] With respect to the CoPc chemical component, its electronic transitions are induced from the promotion of electrons from the highest occupied molecular orbitals (HOMOs) to the lowest unoccupied molecular orbital (LUMO) of the phthalocyanine chromophore.[24,25] For PANI, the absorbance band at 466 nm is responsible for its characteristic green colour corresponding to emeraldine base (EB) and this arises from intra-charge transfer between the negative nitrogen atom sites and the positive $(C_6H_5NH_2^+)_n$ sites on the polymer.[26]

For the PANI-CoPc-flav composite, its electronic spectrum shows comparable broad absorption bands in the 200-500 nm region due to the additive effects of the electronic transitions of the PANI aromatic chains and the *B*-bands of the conjugated Pc. Additionally, the composite exhibits a continuum band above 600 nm, resulting from the sum of the absorbances of the protonated PANI (*viz.* a charge transfer band of quinoid) and the *Q*-band of the incorporated CoPc-flav constituent. The presence of mutual bands due to the individual components confirms the hybrid nature of the PANI-CoPc-flav composite blend.[27,28]

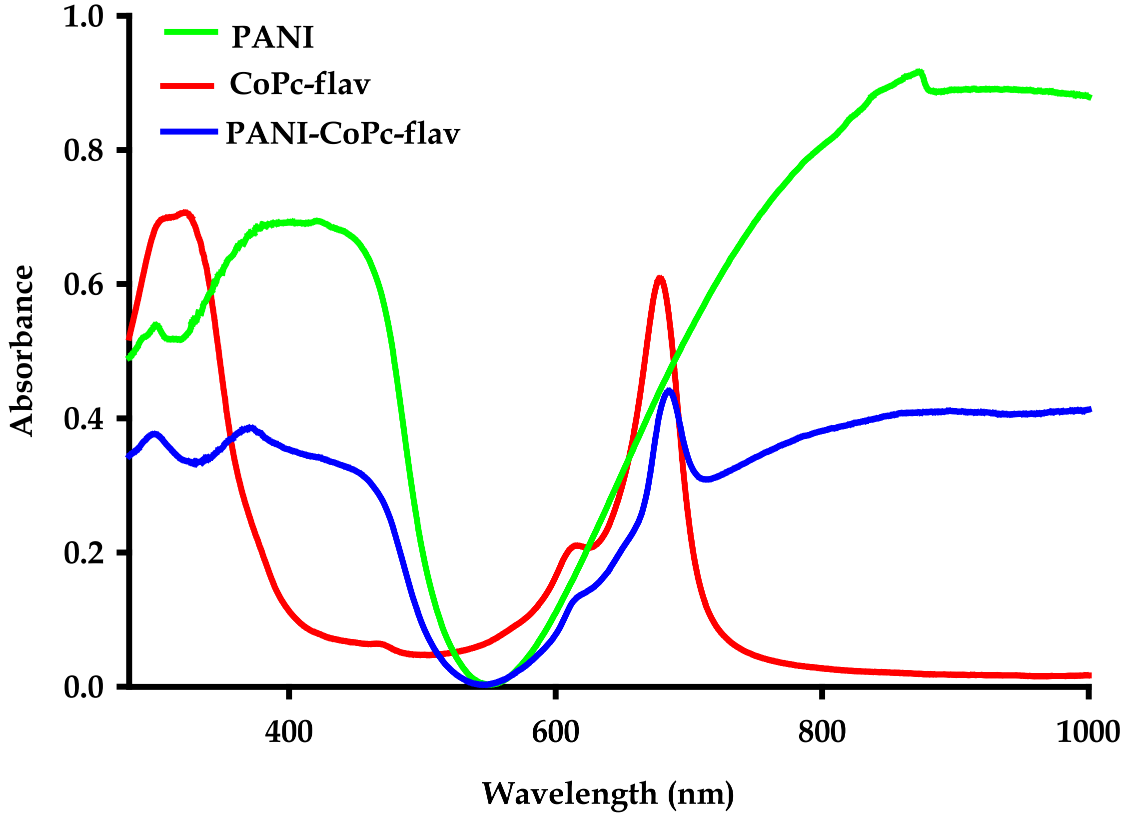

Figure 5.2: *Overlayed UV-Visible absorption spectra of PANI, CoPc-flav and PANI-CoPc-flav nanocomposite.*

The retention of the PANI structure in the PANI-CoPc-flav composite is evident from the vibrational bands assigned to the functional groups of emeraldine (EM), including the overlapping ν(N-H) stretching vibrations at 3531 cm^{-1}, the ν(N-H) stretching vibrations of protonated aniline (-NH_2^+) groups at 2682 and 2343 cm^{-1}, see **Figure 5.3**.[29-31] In addition, the ν(C=N) signals of the quinoid (Q) and benzenoid (B) rings vibrates at 1585 and 1480 cm^{-1}, respectively. In the Fourier-transform infrared (FTIR) spectrum of the PANI-CoPc-flav, the characteristic vibration bands (*i.e.* fingerprint region 1500 to 1600 cm^{-1}) of the CoPc are overshadowed by those of PANI due to its composite nature.

In the FTIR spectra of the PANI-CoPc-flav-*f*-MWCNTs (**1**) and **1**-ENFs, the vibrational bands at 1097, 1252, 1410, 1647 and 2912 cm^{-1} are attributed to the *ν*(C–O), *ν*(C–H), *ν*(O-H), *ν*(C=O) and *ν*(C–H) signals while the N-H and O-H bonds vibrates between 3235 and 3402 cm^{-1}. In the solid-state infrared spectrum of **1**-ENFs, the PANI-related *ν*(N-H) and the PVA-associated *ν*(O–H) signals vibrate broadly centred at 3235 cm^{-1}. This signal occurs at a lower frequency (3223 cm^{-1}) than the analogous signal found in the FTIR spectrum of the PANI-CoPc-flav-*f*-MWCNTs (**1**) (3402 cm^{-1}) which could be ascribed to the encapsulation effect of the PVA shell surrounding the inner core containing **1**.

Other distinctive characteristic infrared stretches include PANI's aromatic and aliphatic C-H which vibrates in the vicinity of 2910 cm^{-1} for the carbon nanotube conjugate **1** and its ENFs derivative, ENFs-**1** which in turns provide additional evidence that **1** were incorporated into nano-scale diameter of ENFs-**1**. The sharp C=O vibrational band of the *f*-MWCNTs' carboxylic acid groups in the FTIR spectrum of **1** can be accounted to its well-dispersity within this nanocomposite. However, in the FTIR spectrum of ENFs-**1**, the *ν*(C=O) signal is broader and weaker due to the encapsulation of **1** by PVA; leading to the dominance of the *ν*(C=O) signal associated with PVA acetate groups.[32,33]

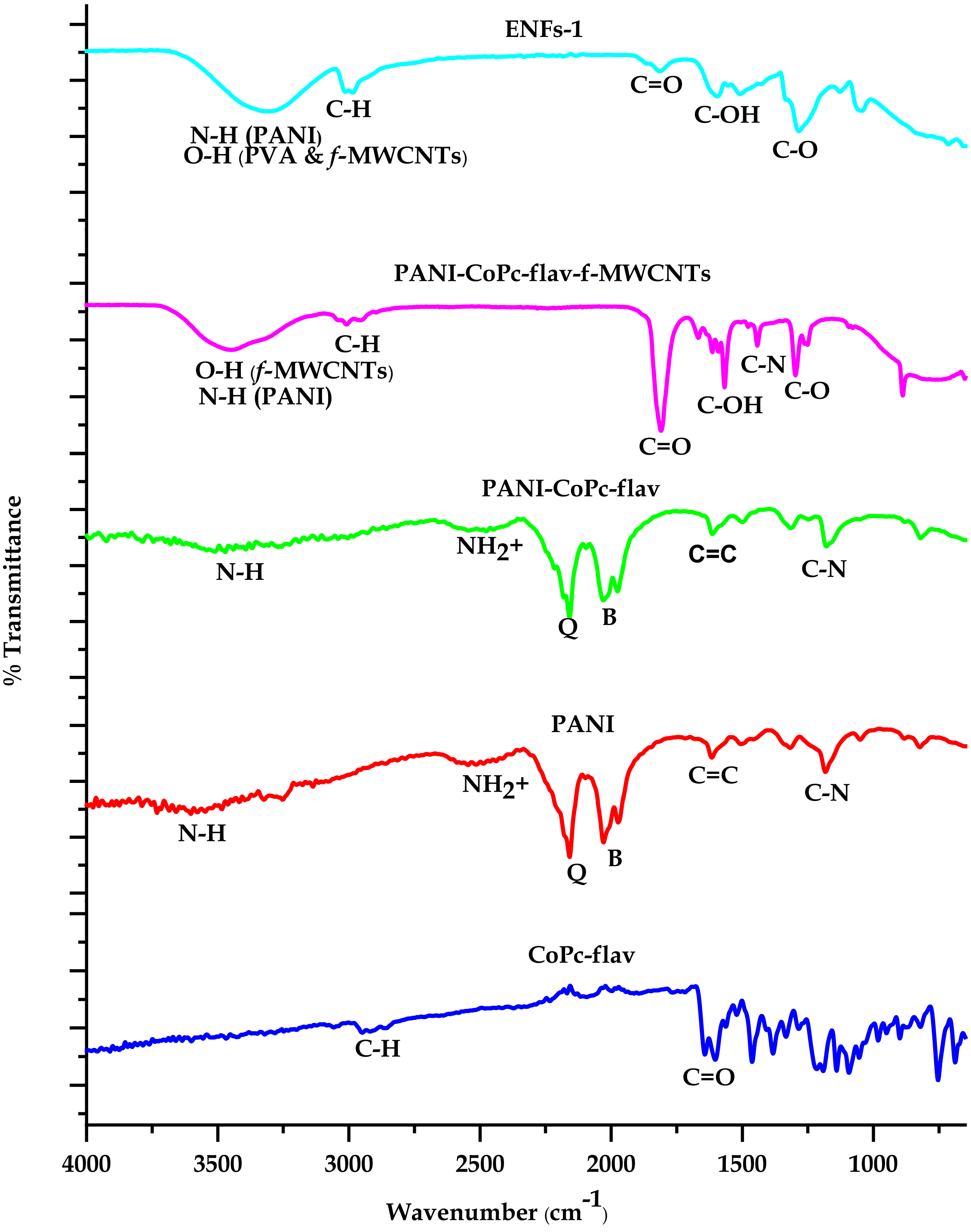

Figure 5.3: *Stacked FTIR spectra of CoPc-flav, 4-(flavone-3-oxy)phthalonitrile, PANI, PANI-CoPc-flav (Q = quinoid, B = benzenoid), PANI-CoPc-flav-f-MWCNTs (**1**) and ENFs-**1**.*

Raman spectral analysis largely concur with the FTIR spectral assignments while distinctive stretching modes of the *f*-MWCNTs were present in the nanoconjugate **1**. In the Raman spectrum of CoPc-flav, characteristic absorption peaks of the Pc are observed, see **Figure 5.4**. The B_1g vibration band at 685 cm^{-1} corresponds to the asymmetric stretching mode of the pyrrole rings within the Pc macrocyclic, while the vibrational band (of B_1g symmetry) at 1545 cm^{-1} is typical of the in-plane bending and displacement modes of the nitrogen-carbon (C=N-C) bridging bonds within the Pc ring.[34] Mutually, the respective Raman spectra of PANI and PANI-CoPc-flav exhibit vibrational peaks related to the backbone stretching modes of PANI only differing in peak intensities.[24,35] In particular, the solid-state Raman spectrum of PANI displays a peak at approximately 1591 cm^{-1}, corresponding to the C=C breathing mode of the phenyl rings and ν(C=N) stretching mode of protonated aniline monomers within the polymer.[36]

Comparative analysis between the Raman spectra of CoPc-flav and its composite, PANI-CoPc-flav, shows that the former's vibrational peak at 1591 are slightly shifted to 1596 cm^{-1} for the composite, PANI-CoPc-flav. The distinct stretching band appearing at 1545 cm^{-1} in the Raman spectrum of CoPc-flav is masked by the intense PANI-related vibrations occurring in the region between 1500 – 1600 cm^{-1} within the Raman spectrum of the PANI-CoPc-flav composite. Additional peaks in the Raman spectrum of PANI-CoPc-flav include those at 1259 cm^{-1} and 1255 cm^{-1}, corresponding to the stretching of the C-N bonds in the polymer backbone. The C-H bending mode is observed around 1168 cm^{-1} and 1176 cm^{-1}, reflecting the in-plane deformation of the C-H bonds. Characteristically, the ν(C=N) stretching band appears around 1334 cm^{-1}, indicating the presence of the emeraldine base salt of PANI.[36,37]

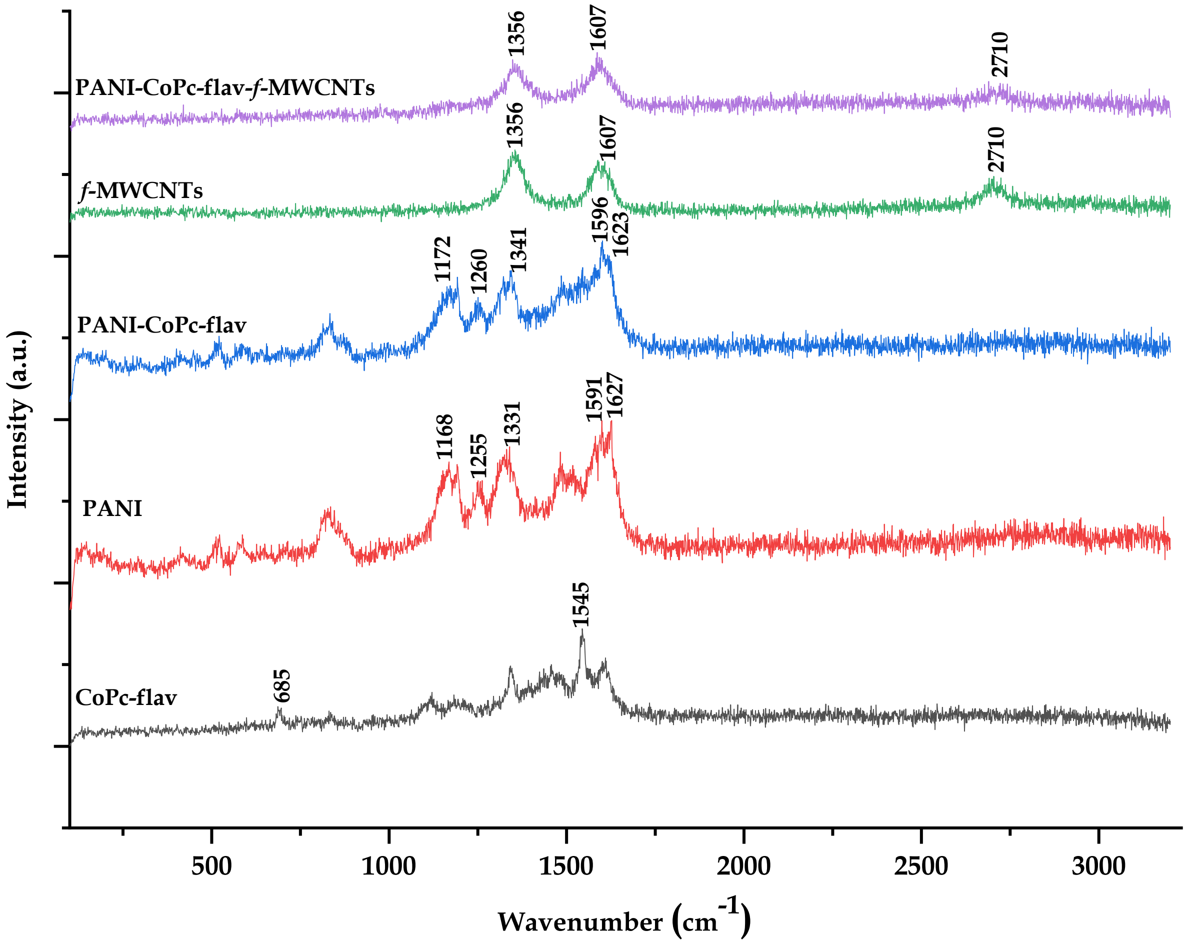

Figure 5.4: *Stacked Raman spectra of CoPc-flav, PANI, PANI-CoPc-flav, f-MWCNTs and PANI-CoPc-flav-f-MWCNTs (**1**) nanocomposite.*

The Raman spectra of PANI-CoPc-flav, *f*-MWCNTs and PANI-CoPc-flav-*f*-MWCNTs (**1**) provide insights into their structural functional groups of the nanomaterials. The spectra of both *f*-MWCNTs and PANI-CoPc-flav-*f*-MWCNTs feature intense peaks around 1605 cm^{-1} and 2710 cm^{-1} (ascribed to the *G*- and *G′*-bands, respectively) while the *D*-band resonate around 1350 cm^{-1}. The *D*-band represents the vibrational mode associated with defects or disorder in the carbon lattice, while the *G*- and *G′*-bands correspond to the vibrational mode of *sp*^{2}-bonded carbon atoms within the graphene plane.[38]

The intensity ratio of the *D*-band to the *G*-band, (I_D/I_G), provides information about the fractional density of graphic lattice and hence defects or disorders in the nanomaterials. The I_D/I_G ratio for the *f*-MWCNTs was found to be 1.18, indicating a relatively higher density of defects. However, for the PANI-CoPc-flav-*f*-MWCNTs, the I_D/I_G ratio decreases to 0.95.[39] The lowering of the I_D/I_G ratio after doping of the *f*-MWCNTs with PANI-CoPc-flav; suggest that clear molecular interactions between the two materials where complementary stabilization interactions occur *via* intermolecular pi-stacking and complementary hydrogen-bonding.[39] It is worth noting that the peaks associated with PANI-CoPc-flav are not observed in the PANI-CoPc-flav-*f*-MWCNTs (**1**) nanocomposite which is tentatively ascribed to the dominance of the MWCNTs' inherent photon-absorption properties.

The XRD pattern of CoPc-flav shown in **Figure 5.5** reveals broad peaks at 2θ angles of 7.29° and 19.71°, corresponding to the (100) and (104) planes of CoPc, respectively.[40,41] PANI exhibits a sharp peak centred at 2θ angle of 25.5°, along with two low-intensity broad peaks at approximately 20.9° and 14.8°, corresponding to the (200), (020) and (011) semi-crystalline planes of the emeraldine salt (ES) form of PANI.[42,43] The XRD of the PANI-CoPc-flav nanocomposite illustrate common peaks to those observed in the XRDs of pure PANI and CoPc-flav. In particular, the PANI-derived intense peak at 2θ angle of 7.29° in the XRD of the composite, indicates the successful integration of PANI and CoPc-flav in the nanoconjugate.[40] The XRD pattern of *f*-MWCNTs shows characteristic peaks at 2θ angles of 25.65°, 43.44°, and 53.25°, corresponding to the (002), (100), and (004) planes of graphite, respectively.

These peaks are consistent with the crystalline structure of *f*-MWCNTs reported in previous studies.[44,45] The XRD pattern of the PANI-CoPc-flav-*f*-MWCNTS (**1**) nanoconjugate exhibits similar peaks to *f*-MWCNTs, but with reduced intensities, thereby conversely confirming the presence of PANI and CoPc-flav in the composite. In the diffractogram of ENFs-**1**, a broad peak is observed at a 2θ angle of approximately 19.53°, corresponding to the (011) plane. The broadness of this peak indicates the amorphous nature of ENFs-**1** which is implies that the nanohybrids of **1** has irregular orientations in the nanofibers, ENFs-**1**.[46] In addition, the absence of peaks related to the PANI-CoPc-flav-*f*-MWCNTs nanocomposite suggest that the latter has been predominately concealed by a PVA outer layer in **1**.

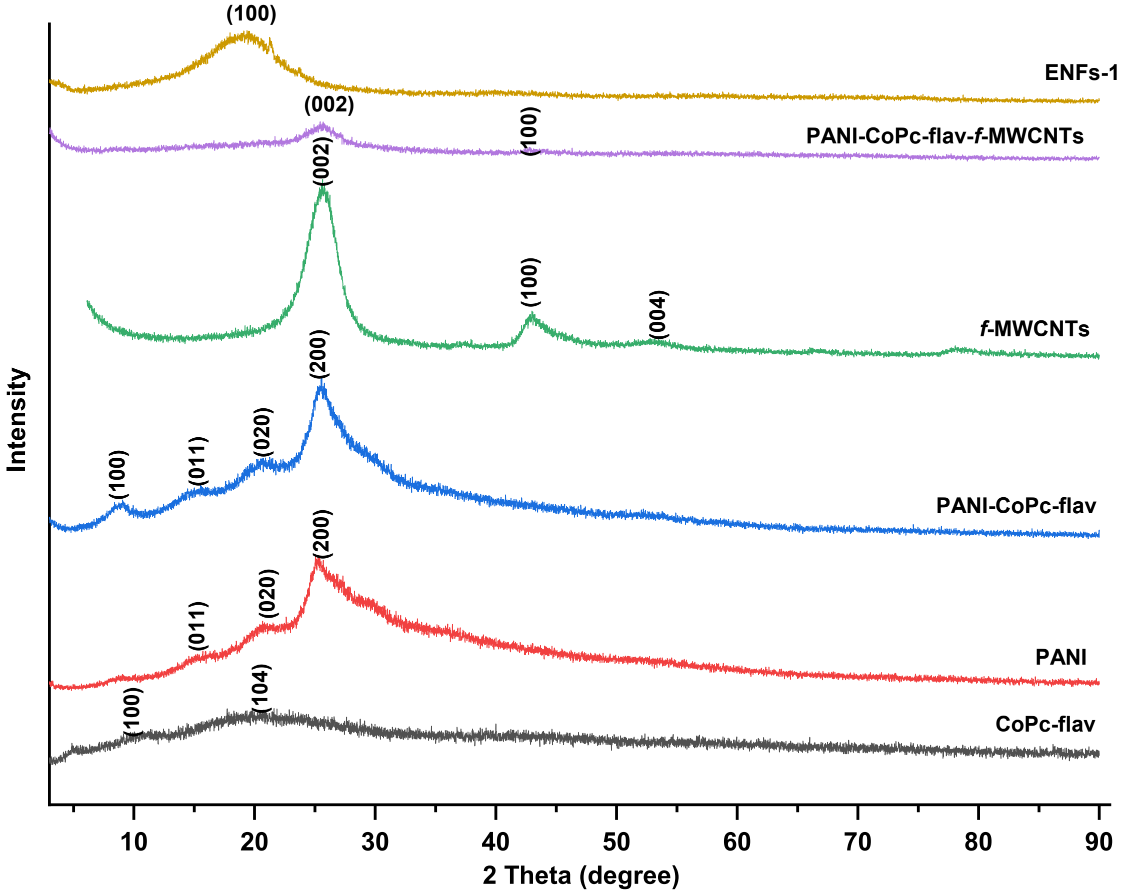

Figure 5.5: *Stacked X-ray diffractograms of CoPc-flav, PANI, PANI-CoPc-flav, f-MWCNTs, PANI-CoPc-flav-f-MWCNTs nanocomposite and ENFs-***1**.

Scanning electron microscopy (SEM) in conjunction with energy dispersive X-ray (EDX) analysis were performed to probe morphological features and elemental composition of the N_4-metallocyclic complex, CoPc-flav and its composite material. The micrograph of CoPc-flav shows homogeneously dispersed and spherically-shaped particles which are clumped to producing non-uniform and larger aggregates, see **Figure 5.6A**.[47] Since both the micrographs of CoPc-flav and PANI-CoPc-flav illustrate large aggregates with relatively rough surface areas, the non-distinguishment between these micrographs suggest that the majority of the CoPc-flav aggregates have been imbedded within the bulk PANI polymer matrix, see **Figures 5.6B** and **C**. The interlinked networks of PANI and CoPc clusters promote particle aggregation, facilitating swift charge hopping and enhanced electrical conduction within the rough crystallites.[48,49]

The incorporation of *f*-MWCNTs in the PANI-CoPc-flav composite alters its microstructure, as observed in the SEM micrographs of the PANI-CoPc-flav-*f*-MWCNTs nanoconjugate presented in **Figure 5.6D**. More specifically, the micrograph displays uniform woven fibre-mats wherein the PANI-CoPc-flav is dispersed over the surface of the *f*-MWCNTs surface, creating a three-dimensional microstructure with a higher surface area. This increases the number of accessible active sites and thus enhances the electrochemical interactions when the material is used as an electron-mediating film.[50]

The ENFs produced in the absence of *f*-MWCNTs had smooth and uniform surface morphology, as shown in **Figure 5.6E**. However, those ENFs (*viz*. ENFs-**1**) containing *f*-MWCNTs were extruded as uniform woven mats wherein the PANI-CoPc-flav nanoconjugates are beaded on the surface of the *f*-MWCNTs due to the bigger projection diameter of the latter. Additionally, the fibres exhibited non-uniform diameters and different surface roughness, as visualized in **Figure 5.6F.**

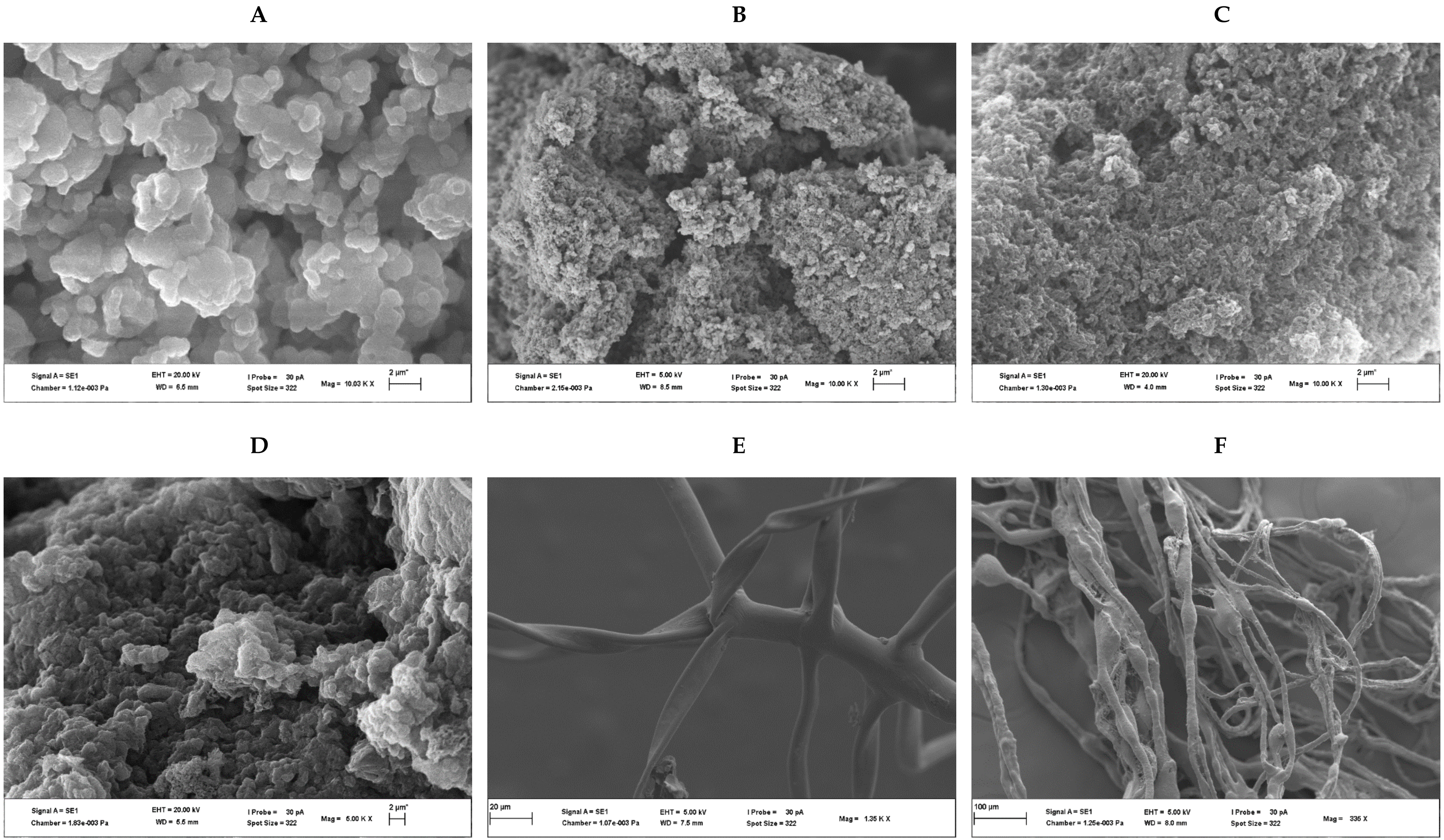

Figure 5.6: *SEM micrographs of (**A**) CoPc-flav, (**B**) PANI, (**C**) PANI-CoPc-flav, (**D**) PANI-CoPc-flav-f-MWCNTs (**1**), (**E**) ENFs-CoPc-PANI excluding f-MWCNTs and (**F**) ENFs-**1** (i.e. ENFs with embedded f-MWCNTs showing beaded woven-mats ENFs-**1**).*

Figure 5.7 presents the EDX spectra of synthesized ENFs and ENFs-**1**. In **Figure 5.7A**, the EDX analysis of ENFs confirmed the presence of carbon, chlorine, nitrogen, and oxygen atoms, characteristic of PANI, PVA, and HCl (employed as an acidic medium for PANI synthesis). In **Figure 5.7B**, EDX analysis of ENFs-**1** also confirmed the presence of carbon, chlorine, nitrogen, cobalt, and oxygen atoms, characteristic of PVA, PANI, HCl, and CoPc-flav embedded within the ENFs. This substantiates the formation of ENFs-1 and the acid doping of PANI.

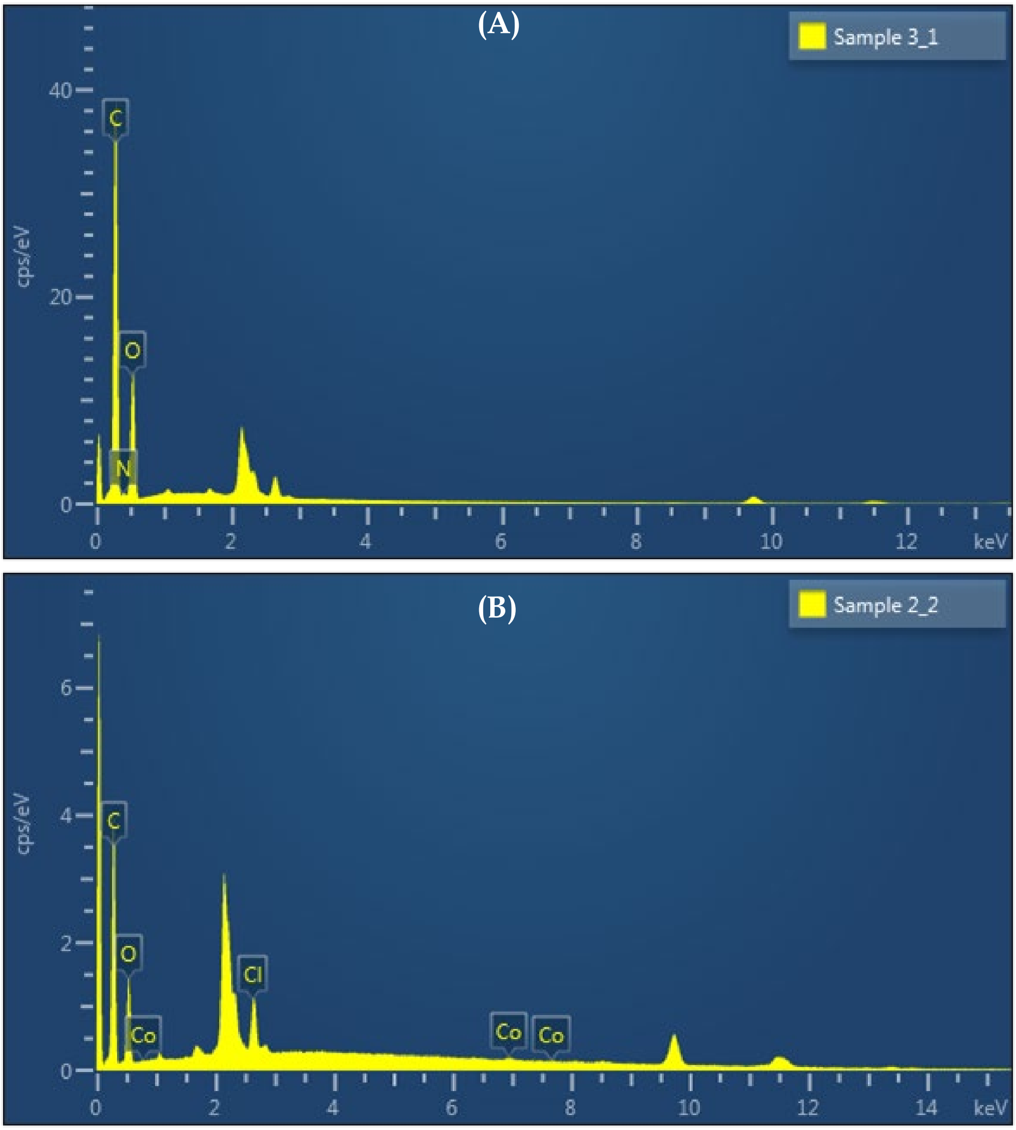

*Figure 5.7: EDX micrographs of (A) ENFs and (B) ENFs-**1**.*

5.3.2. Comparative electron-transfer rates between the bare and respective CMEs

Cyclic voltammetry (CV) responses of 5 mM $[Fe(CN)_6]^{3-/4-}$ in 0.1 M KCl at various modified and bare electrode interfaces were recorded. All electrodes, but the Nafion-modified (Au|Nf) gave discernible current responses due to the Fe^{2+}/Fe^{3+} redox interconversion, *see* **Figure 5.8**. The bare gold (bare Au|) electrode recorded the least of the current signals when compared to the other investigated electrodes. Its response counter-intuitively contrasted the response of the Nafion gold-modified electrode (Au|-Nf) whose signal was undiscernible, indicating that the Nafion film hinders charge transfer at the electrode interface. This suggests that Nafion served mainly as a polymeric binder for improving the stability of the modified electrode but does not play a catalytic role in the electron transfer process.

On the other hand, the |Au-PANI electrode exhibited low current waves, showing sluggish electron transfer kinetics characterized by high background currents. Given that PANI is a strong electro-conductive polymer, the observed low waves and high background currents of its electrode film are more likely due to the low affinity of the nitrogen atoms of the polymer towards the analyte, which results in poor adhesion. Additionally, this is attributed to the thick PANI film on the electrode surface, which resulted from drop-drying PANI onto the GCE surface rather than electropolymerization. The increased PANI film thickness likely blocked electron transfer between the solution and the electrode, leading to a lack of clear peaks in the cyclic voltammogram. Furthermore, the current responses at the Au|-*f*-MWCNTs, or Au|ENFs-**1**-Nf electrodes were higher than that of the bare Au|, however, to different extents, see the zoomed inset in **Figure 5.8B.**

The response of the Au|CoPc-flav electrode was the least while Au|-*f*-MWCNTs had the highest electrocatalytic activity. This can be rationalized by the oxygen atoms of the CoPc-flav bridging ethers form strong Au-O bonds, and this coupled with the electrocatalytic nature of the CoPc-flav resulted in a slight increase in the current response. The superior conductivity of the *f*-MWCNTs accounts for the observed higher redox currents occurring at the interface the Au|-*f*-MWCNTs electrode.

The response currents of the Au|ENFs-**1**-Nf were intermediate which demonstrates the electrocatalytic and mediating roles of ternary nanoconjugate (ENFs-**1**-Nf) where the Nafion-film causes the depression on the current signal. Noteworthy is that the coating of Nf onto the ENFs-**1** **CME** created a stable top layer for the underneath PANI-CoPc-flav-*f*-MWCNTs nanoconjugate film. Thus, coating Nf onto the ENFs-**1**-film improved the film stability and adherence of the Au|ENFs-**1**-Nf electrode by forming a layer-by-layer nanoconjugate film with enhanced electrochemical charge transfer rate. The aforementioned resulted in superior electrochemical responses towards the $Fe^{3+}|Fe^{2+}$ redox couple compared to the electrodes modified with a single component of the nanoconjugates.

These observations led to the hypothesis that the Au|ENFs-**1**-Nf electrode may have similar electrocatalytic detection capabilities towards some heavy metal ions. Overall, the Au|ENFs-**1**-Nf electrode was the most effective and stable electrochemical sensor for Fe^{3+}/Fe^{2+} standard redox probe. It exhibited good film stability, enhanced electron transfer rates and high sensitivity compared to other modified gold electrodes. Studies to validate the potential of the electrode for the detection and quantitative analysis of Pb(II) ions in real and spiked water samples were conducted as shall be discussed ahead.

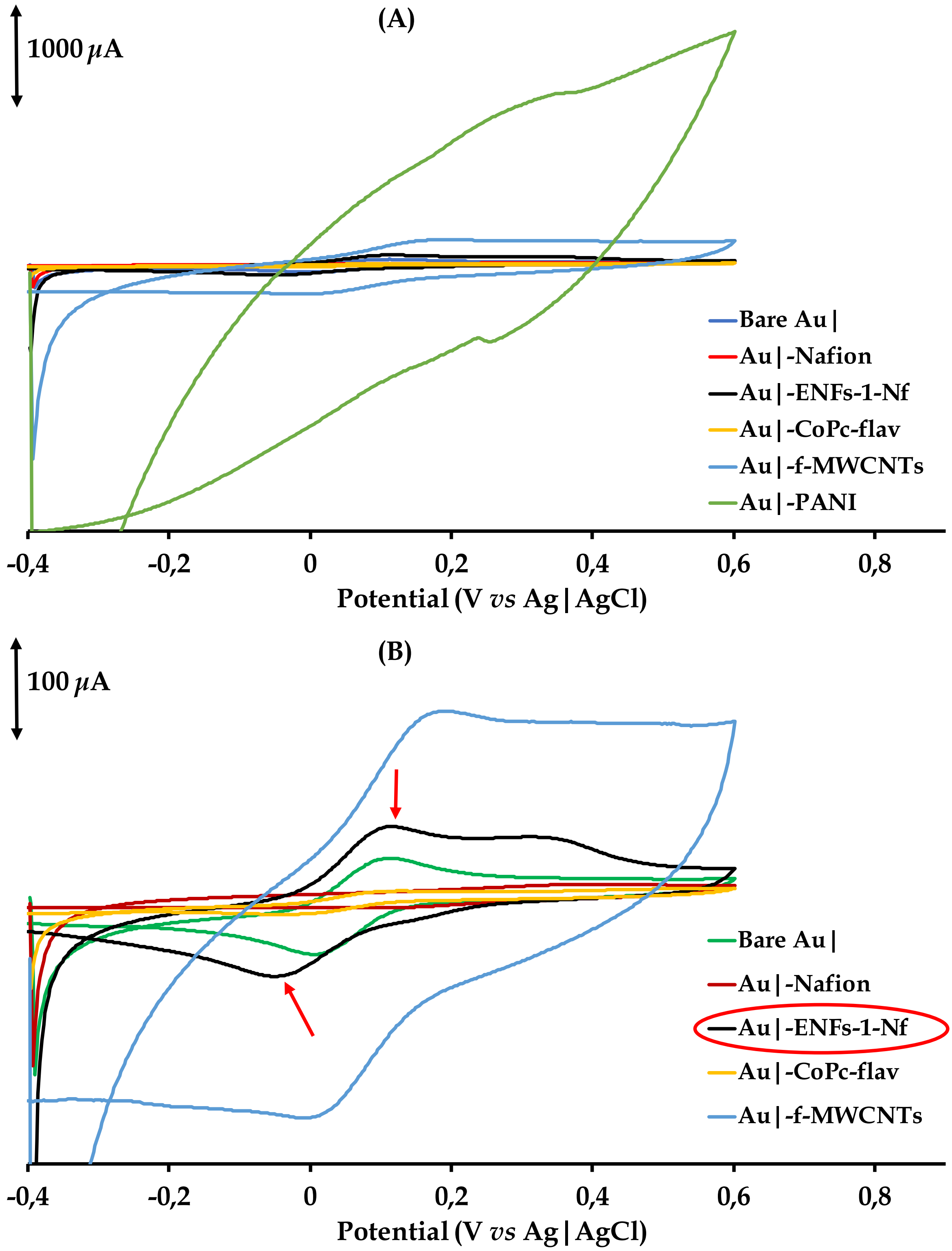

Figure 5.8: *(****A****)Cyclic voltammograms of 5 mM $K_3[Fe(CN)_6]$ in 0.1 M KCl. (****B****) Zoomed-in plot of all electrodes except Au|-PANI.*

5.4. Electrocatalytic detection of Pb(II) ions by the Au|ENFs-1-Nf

5.4.1. Differential pulse anodic stripping voltammetry (DPV)

The capabilities of the bare electrode and the various CMEs were explored to detect Pb(II) ions using a 3.0 mM Pb(II) standard solution buffered at pH 5 (acetic/sodium acetate) using differential pulse anodic stripping voltammetry (DPASV),. The DPASV response of the Au| electrode exhibited the weakest signal for Pb(II) at -0.557 V, with additional neighbouring peaks within the -0.1 to -0.55 V range, see **Figure 5.9**. These peaks are due to the reduction of electrolyte species. This indicates that the Au|electrode lacks selectivity for Pb(II) since it detected other analytes which have similar redox potentials as that of Pb(II) ions

The presence of the Nafion (an ion-exchanger) polymeric film improved the current response slightly as well as shifted the potential to -0.532 V compared to the peak potential attained using the bare Au electrode. However, the oxidation of matrix species is still evident and the interfering peak intensities are reduced. Both the Au|-CoPc-flav and Au|-*f*-MWCNTs electrodes exhibited the highest current signals for Pb(II), but they were accompanied by two other peaks in the range -0.1 to -0.55 V, indicating poor selectivity towards Pb(II) ions.

These additional peaks are also observed for the Au|-PANI electrode in addition to a broad intense peak spanning the range, -0.1 V to 0.8 V and are attributed to redox reactions of the electrolyte species, refer to **Figure 5.9B**. This high background current peak is also observed in the DPASV response of the Au|ENFs-**1**-Nf electrode, where PANI is a component of the composite film though to a lesser extent. In contrast, the Au|ENFs-**1**-Nf electrode gave a well-defined peak for Pb(II) ions at -0.506 V with no additional peaks at higher oxidation potentials, as observed for the other five CMEs. This suggests that the ENFs-**1**-Nf film not only electrocatalyzes the detection of Pb(II) but also exhibits high specificity, experiencing minimal analyte solution matrix effects within the narrow potential window of -0.55 V to -0.1 V. The low background current is accounted for by the high stability of the ENFs-**1**-Nf film in which the active electrocatalysts are embedded. This demonstrates the advantage of electrode modification using ENFs where electrocatalysts of varying physical properties are agglomerated into one nanocomposite since the Au|ENFs-**1**-Nf electrode showed superior performance and selectivity for the detection of Pb(II) ions. In addition, these ENFs have intrinsically higher electrocatalytic surface areas than the individual materials as well as the composite, PANI-CoPc-flav and the nanocomposite, PANI-CoPc-flav-*f*-MWCNTs.

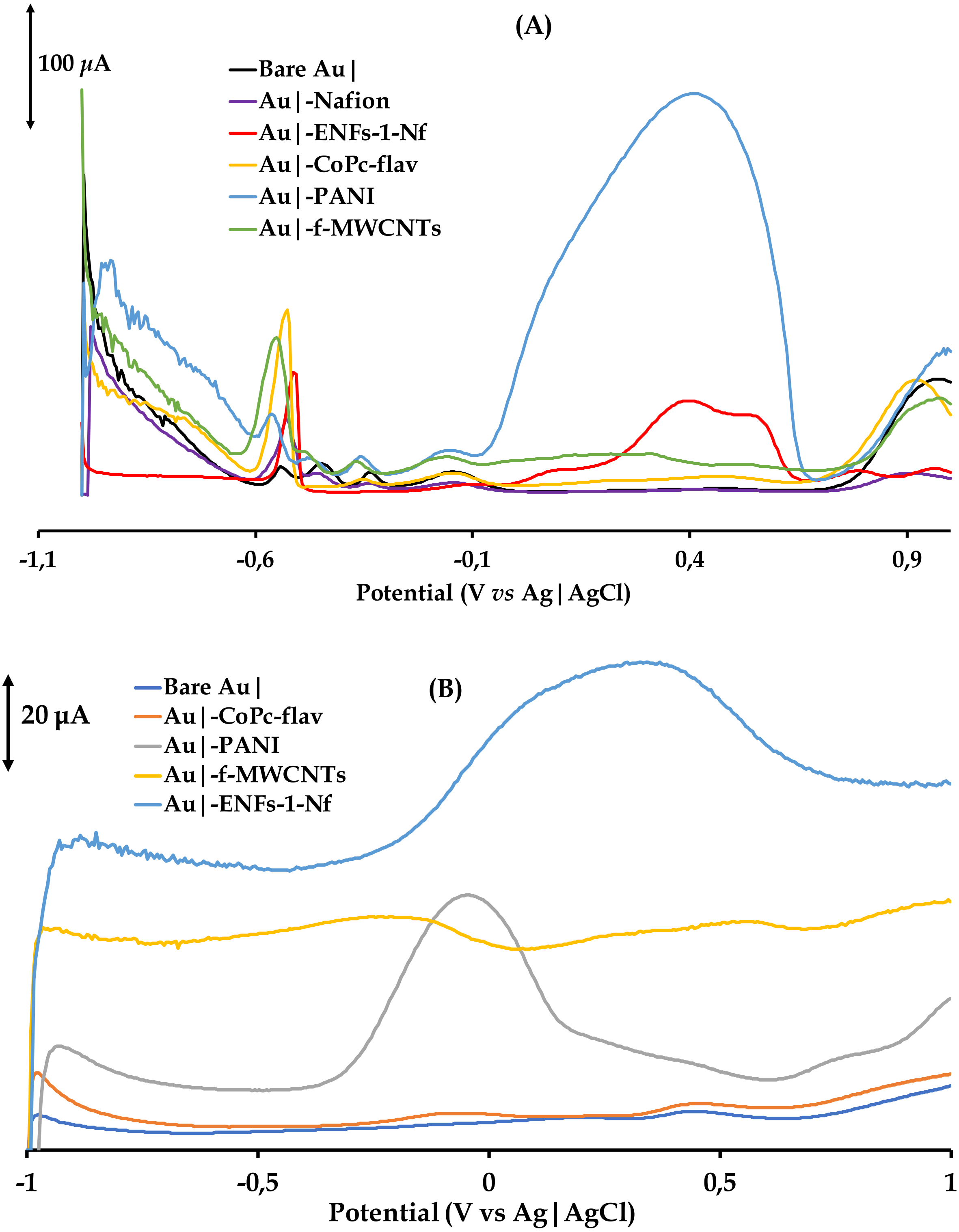

Figure 5.9*: (A)DPASVs responses of 3 mM Pb(II) in 0.1 M sodium-acetate buffer (pH 5.0) obtained using the |Au, |Au-Nf, |Au-CoPc-flav, |Au-PANI, |Au-f-MWCNTs) and |Au-ENFs-**1**-Nf electrodes. **(B)** responses of each electrode in the electrolyte/buffer solution (no analyte).*

5.4.2. *Signal stability of the modified electrodes*

Signal stabilities of the CMEs were assessed in the analyte solution over consecutive DPV scans, **see Figure 5.10**. The Au|-CoPc-flav and Au|-*f*-MWCNTs electrodes showed current responses towards Pb(II) in the respective first scans, which disappeared in subsequent scans. This indicated that the modifying layers of CoPc-flav and *f*-MWCNTs were susceptible to fouling by adsorbed Pb, which leads to saturation of electrocatalytic sites that causes loss of sensitivity for Pb(II) detection. Therefore, these CMEs were not suitable for stable and reliable Pb(II) sensing due to surface fouling of the CME interface; leading to deactivation of the respective thin films.

The Au|-PANI electrode recorded a stable and background free current response around the vicinity of the redox peak for Pb(II) . However, there was an intense broad, low background peak within the higher potential range, making it less reliable for accurate sensing and quantitative analysis of Pb(II) ions. The presence of interferences might hinder the clear and specific detection of Pb(II) at this electrode, reducing its selectivity and sensitivity.

In contrast, Au|ENFs-**1**-Nf electrode render a well-defined and stable response for Pb(II) ions with no significant background interferences in the vicinity of the analyte peak or at a higher potential range. The experimental results demonstrated that the adsorbed ENFs for this electrode interlinked to and intertwined with the permeable Nf polymeric film thereby providing a hybrid nanoconjugate with better electrochemical sensing abilities. The absence of significant background interferences and the more stable response towards Pb(II) ions confirmed the superior performance and reliability of this CME. The functionalities of the fabricated ENFs-**1**-Nf film are analogous to that of metal organic frameworks (MOFs) in that it forms intricate channels similar to that of the latter. Therefore, it be deduced that the amorphous ENFs-**1**-Nf nanohybrid film can selectively trap analytes of appropriate size similar to the primary mechanism of electrocatalytic activity for MOF-modified electrodes containing crystalline cavities.[51] Furthermore, the exposing functional groups within their channels plays an integral role in promoting the selective uptake of a specific analyte.

The Au|ENFs-**1**-Nf electrode is resistance to poisoning and maintain a stable as well as specific response towards Pb(II) ions and this sets it apart from the other unitary modifying nanomaterials such as CoPc-flav, *f*-MWCNTs, and PANI which experienced limited film stability and sensitivity. As shown in **Figure 5.10C,** the electrode exhibited good precision (%RSD = 1.71%, N = 5) towards sensing Pb(II) ions. These attributes made the Au|ENFs-**1**-Nf electrode the most suitable candidate electrode for accurate and reliable electrochemical sensing of Pb(II) ions in complex sample matrices. Thus, its applicability for environmental monitoring and trace analysis of heavy metal pollutants is foreseen as feasible.

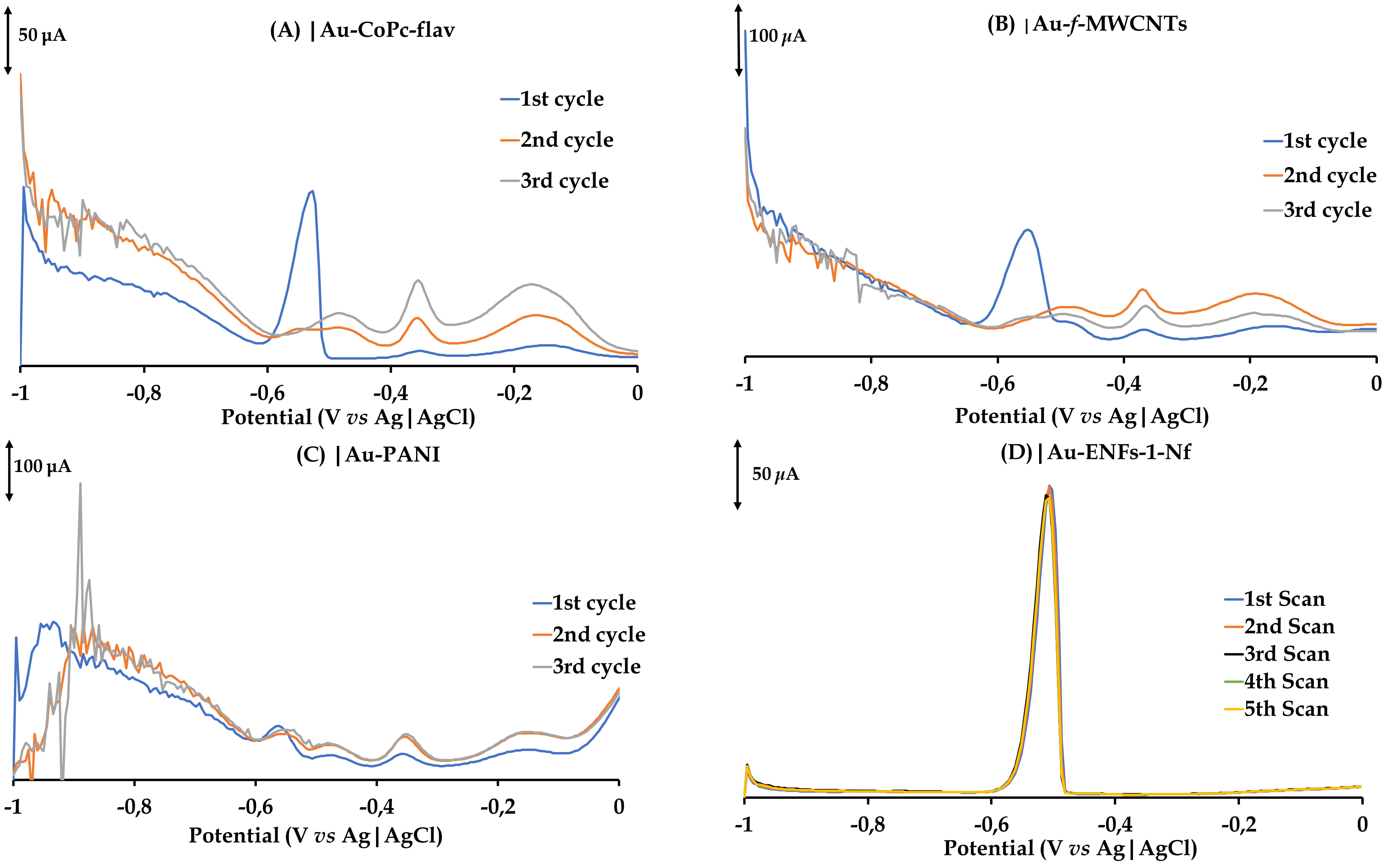

Figure 5.10: *Triplicated DPV scans of modified gold electrodes: (**A**) Au | -CoPc-flav, (**B**) Au | -f-MWCNTs, (**C**) Au | -PANI and Replicated DPASVs of (**D**) Au | ENFs-**1**-Nf in 1 mM Pb(II) ions dissolved in 0.1 M acetate buffer at pH 5.0.*

5.4.3. *Effective surface area and surface coverage*

The superior electrochemical performances of the Au|ENFs-**1**-Nf CME in the $K_3[Fe(CN)_6]$ redox probe were rationalized by estimating its effective surface area from its responses to 5 mM $K_3[Fe(CN)_6]$ in 0.1 M KCl at increasing scan rates (**Figure. 5.11**). The effective surface area was calculated using the Randles-Sevcik equation (*Eq. 5.1*):

$$I_{pa} = 2.69\ x10^5 n^{3/2} AC\sqrt{Dv} \qquad \textbf{(5.1)}$$

In the equation, *A* represents the effective surface area, *D* is the diffusion coefficient (6.67×10^{-6} cm^2/s at 298 K) of $K_3Fe(CN)_6$, ν is the scan rate, *C* is the substance concentration of $K_3Fe(CN)_6$, and *n* is the number of electrons transferred (*n* = 1).

Using the slope obtained from the I_{pa} *vs.* $\nu^{1/2}$ plots as presented in **Figure 5.11B**, the effective surface area was calculated and found to be 0.807 cm^2. This value is approximately eleven times higher than the area (0.071 cm^2) of the bare Au electrode.

To further characterize the Au|ENFs-**1**-Nf electrode, the surface coverage (Γ, mol/cm^{-2}) of the electrode was calculated. The integrated peak current area under the oxidation peak at a scan rate of 50 mV/s (Q/ν), and the effective surface area (0.807 cm^2) were applied in *Eq.* ***5.2*:**

$$\Gamma = \frac{Q}{nFA} \qquad \textbf{(5.2)}$$

Here, *Γ* represents the surface coverage, *n* is the number of transferred electrons, *F* is the Faraday constant, and *A* is the effective surface area. The calculated surface coverage for ENFs-**1**-Nf on the electrode was found to be 2.413×10^{-9} mol cm^{-2}, which is significantly larger than the value of 1×10^{-10} mol cm^{-2}, corresponding to a Pc molecule lying flat on the substrate's surface [52]. The higher surface coverage of the CME substantiates its improved electrochemical parameters compared to the bare Au electrode. The larger surface coverage contributes to the enhanced electrochemical sensitivity of the Au|ENFs-**1**-Nf electrode, making it a highly efficient and reliable sensor for the detection of Pb(II) ions.

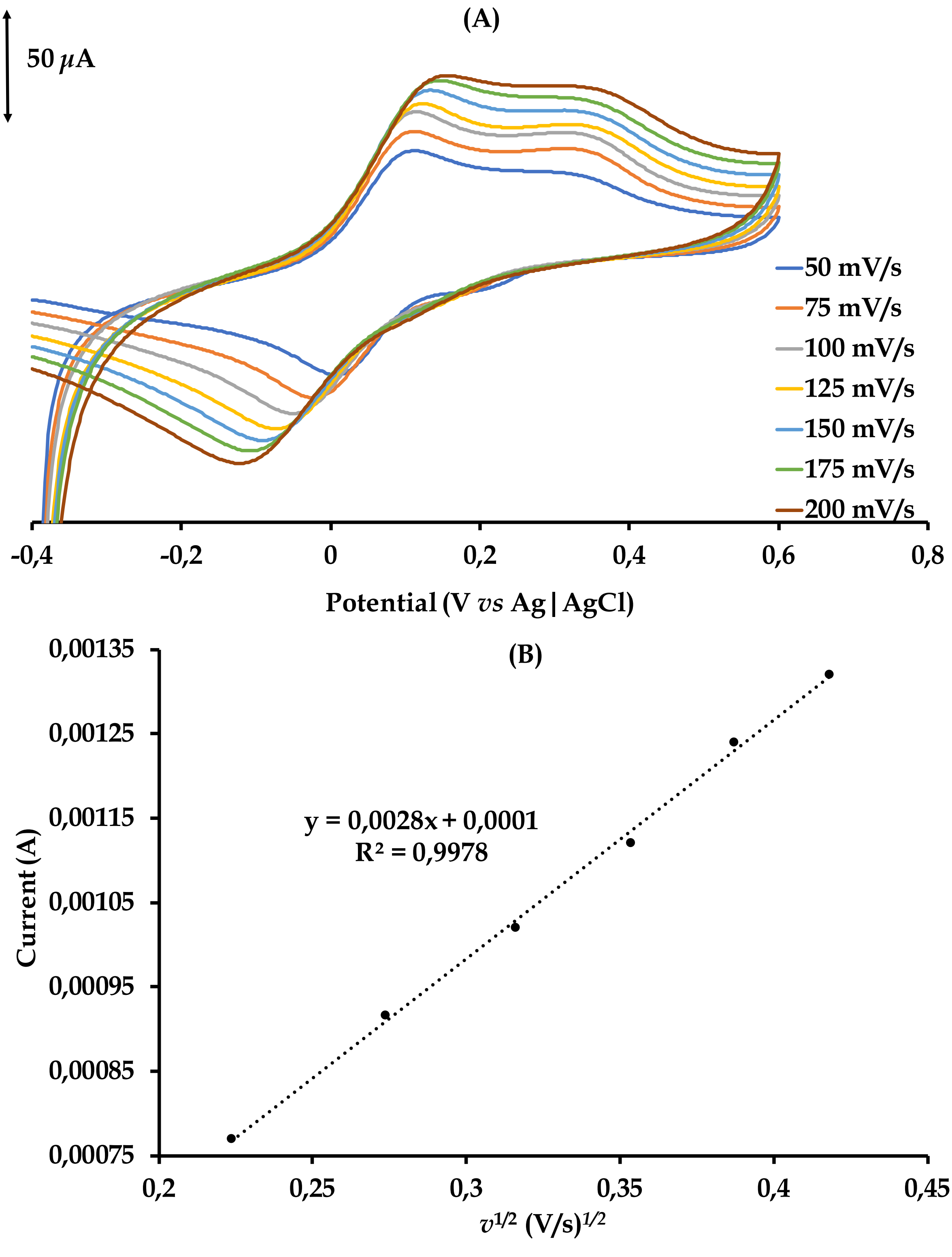

Figure 5.11: *(**A**) CVs of 5 mM $K_3Fe(CN_6)$ containing 0.1 M KCl (aq) at increasing scan rates as measured using the Au|ENFs-1-Nf electrode. (**B**) Plot of I_{pa} vs square root of scan rate.*

5.4.4. Electrochemical impedance spectroscopy studies

To gain a better understanding of the electron transport characteristics for the Au|ENFs-**1**-Nf film, its charge transfer resistance together with that of the bare (Au|) were probed in a 5 mM $K_3Fe(CN)_6$ solution within the frequency range of 0.1 Hz to 100 kHz. At higher frequencies, where charge transfer is diffusion-controlled, the plots exhibit semi-circular correlations whose diameters are inversely related to the intrinsic resistance (represented by R_{CT} in the Randles' equivalent circuit) of the cell components. The results show that the bare Au substrate induces greater charge transfer resistance than the interface of the Au|ENFs-**1**-Nf electrode for the Fe^{3+}/Fe^{2+} interconversion (**Figure 5.12**).

Moreover, the Nyquist plots display a linear plot whose slope is a measure of the Warburg impedance (Z_W) of the cell components at lower frequencies. The data was fitted to the Randles equivalent circuit which includes the following circuit elements: electrolyte resistance (Rs), charge transfer resistance (R_{CT}), constant phase element (CPE), and the Warburg impedance (Z_W). The inclusion of the non-ideal capacitor, the constant phase element (CPE) is motivated by the surface roughness of the Au|ENFs-**1**-Nf electrode. The low errors obtained between the experimental and fitted data validate the accuracy and reliability of the simulated Randles equivalent circuit, as shown in **Table 5.1**.

Comparing the R_{CT} values of the bare and the modified electrode reveals that the latter value is significantly smaller, implying that the electrocatalyst in the CME is more amenable to charge transfer. Additionally, the CME's electrocatalyst components are permeable to $Fe^{2+/3+}$ cations, considering that the main analyte of concern, Pb(II) must be exposed to its N, O, S-donor atoms. These results demonstrate that the Au|ENFs-**1**-Nf electrode possesses improved electron transport characteristics and enhanced conductivity compared to the bare Au electrode. As the electrocatalyst in the CME allows for efficient penetration of $Fe^{2+/3+}$ cations, it was foreseen that it will effectively facilitate the detection of Pb(II) ions.

***Table 5.1**: EIS data collected in a 5 mM $K_3Fe(CN)_6$ using bare|Au and Au|ENFs-**1**-Nf electrodes.*

Electrode	R_S (Ω)	R_{CT} (Ω)	Z_W (µMho)	C_{dl} (µMho)	*n*
bare|Au	101.0 (0.7)	1.96 (1.0)	236 (3.4)	33.8 (5.2)	0.715
Au|ENFs-**1**-Nf	94.1 (1.4)	1.10 (3.6)	900 (6.3)	650 (7.8)	0.646

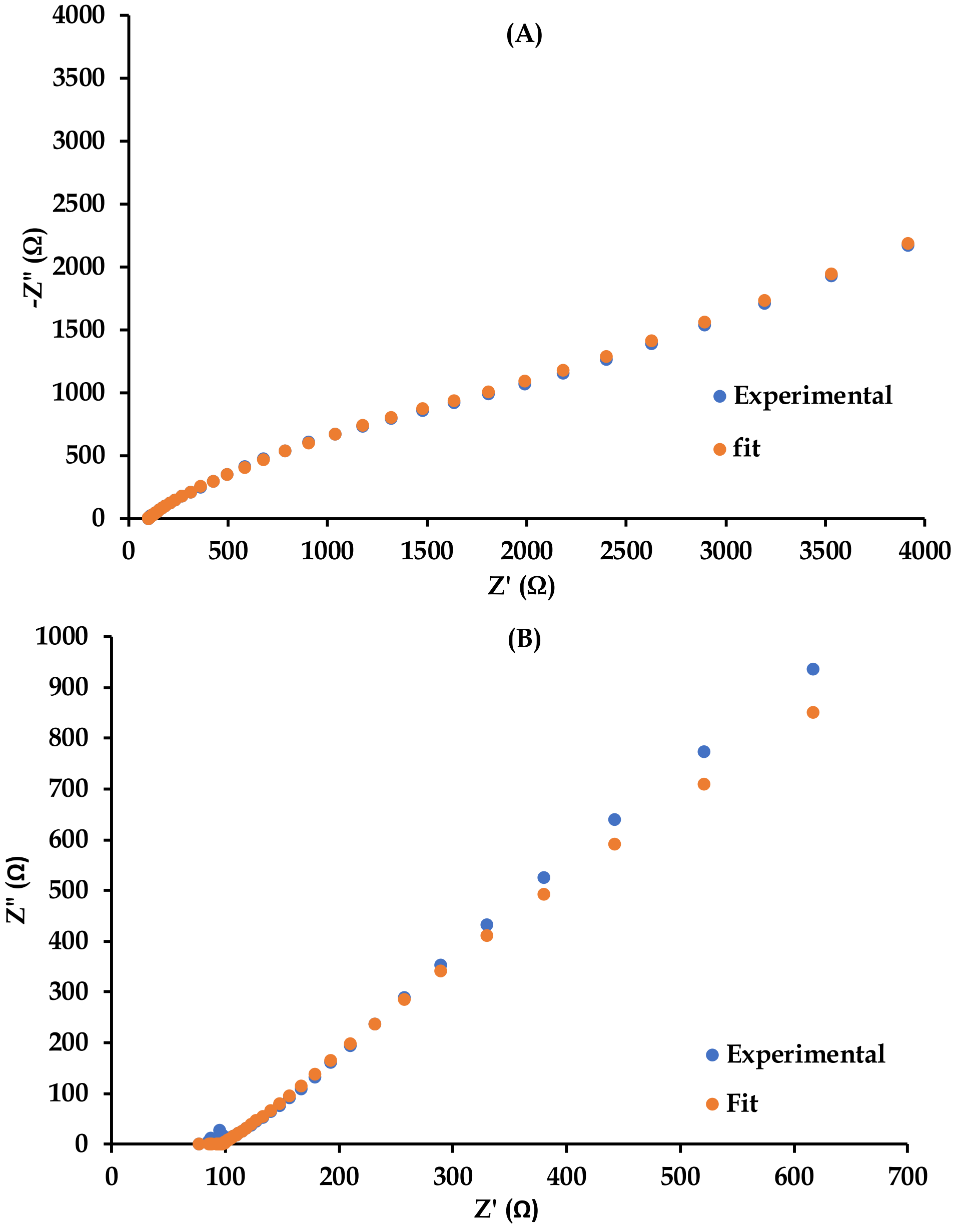

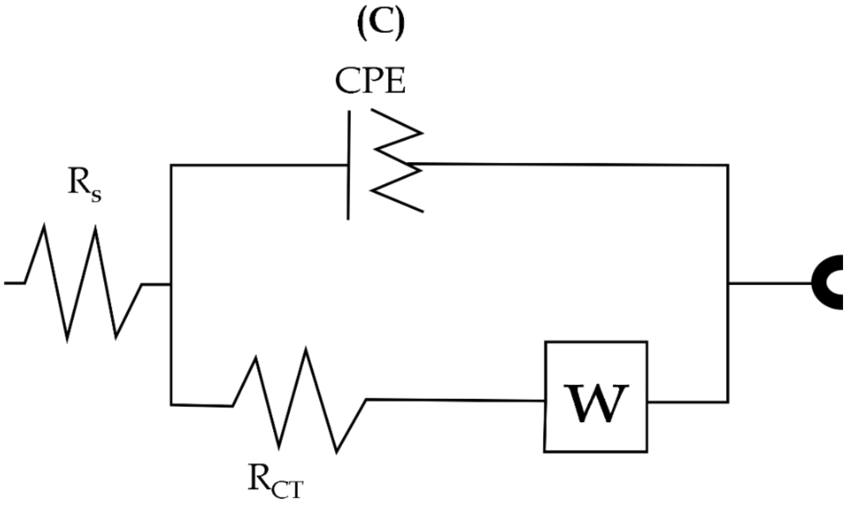

Figure 5.12: *Nyquist plots of 5 mM* $K_3Fe_3(CN)_6$ *dissolved in 0.1 M KCl at (**A**) |Au and electrode and (**B**) Au|ENFs-**1**-Nf electrodes. (**C**) The equivalent circuit is used to fit the EIS data.*

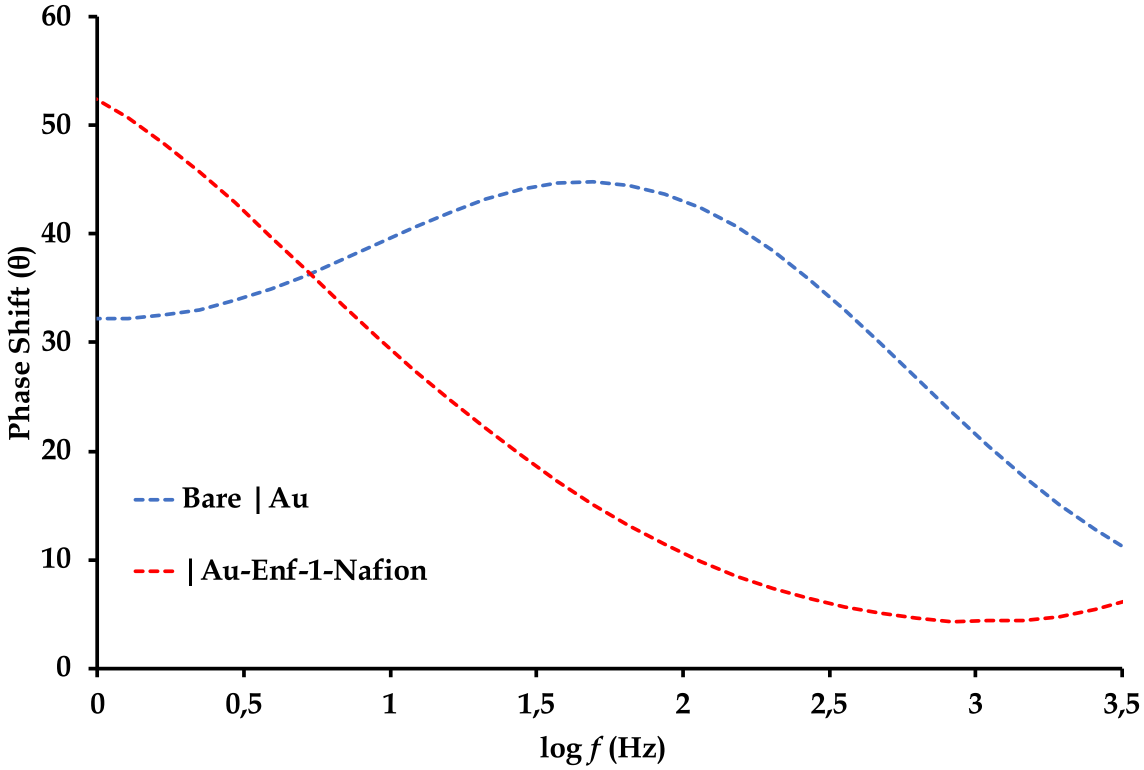

Figure 5.13: *Bode plots generated at 5 mM* $K_3Fe(CN)_6$ *dissolved in 0.1 M KCl with bare |Au and Au|ENFs-**1**-Nf electrodes.*

The phase angle of 2.9° exhibited by the Au|ENFs-**1**-Nf electrode and the phase angle of 44.7° observed in the bare gold electrode, as shown in **Figure 5.13**, are both significantly lower than 90°, which is the optimal phase angle value for a capacitor. This deviation is greater for Au|ENFs-**1**-Nf electrode indicating that the electrode behaves almost like a non-ideal capacitor due to the uneven surface morphology of its surface confirmed in the calculated surface roughness factor, Γ.[53] The non-uniformity of the immobilized electron-mediating film is substantiated by the n-value (a constant associated with the depression angle) which is less than 1.[11] The deviation of the bare Au electrode's n-exponent could be related to chemical edging when the electrode was cleaned with the piranha solution. The electrocatalytic properties of the ENfs-**1**-Nf thin film can involve redox reactions with the analytes, causing semi-capacitive behaviour.

5.5. Optimization of parameters for DPASV analysis of Pb(II) using the Au|ENFs-1-Nf

5.5.1. The effect of accumulation potential

The effect of accumulation potential on the stripping current of 1 mM Pb(II) at the Au|ENFs-**1**-Nf electrode interface was studied in a 0.1 M sodium acetate buffer solution within the potential range of +4.0 V to -1.0 V while keeping other variables constant. Choosing the right accumulation potential is crucial in electrochemical sensing to achieve the highest sensitivity and accuracy for target analytes. The stripping current due to pre-accumulated Pb atoms at the Au|ENFs-**1**-Nf electrode varied as shown in **Figure 5.14** when the accumulation potential was changed from positive to negative values. The peak stripping current for Pb(II) was observed at -0.8 V and any deviation from this potential led to lower peak currents. This indicates that -0.8 V is the optimum potential at which the Pb(II) ion can be accumulated for the subsequent detection using DPASV. At this accumulation potential, the maximum number of Pb(II) ions can be effectively preconcentrated on the electrode surface, leading to the highest sensitivity and signal-to-noise ratio during the stripping analysis. Thus, the accumulation potential of -0.8 V was chosen for the reliable and efficient detection of Pb(II) in this study.

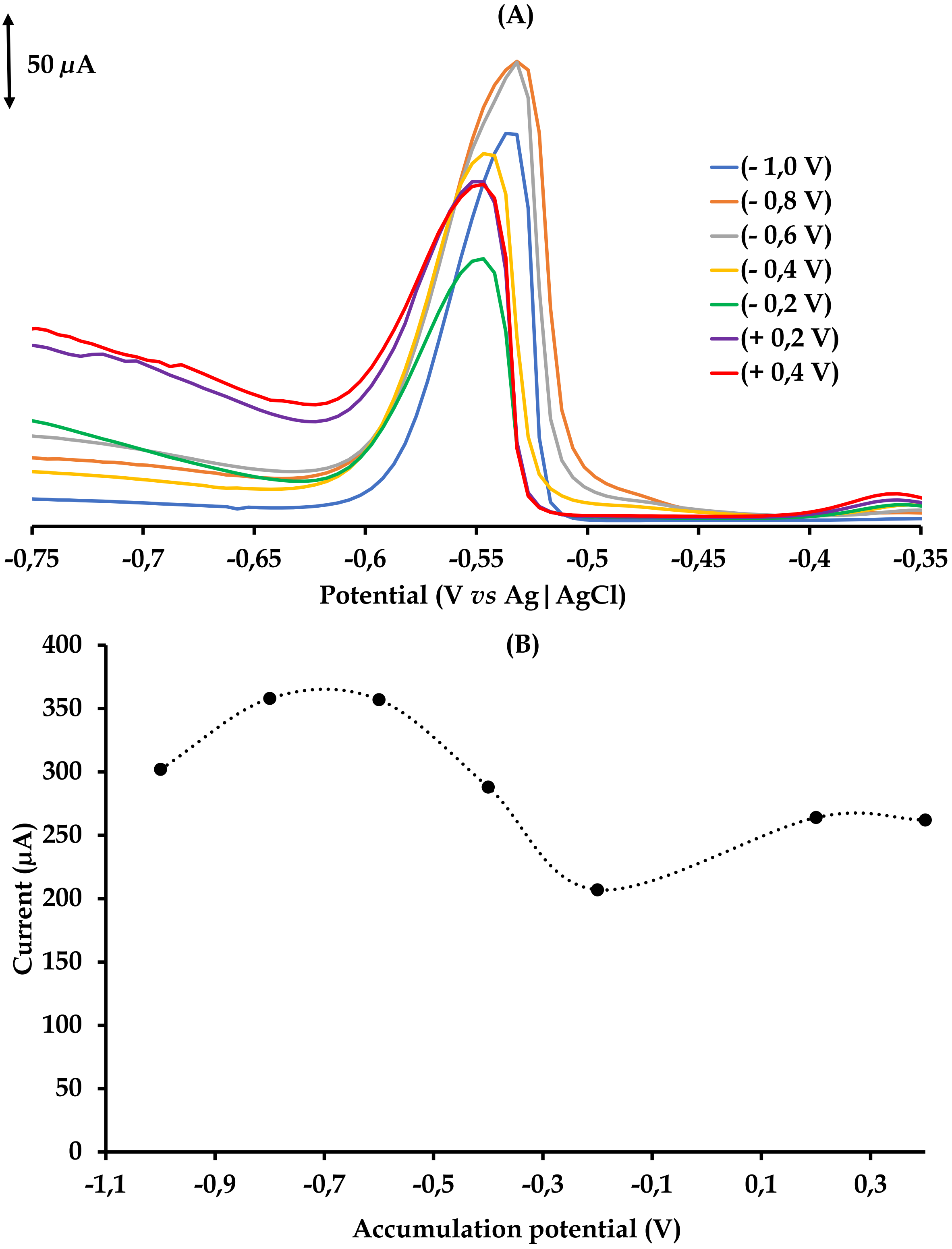

Figure 5.14*: DPASV responses of 1 mM Pb(II) at different accumulation potentials at theAu|ENFs-***1***-Nf electrode (at a deposition pH 1.15 and deposition time of 250 s).*

5.5.2. Accumulation time

Figure 5.15 displays the differential pulse anodic stripping voltammograms (DPASVs) obtained for 1 mM Pb(II) in acetate buffer while varying the accumulation time of Pb on the Au|ENFs-**1**-Nf electrode from 25 to 300 s. The current responses corresponding to Pb(II) accumulation at different times showed a general increase, reaching a steady plateau after 250 s. For initial accumulation times with 25 to 150 s, the peak current exhibited some gradual increase which were punctuated by some slight fluctuations. However, accumulation times greater than 250 s, recorded peak currents that were non-increasing, indicating that the analyte Pb(II) had reached its steady-state concentration of adsorption onto the active sites of the Au|ENFs-**1**-Nf film.

For these accumulation times, the maximum number of Pb(II) ions had accumulated on the electrode surface, leading to higher but non-increasing signal responses. Based on these observations, an accumulation time of 250 s was considered the best for further studies. At this optimized accumulation time, the Au|ENFs-**1**-Nf electrode had its best sensitivity for the detection of Pb(II) ions. The steady-state accumulation equilibrium achieved at 250 s ensures that the electrode has fully captured the target analyte, providing a reliable and reproducible detection platform.

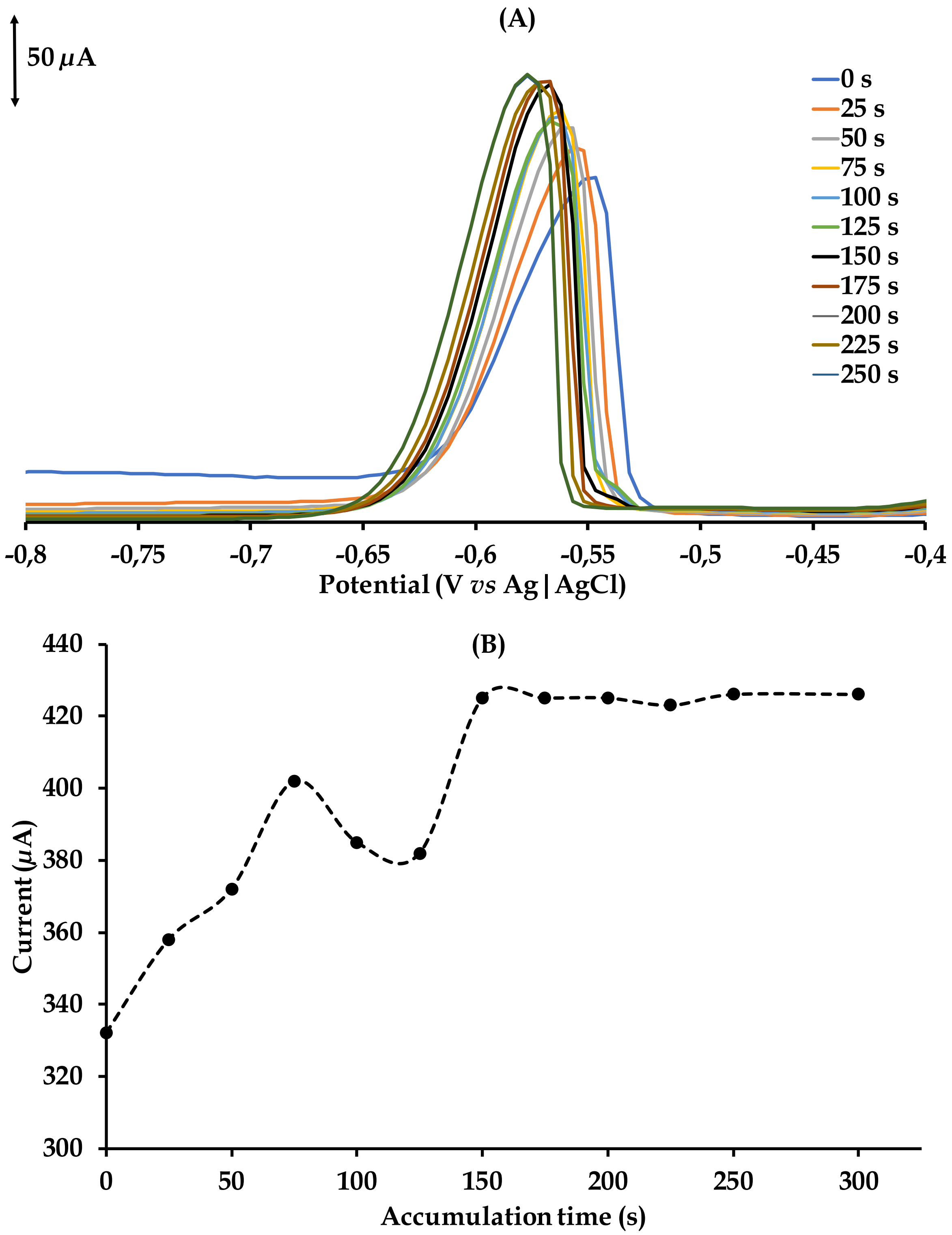

Figure 5.15: *DPASV responses of 1 mM Pb(II) at different accumulation time measured using theAu|ENFs-1-Nf electrode (at a deposition pH 1.15 and deposition of -0.8 V).*

5.5.3. *The effect of pH*

The effect of pH on the stripping currents of 1 mM Pb(II) was investigated in the pH range of 1 – 6 using the Au|ENFs-**1**-Nf electrode. The deposition potential was set to -0.8 V and the deposition time was 250 s**. Figure 5.16** shows that as the pH increases, the response in the stripping current of Pb(II) gradually decreases. This behaviour is expected since the pH of the solution affects the speciation of metal ions and their interactions with the electrode surface.

At pH values higher than 6, a white precipitate of $Pb(OH)_2$ was formed. It reduced the availability of free Pb(II) ions for electrochemical detection and led to a decrease in the stripping current.[54] Hence, the pH range above 6 is not suitable for accurate and reliable detection of Pb(II) ions using the Au|ENFs-**1**-Nf electrode. The stripping current responses of the electrode towards Pb(II) were highest at pH 1.15, indicating that high acidity ensures efficient interactions between the components of the ENF nanoconjugates and Pb(II) ions which results in the sensitive detection of the latter at the Au|ENFs-**1**-Nf electrode surface.

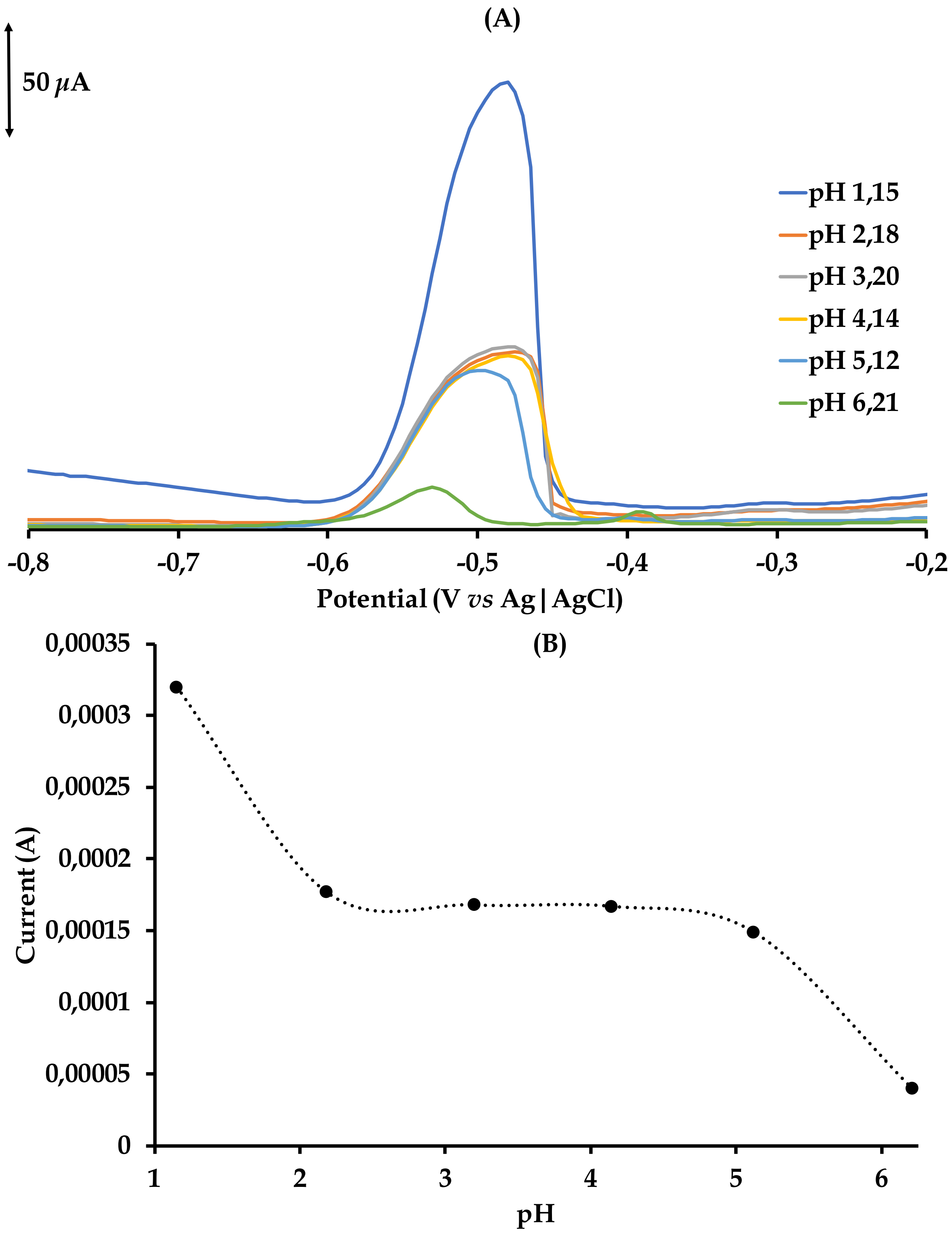

Figure 5.16: *DPASV responses of 3 mM Pb(II) at different pHs in acetate buffer at the Au|ENFs-***1***-Nf (at a deposition potential -0.8 V and deposition time of 250 s).*

5.5.4. Detection of Pb(II) ions using the Au|ENFs-1-Nf electrode

The Au|ENFs-**1**-Nf electrode demonstrated excellent electrochemical performance for the detection of Pb(II) in the concentration range of 1.55 μM to 125 μM. The anodic stripping current exhibited a linear relationship with increasing concentration of Pb(II), as depicted in **Figures 5.17A** and **B**, with a high correlation coefficient (R^2 = 0.9982). The calibration equation obtained from the linear regression analysis is given as follows:

$$I = 2.0 \, x \, 10^{-6}[Pb(II)] + 1.0 \times 10^{-4} \qquad (\mathbf{5.3})$$

Using this calibration equation, the LOD and LOQ values for the Au|ENFs-**1**-Nf electrode towards the detection of Pb(II) ions were found to be 0.51 μM and 1.55 μM, respectively. With a calculated %RSD of 3.92% (N = 3), this indicates that the electrode is reproducible and capable of accurately detecting Pb(II) ions at very low concentrations with high sensitivity.

Comparing the calibration parameter values for the detection of Pb(II) measured by the Au|ENFs-**1**-Nf electrode and other gold-modified electrodes encompassing similar modifiers as reported in the literature, the former exhibits a wider linear range (8 - 125 μM) and slightly higher LOD (0.51 μM) than most of the examples shown in **Table 5.2**. Wu *et al.* (2008)[55] reported a DMTD/Au electrode for Pb(II) detection with a LOD of 0.1 μM and a linear range of 1 - 45 μM. The Au|ENFs-**1**-Nf electrode showed comparable LOD and linear range compared to this electrode. The gold nanoparticle/polyaniline/graphene/glassy carbon electrode (GNP/PANI/GR/GCE): reported by Dong *et al.* (2014)[56] achieved an impressive LOD of 0.1 nM and a linear range of 0.5 - 10 nM for Pb(II) detection, making it more sensitive at low concentrations compared to the Au|ENFs-**1**-Nf electrode. Despite the inferior electrocatalytic performance of Au|ENFs-**1**-Nf electrode compared to GNP/PANI/GR/GCE, the former has a broader linear range. More specifically, based on our knowledge, no data for lead electrochemical sensing at surfaces of electrodes modified with PANI/PVA ENFs have been reported yet.

Table 5.2: *Comparison of LOD and LOQ values of the CMEs reported Pb(II) values in literature.*

Type of electrode	**LOD**	**Linear range**	**Reference**
Au|ENFs-**1**-Nf electrode	0.51 µM	8-125 µM	This work
DMTD/Au electrode	0.1 µM	1-45 µM	[55]
GNP/PANI/GR/GCE	0.1 nM	0.5-10 nM	[56]
Bi-Poly1,8-DAN/CPE	0.3 µg L^{-1}	0.5 -50 µg L^{-1}	[57]
GNPs/SPGE	2.2 ppb	20 -200 ppb	[58]
GNPs/PPy/SPCE	0.36 nM	0.5-10 nM	[59]

Abbreviations: DMTD/AuE: 2,5-Dimercapto-1,3,4-thiadiazole/gold electrode, **GNP/PANI/GR/GCE:** gold nanoparticle/polyaniline/graphene/glassy carbon electrode, **Bi-Poly1,8-DAN/CPE:** Poly(1,8-diaminonaphthalene) and bismuth film/Carbon paste electrode, **GNPs/SPGE:** gold nanoparticles/Screen printed gold electrode. **GNPs/PPy/SPCE:** gold nanoparticles/Polypyrrole/Screen printed carbon electrode

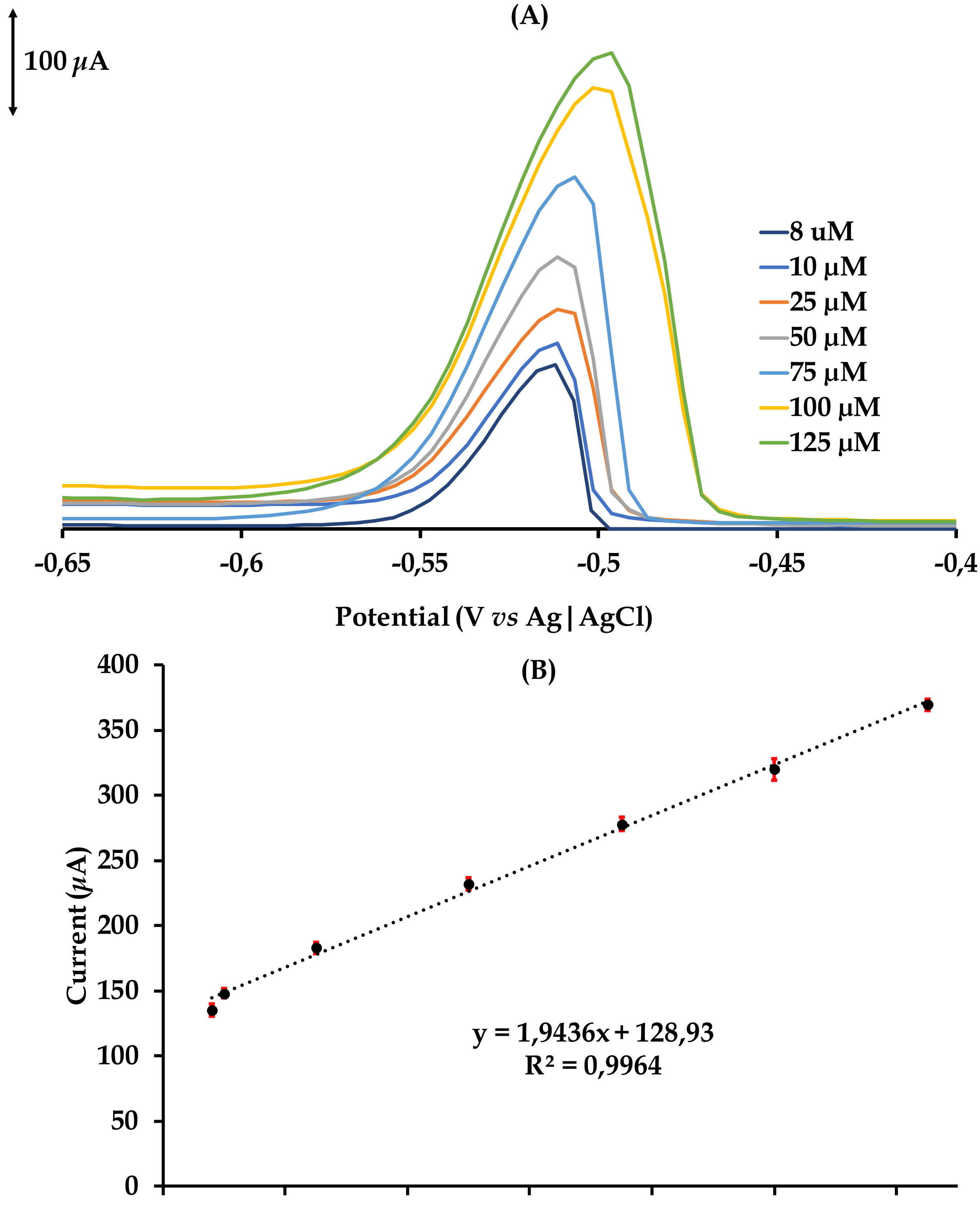

Figure 5.17: *(**A**) DPASV responses to different concentrations of Pb(II) at the Au|ENFs-**1**-Nf electrode. (**B**) Linear calibration plot. With a %RSD ≤ 5%, N = 3.*

5.5.5. *Interference/Selectivity studies*

Figure 5.18 presents the *DPASV* analysis of 1.0 g L^{-1} solution mixture of Pb(II), Hg(II) and Cd(II) at the Au|ENFs-**1**-Nf electrode. These concentrations translate to 4.98 mM Hg(II), 4.83 mM Pb(II) and 8.89 mM Cd(II) in 0.1 M sodium acetate buffer. The DPASV showed stripping current peaks that are well-separated although the peak for Pb(II) is suppressed. This indicates that the modified electrode was able to distinguish and detect each metal ion individually. However, the presence of Cd(II) and Hg(II) ions suppressed the current signal of Pb(II) and also caused a shift in the stripping potential of Pb(II) from its original value of -0.557 V to about -0.7 V, see **Figure 5.18B**. This potential shift can be attributed to the competitive adsorption of Cd(II) and Hg(II) on the electrode surface, leading to changes in the electrochemical behaviour of Pb(II).[60]

Despite the potential shift, the modified electrode still demonstrated acceptable peak separation for all the chosen metal ions. This suggests that the Au|ENFs-**1**-Nf electrode has good selectivity towards the detection of Pb(II) even in the presence of interfering cations like Cd(II) and Hg(II). However, it's important to note the potential current suppression and the shifts which was caused by the presence of interfering cations prior to separation of the interference may be required to ensure accurate quantification of Pb(II) in complex sample matrices.

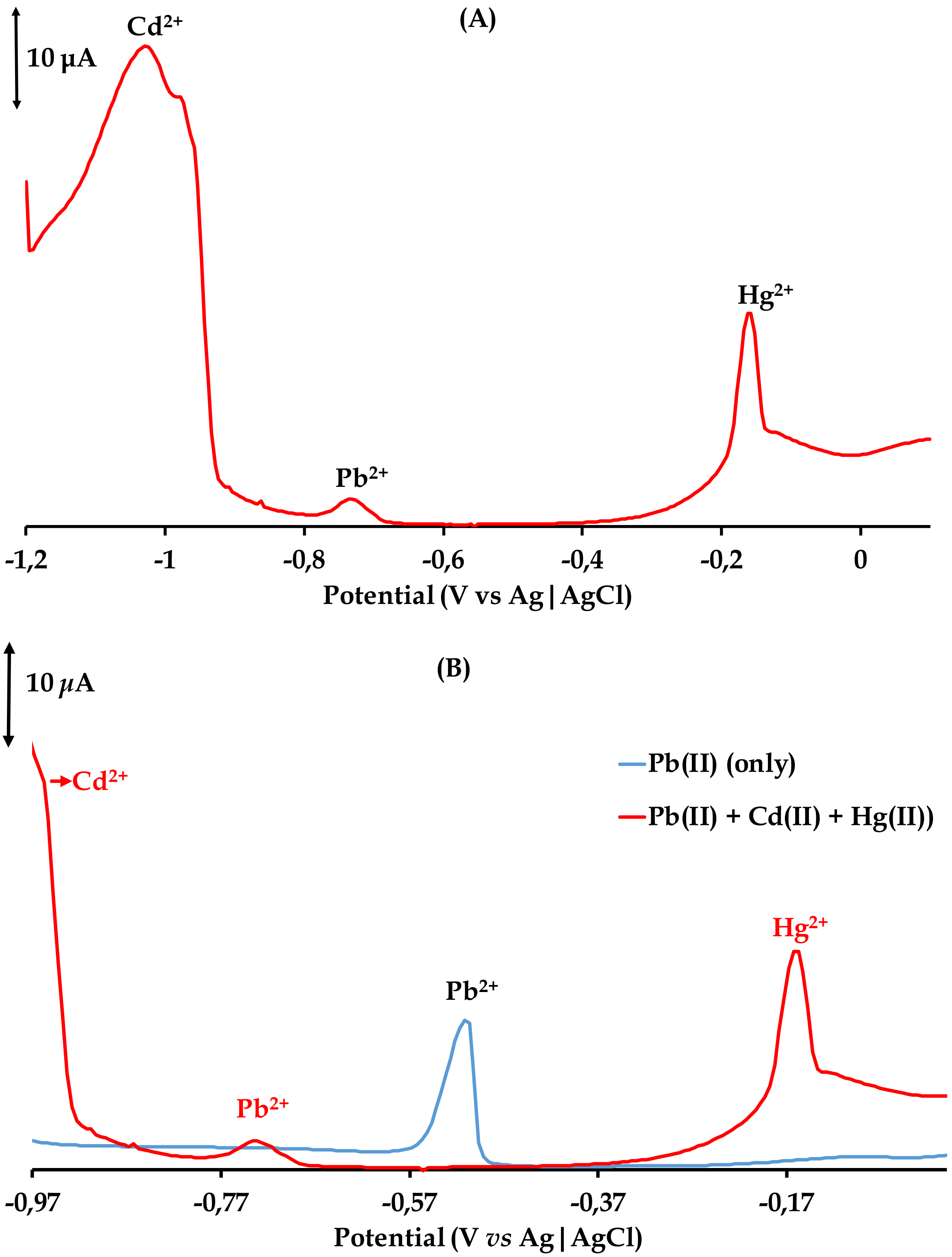

Figure 5.18: (A)*DPASV analysis of a mixture of 1.0 g* L^{-1} *of Hg(II), Cd(II) and Pb(II) prepared in 0.1 M sodium acetate buffer solution using Au|ENFs-***1***-Nf, deposition conditions: pH = 1,15, accumulation time 250 s and accumulation potential -0.8 V.* ***(B)*** *Overlayed vollammograms of Pb(II) alone and Pb(II) in the presence of Cd(II) and Hg(II).*

5.5.6. Standard addition of Pb(II) to the real water sample

The concentration of Pb(II) ions in a water sample taken from the Amanzimtoti wastewater treatment plant was determined using the Au|ENFs-**1**-Nf electrode. The responses of the electrode to the Pb(II) calibration standards and the real water are depicted in **Figures 5.19A** and **B**. As shown for the real water sample in the **Figure 5.19A**, no discernible signal for the real water was observed, implying that the concentration of Pb(II) in the Amanzimtoti water sample was below the LOD (0.51 mM) of the Au|ENFs-**1**-Nf electrode.

Hence the sample was spiked with incremental volumes (20 µL) of 1000 ppm Pb(II) standard, and a calculation from the calibration data gave a percentage recovery of Pb(II) of 103% with a %RSD = 6.07% (N=3). The value is within the acceptable accuracy range of 95-105%. This demonstrates that the Au|ENFs-**1**-Nf electrode is capable of accurately detecting and quantifying Pb(II) ions in real samples, making it a reliable sensor for environmental monitoring applications.

Additionally, a real water sample was analysed by ICP-OES before and after spiking with 3.0 ppm Pb(II) giving results shown in the **Table 5.3** to get the recovery of Pb(II). This was also undertaken to validate the accuracy of Au|ENFs-**1**-Nf towards the detection of Pb(II) in real samples by comparing it with ICP-OES. The concentration of Pb(II) in the water sample before and after was found to be 0.77 and 3.47 ppm, respectively, leading to a Pb(II) recovery of 115%.

This value is close to 3.11 ppm (103%) estimated from the standard method using the Au|ENFs-**1**-Nf electrode. The close agreement between the value of the Au|ENFs-**1**-Nf electrode and the more sensitive ICP-OES validates the high accuracy and reliability of the Au|ENFs-**1**-Nf sensor towards the detection of Pb(II) in real water samples. These findings demonstrate that the Au|ENFs-**1**-Nf electrode is an effective and practical tool for detecting Pb(II) in water samples. Its high percentage recovery and close agreement with the ICP-OES results affirm its potential for the quantitative monitoring of Pb(II) ions in environmental water samples. The use of this CME as a Pb(II) ion sensor could reduce the cost of monitoring contamination of water by Pb(II) and thus help ensure the safety of water sources and environmental health.

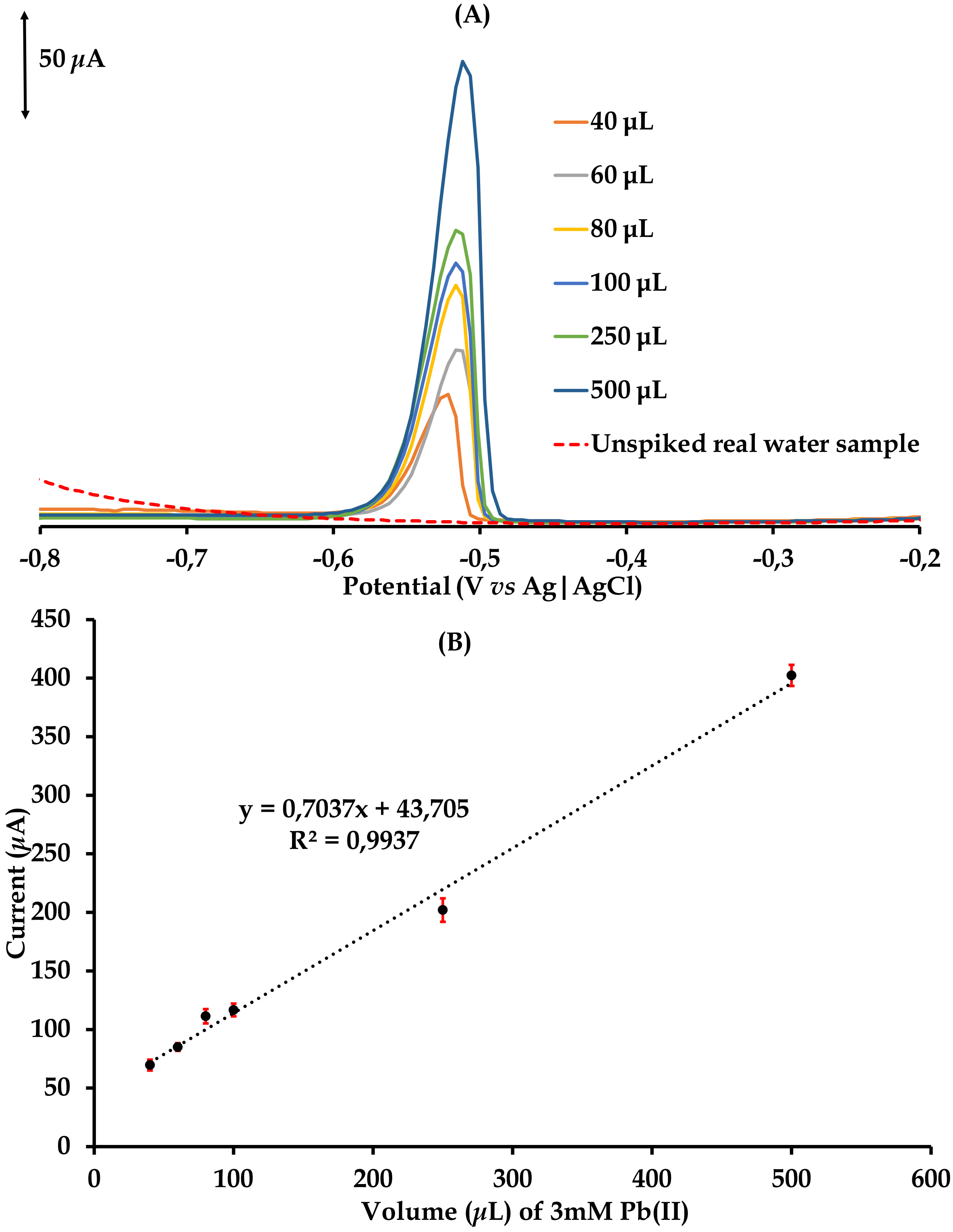

Figure 5.19: *(**A**) DPASV responses at the Au|ENFs-1-Nf electrode after the standard addition of incremental volumes (μL) of 3.0 mM Pb(II) to 20 mL of real water sample. (**B**) Linear calibration plot.*

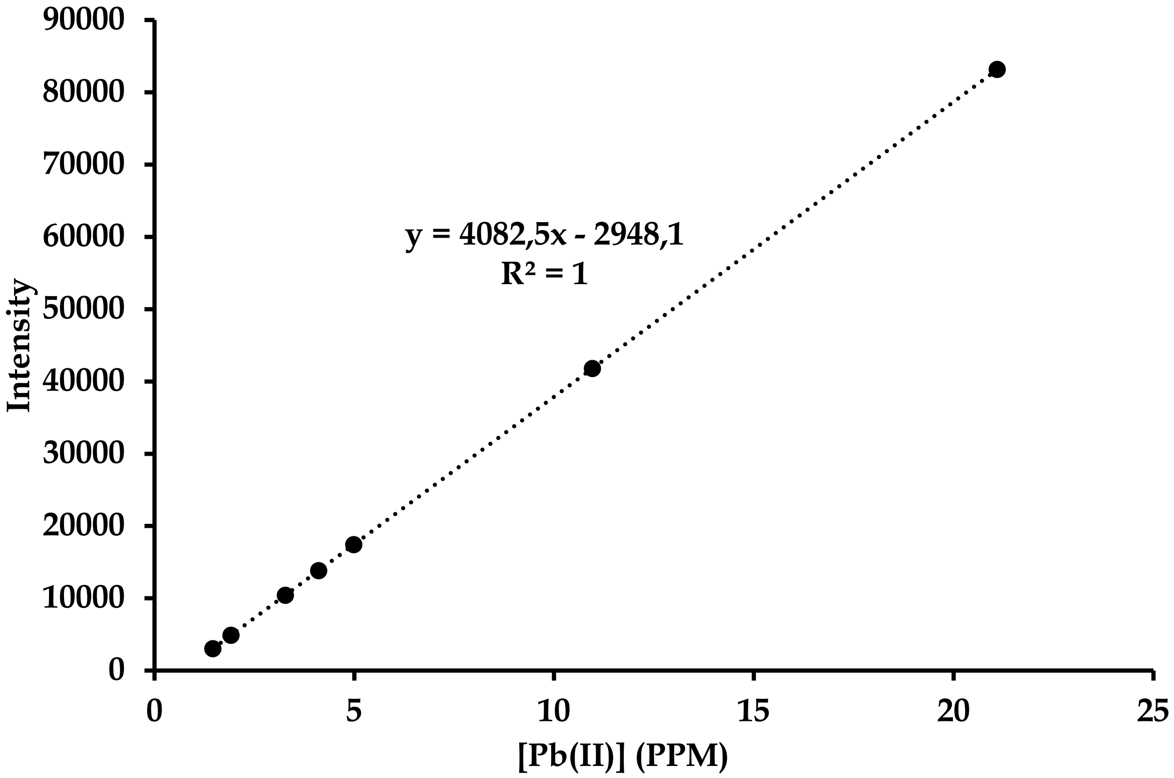

Figure 5.20. *A plot of emission intensity with increasing concentration of Pb(II) for the linear calibration of the ICP-OES.*

Table 5.3: *Measured concentration of Pb(II) ions for the unspiked and spiked Amanzimtoti water samples by ICP-OES.*

Sample name	**[Hg], ppm**
Unspiked Amanzimtoti water (20.00 mL)	0,77
Amanzimtoti water spiked at 12 ppm Pb(II)	4.24

5.6. Conclusions

The morphological features of CoPc-flav, *f*-MWCNTs, PANI, PANI-CoPc-flav-*f*-MWCNTs composite and their network-shaped ENFs-**1** were extensively analysed and confirmed using various spectroscopic and microscopic techniques, including FTIR, Raman spectroscopy, powder X-ray diffraction and SEM-EDX. The performance of the Au|ENFs-**1**-Nf electrode was found to surpass that of the bare Au electrode. In addition, the Au|ENFs-**1**-Nf electrode exhibited excellent stability in Pb(II) detection, outperforming the Au|PANI, Au|*f*-MWCNTs, and Au|CoPc-flav electrodes.

The electrocatalytic activity of the Au|ENFs-**1**-Nf electrode towards Pb(II) was significantly superior. Moreover, it demonstrated selectivity for Pb(II) ions in the presence of other interfering heavy metal ions like Hg(II) and Cd(II). The performance of the CME in sensing the Pb(II) cations in a real water sample was comparable to that of ICP-OES. In particular, the percentage Pb(II) recoveries of 115% and 103% were attained when using ICP-OES and the CME, respectively.

5.7. References

(1) Eqani, S. A. M. A. S.; Khalid, R.; Bostan, N.; Saqib, Z.; Mohmand, J.; Rehan, M.; Ali, N.; Katsoyiannis, I. A.; Shen, H. *Chemosphere* **2016**, *155*, 259.

(2) Ghorbani, M.; Akbarzade, S.; Aghamohammadhasan, M.; Seyedin, O.; Lahoori, N. A. *Analytical Methods* **2018**, *10*, 2041.

(3) Nriagu, J. O.; Blankson, M. L.; Ocran, K. *Science of the Total Environment* **1996**, *181*, 93.

(4) Ghorbani, M.; Seyedin, O.; Aghamohammadhassan, M. *Journal of Environmental Management* **2020**, *254*, 109814.

(5) Su, W.; Cho, M.; Nam, J.-D.; Choe, W.-S.; Lee, Y. *Biosensors and Bioelectronics* **2013**, *48*, 263.

(6) Albalawi, I.; Hogan, A.; Alatawi, H.; Moore, E. *Sensing and Bio-Sensing Research* **2021**, *34*, 100454.

(7) Gounden, D.; Nombona, N.; Van Zyl, W. E. *Coordination Chemistry Reviews* **2020**, *420*, 213359.

(8) Nyokong, T. *Functional Phthalocyanine Molecular Materials* **2010**, 45.

(9) Tau, P.; Nyokong, T. *Electrochimica acta* **2007**, *52*, 3641.

(10) Mbambisa, G.; Tau, P.; Antunes, E.; Nyokong, T. *Polyhedron* **2007**, *26*, 5355.

(11) Kantize, K.; Booysen, I. N.; Mambanda, A. *International Journal of Electrochemical Science* **2022**, *17*, 22067.

(12) Promphet, N.; Rattanarat, P.; Rangkupan, R.; Chailapakul, O.; Rodthongkum, N. *Sensors and Actuators B: Chemical* **2015**, *207*, 526.

(13) Lu, T.-L.; Tsai, Y.-C. *Sensors and Actuators B: Chemical* **2011**, *153*, 439.

(14) Prabhudass, J.; Palanikumar, K.; Natarajan, E.; Markandan, K. *Materials* **2022**, *15*, 506.

(15) Li, M.; Jing, L. *Electrochimica Acta* **2007**, *52*, 3250.

(16) Huang, J.; Wang, D.; Hou, H.; You, T. *Advanced Functional Materials* **2008**, *18*, 441.

(17) Guo, Q.; Liu, D.; Zhang, X.; Li, L.; Hou, H.; Niwa, O.; You, T. *Analytical Chemistry* **2014**, *86*, 5898.

(18) Al-Dhahebi, A. M.; Gopinath, S. C. B.; Saheed, M. S. M. *Nano Convergence* **2020**, *7*, 1.

(19) Kumar, S.; Tripathy, S.; Singh, O. K.; Singh, S. G. *Bioelectrochemistry* **2021**, *138*, 107725.

(20) Li, D.; Pang, Z.; Chen, X.; Luo, L.; Cai, Y.; Wei, Q. *Beilstein Journal of Nanotechnology* **2014**, *5*, 346.

(21) B Kondawar, S.; T Patil, P.; P Agrawal, S. *Advanced Materials Letters* **2014**, *5*, 389.

(22) Chohan, S.; Booysen, I. N.; Mambanda, A. *Polyhedron* **2015**, *102*, 284.

(23) Zoromba, M. S.; Alghool, S.; Abdel-Hamid, S.; Bassyouni, M.; Abdel-Aziz, M. *Polymers for Advanced Technologies* **2017**, *28*, 842.

(24) Sudhakara, S. M.; Kotresh, H. M. N.; Devendrachari, M. C.; Khan, F. *Electroanalysis* **2020**, *32*, 1807.

(25) Ninh, D. H.; Thao, T. T.; Long, P. D.; Dinh, N. N. *Open Journal of Organic Polymer Materials* **2016**, *6*, 30.

(26) Dhibar, S.; Bhattacharya, P.; Hatui, G.; Sahoo, S.; Das, C. *ACS Sustainable Chemistry & Engineering* **2014**, *2*, 1114.

(27) Sudhakara, S. M.; Devendrachari, M. C.; Kotresh, H. M. N.; Khan, F. *Microchemical Journal* **2021**, *161*, 105781.

(28) Cao, Y.; Guo, L.; An, M.; Zhu, L.; Cui, X. *Chinese Journal of Analytical Chemistry* **2006**, *34*, 469.

(29) Furukawa, Y.; Ueda, F.; Hyodo, Y.; Harada, I.; Nakajima, T.; Kawagoe, T. *Macromolecules* **1988**, *21*, 1297.

(30) Chougale, U.; Thombare, J.; Fulari, V.; Kadam, A. *International Conference on Energy Efficient Technologies for Sustainability* **2013**, 1078.

(31) John, A.; Mahadeva, S. K.; Kim, J. *Smart Materials and Structures* **2010**, *19*, 045011.

(32) Kizildag, N.; Ucar, N.; Oztoksoy, M.; Garmestani, H.; Wang, Y.; Dahmen, K. In *The International Istanbul Textile Congress* **2013**, 1.

(33) Qiu, S.; Li, Y.; Xu, H.; Liang, Q.; Zhou, M.; Rong, J.; Li, Z.; Xu, S. *Solid State Sciences* **2022**, *129*, 106905.

(34) Szybowicz, M.; Bała, W.; Fabisiak, K.; Paprocki, K.; Drozdowski, M. i. *Journal of Materials Science* **2011**, *46*, 6589.

(35) Zucolotto, V.; Ferreira, M.; Cordeiro, M. R.; Constantino, C. J.; Moreira, W. C.; Oliveira Jr, O. N. *Sensors and Actuators B: Chemical* **2006**, *113*, 809.

(36) Blaha, M.; Bouša, M.; Vales, V.; Frank, O.; Kalbac, M. *ACS Applied Materials & Interfaces* **2021**, *13*, 34686.

(37) Sharma, A.; Goyal, P. K.; Rawal, I.; Rajpal, A.; Khokhar, A.; Kumar, V.; Dahiya, S. *Optical Materials* **2022**, *131*, 112712.

(38) Aksakal, F. I.; Ciltas, A.; Ozek, N. S. *Chemosphere* **2019**, *225*, 820.

(39) Mallakpour, S.; Abdolmaleki, A.; Azimi, F. *Ultrasonics Sonochemistry* **2017**, *39*, 589.

(40) Kunpatee, K.; Chamsai, P.; Mehmeti, E.; Stankovic, D. M.; Ortner, A.; Kalcher, K.; Samphao, A. *Journal of Electroanalytical Chemistry* **2019**, *855*, 113630.

(41) Ji, X.; Zou, T.; Gong, H.; Wu, Q.; Qiao, Z.; Wu, W.; Wang, H. *Crystal Research and Technology* **2016**, *51*, 154.

(42) Shoba, S.; Bankole, O. M.; Ogunlaja, A. S. *Analytical Methods* **2020**, *12*, 1094.

(43) Yan, J.; Wei, T.; Shao, B.; Fan, Z.; Qian, W.; Zhang, M.; Wei, F. *Carbon* **2010**, *48*, 487.

(44) Kamil, A. M.; Hussein, F. H.; Halbus, A. F.; Bahnemann, D. W. *International Journal of Photoenergy* **2014**, *2014*.

(45) Zhang, G.; Zhang, Y.; Tan, A.; Zhou, H.; Zhao, W.; Chen, W. *Nanomaterials and Nanotechnology* **2022**, *12*, 18479804221096540.

(46) Khalil, M.; El-Kady, M.; El-Subruiti, G.; El-Sayed, E. *Desalin. Water Treat* **2020**, *181*, 436.

(47) Foster, C. W.; Pillay, J.; Metters, J. P.; Banks, C. E. *Sensors* **2014**, *14*, 21905.

(48) Yilmaz, I.; Arslan, S.; Guney, S.; Becerik, I. *Electrochimica acta* **2007**, *52*, 6611.

(49) Shoba, S.; Bankole, O. M.; Ogunlaja, A. S. *Electrocatalysis* **2020**, *11*, 593.

(50) Roy, A.; Ray, A.; Saha, S.; Das, S. *International Journal of Hydrogen Energy* **2018**, *43*, 7128.

(51) Liang, X.-H.; Yu, A.-X.; Bo, X.-J.; Du, D.-Y.; Su, Z.-M. *Coordination Chemistry Reviews* **2023**, *497*, 215427.

(52) Mugadza, T.; Nyokong, T. *Electrochimica Acta* **2010**, *55*, 2606.

(53) Kang, J.; Wen, J.; Jayaram, S. H.; Yu, A.; Wang, X. *Electrochimica Acta* **2014**, *115*, 587.

(54) Ardalani, M.; Shamsipur, M.; Besharati-Seidani, A. *Journal of Electroanalytical Chemistry* **2020**, *879*, 114788.

(55) Wu, Y.; Bing Li, N.; Qun Luo, H. *Microchimica Acta* **2008**, *160*, 185.

(56) Dong, Y.; Zhou, Y.; Ding, Y.; Chu, X.; Wang, C. *Analytical Methods* **2014**, *6*, 9367.

(57) Salih, F. E.; Ouarzane, A.; El Rhazi, M. *Arabian Journal of Chemistry* **2017**, *10*, 596.

(58) Wan, H.; Sun, Q.; Li, H.; Sun, F.; Hu, N.; Wang, P. *Sensors and Actuators B: Chemical* **2015**, *209*, 336.

(59) Ding, J.; Liu, Y.; Zhang, D.; Yu, M.; Zhan, X.; Zhang, D.; Zhou, P. *Microchimica Acta* **2018**, *185*, 1.

(60) Zhu, X.; Liu, B.; Hou, H.; Huang, Z.; Zeinu, K. M.; Huang, L.; Yuan, X.; Guo, D.; Hu, J.; Yang, J. *Electrochimica Acta* **2017**, *248*, 46.

Chapter 6

An electrospun nanofiber composite utilized as an electrocata-lyst for the detection of acetaminophen in multifarious water samples

6.1. Introduction

Phthalocyanines (Pcs) and their derivatives have emerged as versatile compounds with diverse applications in science, engineering and technology.[1,2] In the realm of electrochemical sensors, metallophthalocyanines (MPcs) can serve as appropriate synthons to fabricate thin films which act as electrocatalysts on working electrodes for the detection of water pollutants.[3,4] In particular, chemically modified electrodes (CMEs) with electron-mediating thin films comprising of MPc carbon nanotube (CNT) conjugates have rendered more sensitive electrocatalysis than bare or those modified with the individual components of the conjugate, MPcs or CNTs.[5,6] Moreover, stable CMEs have been fabricated by the covalent linking of MPcs to functionalized (*f*)-CNTs. However, CMEs fabricated from amorphously mixed MPc-CNT conjugates exhibit many challenges due to the gradual loss of the adsorbed components as a result of molecular leaching of constituents making up the CME interface.[7]

The inherent challenges associated with metal phthalocyanine-multiwalled carbon nanotube (MPc-MWCNT) composite-modified electrodes can be effectively addressed by electropolymerizing conductive polymers onto the CME surface. This approach leads to the formation of a more robust CME with improved electron transfer kinetics. A recent study by Kantize *et* al. (2022) demonstrated this strategy by modifying a platinum electrode using a CoPc *tetra*-substituted with coumarin moieties, carboxylic-acid-functionalized multiwalled carbon nanotubes (*f*-MWCNTs), and Nafion (Nf).[8] In the aforementioned study, Nafion was preferred for its high permeability to cations and optimal chemical robustness.[8] A conductive polymer chosen for the same purpose for this study is polyaniline (PANI) which possesses unique stereo-electronic properties that facilitate electron delocalization capabilities within its polymer chains and between them. These properties of PANI manifest in the form of the distinctive redox transformation and high capacitance.[9] Thus, the PANI-modified electrodes have been shown to offer enhanced sensitivity and selectivity towards analytes of interest, making it a highly promising electrochemical mediating polymeric component of CMEs for various electrochemical sensing applications.[10,11]

Furthermore, augmenting the electrocatalytic performances of PANI-modified electrodes can be achieved by the inclusion of carbon-based materials such as carbon nanotubes into PANI composites which can increase the mechanical strength and minimize leaching of CME components from the thin electrocatalytic film.[12] In addition, these polymeric PANI-carbon nanotube conjugates exhibit enhanced electrical conductivity than the nanomaterial or polymer, individually.[13,14] Fabrication of these carbon-nanoconjugates is also more financially feasible than PANI conjugated with precious metals such as platinum.[15] Herein, carboxylic acid functionalized multi-walled carbon nanotubes (*f*-MWCNTs) were conjugated to CoPc-fur and the resultant nanoconjugate, CoPc-fur-*f*-MWCNTs was used as a reinforcing matrix for PANI.

The incorporation of electron mediators into electrospun nanofibers (ENFs) has led to nanohybrids with network structures where the individual ENFs are interlinked.[16] The nano-structural architecture of ENF composite-modified electrodes allows an even electron distribution within their electrocatalysts and their 3D-dimensionality increases the effective electrocatalytic surface areas when compared to electrodes modified with ENFs or the individual electron-mediators, respectively.[17,18] Morphological features such as ENF pore sizes and network cavities can be conveniently altered using electrospinning instrumental and solution parameters to manipulate their selective uptake of analytes on CME interfaces.[19,20] The PANI-CoPc-fur-*f*-MWCNTs conjugate was embedded into a polyvinyl acetate (PVA) shell and the ENFs were subsequently immobilized on a GCE. To mechanically reinforce the ENF film, Nafion (Nf), an ion-exchange polymer, was used as an electrochemical mordant through thermally annealing the former to the GCE surface. The complementarity of their activity is justified by the use of PVA ENFs as effective electrocatalysts for electrode reactions of fuel cells while Nf has been used in battery storage devices.[21-23]

The constructed CME, GCE|ENFs-**2**-Nf was evaluated for the electrocatalytic detection of the common mild painkiller, acetaminophen (APAP). There is a growing concern about increasing concentrations of pharmaceutically derived pollutants in natural water bodies.[24,25] The coexistence of various pharmaceuticals in water systems presents a significant concern, potentially leading to ineffective therapy for individuals reliant on chronic medication. Prolonged stays in hospitals and increased healthcare costs can be expected as a result. Additionally, the presence of antibiotic-resistant bacterial strains in untreated sewage and treated waters is a growing issue.[26-28] These challenges are further amplified by wastewater treatment plants (WWTPs) that may lack the necessary capabilities to effectively eliminate emerging water pollutants from water bodies.[26,29] The detection of APAP in real water samples using a CME is a significant aspect of this study. Acetaminophen, a commonly used painkiller worldwide, can have notable effects on aquatic environments once it enters them. Its presence in aquatic systems can impact various organisms, including fish and invertebrates, by interfering with their physiological processes and potentially disrupting ecosystem balances.[30,31]

6.2. Experimental

6.2.1. *Synthesis of the PANI-CoPc-fur (1) composite and the PANI-CoPc-fur-f-MWCNTs (2) nanoconjugate*

PANI was synthesized by following a previously reported method by Kondawar *et al* 2014.[32] Afterwards, the CoPc-fur (0.1193 g, 0.116 mmol) was added to a 50 mL aqueous solution of 1.0 M HCl and PANI, and the mixture was stirred for an hour to ensure even dispersion of CoPc-fur throughout the solution. The resulting solution was then allowed to stand overnight, allowing the PANI-CoPc-fur to precipitate out. The precipitate was collected through filtration and dried in a vacuum oven at 80 °C. This result in a dark green precipitate representing the PANI-CoPc-fur (**1**) composite.

The electrochemical properties of **1** were enhanced by the incorporation of functionalized multi-walled carbon nanotubes (*f*-MWCNTs). More specifically, a mass of 0.2100 g of *f*-MWCNTs was added to a mixture containing 0.5006 g of PANI-CoPc-fur in 3 mL of *N, N'*-dimethylformamide (DMF). The mixture was subjected to sonication for 3 h to form the PANI-CoPc-fur-*f*-MWCNTs (**2**) composite with uniformly dispersed *f*-MWCNTs within the (**1**) matrice.

6.2.2. *Fabrication of PVA-based ENFs*

The fabrication of PVA-based ENFs was done following the method reported in **Chapter 2**.

6.2.3. *Fabrication of the GCE|ENFs-2-Nf CME*

The bare glassy carbon electrode (GCE|) was thoroughly polished with aqueous alumina slurries, followed by sonication in DMF and ethanol. The electrode was then rinsed with ultra-pure water to remove any alumina residue. Next, a 10 mg mass of ENFs-**2** was dispersed in 2 mL of DMF and sonicated for 1 h to obtain a well-dispersed suspension. The suspension was thereafter drop-casted onto the surface of the GCE| electrode and dried in the oven (40 ^{o}C) for 24 h. After 24 h, a 20 µL solution of 0.05 (w/v)% Nafion (Nf) was loaded onto the pre-dried GCE|ENFs-**2** CME. Upon drying under a stream of nitrogen at room temperature, the targeted CME (GCE|ENFs-**2**-Nf) was fabricated.

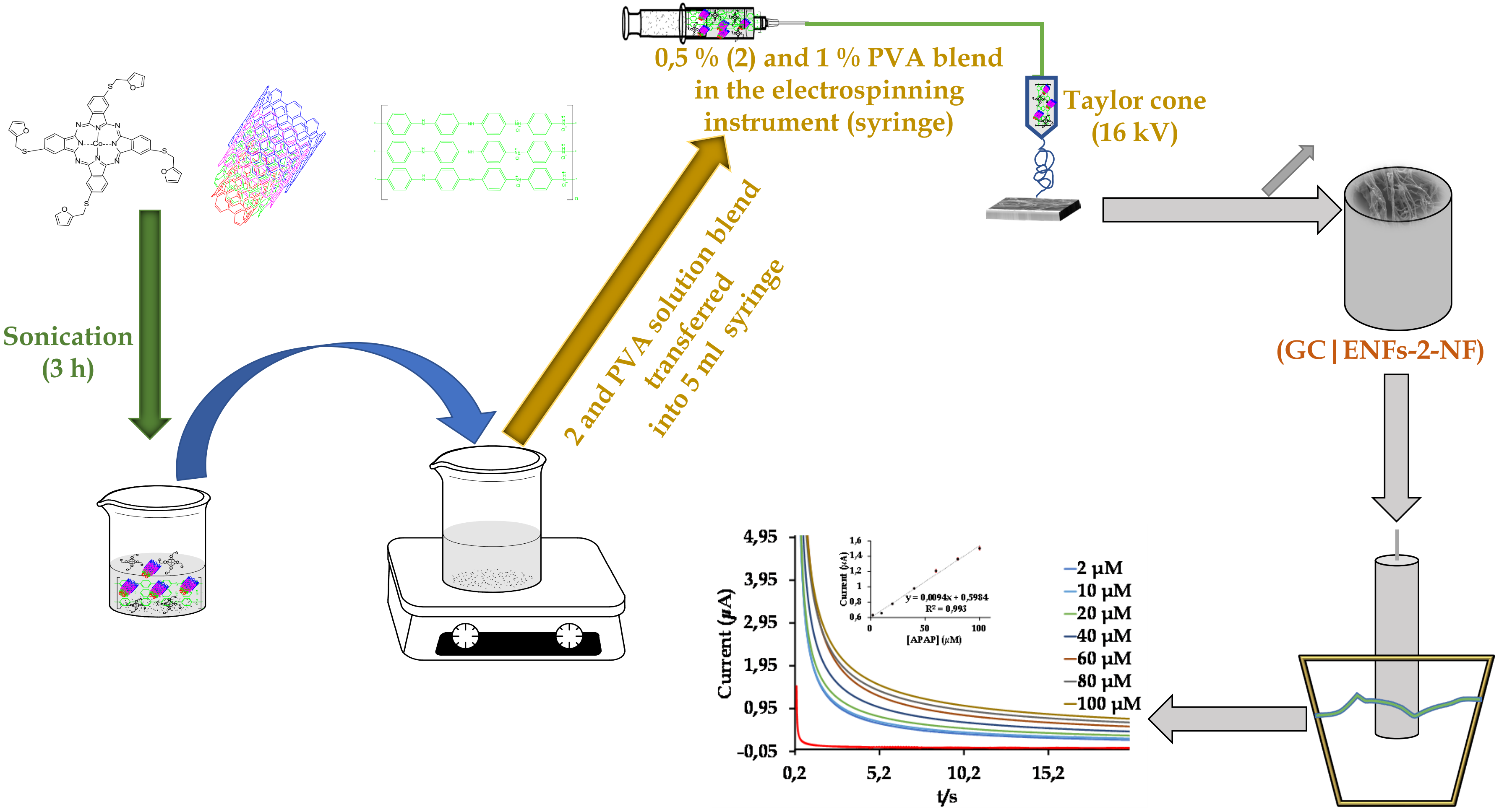

Scheme 6.1: *The sequential nanofabrication methods of the ENFs and electrode modification techniques employed to afford the CME.*

6.3. Results and discussion

6.3.1. *Synthesis, nanofabrication and characterization*

As per a previously reported method in our research group by Chohan *et al.*[33] the synthesis of CoPc-fur (**Figure 6.1**) involved the cyclotetramerization of 4-(furan-2-methylthio)phthalonitrile onto the Co(II) ion in the presence of a mild base, 1,8-diazabicyclo[5.4.0]undec-7-ene (DBU), at an elevated temperature of 210°C under an inert atmosphere.[33] The structural elucidation of CoPc-fur was confirmed through mass spectrometry, and the obtained data were consistent with previously published results.

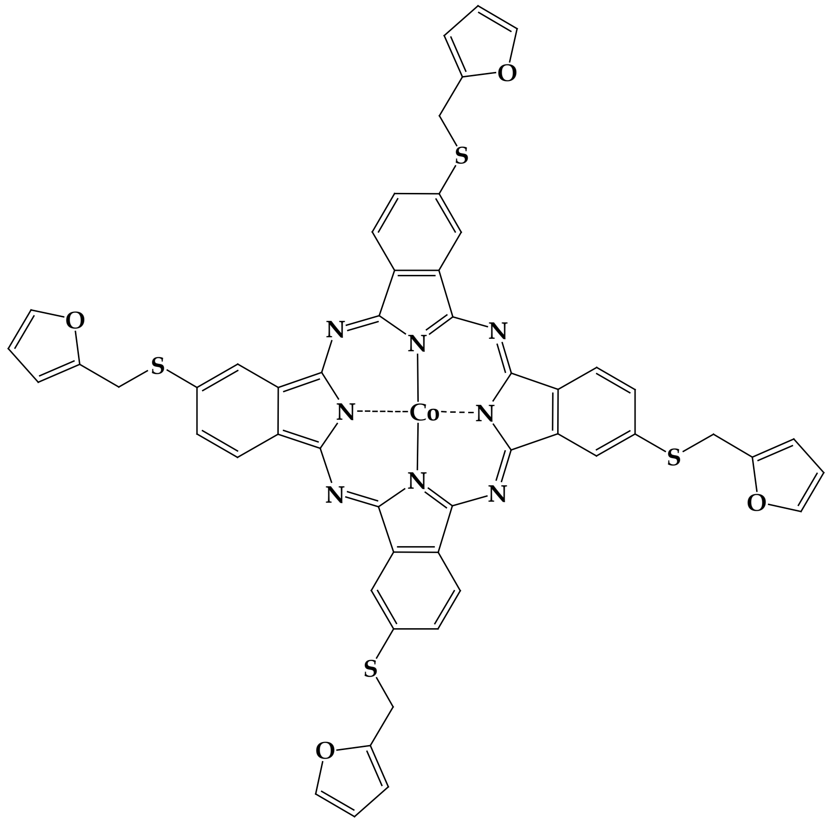

Figure 6.1: *The structure of CoPc-fur.*

A stepwise nanofabrication route towards the ENFs-**2** is depicted in S**cheme 6.1**. Firstly, a bulk polymeric solution of PANI was sequentially mixed with CoPc-fur and *f*-MWCNTs. This polymeric composite, PANI-CoPc-fur-*f*-MWCNTs were confined to the nanoscale size *via* electrospinning where this material was imbedded in PVA

ENFs. Even though PVA is an insulator under standard temperature and pressure conditions, literature illustrates that the doping of PVA with nanomaterials alters their electronic properties.[34,35] Successful characterization of the ENFs-**2** nanocomposite was microscopically and spectroscopically confirmed.

UV-Vis spectrophotometry was employed to confirm the inclusion of the metal complex, CoPc-fur, and the bulk polymer, PANI, into the hybrid polymeric material, PANI-CoPc-fur, *see* **Figure 6.2**. Specifically, the electronic spectrum of **1** revealed the characteristic Pc-based *Q*- (at 670 nm) and *B*-bands (at 359 nm), arising from π-π^* electronic transitions of the CoPc-fur component.[36] In the UV-Vis spectrum of the metal complex (CoPc-fur), analogous electronic transitions were observed at 685 nm and 335 nm. The combination of PANI and CoPc-fur resulted in a blue shift in the CoPc *Q*-band and a red shift in its Soret band. The blue shift in the *Q*-band is associated with the decreasing electron density of the cobalt center, due to the donation from the *d*-orbitals of Co to a π^* orbital of PANI.[37] Additionally, common broad charge transfer (CT) bands at 619 nm in the electronic spectra of free PANI and its conjugate were found close to the CT-band at 610 nm of the CoPc-fur. The PANI bands between 320 and 390 nm are due to π-π^* electron transitions (benzenoid segments) associated with the structural units of PANI chains.

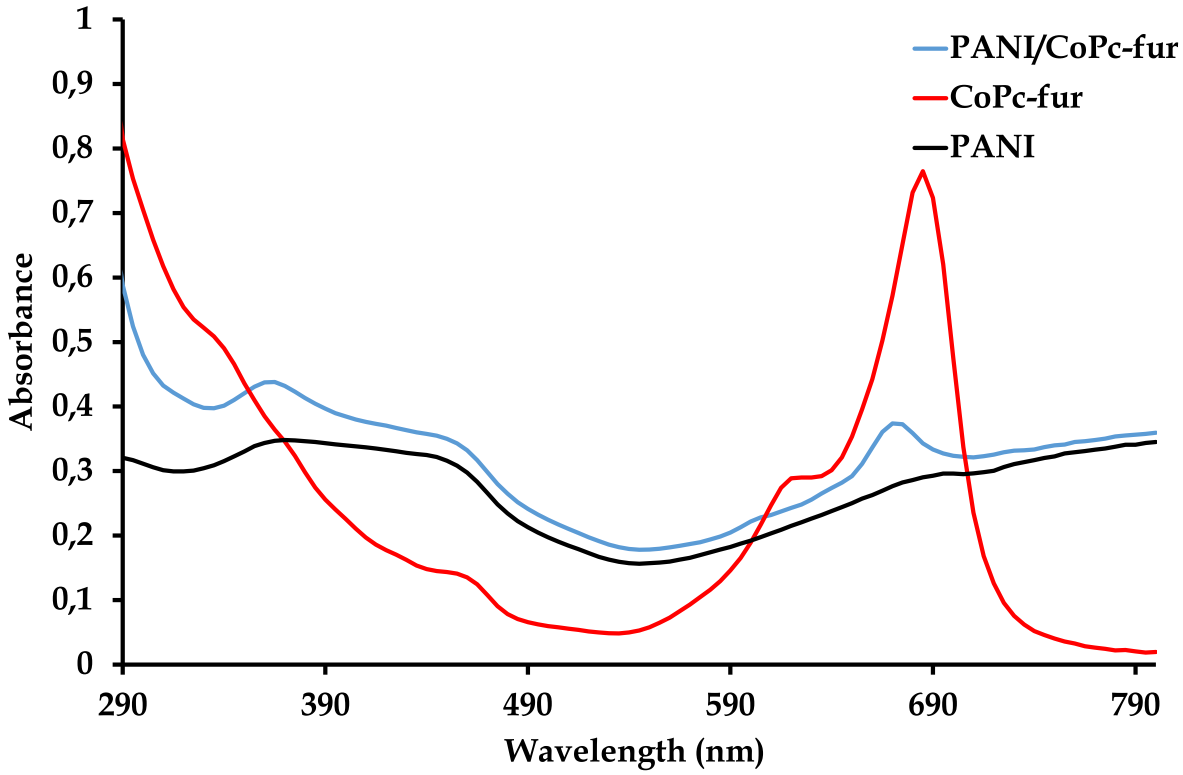

Figure 6.2: *Overlay UV-Vis spectra of PANI, CoPc-fur and the PANI-CoPc-fur nanocomposite.*

Composition analysis of the composite and its nanoconjugate was confirmed using solid-state infrared spectroscopy. More specifically, several commonalities were found when comparing the FTIR spectrum of the nanocomposite **2** with those of the doped PANI polymer and the PANI-CoPc-fur composite, *see* **Figure 6.3**. The v(C=C) signals of the respective FTIR spectra of PANI and PANI-CoPc-fur appear at the same stretching frequency at 1642 cm^{-1}, while the infrared stretches at 1310 and 1164 cm^{-1} are associated with the secondary aromatic amine v(C-N) signal.[38]

In addition, the fingerprint N-H signals associated with doping of PANI with HCl are common to both infrared spectra of unmodified PANI and its conjugate. More specifically, the broad and weak vibrational bands in the vicinity of 3530 cm^{-1} are assigned to the aliphatic amine bonds while the dominating signals between 2680 and 2350 cm^{-1} are indicative of NH_2^+ vibrations caused by the protonation of NH groups during the synthesis of PANI's emeraldine salt form.[39] The peaks at 1586 and 1480 are due to the vibrations N=Q=N (quinoid (Q)) and N=B=B (benzenoid (B)) rings.[40] On the other hand, the v(C=N) and $v(\text{C-H})_{furan}$ signals observed in the IR spectrum of the CoPc-fur, are absent in the IR spectrum of the PANI-CoPc-fur and this phenomenon could be reminiscent of metal complexes that have been overshadowed by PANI particles. The presence of these characteristic bands in the PANI-CoPc-fur composite indicated that the PANI structure was retained even after incorporating CoPc-fur.

The nanoconjugation of PANI-CoPc-fur with *f*-MWCNTs leads to the suppression of the weakening N-H and NH_2^+ vibrations within the IR spectrum of PANI-CoPc-fur-*f*-MWCNTs suggests that the electronic properties of this PANI constituent differs from that in the PANI-CoPc-fur polymeric composite. The $v(\text{C-N})_{PANI}$ signal vibrates of the nanoconjugate (1178 cm^{-1} for PANI-CoPc-fur and 1252 cm^{-1} for PANI-CoPc-fur-*f*-MWCNTs) at higher energies while a new C-H stretch is observed at 2950 cm^{-1}. Analysis of the IR spectrum of the nanoconjugate also illustrates intense vibrations corresponding to the carboxylic acid groups v(O-H) at 3441 cm^{-1} and v(C=O) 1639 cm^{-1} of the *f*-MWCNTs constituents.[41]

The embedding of the PANI-CoPc-fur-*f*-MWCNTs nanoconjugate into the PVA matrix leads to a decrease in the *f*-MWCNTs-related stretches while the broad vibration experiences blue-shifting from 3441 cm^{-1} to 3254 cm^{-1} and this signal can now be attributed to the OH groups of PVA and *f*-MWCNTs as well as the N-H bonds of PANI. The distinctive peak at 2912 cm^{-1} indicated the stretching vibration of the aromatic C-H groups of PANI and the aliphatic C-H groups of PVA.[42,43]

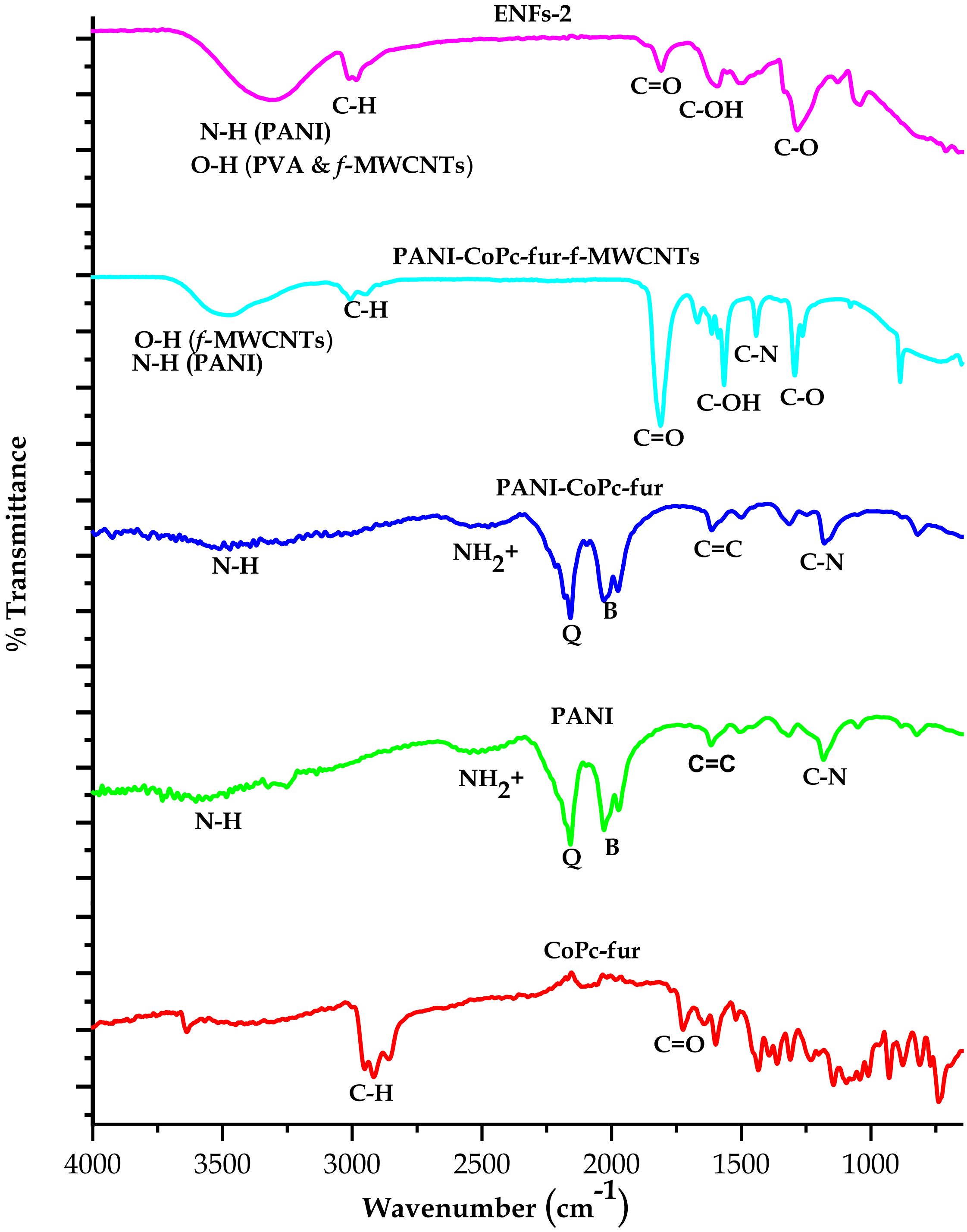

Figure 6.3: *Stacked FT-IR spectra of PANI, CoPc-fur, PANI-CoPc-fur, PANI-CoPc-fur-f-MWCNTs and ENfs-*2.

The Raman spectrum of CoPc-fur in **Figure 6.4** showed B_1g bands characteristic at 689 cm^{-1} and 1548 cm^{-1}, corresponding to the asymmetric stretching of the *v*(N-C) bonds and the in-plane bending and displacements of the nitrogen-carbon (C-N-C bridge) bonds in the phthalocyanine ring, respectively. These bands are consistent with the presence of CoPc-fur and provide valuable structural information about the phthalocyanine ring.[44]

Comparative analysis of the Raman spectra of PANI and PANI-CoPc-fur, showed that the backbone stretching mode at 1596 cm^{-1} was observed, and this is attributed to the C=C stretching of the phenyl rings in the conductive phase for the emeraldine salt form of polyaniline. Other characteristic bands included the C-N stretching mode at 1243 cm^{-1}, the C-H bending modes at 1168 and 1172 cm^{-1}, and the C=N stretching modes at 1327 and 1335 cm^{-1}. These bands confirmed the presence of PANI and the successful incorporation of CoPc-fur in the PANI-CoPc-fur composite.[45]

In the Raman spectra of *f*-MWCNTs and PANI-CoPc-fur-*f*-MWCNTs, the D-band at 1353 cm^{-1} was observed, corresponding to the defects of the graphitic structure in the nanotubes. The G-band peaks at 1604 and G'-band 2710 cm^{-1} represents the crystalline graphitic planes of *f*-MWCNTs and PANI-CoPc-fur-*f*-MWCNTs.[46]

The intensity ratio of the D-band to the G-band peak (I_D/I_G ratio) in Raman spectroscopy is indicative of the extent of formation and defects in carbon-based materials like *f*-MWCNTs. In this study, the I_D/I_G ratio for *f*-MWCNTs was found to be 1.15, while for PANI-CoPc-fur-*f*-MWCNTs, it reduced to 0.97. This reduction in the I_D/I_G ratio suggests molecular interactions between PANI-CoPc-fur and *f*-MWCNTs.[46] The intense bands of the carbonaceous nanomaterial in the Raman spectrum of the nanoconjugate dwarf the vibrations of the other constituents, PANI and CoPc-fur. This suggests that the *f*-MWCNTs were well-dispersed into the nanocomposite, hence affecting the Raman signals of the PANI-CoPc-fur component.

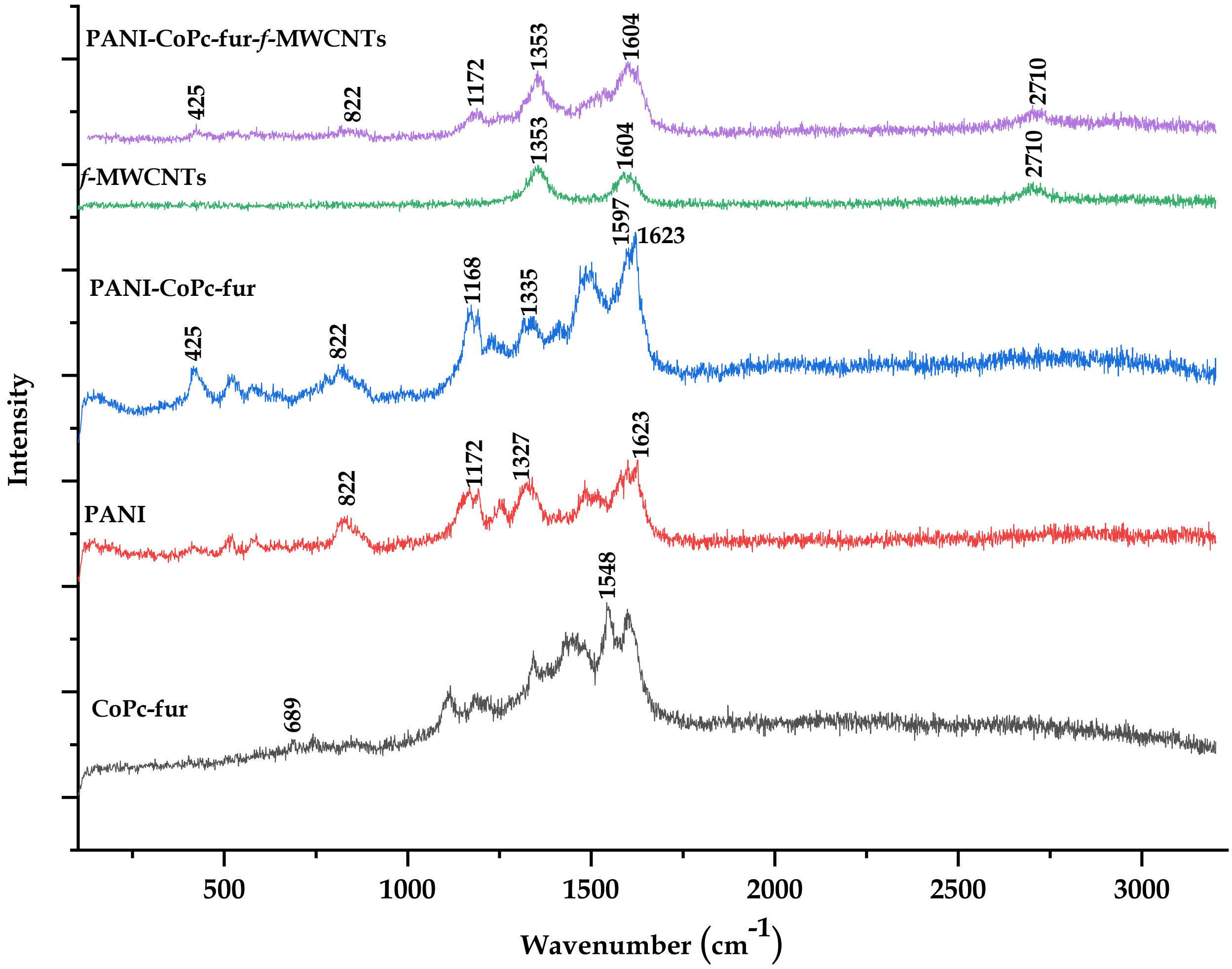

Figure 6.4: *Stacked Raman spectra of CoPc-fur, PANI, PANI-CoPc-fur, f-MWCNTs and PANI-CoPc-fur-f-MWCNTs.*

X-ray diffraction patterns of CoPc-fur, PANI, PANI-CoPc-fur, PANI-CoPc-fur-*f*-MWCNTs and ENFs-**2** were analyzed to support the fabrication of the various composite materials, see **Figure 6.5**. The XRD pattern of CoPc-fur displayed peaks at 7.29° and 19.71°, which can be attributed to the (100) and (104) planes of the metallic Co in the phthalocyanine ring; providing concrete evidence that confirms the formation of CoPc-fur and its crystalline nature.[47] The broadness of the XRD peak at 19.71° is typical of the amorphous nature of MPcs.

X-ray analysis of PANI illustrated a relatively sharper peak at 25.5°, along with two low-intensity broad peaks around 20.9° and 14.8°. These respective peaks correspond to the (200), (020), and (011) planes which are characteristic of the semi-crystalline structure of PANI in its emeraldine salt (ES) form.[10,48] In the XRD pattern of the PANI-CoPc-fur polymeric composite, similar peak angles were observed as in pure PANI and a peak at 7.29° can be directly correlated with CoPc-fur. The aforementioned spectral trends substantiate the successful incorporation into the PANI matrix.[10,47]

The XRD of *f*-MWCNTs showed characteristic peaks at $2\theta = 25.63°$ (002), 43.44° (100), and 53.26° (004), consistent with the crystalline structure of multi-walled carbon nanotubes.[49,50] In the XRD spectrum of PANI-CoPc-fur-*f*-MWCNTs nanoconjugate, analogous peaks to those of *f*-MWCNTs were found, but with reduced intensities which support the nanoconjugation of PANI-CoPc.[51] In the XRD spectrum of ENFs-**2**, a single peak at 19.53° (011) was observed which is attributed to the semi-crystalline PVA.[52]

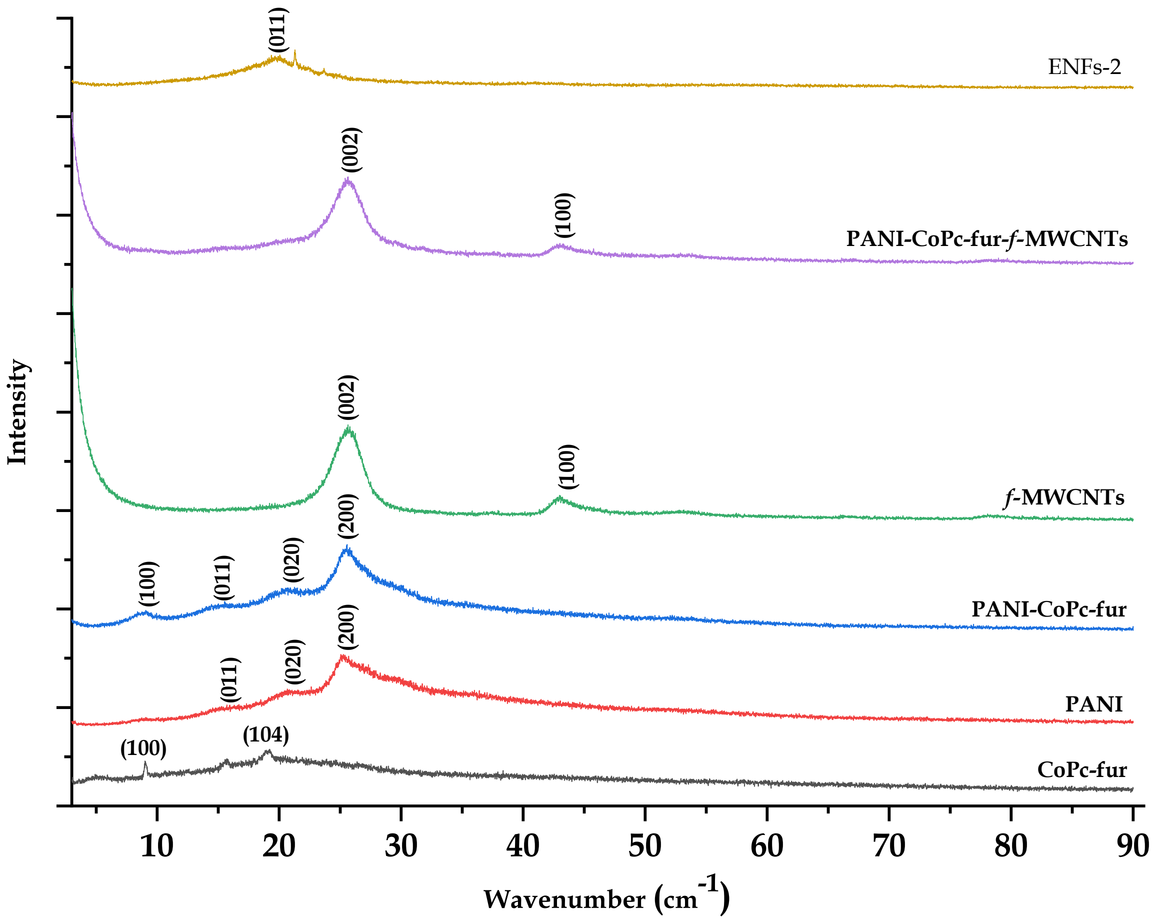

Figure 6.5: *Stacked X-ray diffractograms (XRDs) of CoPc-fur, PANI, PANI-CoPc-fur, f-MWCNTs, PANI-CoPc-fur-f-MWCNTs and ENFs-***2** *composites.*

The SEM micrographs of CoPc-fur, PANI, PANI-CoPc-fur, PANI-CoPc-fur-*f*-MWCNTs, and ENFs-**2** were captured to investigate the morphological changes that occur during the stepwise fabrication process depicted in **Scheme 6.1**. Indicative of literature trends, the SEM micrograph of the CoPc-fur shows smooth clumped particles that emphasize the aggregation occurring between the planar *pi*-conjugated molecules, see **Figure 6.6.**[53,54] Both the SEM micrographs of PANI and PANI-CoPc-fur displayed nanofibrous morphologies. The enhanced nanofibrous aggregation seen in the SEM micrograph of the PANI-CoPc-fur showed the interconnection between PANI network fibers, which could promote charge hopping and thereby improve the electrochemical properties of PANI composite fibres.[55]

An agglomeration of the morphological features of the *f*-MWCNTs and PANI-CoPc-fur was observed in the SEM micrograph of the PANI-CoPc-fur-*f*-MWCNTs nanocomposite. The coarseness of the nanofibrous particles is due to the presence of tubular-shaped *f*-MWCNTs. As expected in the case of ENFs containing no *f*-MWCNTs smooth, uniform nanofibers were produced. However, upon the incorporation of the *f*-MWCNTs in the ENFs-**2**, beaded nanofibers were formed. Therefore, the agglomeration effects observed in the SEM micrograph of the PANI-CoPc-fur-*f*-MWCNTs nanoconjugate are concentrated in the beads along the ENFs-**2** strands, which resulted in non-uniform and rough surfaces of the nanofibers.

The EDX spectra of ENFs-**2** and ENFs (which only include PVA and PANI) are shown in **Figure 6.7**. Carbon, chlorine, nitrogen and oxygen atoms from PANI, PVA and HCl (used as an acidic medium for PANI doping) were detected in ENFs by EDX analysis. The presence of carbon, chlorine, nitrogen, cobalt, sulphur and oxygen atoms characteristic of PVA, PANI, HCl and CoPc-fur embedded inside the ENFs was further confirmed by EDX analysis of ENFs-**2** in **Figure 6.7**B.

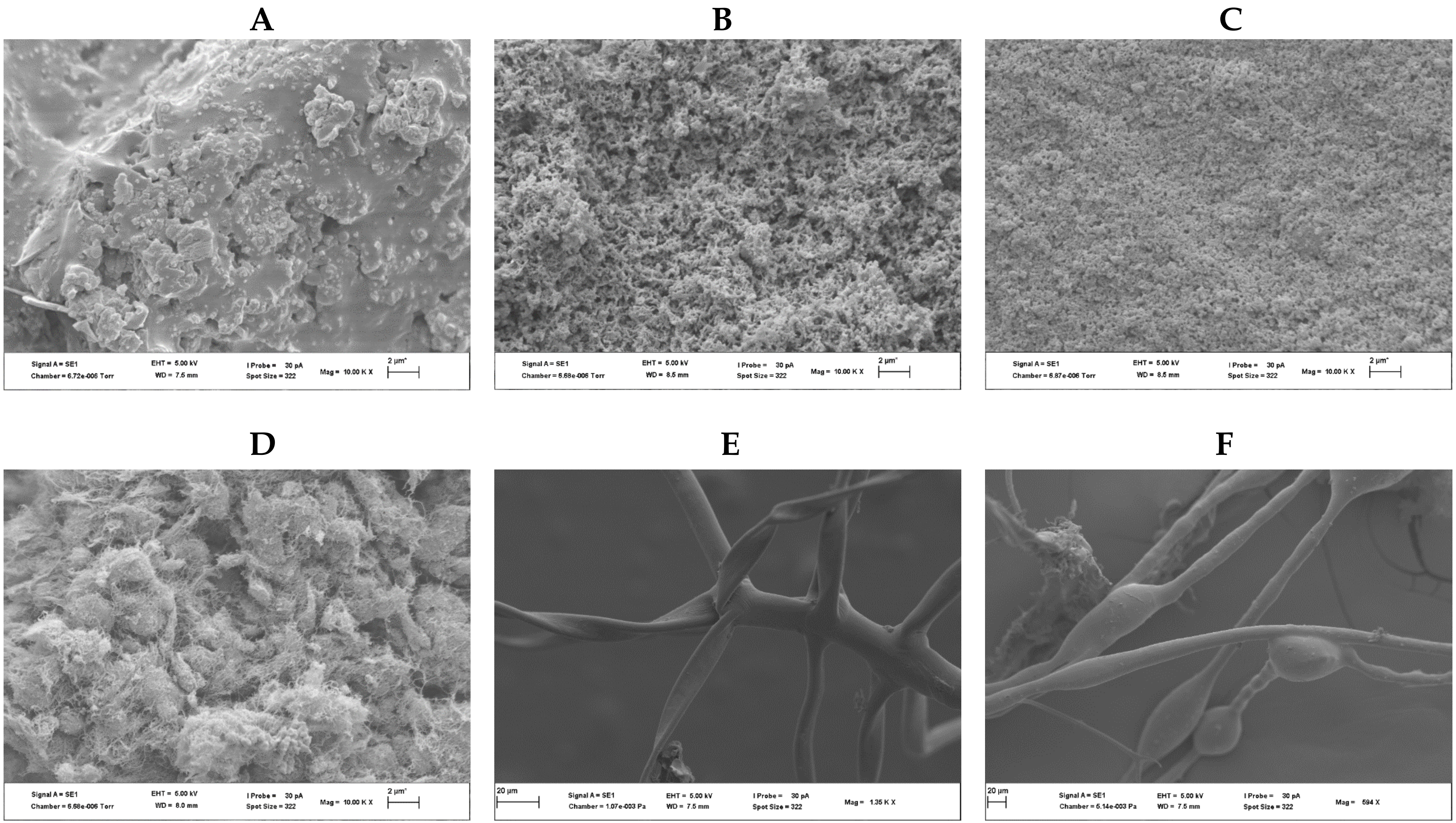

Figure 6.6: *SEM images of (**A**) CoPc-fur, (**B**) PANI, (**C**) PANI-CoPc-fur, (**D**) PANI-CoPc-fur-f-MWCNTs, (**E**) (PANI-CoPc-fur)PVA ENFs and (F) ENFs-2.*

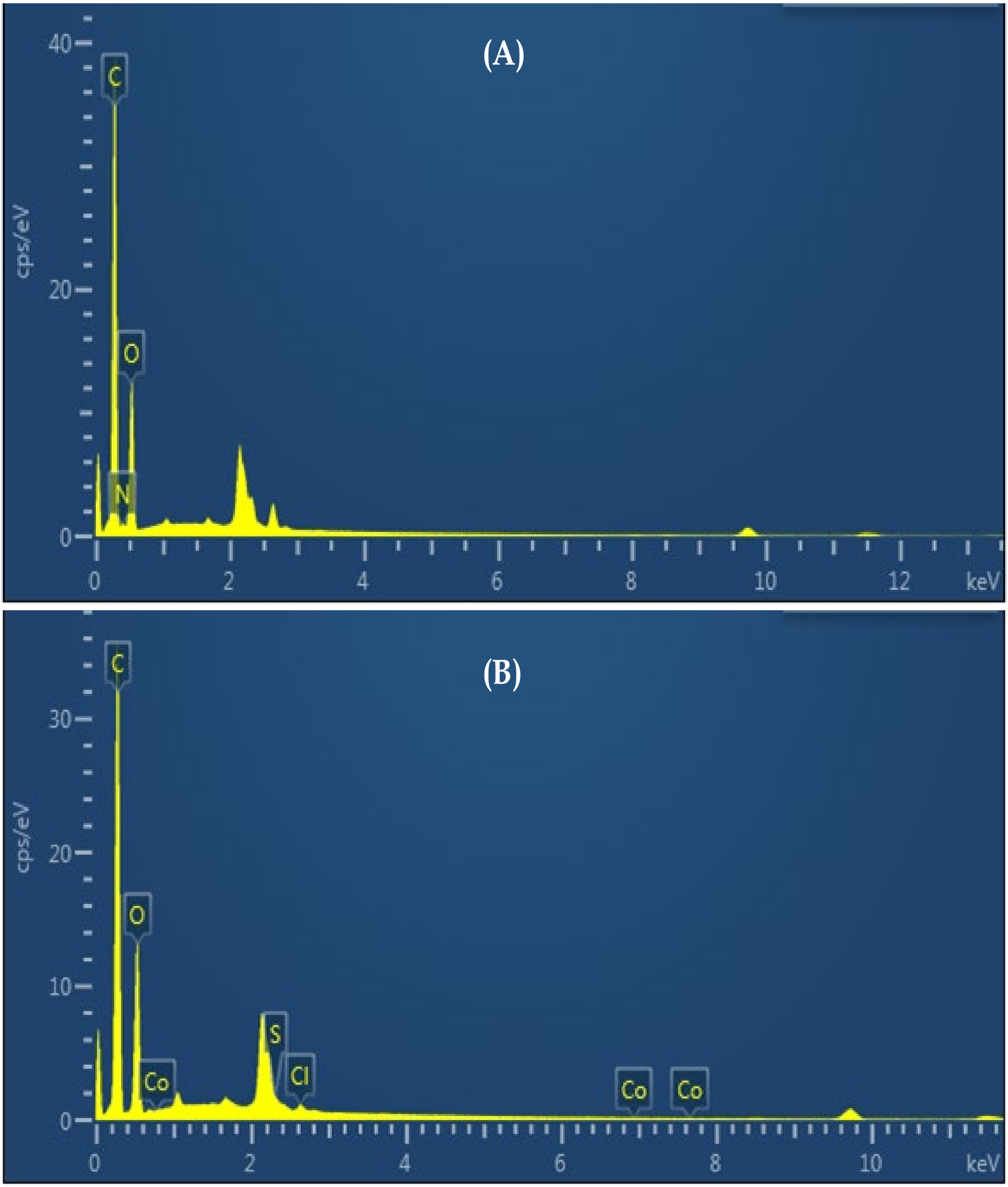

Figure 6.7: *EDX spectra of (A) ENFs and (B) ENFs-***2***.*

6.3.2. Electrocatalytic responses of the CMEs

Cyclic voltammetry was used to investigate the electrocatalytic activities of the various CMEs relative to that of the bare electrode. Acetaminophen (APAP) generally undergoes a two-electron quasi-reversible redox process on CME interfaces but the redox process can be significantly retarded on bare substrates culminating in irreversibility accompanied by low sensitivity, see **Figure 6.8**.[56] Literature trends illustrate that APAP oxidation at the CME surfaces occurs by multistep redox transformations, see **Scheme A2**. At the bare glassy carbon electrode (GCE|) surface, APAP showed respective anodic and cathodic peak currents at peak potentials of 0.376 V and 0.110 V, see **Figure 6.9**. After modifying the bare GCE with Nafion (NF), the anodic peak current at GCE|Nf was reduced compared to the bare |GCE, and the oxidative peak potential shifted favourably from 0.376 to 0.620 V.

On the GCE|ENFs-**2**-Nf, two distinct redox waves for the anodic and cathodic processes of APAP were observed at 0.508 V and 0.366 V, respectively. Additionally, greater anodic and cathodic peak currents were observed compared to the other modified electrodes, indicating a higher sensitivity and responsiveness to APAP. The higher electroactive surface area of the modified GCE|ENFs-**2**-Nf is accounted for by the larger peak currents, as it provides more active sites to induce electrocatalysis of the redox processes of APAP. Another favourable attribute of the CME is its faster electron-transfer kinetics based on the lower ΔE value (142 mV) as opposed to those of the bare GCE (266 mV) and GCE|Nf (244 mV).

The responsive intensity of APAP was high for GCE|PANI. however, the peak of APAP was not observed. This is attributed to the thick PANI film on the electrode surface, which resulted from drop-drying PANI onto the GCE surface rather than electropolymerization. The increased PANI film thickness likely blocked electron transfer between the solution and the electrode, leading to a lack of clear APAP peaks in the cyclic voltammogram.[57] Based on the observed results, the order of current response sensitivity for APAP is as follows: GCE|PANI > GCE|ENFs-**2**-Nf > Bare GCE| > GCE|CoPc-fur and GCE|Nf.

Considering the optimal electrocatalytic activity of the GCE|ENFs-**2**-Nf, it was used to conduct the optimization, kinetics, interference and real sample studies.

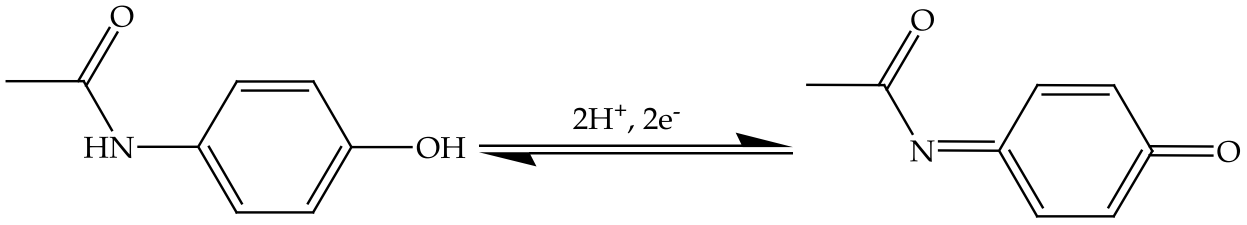

Figure 6.8: *APAPs two electron quasi-reversible redox process on CME.*

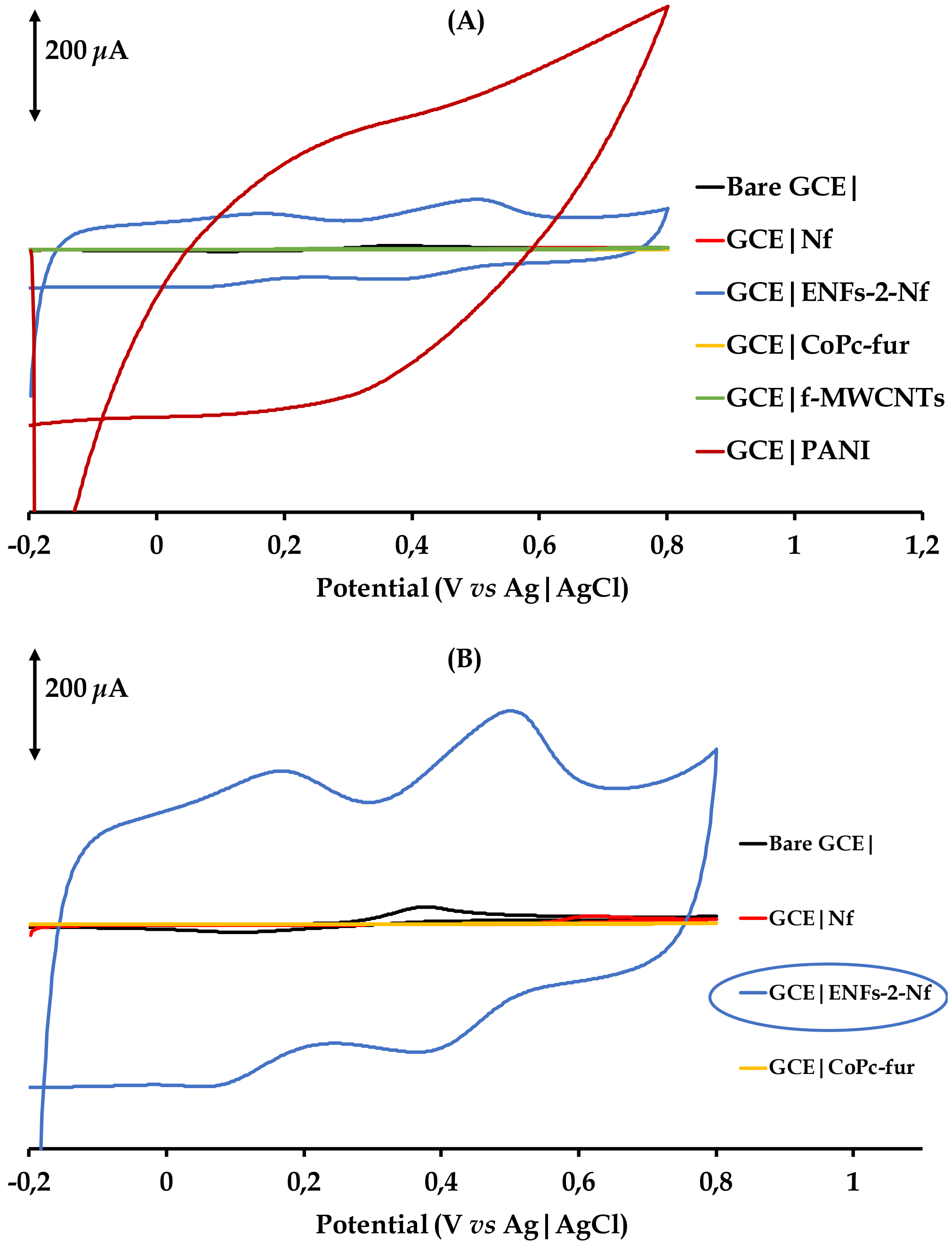

Figure 6.9: *CVs of 0.2 mM acetaminophen (APAP) in PBS using the bare GCE, GCE|Nf, GCE|CoPc-fur, GCE|PANI, GCE|f-MWCNTs and GCE|ENFs-***2***-Nf.*

6.3.3. *Stability and reproducibility*

The stability of the current response for the GCE|ENFs-**2**-NF toward APAP was investigated by performing 5 successive scans of 1.00 mM APAP in a pH 3.1 PBS solution (see **Figure A3**). During the first scan, the peak current slightly decreased, and the peak potential shifted toward a lower value. This initial behavior is attributed to redox active impurities accrued onto the surface GCE|ENFs-**2**-NF during its conditioning which affected the electrochemical response of the electrode toward the analyte. However, after the second scan, both the peak current and the peak potential stabilized, indicating that the modified electrode had reached a consistent state.

The stabilization of the peak current and potential after the second scan suggests that the initial surface effects or conditioning effects have been minimized, and thus , the electrode interface was pristine for the accurate electrochemical sensing of APAP. The average relative standard deviation (%RSD) calculated from the five successive measurements of the peak current was found to be 0.77% which is an indication of good reproducibility. The optimal stability of the |GCE-ENFs-**2**-NF makes it a highly reliable and robust nanocomposite material for the electrochemical sensing of APAP with good signal fidelity.

6.3.4. *The effect of pH*

The investigation of the pH effect on the current responses of a 1 mM APAP in phosphate-buffered saline (PBS) using square-wave voltammetry at GCE|ENFs-**2**-Nf revealed interesting pH-dependent behaviour, as shown in **Figure 6.10**. As the pH increased from 2 to 7, the peak potential for APAP shifted towards more negative values. This suggests that the oxidation of APAP is influenced by the pH of the solution. At lower pH levels, the peak potential was more positive, indicating a faster oxidation process, whereas at higher pH levels, the peak potential shifted towards more negative values, suggesting a slower oxidation process.

At pH 3.09, the maximum peak current was reached, indicating that the oxidation of APAP is most favourable at this pH value. Hence, pH 3.09 was chosen for further studies as it provided the best electrode activity for detecting APAP using the GCE|ENFs-**2**-Nf modified electrode. Similar pH-dependent behaviour for the oxidation of APAP has been reported in previous studies.[58] The pH-dependent behaviour can be attributed to changes in the protonation state of APAP and the electroactive species involved in the oxidation process. The protonation of functional groups in APAP can influence its redox behaviour, leading to shifts in peak potentials.[59]

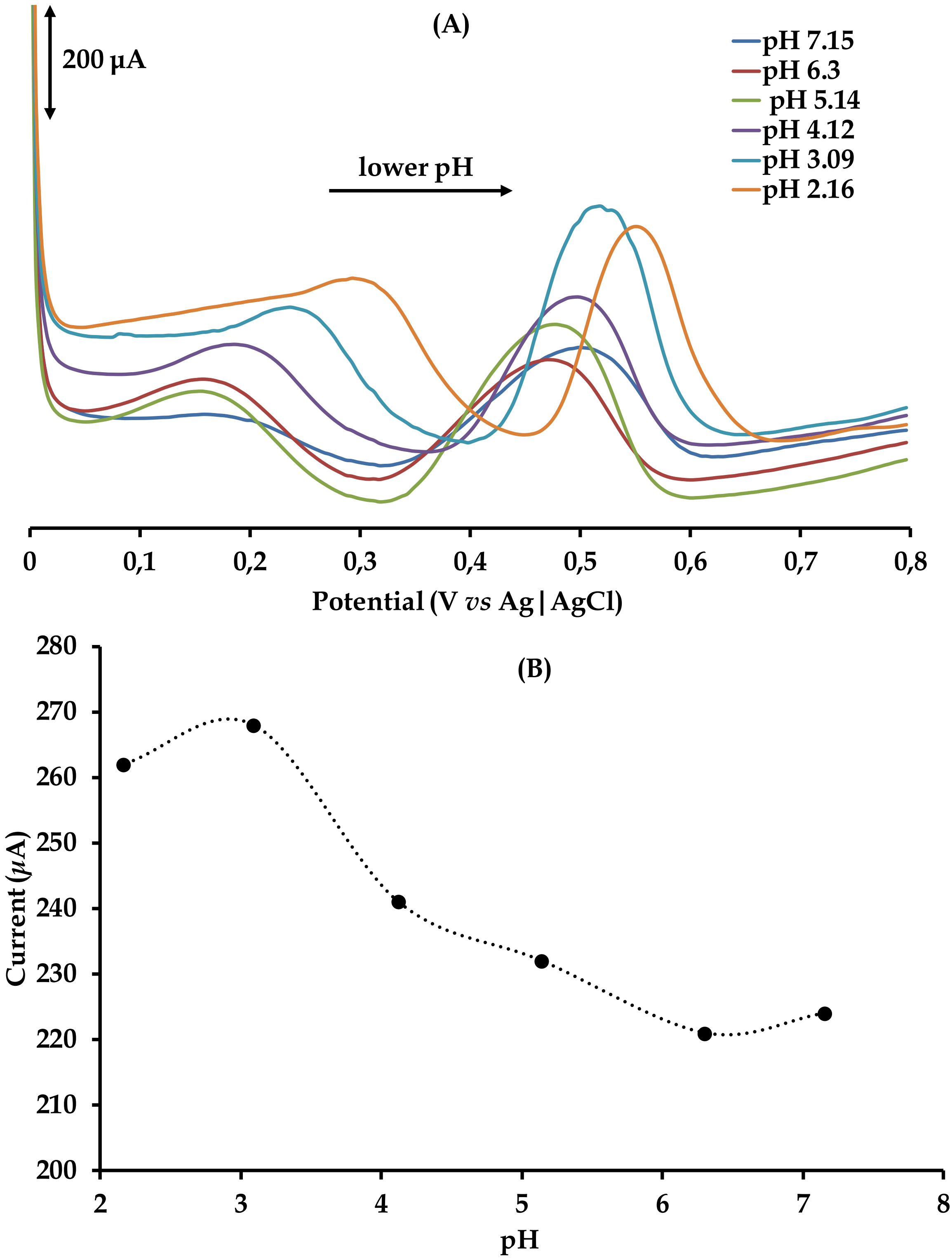

Figure 6.10: *DPV responses of APAP for the optimization of pH effects in PBS using the GCE|ENFs-*2*-NF.*

6.3.5. Effective surface area and surface coverage

The effective surface area of the chemically modified electrode (CME), GCE|ENFs-**2**-Nf, was determined using cyclic voltammetry measurements of $K_3[Fe(CN_6)]$ at increasing scan rates, as shown in **Figure 6.11**. The Randles-Sevcik equation (Eq**. 6.1**) was used to calculate the effective surface area:

$$I_{pa} = 2.69\ x10^5 n^{3/2} AC\sqrt{Dv} \tag{6.1}$$

where A is the effective surface area, D is the diffusion coefficient of $K_3[Fe(CN_6)]$, v is the scan rate, C is the substance concentration of $K_3[Fe(CN)_6]$, n is the number of electrons transferred (n = 1). By plotting I_{pa} vs $v^{1/2}$ plots, the slope of the resulting linear plot is used to calculate the effective surface area of the modified electrode. The calculated effective surface area for GCE|ENFs-**2**-Nf was found to be 1.58 cm^2, which is significantly higher than the area of the bare electrode (0.071 cm^2). This substantial increase in surface area can be attributed to the presence of PANI and *f*-MWCNTs in the nanofibers, which provide additional electrocatalytic sites.

The calculated effective surface areas determined in equation 6.1, and the total charge under the oxidation peak currents were both used to calculate the surface coverage (Γ) of GCE|ENFs-**2**-Nf using equation **6.2**:

$$\Gamma = \frac{Q}{nFA} \tag{6.2}$$

Γ is the surface coverage, n is the number of transferred electrons, F is the Faraday constant and A is the effective surface. The calculated surface coverage for GCE|ENFs-**2**-Nf was found to be 4.497 x 10^{-9} mol cm^{-2}. This value is higher than the value of 1 x 10^{-10} mol cm^{-2} that corresponds to a MPc molecules lying flat on the electrode surfaces.[60] The higher surface coverage of the CME directly translates to the accessibility of electrocatalytic sites, which in turn render increased electrical conductivity.

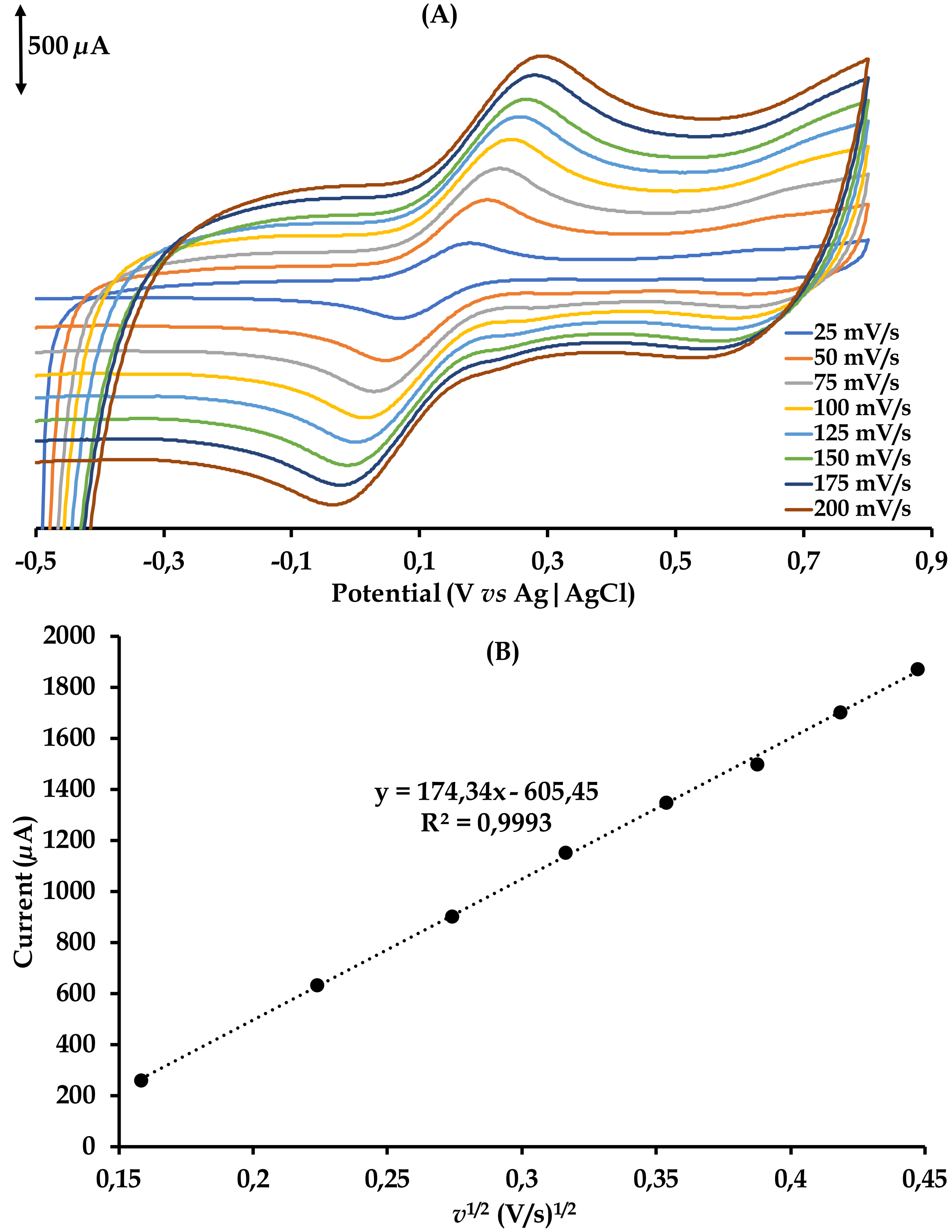

Figure 6.11: *(**A**) CVs at increasing scan rates of 5 mM K$_3$[Fe(CN$_6$)] prepared in an aqueous solution containing 0.1 M KCl at GCE|ENFs-**2**-Nf. (**B**) Plot of I$_{pa}$ vs square root of scan rate.*

6.3.6. Electrochemical impedance spectroscopy studies

EIS was employed to study the electrochemical impedance and electron transfer capacity differences across the bare electrode and GCE|ENFs-**2**-Nf. The measurements were conducted in a solution containing potassium ferricyanide and 0.1 M KCl as the supporting electrolyte. The Nyquist plots obtained for both the bare GCE| and GCE|ENFs-**2**-Nf are presented in **Figure 6.12**.

Using the equivalent circuit shown in **Figure 6.12(c)**, good correlations are found between the experimental and simulated data. The circuit is made up of Rs, R_{ct}, C_{dI} and Z_w which are the solution-electrolyte resistance, charge-transfer resistance, constant phase element and Warburg impedance, respectively. The EIS plots are composed of a semicircle arc in the high-frequency range and a straight line in the low-frequency range. The arc corresponds to the charge transfer limiting process due to the CPE being in parallel to R_{ct}, while the straight line is related to the diffusion-controlled mass transport of ferric ions to the electrode interface.[61] The tabulated EIS parameters indicate that the GCE|ENFs-**2**-Nf has a lower R_{ct} (1.10 Ω) value compared to the bare GCE (6.87 Ω), which emphasizes the influence of the electron-mediating thin film improving the charge transfer performance of the CME, refer to **Table 6.1**.

Table 6.1*: EIS data collected in a 5 mM [$K_3Fe(CN)_6$] using bare and modified (|GCE-ENFs-**2**-Nf) electrodes.*

GC electrode	**Rs (Ω)**	**Rct (Ω)**	**Zw**	**C_{dI} (µMho)**	***n***
Bare	39.1 (0.4)	6.87 (3.3)	152 (3.6) µMho	14.5 (4.6)	0.938
Modified	71.7 (0.9)	1.10 (2.8)	1.10(5.8) TMho	7.45 (6.2))	0.672

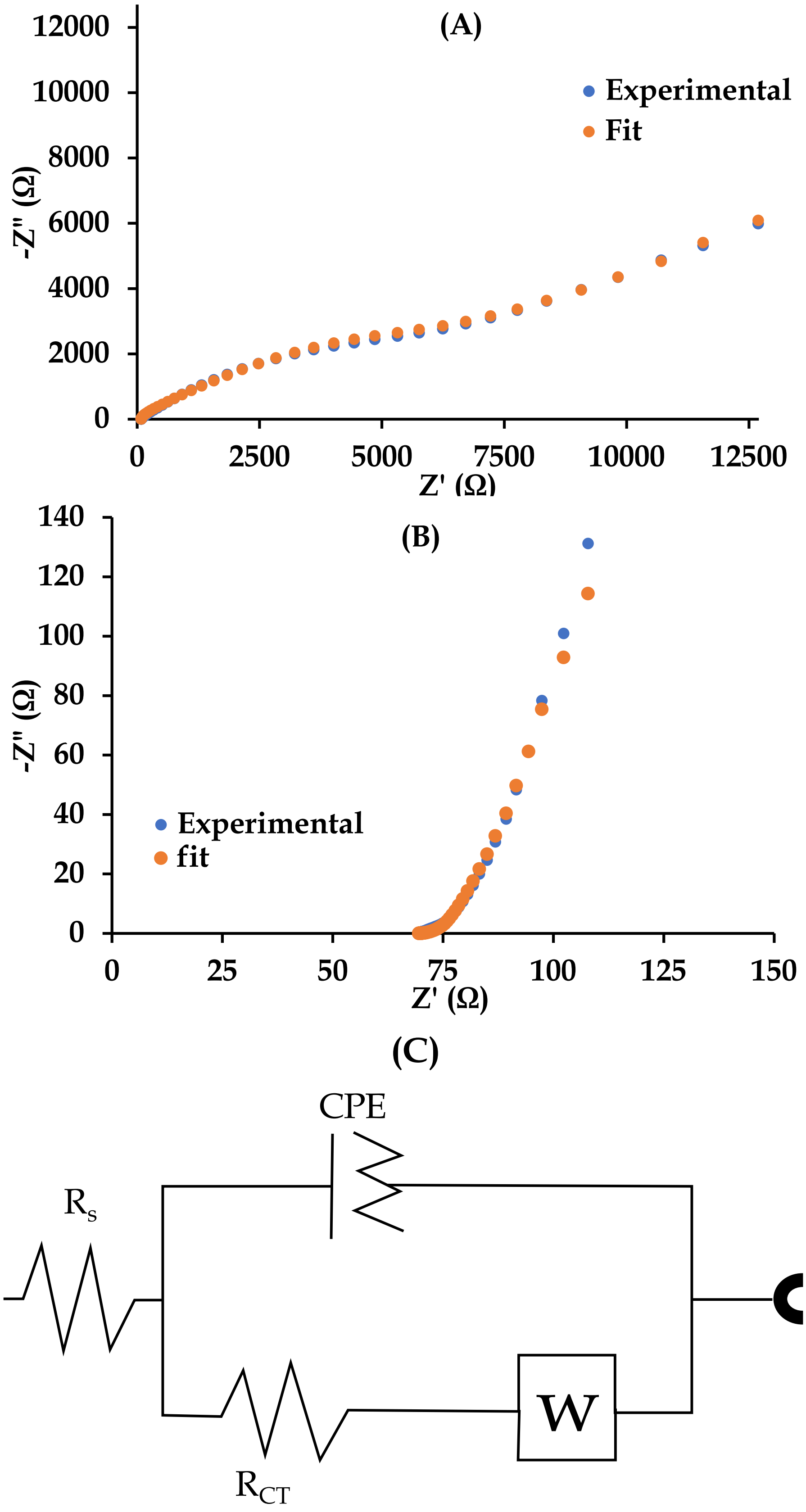

Figure 6.12: *Nyquist plots of 5 mM [Fe(CN)$_6$] prepared in 0.1 M KCl using the (**A**) bare GCE and (**B**) GCE|ENFs-**2**-NF. (**C**) The equivalent circuit is used to fit the EIS data.*

The phase angle for the bare GCE ~ 53.4° was higher than that obtained for GCE|ENFs-**2**-Nf ~ 0.93°, see **Figure 6.13**. This implies that both phase angle values for the studied electrode surfaces in this work are less than the ideal 90° for a true capacitor. The superior electrocatalytic activity of GCE|ENFs-**2**-Nf towards the oxidation of APAP is further confirmed by its Bode plot when compared to that of the bare GCE. In particular, the non-uniformity of the constituent components of the CME thin film culminates in higher surface roughness ($n < 1$) leading to the phase angle shifting towards lower frequency.[62]

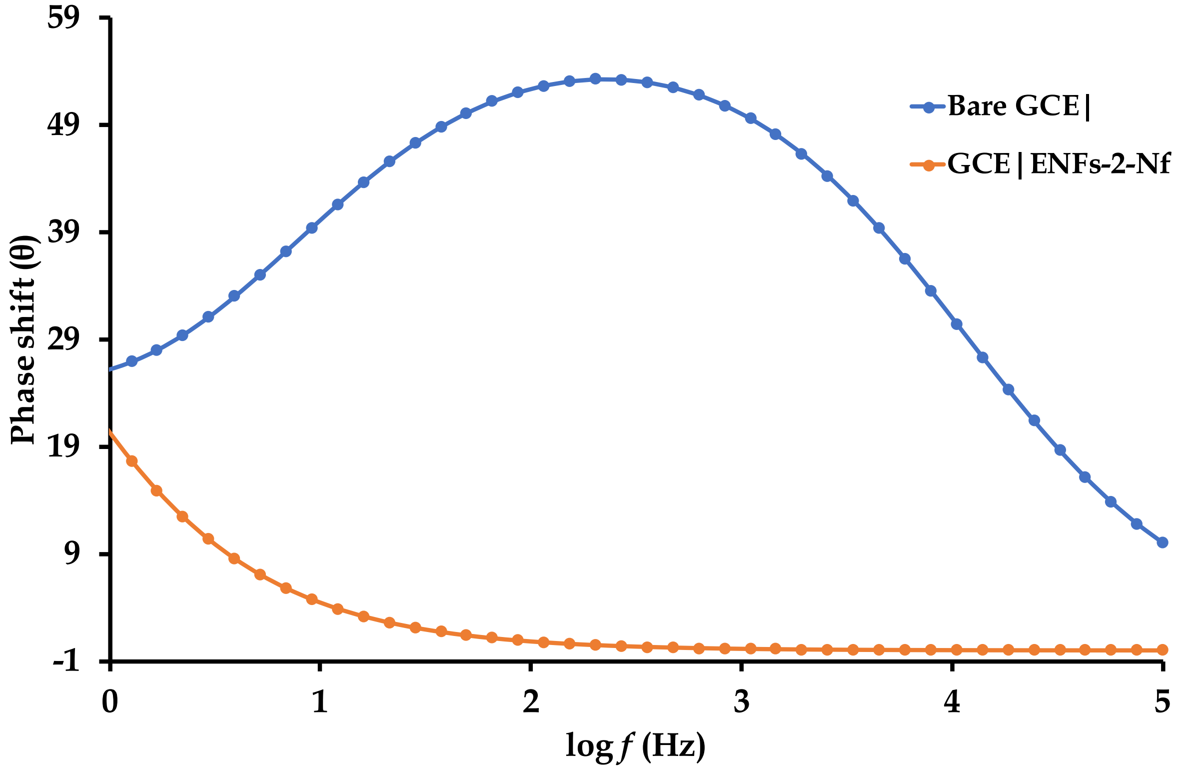

Figure 6. 13: *Bode plots generated at 5 mM [Fe(CN)₆] prepared in 0.1 M KCl with bare GCE and GCE|ENFs-2-Nf.*

6.3.7. Mechanism of electrocatalysis

Cyclic voltammetric responses of increasing scan rates for acetaminophen (APAP) using the GCE|ENFs-**2**-Nf are presented in **Figure 6.14**. A plot of oxidation peak currents versus the square root of scan rates displays high linearity based on the correlation coefficient (R^2) of 0.9971, see **Figure 6.14B**. In addition, the progressive of oxidation peak currents affirms that mass transport of APAP towards the CME surface is diffusion controlled. **Figure 6.14C** shows the linear relationship between the oxidation peak potential (E_{pa}) and the logarithm of the scan rates (Log v) and this Tafel plot was used to calculate the Tafel slope (Eq. 3):

$$E_{pa} = \frac{2.3RT}{2(1-\alpha)Fn_{\propto}} \log v + K, \qquad (\mathbf{6.3})$$

where the number of electrons involved in the rate-determining step is $n_{\propto}$, the scan rate is v, K is the intercept from the linear equation and the transfer coefficient is defined as α. The calculated Tafel slope is 205.4 mV/decade and it is higher than the 30-120 mV/decade range, where electrocatalysis is determined by electron-transfer kinetics. Higher Tafel slopes are due to substrate-catalyst interactions, where the substrate binds tightly to the catalyst as the reaction intermediate.[63]

In fact, the drifting of the APAP oxidation peak potentials with incrementing scan rates within **Figure 6.14A** is a typical feature of analytes being adsorbed on CME surfaces. Indicatively, shifts in the reduction potentials of the adsorbed oxidized DA can be readily assigned to the stripping of the DA from the CME surface. Of particular importance is that when using the same GCE|ENFs-**2**-Nf CME in triplicate, no surface fouling is observed given the high reproducibility between consecutive cyclic voltammetry runs at the same scan rates, see **Figure 6.14C**. The reproducibility in the electrocatalytic sensitivities of the CME is testimony to the stability and efficacy of the CME.

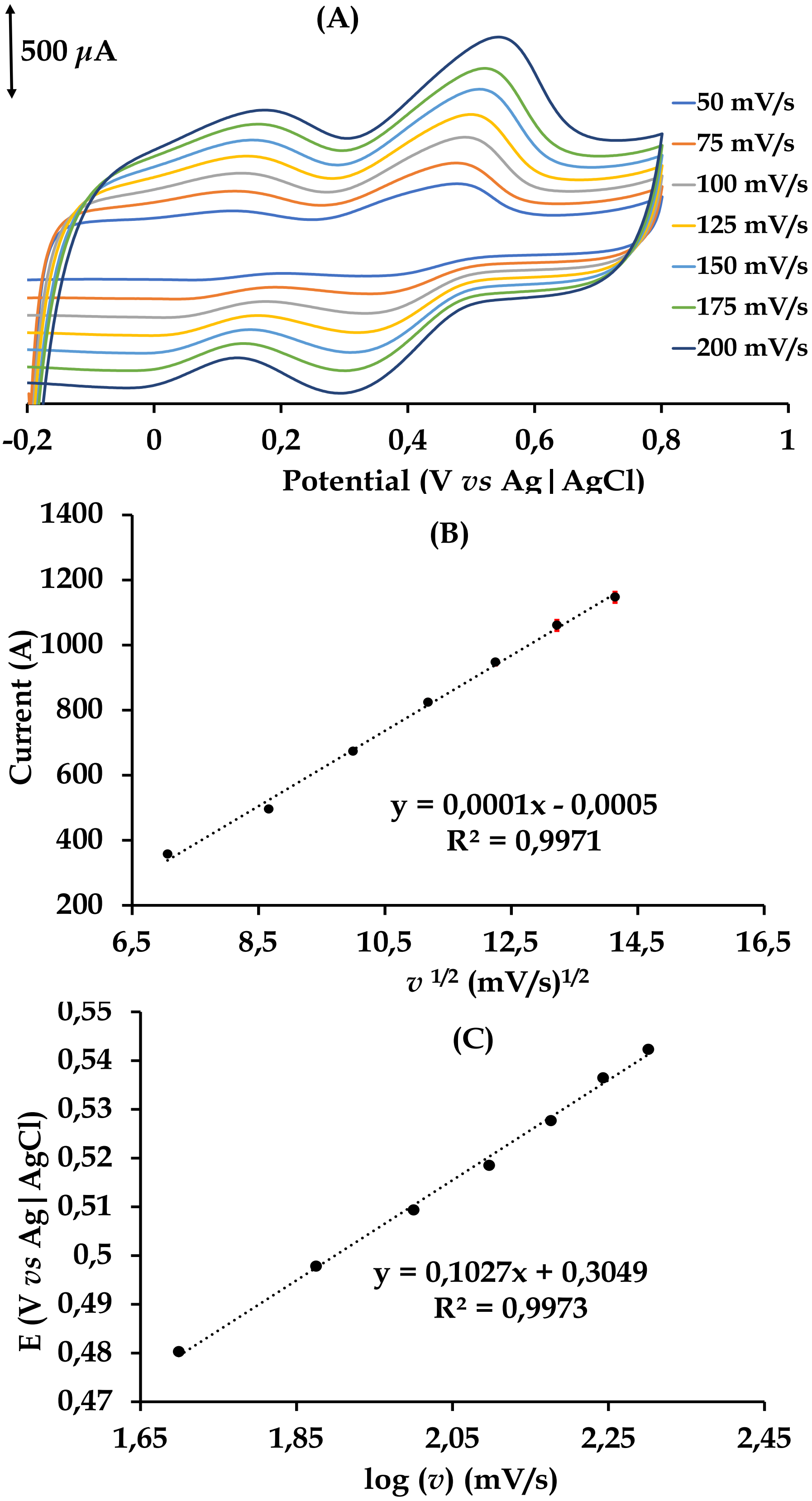

Figure 6.14: ***(A)*** *Electrocatalytic CVs of APAP recorded at increasing scan rates (50-200 mV/s) using the GCE|ENFs-2-Nf.* ***(B)*** *The plot of peak current against the square root of scan rate and* ***(C)*** *plot of oxidation peak potential (E_{pa}) against the Log of scan rate.*

6.3.8. Hydrodynamic kinetic studies

The convection-controlled kinetics of GCE|ENFs-**2**-Nf were investigated using a rotating disk electrode (RDE) at various rotation rates while collecting linear sweep voltammograms at a low scan rate to minimize diffusion, **Figure 6.15A**. The convection-controlled mass transport was substantiated by applying the Levich equation (**Eq. 6.4**) where a linear relationship was attained between the limiting current (I_L) and the square root of the rotational speeds ($w^{1/2}$) of the rotating disk electrode (RDE).

$$I_L = 0.62nFAD^{2/3}v^{-1/6}\omega^{1/2}C_0 \quad \textbf{(6.4)}$$

D is the diffusion coefficient, A is the CME surface area, v is the kinematic viscosity, ω is the rotation rate and C_0 is the bulk concentration of APAP.

In general, the kinetic and mass transport parameters may be separated using the Koutecky-Levich equation (**Eq. 6.5**), and the convection-controlled rate constant can be calculated using this equation.[64]

$$\frac{1}{I_L} = \frac{1}{nFC_0k\Gamma} + \frac{1}{0{,}62nFAD^{\frac{2}{3}}v^{-\frac{1}{6}}C_0\omega^{\frac{1}{2}}} \quad (\textbf{6.5})$$

The Koutecky-Levich plot of $1/I_L$ against $1/\omega^{1/2}$ gave a linear relationship and the *y*-intercept of this plot was used to calculate a rate constant which was found to be 1.64 x 10^2 $M^{-1}s^{-1}$ for the oxidative reaction of APAP occurring at the GCE|ENFs-**2**-Nf surface, **Figure 6.15C**. The magnitude of GCE|ENFs-**2**-Nf is approximately half that of GCE|CoPc-bo-*f*-MWCNTs (6.9 x 10^4 $M^{-1}s^{-1}$) and GCE|CoPc-flav-*f*-MWCNTs (3.48 x 10^4 $M^{-1}s^{-1}$) electrodes prepared kantize et al., (2019) suggesting a slower convection mass transport rate.[65]

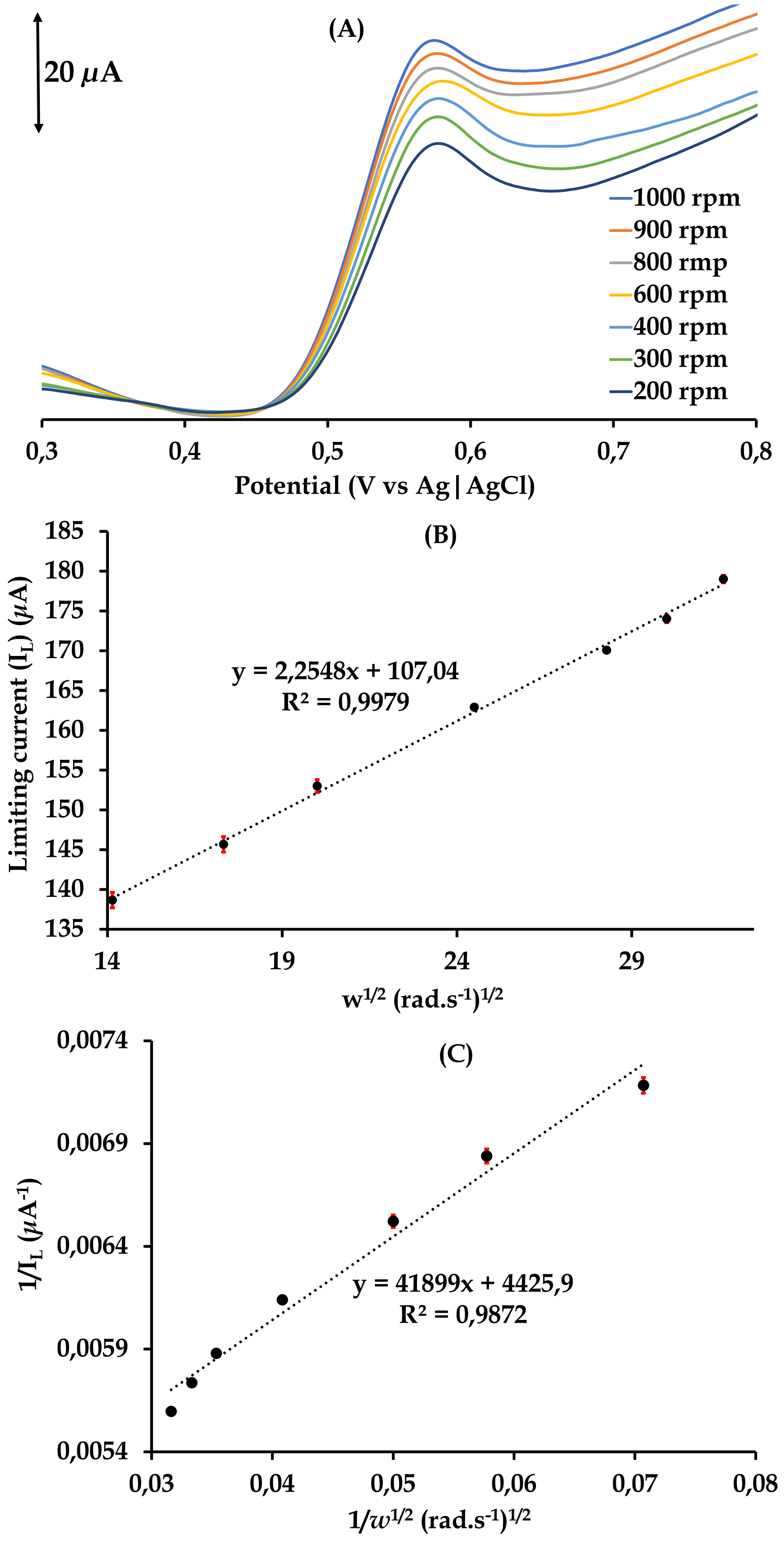

Figure 6.15: *(**A**) RDE-LSVs of GCE|ENFs-**2**-Nf (1) in PBS (pH 3.09) in the presence of 1 mM APAP and a scan rate of 0.010 V/s, (**B**) the Levich, (**C**) and the Koutecky-Levich plots.*

6.3.9. Diffusion-controlled kinetics

The single-step chronoamperometry (CA) experiment using the GCE|ENFs-**2**-Nf allowed for the calculation of the diffusion-controlled electro-oxidation rate constant for acetaminophen (APAP), see **Figure 6.16**. An overpotential of 0.508 V was applied with respect to the oxidation peak potential (E_{pa}) obtained from the cyclic voltammograms of APAP. The data were collected at intervals of 5 to 20 seconds, enabling the calculation of the kinetic rate constants. The simplified equation (**Eq. 6.6**) was used to calculate the electrocatalytic rate constant:

$$\frac{I_c}{I_b} = \pi^{1/2}(kC_o t)^{1/2} \qquad (\mathbf{6.6})$$

where I_c and I_b are the catalytic currents attained at GCE|ENFs-2-Nf in the presence and absence of APAP, respectively. In addition, the catalytic rate constant (k) is expressed in $M^{-1}\ s^{-1}$ for APAP oxidation and t = time elapsed (s). The linear plots for the I_{cat}/I_{buf} *vs* $t^{1/2}$ at different concentrations are presented in **Figure 6.16B**. The slopes of these plots were expressed against the concentrations of APAP to obtain another linear relationship shown in **Figure 6.16C** which is represented by **Eq. (6.7)**

$$y = 1.1748 \times 10^6\ [APAP] + 51.114,\ R^2 = 0.9621 \qquad (\mathbf{6.7})$$

As the slope of **Eq. (6.7)** is equal to πk, the calculated rate constant is $3.73 \times 10^5\ M^{-1}\ s^{-1}$. This rate constant is in the order of $10^5\ M^{-1}\ s^{-1}$ and is larger than the values reported in previously reported studies for modified GCEs used in the detection of APAP, refer to **Table 6.2**. The faster APAP diffusion-controlled kinetics of the ENFs-2-Nf conductive film on a GCE re-emphasizes the synergistic effects of its elementary constituents.[66]

Table 6.2: *Comparison of catalytic rate constants for the detection of APAP using CME*

Modifying Layer	**Analyte**	**K ($M^{-1}s^{-1}$)**	**Reference**
ENFs-**2**-Nf	APAP	1.07 x 10^2	This work
CoPc-fur-*f*-MWCNTs	APAP	1.67 x 10^2	[65]
NGQDs	APAP	3.26 × 10^2	[67]
N,N,N-CoPc@NGQDs	APAP	3.08 × 10^4	[67]
AuNPs/poly(trisamine)	APAP	2.28 × 10^3	[68]
CHM	APAP	1.12 x10^2	[69]

Abbreviation: **CoPc-fur-MWCNTs:** Cobalt phthalocyanine-furone-MWCNTs, **N,N,N-CoPc@NGQDs:***N,N',N''*-(((23-(4-aminophenoxy)phthalocyanine-2,9,16-triyl)tris(oxy))tris(benzene-4,1-diyl))triacetamidocobalt(II) covalently bonded to NGQDs, **AuNPs:** gold nanoparticles, **CHM:** cobalt hydroxide nanoparticles

6.3.10. Determination of analytical parameters

Linear ranges of APAP detection were readily determined from calibration graphs generated using CA, RDE-LSV and SWV, respectively. Also, the limits of detection and quantification (LOD and LOQ) values were calculated using the different calibration plots from the following equations: LOD = (3*stdb/k) and LOQ = (10*stdb/k), where stdb is the standard deviation of the blank and k is the slope of the linear calibration curve, see **Figure 6.16(A)**. A linear range of 2-100 μM using the CA technique was attained.The calibration equation obtained from the linear regression analysis is given as follows:

$$I = 0.0094\,[APAP] + 0.5964,\ R^2 = 0.993 \qquad (\mathbf{6.8})$$

The LOD and LOQ were found to be 2.99 μM and 9.97 μM, respectively. A calibration reproducibility ranging from 0.31 to 2.7% RSD (N=3) was established at different concentrations of APAP.

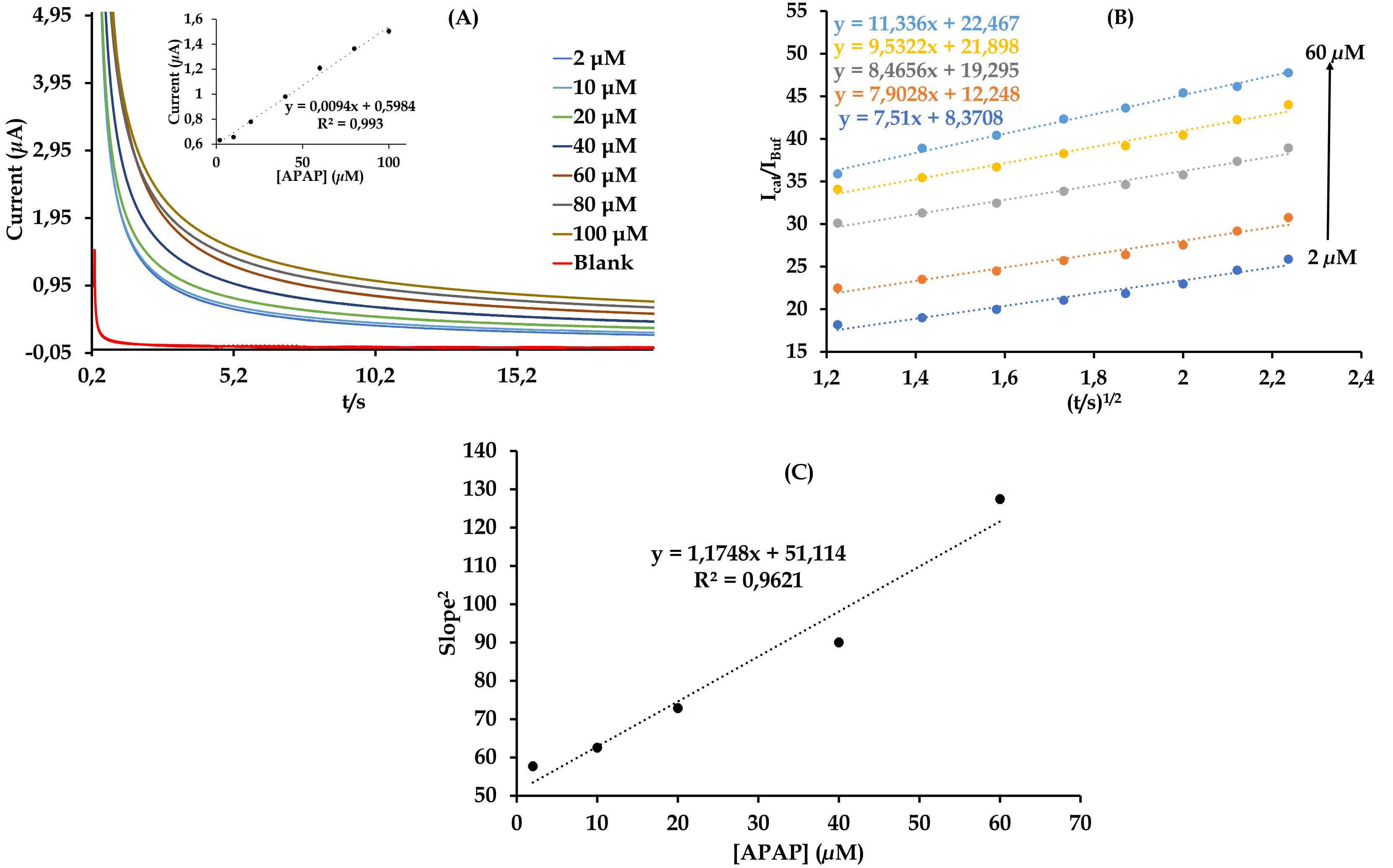

Figure 6.16: *(A) Chronoamperograms for GCE|ENFs-***2***-Nf in varying concentrations of mM APAP in pH 3.09 PBS buffer. Potential of 0.508 V was applied (***insert calibration graph at t = 5 s***), (***B***) plot of $t^{1/2}$ Vs (I_{cat}/I_{buf}) and (***C***) plot of concentration vs slope.*

Furthermore, using the GCE|ENFs-**2**-Nf, a direct proportional relationship was attained between the APAP oxidation LSV currents and increasing APAP concentrations in a range of 10-100 μM. The RDE-LSV data were obtained at a fixed rotation speed of 100 rpm and a scan rate of 10 mV/s, see **Figure 6.17**. The calibration equation obtained from the linear regression analysis is given as follows:

$$I = 0.0251[APAP] + 1.2864, R^2 = 0.9869 \qquad (\mathbf{6.9})$$

The calculated LOD and LOQ for GCE|ENFs-**2**-Nf are 1.72 μM and 5.23 μM, respectively. A calibration reproducibility ranging from 1.9 to 6.9% RSD (N=3) was established at different concentrations of APAP and the values are within the acceptable range at the 95% confidence level.

The SWV responses of GCE|ENFs-**2**-Nf towards increasing concentrations of APAP are shown in **Figure 6.18**. The oxidation currents of APAP at the GCE|ENFs-**2**-Nf interface increased linearly as its concentration increased from 10 µM to 200 µM.

$$I = 0.0224\ [\mu M][APAP] + 0.5889\ ,\ (R^2) = 0.9981 \qquad (\mathbf{6.10})$$

The limit of detection for acetaminophen was determined to be 0.094 µM, while the limit of quantitation was found to be 0.28 µM using the square wave voltammetry technique. A calibration reproducibility ranging from 1.3 to 4.2% RSD (N=3) was established at different concentrations of APAP.

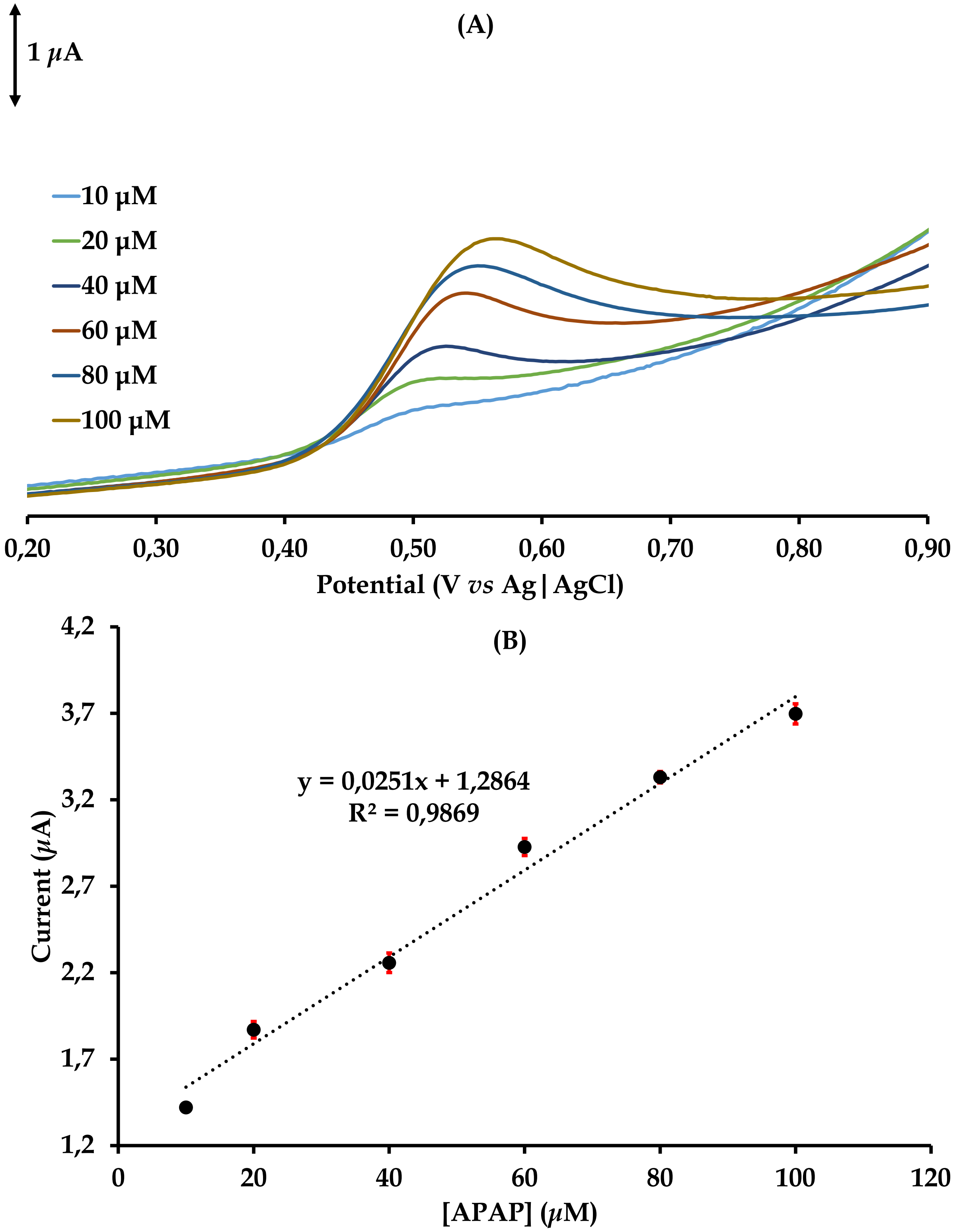

Figure 6.17: ***(A)*** *Linear sweep voltammograms at GCE|ENFs-**2**-Nf in different concentrations of APAP, PBS buffer (pH = 3.09).* ***(B)*** *Calibration curve of current response vs concentration.*

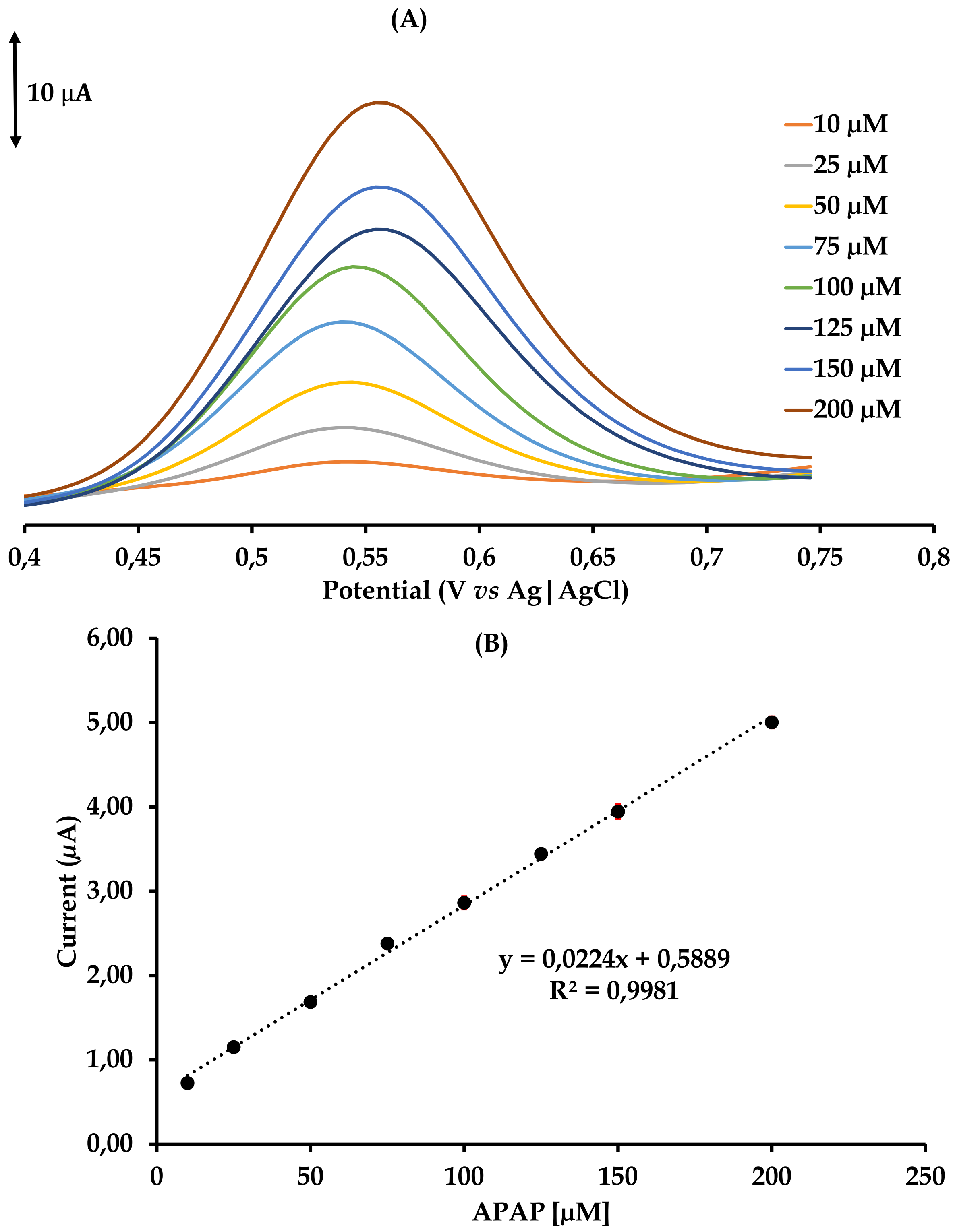

Figure 6. 18: ***(A)*** *SWVs were recorded at different concentrations of APAP prepared in 0.1 M PBS (pH 3.11) using the |GCE-ENF-2-NF.* ***(B)*** *Calibration curve of the current response against APAP concentration (10 to 200 µM).*

Remarkably, SWV exhibited superior LOD and LOQ compared to other electrochemical techniques such as linear sweep voltammetry with a rotating disk electrode (LSV-RDE) and chronoamperometry (CA), refer to **Table 6.3**. Moreover, SWV produces a higher linear correlation coefficient of 0.998 compared to those attained using RDE-LSV (0.987) and CA (0.9621). The aforementioned trend could be rationalized from the SWV technique simultaneously adsorbing APAP on the CME interface via oxidation followed by seamless removal of the oxidized APAP species during the reverse potential cycle. In the process, the electrocatalytic sites of the CME are replenished as opposed to RDE-LSV and CA where only the DA oxidation process is investigated. In light of the better analytical parameters attained using SWV, the study was further advanced using this technique

In comparison to other chemically modified GCEs reported in the literature, the GCE modified with ENFs-**2**-Nf demonstrated comparable LOD values for APAP electrochemical sensing, *see* **Table 6.3**. For instance, the *f*-MWCNT–CoPc/AuNPs/GCE produced a LOD value of 0.135 µM and a linear range of 1.49 – 47.6 µM.[70] The GCE|ENFs-**2**-Nf has a lower LOD than the aforementioned CME, highlighting its competitive analytical sensitivity. However, the PANI/ZnO/GCE achieved a lower LOD value of 0.01 µM and a linear range of 0.01 - 0.07 µM for APAP detection, making it more sensitive at lower concentrations compared to the GCE|ENFs-**2**-Nf.[71] Noteworthy, the GCE|ENFs-**2**-Nf has a linear range of detection which expands over a wider potential window than PANI/ZnO/GCE.

Table 6.3: *Comparison of LOD values for GCE|ENFs-***2***-Nf towards the detection of APAP values reported in the literature.*

Type of electrode	**Technique**	**LOD**	**Linear RANGE**	**Reference**
GCE|ENFs-2-Nf	SWV	0.094 µM	10 – 200 µM	This work
GCE|ENFs-2-Nf	LSV	1.72 µM	10 - 100 µM	This work
GCE|ENFs-2-Nf	CA	2.99 µM	10 - 100 µM	This work
f-MWCNT–CoPc/AuNPs/GCE	SWV	0.135 µM	1.49- 47.6 µM	[70]
PANI/ZnO/GCE	DPV	0.01 µM	0.01 -0.07 µM	[71]
film-**1**/ITO	DPV	1.3 µM	1 - 100 µM	[72]
PANI-MWCNTs-GCE	SWV	0.25 µM	1-100 µM	[57]
PNR/MWCNT/GCE	DPV	0.015 µM	2.0–70 µM	[73]

Abbreviations: Film-1/ITO: dimeric bis(phthalocyaninato) europium complex/Indium Tin Oxide electrode, **PANI:** Polyanilline, **MWCNTs:** Multi wall carbon nanotubes, **GCE:** Glassy carbon electrode, **ZnO:** Zinc Oxide, **CoPc:** Cobalt Phthalocynine, **AuNPs:** Gold nanoparticles, **PNR:** poly(neutral red)

6.3.11. Interference/Selectivity studies

The selectivity of the GCE|ENFs-**2**-Nf electrode towards APAP was assessed in the presence of metronidazole (MTZ) and dopamine (DA). The SWV responses for 1 mM APAP in PBS at the GCE|ENFs-2-Nf electrode in the presence of 1 mM of MTZ and DA are presented in **Figure 6.19**. The SWV response at GCE|ENFs-**2**-Nf exhibited a notable peak separation between APAP and MTZ, indicating that the electrode can selectively detect APAP even in the presence of MTZ. However, the peaks corresponding to DA and APAP were not well resolved, suggesting competitive binding to the electrocatalytic sites of the CME. The comparable redox potentials of DA and APAP can be justified by their close structural similarities. In fact, this trend is common in electrochemical sensing of APAP in biological fluids, where its co-existence of APAP with ascorbic acid (AA) and dopamine (DA) poses a peak overlap difficulty due to their similar redox potentials.[65] In this case, the presence of DA affects the peak current of APAP by causing an increase in the APAP current peak due to overlapping signals. **Figure 6.19(B)** demonstrates this effect, showing the impact on APAP's peak current when DA is present.

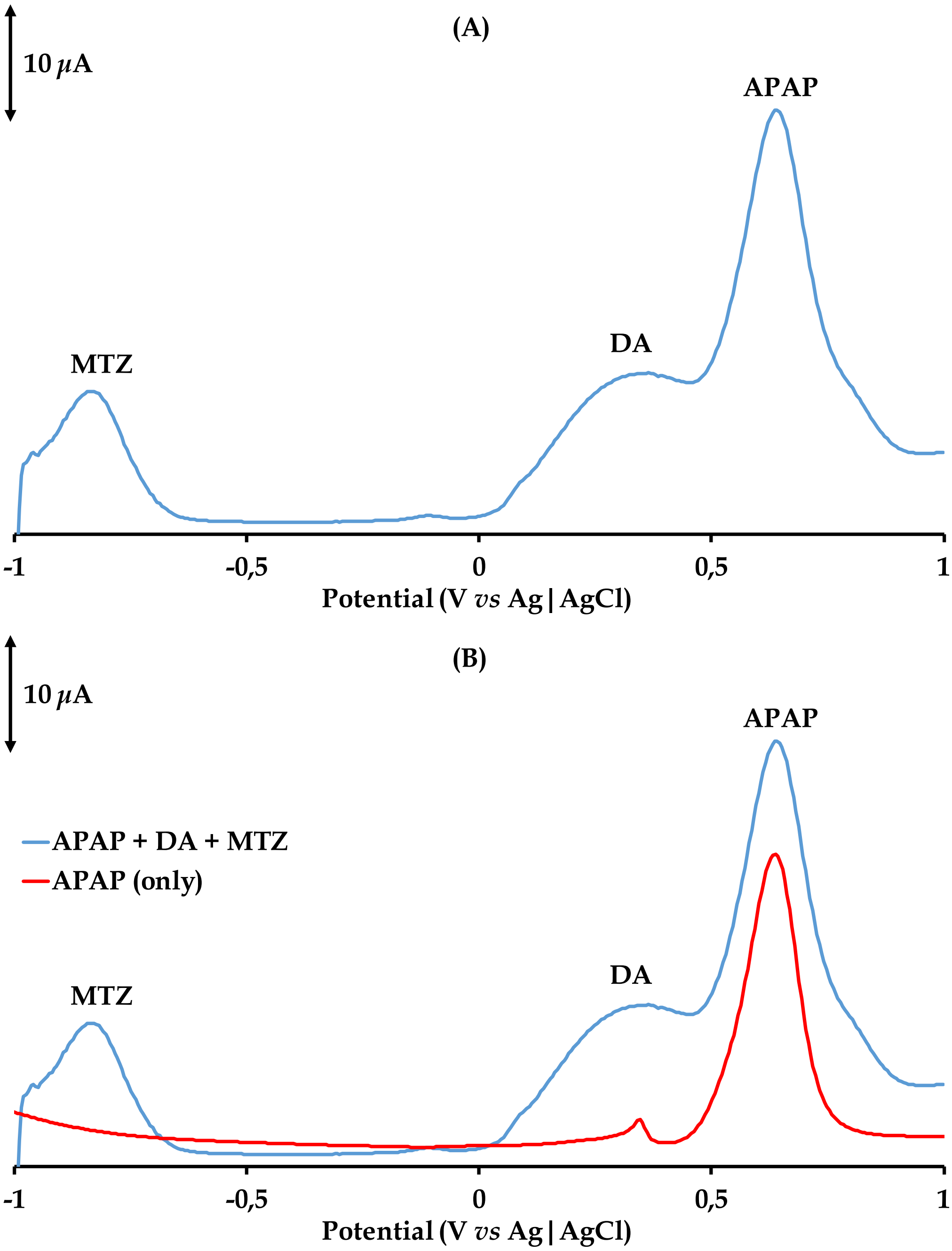

Figure 6.19: *SWV responses of* ***(A)*** *1 mM APAP in 0.1 M PBS in the presence of 1 mM of MTZ and DA, using the GCE|ENFs-***2***-Nf and* ***(B)*** *a comparison of the current responses of 1 mM APAP alone and in the presence of potential interferences (1 mM each of MTZ and DA).*

6.3.12. *Real water sample analysis*

The detection of APAP in an actual sample taken from the Umsunduzi River was performed using the GCE|ENFs-**2**-Nf electrode. To assess the sensor's performance, a recovery study was conducted to verify its accuracy and reliability, see **Figure 6.20**. The sample from the river had an APAP content below the limit of detection (LOD) of the electrode. Therefore, the standard addition method was used to calculate the percentage recovery, which allowed the evaluation of the sensor's applicability. In the recovery study, a 3 mM standard solution of APAP was added to the genuine river samples in 0.5 mL increments. The calculated percentage recovery was determined to be 103.8% (%RSD = 3.60, N = 3), falling within the acceptable range of 95-105%. This result indicates that the GCE|ENFs-**2**-Nf is capable of accurately detecting and quantifying APAP in actual environmental samples, establishing it as a reliable sensor for environmental monitoring applications.

Moreover, to assess the accuracy of the GCE|ENFs-**2**-Nf in detecting APAP in real samples, incremental volumes of 10 μM APAP were spiked into the electrode and analyzed using HPLC-MS. The results are presented in **Table 6.4** and **Figure 6.21**. A 106% recovery of APAP was calculated from the calibration curve. This reference data validates the accuracy of the fabricated GCE|ENFs-**2**-Nf in detecting trace amounts of APAP. Notably, this recovery value closely aligns with the 103.8% estimated from the standard method using the GCE|ENFs-**2**-Nf. The close agreement between the values obtained from the GCE|ENFs-**2**-Nf and the HPLC-MS reference method underscores the high accuracy and reliability of the GCE|ENFs-**2**-Nf sensor for detecting APAP in real water samples.

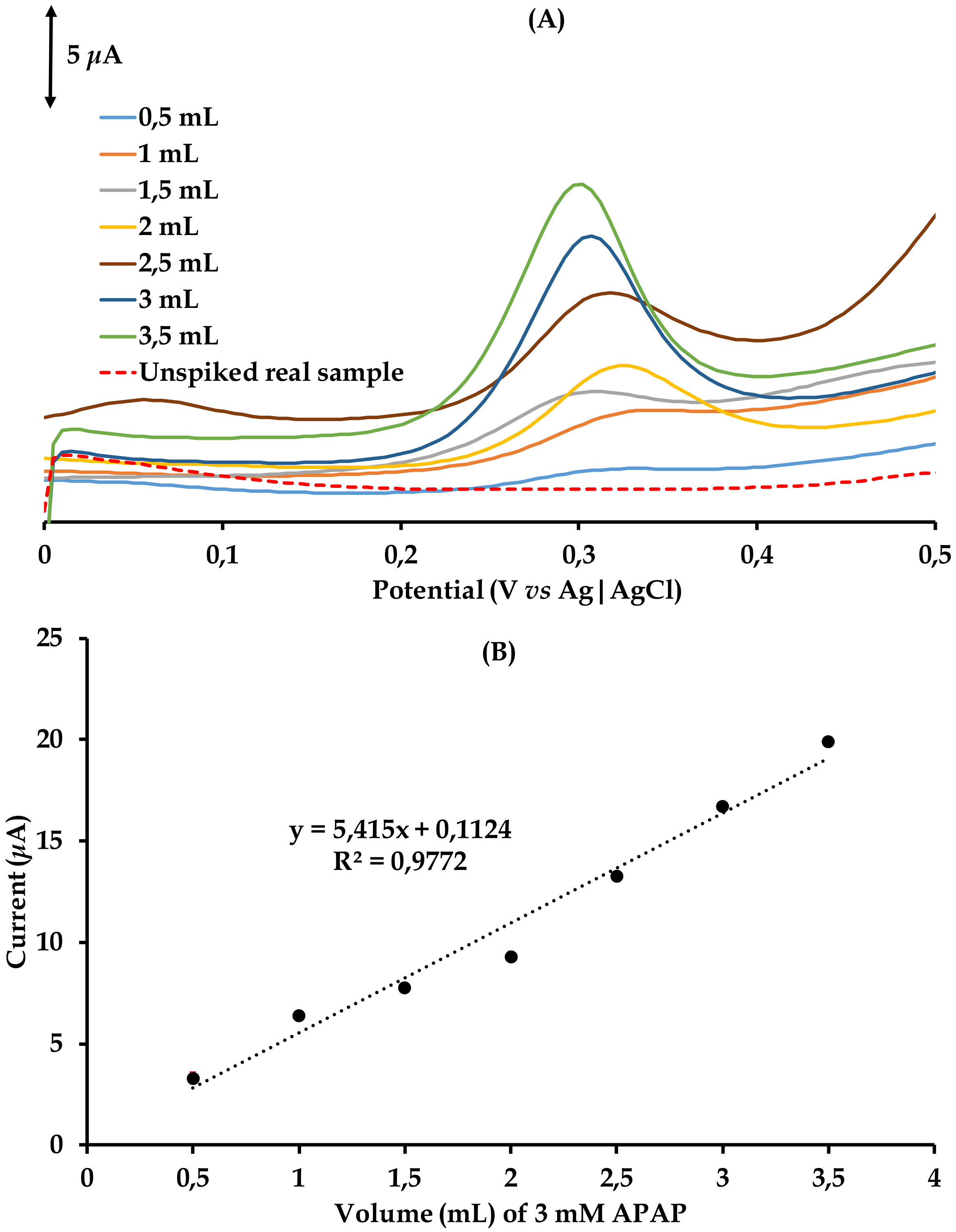

Figure 6.20: *(A) Overlay DPVs of the real water sample spiked with incremental volumes (0.5 mL) of the 3mM standard of APAP at the GCE|ENFs-2-Nf collected from the UMsunduzi river,* ***(B)*** *The standard addition calibration plot.*

Table 6.4: *The measured LC-MS peak areas of APAP spiked in 20 mL of the Umsunduzi River water sample after the incremental addition of 2 mL of 10 µM APAP.*

Volume (mL)	Retention Time (minutes)	Peak Area
2	6.162	2921200
4	6.200	3857781
6	6.161	4766368
8	6.120	5565205
10	6.166	6798326
12	6.134	7600492

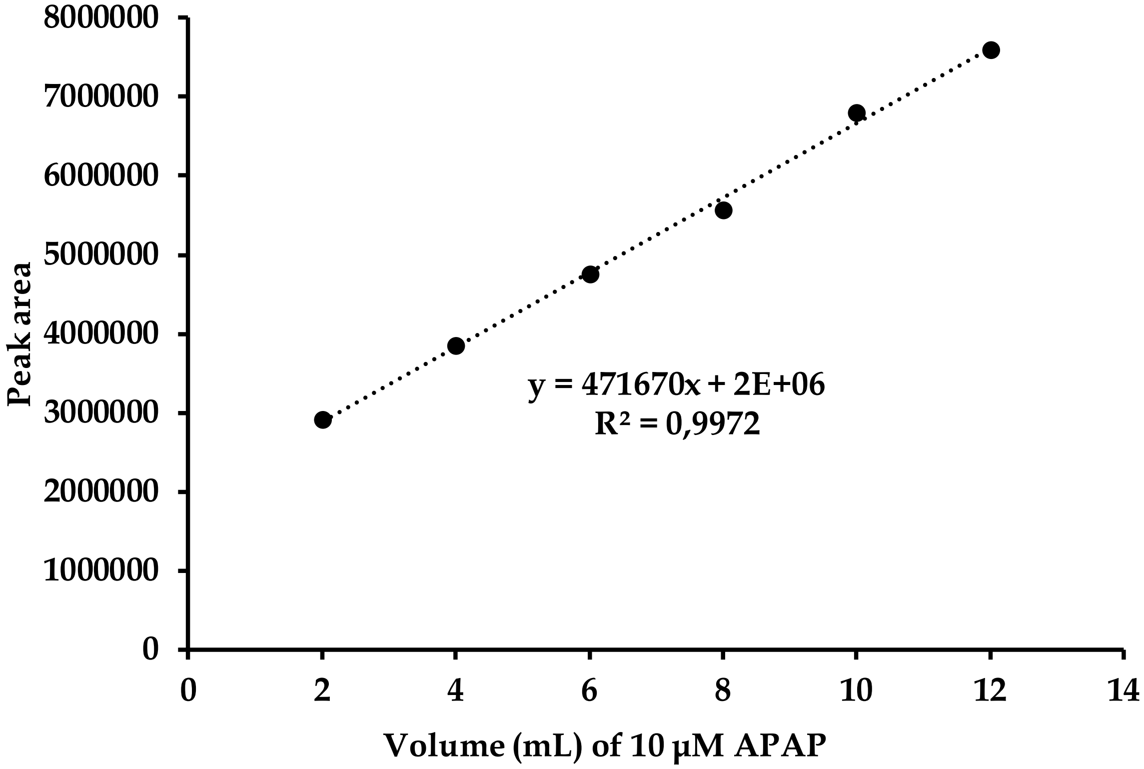

Figure 6.21: *The real water sample spiked with incremental volumes (2 mL) of the 10 µM standard of APAP detected using LC-MS (collected from the UMsunduzi River).*

6.4. Conclusions

Morphological probing and elemental compositional analysis of the core-shell polymeric nanoconjugate, ENFs-**2** were performed using SEM-EDX. The encapsulation of the PANI-CoPc-fur-*f*-MWCNTs inner core by the PVA outer shell was confirmed by solid-state FTIR and Raman spectroscopy as well as powder X-ray diffraction. The performance of the GCE|ENFs-**2**-Nf electrode surpasses that of the bare GCE electrode or other prepared CMEs. Under the optimized electrocatalytic conditions, SWV exhibited superior LOD and LOQ of 0.094 and 0.28 µM respectively, compared to other electrochemical techniques such as linear sweep voltammetry with a rotating disk electrode (LSV-RDE) and chronoamperometry (CA). Additionally, it demonstrated selectivity for APAP in the presence of other interfering pharmaceuticals such as MTZ and DA. Furthermore, the performance of the CME in sensing APAP in a real water sample was comparable to that of HPLC-MS. Specifically, APAP percentage recoveries of 106% and 104% were achieved when using HPLC-MS and the CME, respectively.

6.5. References

(1) de la Torre, G.; Claessens, C. G.; Torres, T. *Chemical Communications* **2007**, 2000.

(2) Aftab, J.; Farajzadeh, N.; Yenilmez, H. Y.; Özdemir, S.; Gonca, S.; Bayır, Z. A. *Dalton Transactions* **2022**, *51*, 4466.

(3) Demir, F.; Yenilmez, H. Y.; Koca, A.; Bayır, Z. A. *Journal of Electroanalytical Chemistry* **2019**, *832*, 254.

(4) Palanna, M.; Aralekallu, S.; Prabhu, C. K.; Sajjan, V. A.; Sannegowda, L. K. *Electrochimica Acta* **2021**, *367*, 137519.

(5) Xing, R.; Yang, H.; Li, S.; Yang, J.; Zhao, X.; Wang, Q.; Liu, S.; Liu, X. *Journal of Solid State Electrochemistry* **2017**, *21*, 1219.

(6) Mphuthi, N. G.; Adekunle, A. S.; Fayemi, O. E.; Olasunkanmi, L. O.; Ebenso, E. E. *Scientific Reports* **2017**, *7*, 43181.

(7) Su, J.; Zhang, J.-J.; Chen, J.; Song, Y.; Huang, L.; Zhu, M.; Yakobson, B. I.; Tang, B. Z.; Ye, R. *Energy and Environmental Science* **2021**, *14*, 483.

(8) Kantize, K.; Booysen, I. N.; Mambanda, A. *International Journal of Electrochemical Science* **2022**, *17*, 22067.

(9) Zare, E. N.; Makvandi, P.; Ashtari, B.; Rossi, F.; Motahari, A.; Perale, G. *Journal of Medicinal Chemistry* **2019**, *63*, 1.

(10) Shoba, S.; Bankole, O. M.; Ogunlaja, A. S. *Analytical Methods* **2020**, *12*, 1094.

(11) Guo, M.; Chen, J.; Li, J.; Tao, B.; Yao, S. *Analytica Chimica Acta* **2005**, *532*, 71.

(12) Yan, J.; Wei, T.; Fan, Z.; Qian, W.; Zhang, M.; Shen, X.; Wei, F. *Journal of Power Sources* **2010**, *195*, 3041.

(13) Che, B.; Li, H.; Zhou, D.; Zhang, Y.; Zeng, Z.; Zhao, C.; He, C.; Liu, E.; Lu, X. *Composites Part B: Engineering* **2019**, *165*, 671.

(14) Thakur, A. K.; Deshmukh, A. B.; Choudhary, R. B.; Karbhal, I.; Majumder, M.; Shelke, M. V. *Materials Science and Engineering: B* **2017**, *223*, 24.

(15) Sonawane, J. M.; Pant, D.; Ghosh, P. C.; Adeloju, S. B. *Energy and Fuels* **2021**, *35*, 3385.

(16) Lee, E.-S.; Lei, D.; Devarayan, K.; Kim, B.-S. *Composites Science and Technology* **2015**, *110*, 111.

(17) Demirci Uzun, S.; Kayaci, F.; Uyar, T.; Timur, S.; Toppare, L. *ACS Applied Materials and Interfaces* **2014**, *6*, 5235.

(18) Teodoro, K. B.; Migliorini, F. L.; Facure, M. H.; Correa, D. S. *Carbohydrate Polymers* **2019**, *207*, 747.

(19) Bagheri, H.; Rezvani, O.; Zeinali, S.; Asgari, S.; Aqda, T. G.; Manshaei, F. In *Solid-Phase Extraction* **2020**, 311.

(20) Devina Merin, D.; Anith Jose, R.; Arulananth, T.; Allwyn Sundarraj, A.; Inbamalar, T.; Getnet Meharie, M. *Journal of Nanomaterials* **2023**, *2023*.

(21) Lin, H.-L.; Wang, S.-H.; Chiu, C.-K.; Yu, T. L.; Chen, L.-C.; Huang, C.-C.; Cheng, T.-H.; Lin, J.-M. *Journal of Membrane Science* **2010**, *365*, 114.

(22) Pan, W.; Lü, Z.; Chen, K.; Huang, X.; Wei, B.; Li, W.; Wang, Z.; Su, W. *Electrochimica acta* **2010**, *55*, 5538.

(23) Huang, S.-L.; Yu, H.-F.; Lin, Y.-S. *Journal of Chemistry* **2017**, *2017*.

(24) Samal, K.; Mahapatra, S.; Ali, M. H. *Energy Nexus* **2022**, *6*, 100076.

(25) Branchet, P.; Arpin-Pont, L.; Piram, A.; Boissery, P.; Wong-Wah-Chung, P.; Doumenq, P. *Science of The Total Environment* **2021**, *766*, 142644.

(26) Hazra, M.; Joshi, H.; Williams, J. B.; Watts, J. E. M. *Chemosphere* **2022**, *303*, 135148.

(27) Bouki, C.; Venieri, D.; Diamadopoulos, E. *Ecotoxicology and Environmental Safety* **2013**, *91*, 1.

(28) Ateba, C. N.; Tabi, N. M.; Fri, J.; Bissong, M. E.; Bezuidenhout, C. C. *Antibiotics* **2020**, *9*, 745

(29) Kumar, R.; Qureshi, M.; Vishwakarma, D. K.; Al-Ansari, N.; Kuriqi, A.; Elbeltagi, A.; Saraswat, A. *Case Studies in Chemical and Environmental Engineering* **2022**, *6*, 100219.

(30) Park, J. C.; Yoon, D.-S.; Byeon, E.; Seo, J. S.; Hwang, U.-K.; Han, J.; Lee, J.-S. *Aquatic Toxicology* **2018**, *204*, 70.

(31) Antunes, S. C.; Freitas, R.; Figueira, E.; Gonçalves, F.; Nunes, B. *Environmental Science and Pollution Research* **2013**, *20*, 6658.

(32) B. Kondawar, S.; T. Patil, P.; P. Agrawal, S. *Advanced Materials Letters* **2014**, *5*, 389.

(33) Chohan, S.; Booysen, I. N.; Mambanda, A.; Akerman, M. P. *Inorganica Chimica Acta* **2016**, *447*, 183.

(34) Alharthi, S. S.; Alzahrani, A.; Razvi, M. A. N.; Badawi, A.; Althobaiti, M. G. *Journal of Inorganic and Organometallic Polymers and Materials* **2020**, *30*, 3878.

(35) Ningaraju, S.; Gnana Prakash, A. P.; Ravikumar, H. B. *Solid State Ionics* **2018**, *320*, 132.

(36) Pauly, A.; Saad Ali, S.; Varenne, C.; Brunet, J.; Llobet, E.; Ndiaye, A. L. *Polymers* **2022**, *14*, 891.

(37) Kang, H.; Staples-West, A.; Washington, A.; Turchiano, C.; Cooksy, A.; Huang, J.; Gu, J. *ChemCatChem* **2023**, *15*, e202300576.

(38) Manuel, J.; Salguero, T.; Ramasamy, R. P. *Journal of Applied Electrochemistry* **2019**, *49*, 529.

(39) Furukawa, Y.; Ueda, F.; Hyodo, Y.; Harada, I.; Nakajima, T.; Kawagoe, T. *Macromolecules* **1988**, *21*, 1297.

(40) Nepomuceno, N. C.; Seixas, A. A. A.; Medeiros, E. S.; Mélo, T. J. A. *Journal of Solid State Chemistry* **2021**, *302*, 122372.

(41) Li, W.; Diao, K.; Qiu, D.; Zeng, Y.; Tang, K.; Zhu, Y.; Sheng, Y.; Wen, Y.; Li, M. *Food Chemistry* **2021**, *350*, 129229.

(42) El-Sawy, A. M.; Abdo, M. m. H.; Darweesh, M. A.; Salahuddin, N. A. *Journal of Molecular Structure* **2023**, *1272*, 134217.

(43) Kizildag, N.; Ucar, N.; Oztoksoy, M. E.; Garmestani, H.; Wang, Y.; Dahmen, K. H., *The International Istanbul Textile Congress* **2013,** *1*, 6

(44) Szybowicz, M.; Bała, W.; Fabisiak, K.; Paprocki, K.; Drozdowski, M. *Journal of Materials Science* **2011**, *46*, 6589.

(45) Sharma, A.; Goyal, P. K.; Rawal, I.; Rajpal, A.; Khokhar, A.; Kumar, V.; Dahiya, S. *Optical Materials* **2022**, *131*, 112712.

(46) Mallakpour, S.; Abdolmaleki, A.; Azimi, F. *Ultrasonics Sonochemistry* **2017**, *39*, 589.

(47) Kunpatee, K.; Chamsai, P.; Mehmeti, E.; Stankovic, D. M.; Ortner, A.; Kalcher, K.; Samphao, A. *Journal of Electroanalytical Chemistry* **2019**, *855*, 113630.

(48) Deshmukh, S. P.; Dhodamani, A. G.; Patil, S. M.; Mullani, S. B.; More, K. V.; Delekar, S. D. *ACS Omega* **2020**, *5*, 219.

(49) Chen, Z.; Luo, J.; Huang, Z.; Cai, C.; Tusiime, R.; Li, Z.; Wang, H.; Cheng, C.; Liu, Y.; Sun, Z.; Zhang, H.; Yu, J. *Composites Communications* **2020**, *21*, 100377.

(50) Chaturvedi, V. K.; Tripathi, A. D.; Minocha, T.; Singh, V.; Singh, M. P.; Yadav, D. P. *Journal of Cluster Science* **2023**.

(51) Kamil, A. M.; Hussein, F. H.; Halbus, A. F.; Bahnemann, D. W. *International Journal of Photoenergy* **2014**, *2014*, 475713.

(52) Zidan, H. M.; Abdelrazek, E. M.; Abdelghany, A. M.; Tarabiah, A. E. *Journal of Materials Research and Technology* **2019**, *8*, 904.

(53) Huang, W.; Li, J.; Xu, X.; Cao, A.; He, Y.; Sun, M.; Kang, L. *New Journal of Chemistry* **2022**, *46*, 7153.

(54) Qiu, S.; Li, Y.; Xu, H.; Liang, Q.; Zhou, M.; Rong, J.; Li, Z.; Xu, S. *Solid State Sciences* **2022**, *129*, 106905.

(55) Lakhdari, D.; Guittoum, A.; Benbrahim, N.; Belgherbi, O.; Berkani, M.; Vasseghian, Y.; Lakhdari, N. *Food and Chemical Toxicology* **2021**, *151*, 112099.

(56) Kang, X.; Wang, J.; Wu, H.; Liu, J.; Aksay, I. A.; Lin, Y. *Talanta* **2010**, *81*, 754.

(57) Li, M.; Jing, L. *Electrochimica Acta* **2007**, *52*, 3250.

(58) Kiaeefar, A.; Bolourian, H.; Raoufi, A.; Rajabi, N.; Ebrahimi, M. *Russian Journal of Physical Chemistry A* **2022**, *96*, 1273.

(59) Gholivand, M. B.; Amiri, M. *Journal of Electroanalytical Chemistry* **2012**, *676*, 53.

(60) Mugadza, T.; Nyokong, T. *Electrochimica Acta* **2010**, *55*, 2606.

(61) Ramadoss, A.; Kim, S. J. *Materials Chemistry and Physics* **2013**, *140*, 405.

(62) Nyoni, S.; Mugadza, T.; Nyokong, T. *Electrochimica Acta* **2014**, *128*, 32.

(63) Zen, J. M.; Senthil Kumar, A.; Chang, M. R. *Electrochimica Acta* **2000**, *45*, 1691.

(64) Sayadi, A.; Pickup, P. G. *Electrochimica Acta* **2016**, *215*, 84.

(65) Kantize, K.; Booysen, I. N.; Mambanda, A. *Journal of Electroanalytical Chemistry* **2019**, *850*, 113391.

(66) Mpeta, L. S.; Nyokong, T. *Journal of Electroanalytical Chemistry* **2019**, *840*, 218.

(67) Nkhahle, R.; Nyokong, T. *Materials Chemistry and Physics* **2022**, *280*, 125842.

(68) Li, T.; Xu, J.; Zhao, L.; Shen, S.; Yuan, M.; Liu, W.; Tu, Q.; Yu, R.; Wang, J. *Talanta* **2016**, *159*, 356.

(69) Houshmand, M.; Jabbari, A.; Heli, H.; Hajjizadeh, M.; Moosavi-Movahedi, A. A. *Journal of Solid State Electrochemistry* **2008**, *12*, 1117.

(70) de Holanda, L. F.; Ribeiro, F. W. P.; Sousa, C. P.; da Silva Casciano, P. N.; de Lima-Neto, P.; Correia, A. N. *Journal of Electroanalytical Chemistry* **2016**, *772*, 9.

(71) Chufamo, S.; Kelita, B.; Berhanu, S.; Kemal, A.; Lelago, A. *Advances in Materials Science and Engineering* **2022**, *2022*, 5186638.

(72) Cai, X.; Wei, C.; Dong, J.; Liu, Q.; Wu, Y.; Lu, G.; Chen, Y.; Jiang, J. *Journal of Materials Science: Materials in Electronics* **2019**, *30*, 1976.

(73) Liang, X.; Zhou, Y.; Almeida, J. M. S.; Brett, C. M. A. *Journal of Electroanalytical Chemistry* **2023**, *936*, 117366.

Chapter 7

Conclusions and future work

7.1. Conclusions

A growing concern revolves around the prevalence of emerging water pollutants and those resistant to environmental degradation in our water bodies. These substances include pharmaceuticals and heavy metals which are typically qualitatively and quantitively analysed by traditional analytical techniques such as GC, HPLC, AAS or ICP which are time-consuming, costly, and require highly skilled experts. Consequently, there has been upsurge in research based on electrochemical sensors development. Electroanalytical techniques are gaining traction in routine water quality control due to their rapid detection capabilities, portability, minimal sample extraction requirements and cost-effectiveness. CMEs, tailored with conductive polymers, carbon nanotubes and N_4-metallocyclic complexes are being developed to facilitate affordable analytical methods designed to tackle the challenges posed by water pollutants. During this research project, CMEs encompassing CoPc composite films were constructed their electrocatalytic activities were explored towards various water pollutants.

The first experimental chapter demonstrates the fabrication of a click-modified glassy carbon electrode (GCE|clicked-α-CoPc-flav3) which exhibited superior response currents and reproducibility in the detection of dopamine standards, even in the presence of interfering pharmaceutical substances like AA and NVP. This CME consistently delivered accurate results when analyzing spiked real water samples, achieving an average recovery rate of 103%. The diffusion-controlled rate constant for the GCE|clicked-α-CoPc-flav3 was found to be in the order of magnitude (10^4 M^{-1} s^{-1}) and it is comparable to the previously reported data and the rate constant calculated for the oxidation of DA at the surface of the rotating GCE|clicked-α-CoPc-flav3. To further affirm its accuracy and reliability in real water samples, it was compared with HPLC-MS recovery which was close to that of GCE|clicked-α-CoPc-flav3, highlighting its potential for environmental water quality monitoring applications.

Subsequently, a novel peripherally benzotriazole (Bzt) cobalt phthalocyanine (CoPc-Bzt) was electrodeposited onto a platinum electrode surface in tandem with the pyrrole electropolymerization. Surface modification of the noble metal surface was confirmed by the ferricyanide redox probe where the higher effective surface area for the CME was attained than the bare Pt electrode. The Pt|PPy/CoPc-Bzt electrode exhibited remarkable electrocatalytic activity for Hg^{2+} and demonstrated selectivity for Hg^{2+} ions, even in the presence of other heavy metal ions like Cd^{2+} and Pb^{2+}. The electrode's performance in detecting Hg^{2+} cations in real water samples proved to be comparable to that of ICP-OES. Notably, it achieved 97% and 112% Hg^{2+} recoveries using CME and ICP-OES, respectively.

Then the morphological features of CoPc-flav, *f*-MWCNTs, PANI, PANI-CoPc-flav-*f*-MWCNTs composite and their network-shaped ENFs-**1** were extensively analysed and confirmed using various spectroscopic and microscopic techniques, including FTIR, Raman spectroscopy, powder X-ray diffraction and SEM-EDX. The performance of the Au|ENFs-**1**-Nf electrode was found to surpass that of the bare Au electrode. In addition, the Au|ENFs-**1**-Nf electrode exhibited excellent stability in Pb(II) detection, outperforming the Au|PANI, Au|*f*-MWCNTs, and Au|CoPc-flav electrodes. The electrocatalytic activity of the Au|ENFs-**1**-Nf electrode towards Pb(II) was significantly superior. Moreover, it demonstrated selectivity for Pb(II) ions in the presence of other interfering heavy metal ions like Hg(II) and Cd(II). The performance of the CME in sensing the Pb(II) cations in a real water sample was comparable to that of ICP-OES. In particular, the percentage Pb(II) recoveries of 115% and 103% were attained when using ICP-OES and the CME, respectively.

Thereafter, morphological probing and elemental compositional analysis of the core-shell polymeric nanoconjugate, ENFs-**2** were performed using SEM-EDX. The encapsulation of the PANI-CoPc-fur-*f*-MWCNTs inner core by the PVA outer shell was confirmed by solid-state FTIR and Raman spectroscopy as well as powder X-ray diffraction. The performance of the GCE|ENFs-**2**-Nf electrode surpasses that of the bare GCE electrode or other prepared CMEs. Under the optimized electrocatalytic conditions, SWV exhibited superior LOD and LOQ of 0.094 and 0.28 μM respectively, compared to other electrochemical techniques such as linear sweep voltammetry with a rotating disk electrode (LSV-RDE) and chronoamperometry (CA). Additionally, it demonstrated selectivity for APAP in the presence of other interfering pharmaceuticals such as MTZ and DA. Furthermore, the performance of the CME in sensing APAP in a real water sample was comparable to that of HPLC-MS. Specifically, APAP percentage recoveries of 106% and 104% were achieved when using HPLC-MS and the CME, respectively.

7.2. Future work

Throughout this PhD thesis, the importance of the CoPc substituents are clearly emphasizes with respect to selectivity, sensitivity and stability of the CMEs. The use of crown ethers (cr) as substituents in symmetrical and asymmetrical CoPcs can tailor their redox properties within the accumulation potentials of heavy metal cations. In addition, the presence of the lone pairs within these organocyclic moieties on the CoPc moiety allow them to serve as host-guest complex. The chemo-sensing capabilities of heavy metal cations using electrodes modified with crown ethers have been demonstrated. Variability in the intracyclic properties between crown ether and crown thioethers leads Crown thia-ethers share similar properties with crown ethers, but the polarizability of the lone pairs where the larger sulphur atoms enhances phase transfer and the extraction of softer Lewis acids, such as late transition metal ions. Heteronuclear crown ethers where sulphur atoms are introduced into the crown ether framework, complexation with soft transition metal ions (*e.g.* $Hg^{2+}$and Pb^{2+}) are generally enhanced.

Another core prospective objective is to fabricate CoPc nanoconjugates with semi-conducting nanoparticles for IR and UV-Vis spectro-electrochemical experiments.[7,8] This vision will be realized by using modifiable screen-printed electrodes and further advanced by using portable hand-held electrochemical instrumentation.[9] Finally, the MPc-based electrochemical sensor development is grateful to the support of the National Research Foundation and the University of KwaZulu-Natal but for the aspirations of fabricating spectroelectrochemical sensors to be realized, the aforementioned national funding agency and institution will need to make investments in sophisticated Autolab spectroelectrochemical instrumentation which can be interfaced with our current Autolab potentiostat-galvanostat equipped with an Electrochemical Impedance module.

References:

(1) Kralj, M.; Tušek-Božić, L.; Frkanec, L. *ChemMedChem* **2008**, *3*, 1478.

(2) Fabre, B.; Simonet, J. *Coordination Chemistry Reviews* **1998**, *178-180*, 1211.

(3) Jackson, D. T.; Nelson, P. N.; Weston, K.; Taylor, R. A. *Sensing and Bio-Sensing Research* **2023**, *41*, 100570.

(4) Jackson, D. T.; Nelson, P. N.; Booysen, I. N. *Journal of Molecular Structure* **2021**, *1227*, 129575.

(5) Siswanta, D.; Nagatsuka, K.; Yamada, H.; Kumakura, K.; Hisamoto, H.; Shichi, Y.; Toshima, K.; Suzuki, K. *Analytical Chemistry* **1996**, *68*, 4166.

(6) Garoz-Ruiz, J.; Perales-Rondon, J. V.; Heras, A.; Colina, A. *Electroanalysis* **2019**, *31*, 1254.

(7) Ghoorchian, A.; Afkhami, A.; Madrakian, T.; Rameshan, R.; Rameshan, C.; Hajian, A. *Sensors and Actuators B: Chemical* **2020**, *324*, 128723.

(8) Salhi, O.; Oularbi, L.; Ez-zine, T.; El Attar, A.; Chemchoub, S.; Aaddane, A.; El Rhazi, M. *ChemElectroChem* **2023**, *10*, e202300053

Appendix

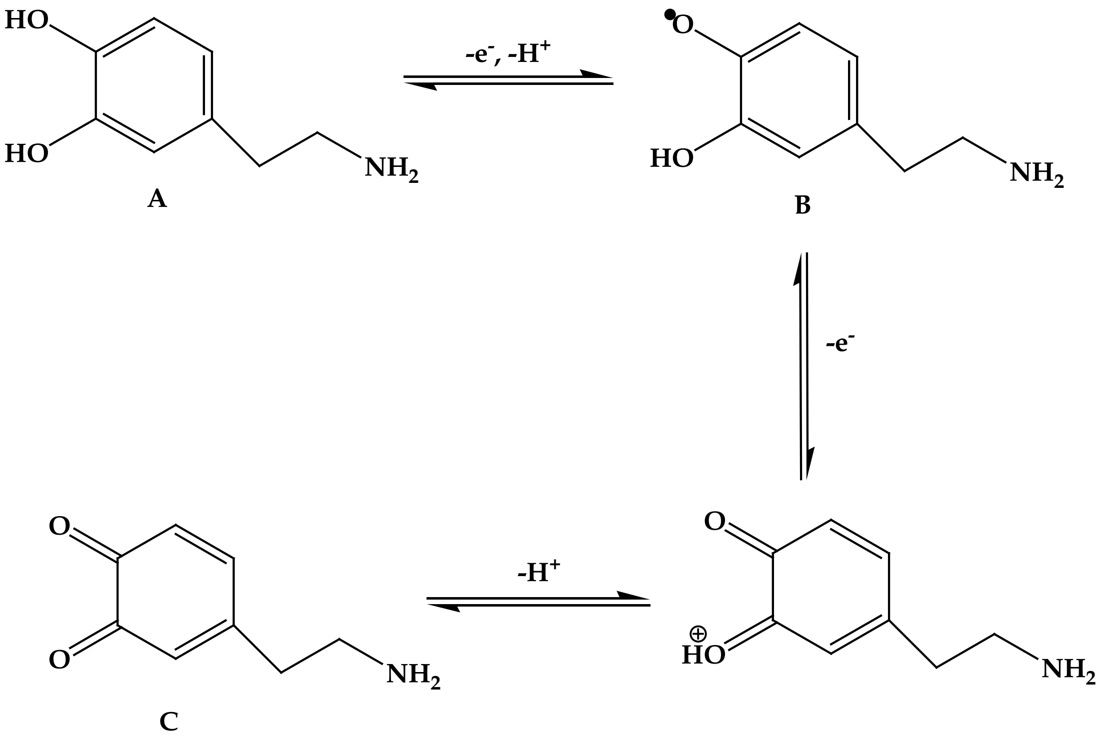

Scheme A1: *The characteristic reversible electrochemical transformations of dopamine using the GCE|clicked-a-CoPc-flav3.*

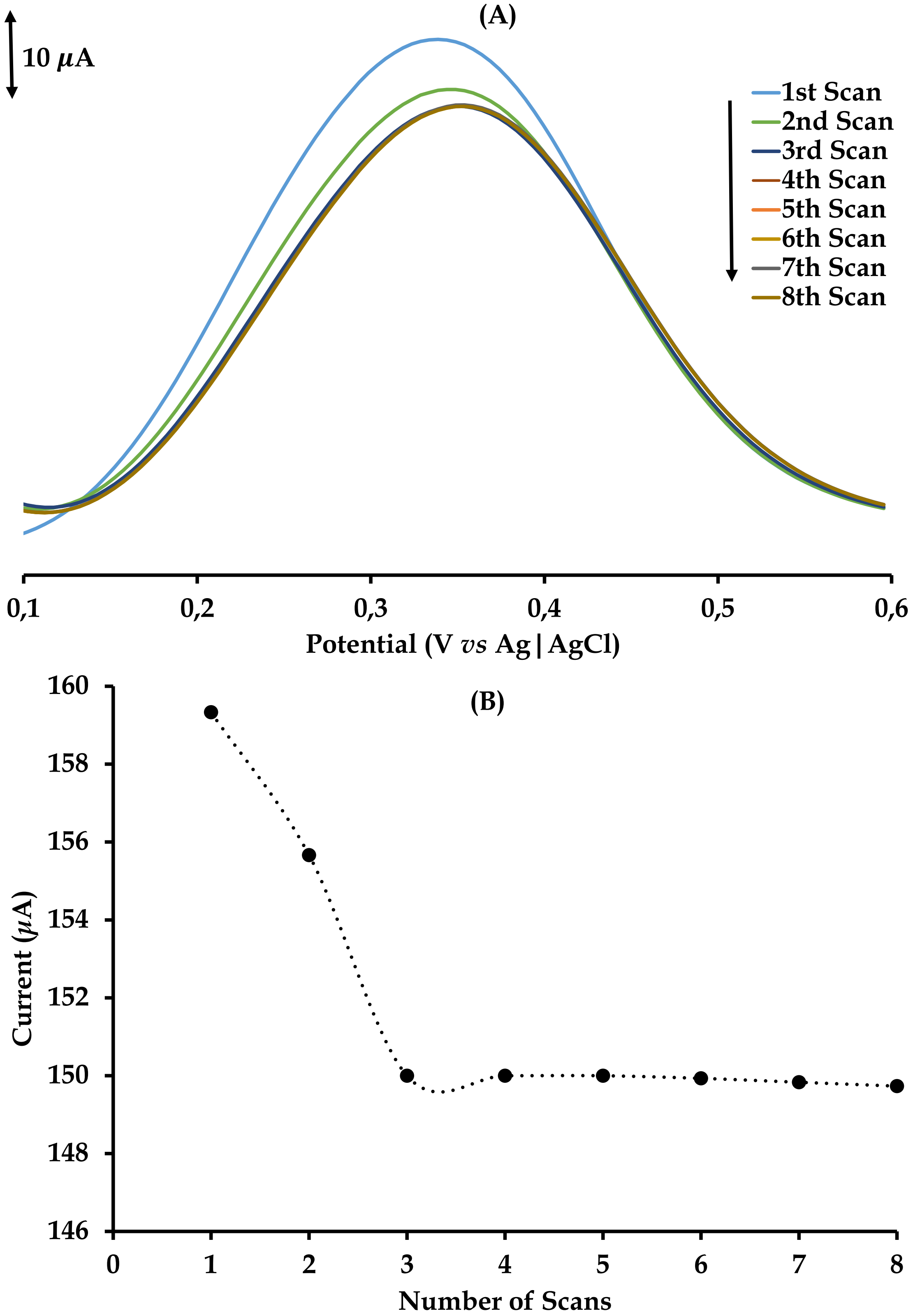

Figure A1: *Repetitive square-wave voltammogram scans (8) and the current responses of 1.00 mM DA at the GCE|clicked-a-CoPc-flav3 prepared in pH 6.20 PBS.*

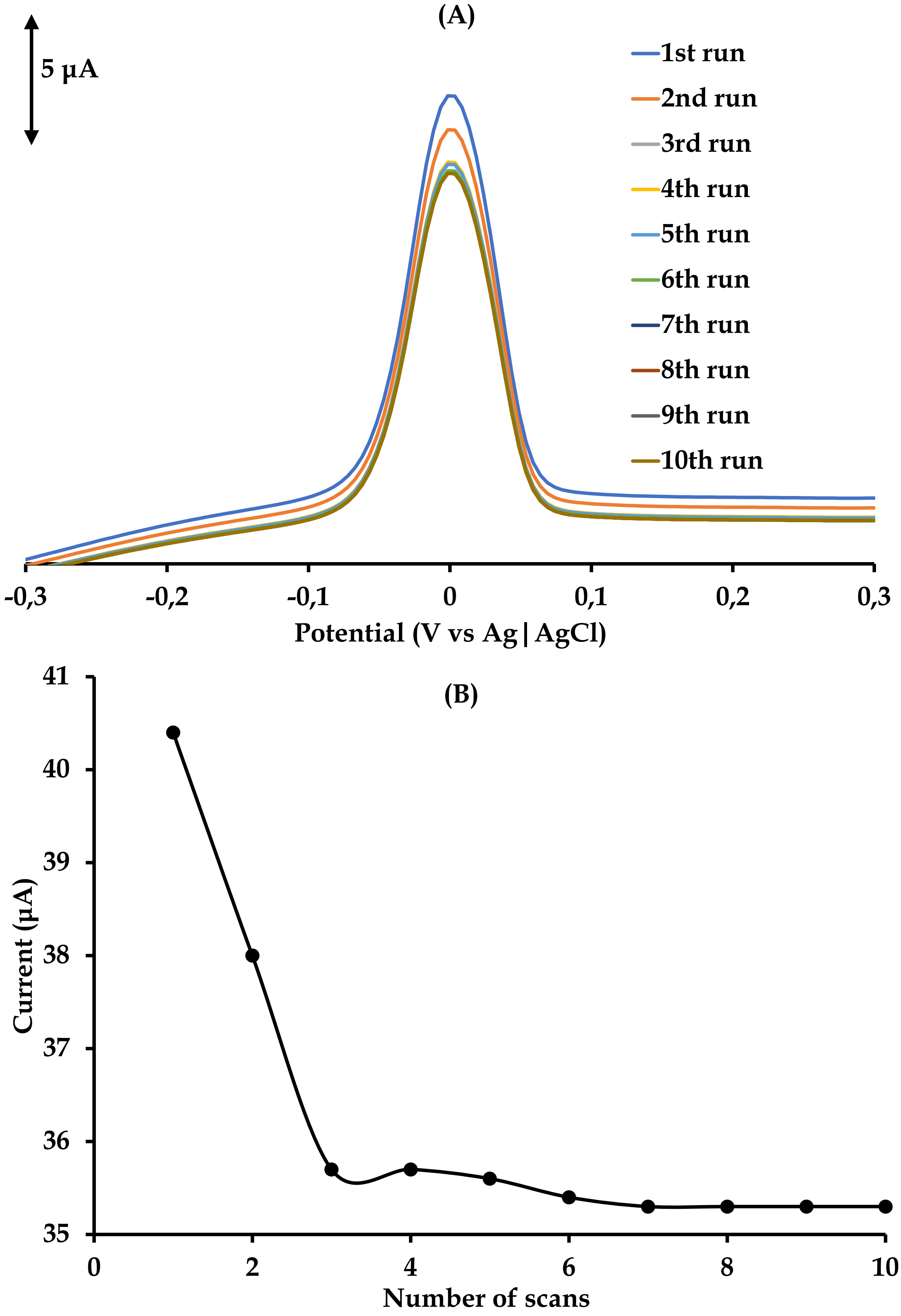

Figure A2: *Repetitive DPASV scans (10) at Pt|PPy/***2** *electrodes in 1 mM Hg(II) dissolved in 0.1 M HCl containing 0.4 M NaCl.*

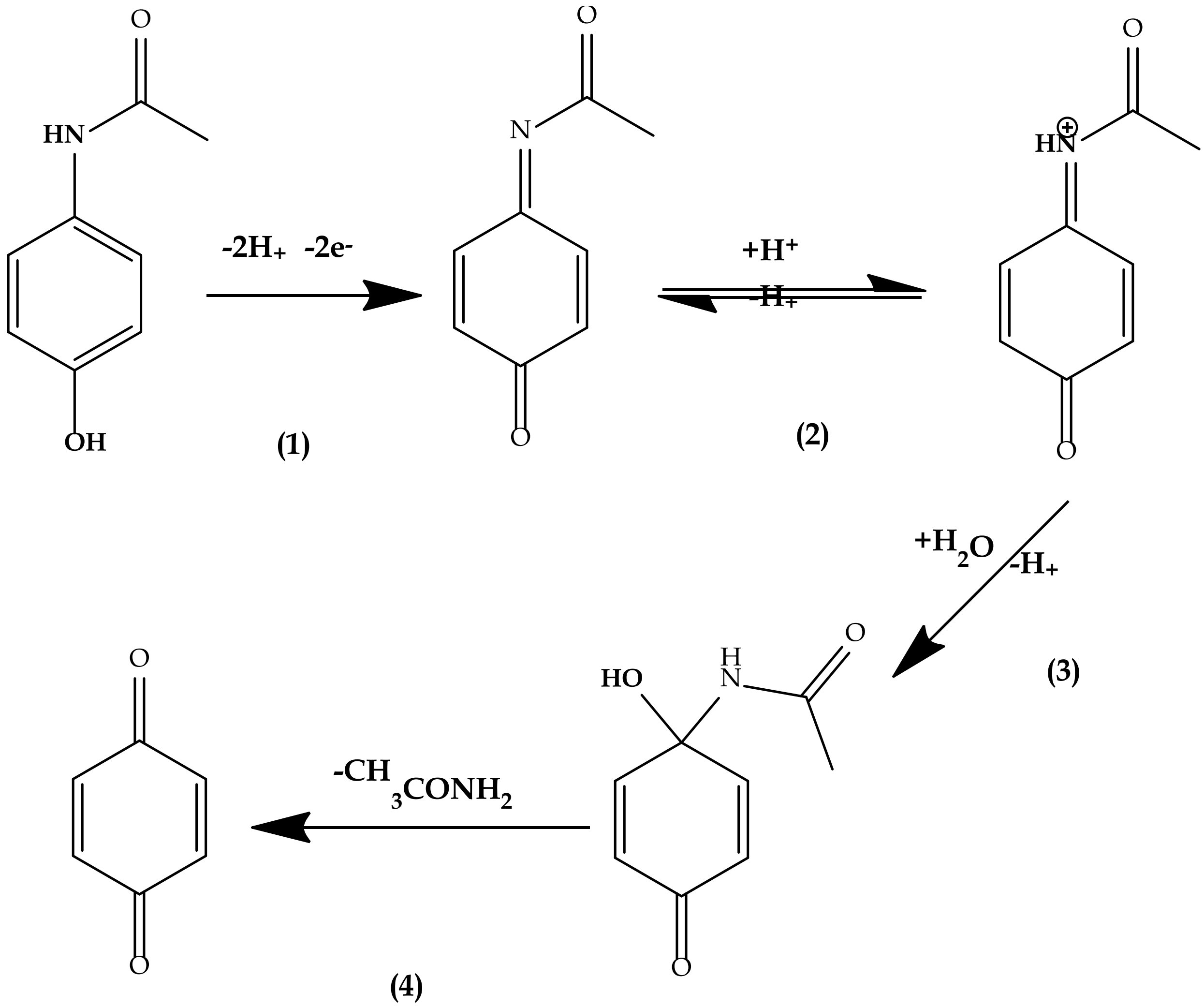

Scheme A2: The electrooxidation mechanism by which the bare and modified glassy carbon electrode detects acetaminophen(APAP).

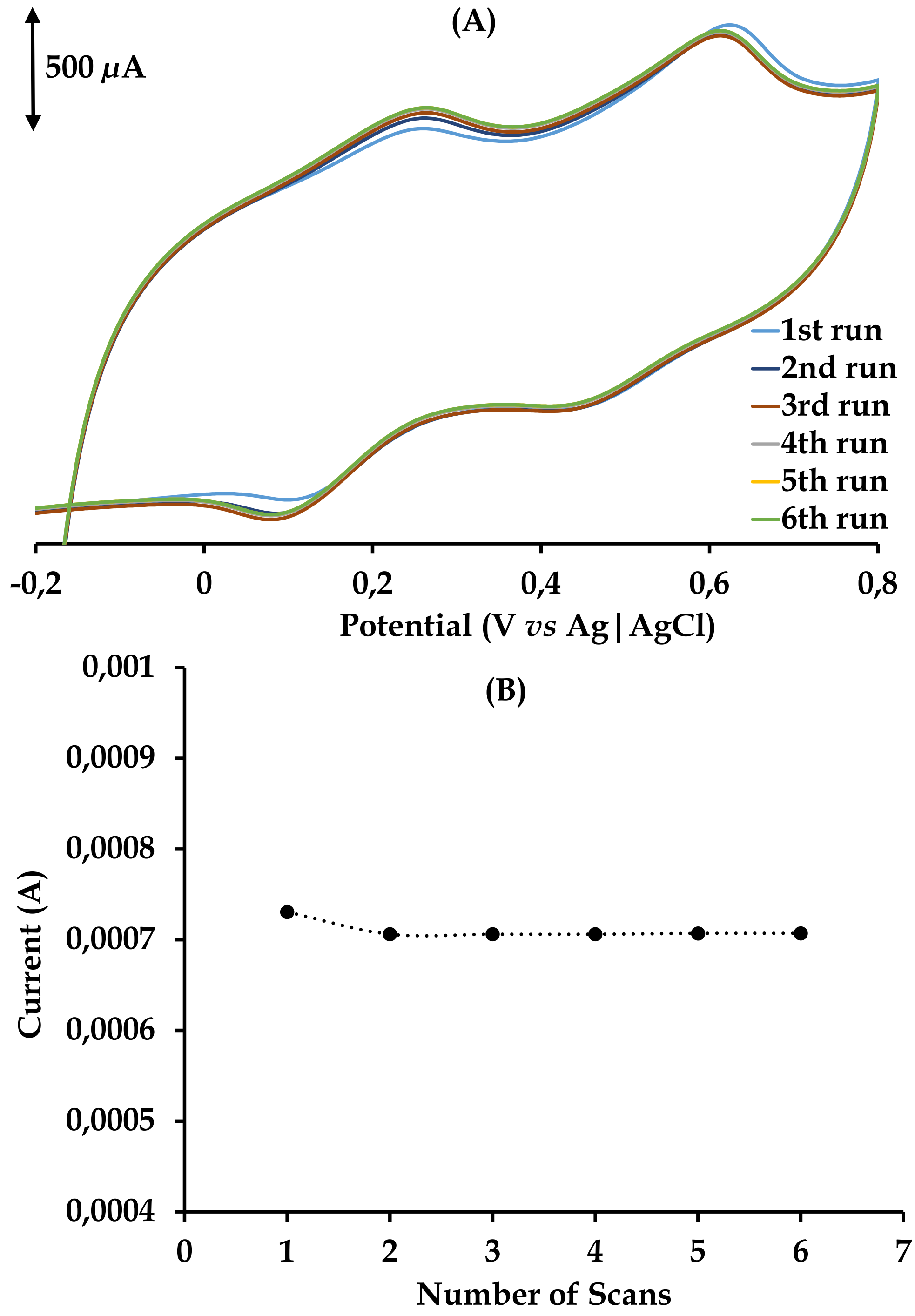

Figure A3: *Repetitive Cyclic voltammogram scans (6) and the current responses of 1 mM APAP at the |GCE-ENFs-2-NF prepared in pH 3.10 PBS.*